Universitat Autònoma de Barcelona

Interplay Between Ferroelectricity and Surface Chemistry in BaTiO3

Irena SPASOJEVIĆ

Universitat Autònoma de Barcelona

POSTGRADUATE SCHOOL

CHEMISTRY DEPARTMENT

Ph. D. THESIS

Interplay Between Ferroelectricity and Surface Chemistry in $BaTiO_3$

Thesis submitted by

Irena SPASOJEVIĆ

to apply for the Degree of DOCTOR at the Universitat Autónoma de Barcelona in the MATERIALS SCIENCE PROGRAM

Thesis Advisor: Dr. Neus DOMINGO MARIMÓN

Thesis Co-Advisor: Prof. Gustau CATALÁN BERNABÉ

Thesis Tutor: Dr. Jordi GARCÍA-ANTÓN AVIÑÓ

prepared at Institut Català de Nanociència i Nanotecnología (ICN2)

defended on:

June 2022

Dra. Neus Domingo Marimón científica titular y líder del grupo **Functional Atomic Force Microscopy** del **Center for Nanophase Materials Sciences (CNMS)** y el Prof. Gustau Catalán Bernabé, científico titular y líder del grupo **Oxide Nanophysics** del **Institut Català de Nanociència i Nanotecnologia (ICN2)**, en calidad de directores de tesis, y el Dr. Jordi García-Antón Aviñó, profesor titular del Departamento de Química de la **Universitat Autònoma de Barcelona**, en calidad de tutor de tesis.

CERTIFICAN:

Que Irena Spasojević, Bachiller en Fisicoquímica, ha realizado bajo su dirección y tutoría el trabajo que lleva por título "Interplay between ferroelectricity and surface chemistry in $BaTiO_3$". Dicho trabajo ha sido desarrollado dentro del programa de doctorado de Ciencia de Materiales y constituye su memoria de tesis doctoral, para optar por el grado de Doctor por la Universitat Autònoma de Barcelona.

Dra. Neus Domingo Marimón	Prof. Gustau Catalan Bernabé	Dr. Jordi García-Antón Aviñó
Functional Atomic Force Microscopy Group Leader	*Oxide Nanophysics Group Leader*	*Associate Proffesor*
CNMS	ICN2-ICREA	UAB

Bellaterra, 20 de abril de 2022

To my family

Acknowledgements

First, I would like to acknowledge financial support of the Secretaria d'Universitats i Recerca -Departament d'Empresa i Coneixement - Generalitat de Catalunya (FI grant reference 2020 FI_B2 00157) and the European Social Fund. This work would not have been possible without the support of this grant.

I wish to thank to the members of the tribunal for taking their time to read and evaluate this thesis. I hope that you enjoy it as much as I did and that it might inspire you in your research.

I would like to express my deepest appreciation to my supervisors Neus Domingo and Gustau Catalán, who introduced me to the exciting field of ferroelectrics and allowed me the opportunity to pursue this thesis in the Oxide Nanophysics Group. While their wealth of knowledge was invaluable in formulating the research questions, their constructive comments and advices throughout the entire journey, always encouraged me to think out of the box and do my best.

Neus, thank you for all of our long and fruitful conversations, your devotion and persistent help, as well as for motivating me to sharpen my scientific thinking. I thoroughly enjoyed all of our synchrotron beamtimes and those decision-making moments, when we would leave knowing that the long days had been well worth it. I also consider myself extremely fortunate to have the opportunity to study Atomic Force Microscopy under your guidance.

Gustau, thank you for your thorough revisions of this thesis, as well as for your numerous experimental ideas, remarks and insightful suggestions, from which I have learned a lot. Your advices will never be forgotten.

I am also grateful to Jordi García-Antón Aviñó, who accepted to be a tutor of this thesis. I sincerely appreciate your promptness in responding to all of my concerns.

I express my sincere gratitude to José Santiso, for his help and enthusiasm with the diffraction measurements and interpretation of the obtained results. Your great expertise and ability to explain the complicated phenomena in a simple way have always been an inexhaustible source of motivation.

I would like to offer my special thanks to my friend José Manuel Caicedo Roque for his support from the moment I arrived to the group. Thank you for your dedication and patience in learning

me how to operate the Pulsed Laser Deposition system and guiding me on how to produce those amazing ferroelectric thin films. Every day's jokes were an important part of getting me through the tough days.

To my office and doctoral thesis companions:

Laura, I appreciate you being there for me, listening to me, and offering your support. Your presence and your character would always make me calm and relaxed in stressful situations.

Christina, we started our doctoral journeys nearly at the same time and now we are about to finish it. I am thankful for the days (and nights) we spent together in the synchrotron and in the AFM lab, patiently waiting to capture the phase transition. I am grateful for our chance to share some exciting moments, like our first oral presentations, where we would support and cheer each other on.

Pablo, I was happy to share the office with you during my PhD. Our daily conversation about random things and your positive attitude would always cheer me up.

I am indebted to the past and present members of the group who supported me along this journey: Fabian, Kumara, Nathalie, Ela, Martí, Xin, Ying, David, Saptam, Gabriele, Blai and Nona. I want to thank you for making this stage of my life memorable for me through your valuable suggestions, help in the lab, or simply our daily conversations. I hope that our paths will cross again.

I am also very grateful to Jessica Padilla, who provided me with the results of numerous diffraction measurements efficiently, often in the short time frame, for the ongoing experiments. I also want to thank to Guillaume Sauthier and Nacho Villar for their generous help with X-ray photoelectron spectroscopy measurements at ICN2 and in ALBA synchrotron.

I also wish to thank to my Serbian friends in Barcelona Milena and Mina, who made me feel like I was at home.

The most important pillars in my life, as well as during this thesis, were my parents Svetlana and Vojislav. My appreciation for your patience, your wise advices, your unconditional support, and the emotional rollercoaster you had to endure standing by my side cannot be expressed in words. Hvala vam za svaku reč podrške tokom celokupnog školovanja pa tako i ovog doktorata, za svaku ohrabrujuću poruku poslatu rano ujutru ili kasno uveče, za svako "Ti

to možeš", za sva vaša odricanja zarad mog dobra. Vi ste vetar u mojim jedrima i moja sigurna luka. Trojanci, volim vas najviše na svetu.

I would also like to thank to my aunt, uncle, all my cousins and especially to my grandma for their messages of support and their understanding for my frequent absences. Hvala vam što stalno mislite na mene i što se uvek verovali u moj uspeh tamo negde daleko. Bako, hvala ti za svaku najlepše napisanu rođendansku čestitku i moju omiljenu lisnatu pogaču.

Cristian, I cannot thank you enough for your compassion, constant encouragement and your selfless care for me, especially during those times when I couldn't. My daily motivation comes from you, a ray of sunshine on a gloomy day that makes me smile. My special thanks goes to your family for the special moments and also to yours (and also a bit mine) German shepherd dog called Duck (yes, you have read correctly, it's a fluffy dog named after a bird).

Abstract

Ferroelectric materials possess permanent electric polarization, which can be reoriented between possible equilibrium states by the application of external electric field of proper orientation and magnitude. Due to the finite size of ferroelectric materials, a discontinuity of polarization arises at the interface between ferroelectric and surrounding medium, giving rise to the bound charge and a depolarizing field. In some cases, this field might be sufficiently high to jeopardize ferroelectric stability if not properly screened. Necessary screening charges can be supplied internally in the form of free charge carriers, externally by metallic electrodes or, alternatively in case of bare (electrode-free samples), by different adsorbate species.

Water, as the most common atmospheric adsorbate, is able to provide efficient dipolar screening due to its polar nature, but will also dissociate on charged species such as hydroxyl (OH^-) and hydronium (H_3O^+) ions which actively participate in the screening process. This is of particular importance for the bare ferroelectric thin films whose properties are commonly studied in ambient conditions by piezoresponse force microscopy (PFM). It has been demonstrated that the stability and growth of domains (which would be the 'bits' in ferroelectric memories), artificially patterned by biased tips in Atomic Force Microscopy (AFM), are influenced by relative humidity (RH) in different possible ways, with the general trend of increasing domain size as a function of RH. Besides the fundamental importance of RH in the screening processes, the effect of RH on domain size (and therefore bit density), coercive voltage, and maximum speed at which information can be encoded in ferroelectric thin films is of practical interest for information storage applications.

Driven by the depolarization field screening, ferroelectrics can also develop polarization-specific surface chemical states (e.g. stoichiometry, electronic and structural configurations), which further govern adsorption, desorption and barriers for chemical reactions of adsorbate molecules on polarized ferroelectric surfaces. Therefore, it can be expected that oppositely-polarized surfaces will exhibit different surface chemical compositions. Exploration of ferroelectric surface chemistry is of vital importance since i) it enables recognition of chemical species and their role in polarization screening of particularly oriented ferroelectric polarization and ii) the unique coupling between polarization and surface chemical activity, whereby the latter can be tuned by the change of polarization by external parameters such as temperature, stress or electric field, makes ferroelectrics superior candidates for catalysis, compared to

surfaces with fixed adsorbate-substrate interactions. Besides changes in surface chemical activities, modification of polarization magnitude by change of temperature or application of stress also implies emergence of temporary surface charge, which is a driving force for surface redox reaction in the processes of pyroelectrocatalysis and piezoelectrocatalysis, respectively.

Moreover, the relation between surface chemistry and ferroelectricity is bidirectional: any change in the surface-chemical composition leads to a change in surface boundary conditions and depolarizing fields, that altogether may have profound effect on the dipolar interactions and ferroelectric properties of thin films, where surface-to-volume ratios are high. In turn, this opens new pathways towards chemically controlled ferroelectricity, where by the tuning of surface chemistry desired ferroelectric properties could be achieved or, vice versa, the modification of polarization by external fields can be exploited in (ferro)catalytic processes. However, in reality these are challenging tasks due to severe limitations in our experimental knowledge of the chemical interactions at the surfaces of ferroelectric thin films. These limitations include both the actual chemical species involved, and the dynamics of the electrochemical screening process - which, in turn, affect the maximum switching speeds that can be reached in the ferroelectric film. This doctoral thesis sets out to explore these aspects. Specifically:

- In order to understand complex processes occurring at the ferroelectric surfaces and take advantage of them, it is important to identify all the chemical species (the *main players*) and their behavior (the *game they play*) in different experimental frameworks and time scales. Besides so far established water and hydroxyl groups, somewhat more complex chemical species such as metal-peroxide compounds can be expected, which can evolve as a function of time exposure to ambient conditions and ferroelectric polarization. In this thesis, I explore the surface composition of $BaTiO_3$ thin films as a function of the ferroelectric polarization direction and time exposure by means of X-Ray Photoelectron Spectroscopy (XPS).

- It is also of particular importance to study the evolution of surface-chemical composition during dynamical modulation of polarization by, for instance, temperature. Such dynamic polarization modulation has been reported in pyrocatalytical reactions used for H_2 production, whose concentration is typically measured at the end of temperature cycles. However, the evolution of surface chemistry during the pyrocatalytical processes has not been reported so far. Moreover, in the case of ferroelectric thin films/single crystals with surface adsorbed water, the direction of polarization plays a crucial role by determining type

of surface redox processes taking place. Therefore, in-situ studies of surface chemical composition and associated domain structure during cyclical temperature changes are desirable. In this thesis, I will study the evolution of ferroelectric domain structure, surface chemical species and possible reactions paths across paraelectric-to-ferroelectric phase transition of $BaTiO_3$ single crystals in water vapor atmosphere, by means of near ambient pressure XPS (AP-XPS), X-Ray diffraction and piezoresponse force microscopy (PFM).

- Ferroelectric polarization does not only affect water-mediated chemical reactions at the surface, but adsorbed water molecules can also influence the ferroelectric polarization switching dynamics. In this sense, all previous studies of the relative humidity influence on ferroelectric domain growth were based on static point measurements, by applying DC voltage pulses of distinct amplitude and length to AFM tips at fixed points of the sample. However, some of the set-ups proposed in the literature for ferroelectric bit encoding envision writing as a dynamic scanning process, whereby "ferroelectric record disk" is rotated while biased AFM-like needle is used for domain switching as it scans the surface. As the rotational speed is increased, the successfulness of single-bit writing decreases. Beyond the bit density, the maximum speed at which information can be encoded is of crucial importance for the application of ferroelectric materials in memory devices. Moreover, the majority of experiments have been performed for high RH, while the detailed studies in low RH regime (i.e. under 10 % RH) are scarce. This region is of particular interest, since processes such as formation of hydroxyl groups and emergence of first monolayer of water are expected to take place, overall having pronounced influence on domain size and switching dynamics which otherwise might be obscured at high RH. In this thesis, I study the ferroelectric switching dynamics of $BaTiO_3$ thin films from a novel perspective and in a wide range of RH, expanding from 2.5 % up to 60 %, and derive conclusions related to the effects of water adsorption on the maximum speed of writing, domain wall velocity and size of ferroelectric domains.

- With respect to the high susceptibility of surface chemistry to external parameters, one could imagine that water-based adsorbate layers are difficult to control and could cause undesirable effects, including chemically-assisted polarization switching. These stability issues may be overcome by deliberate chemical functionalization of ferroelectric surfaces with "electroactive" or tunable molecules, therefore enabling stable and predictable surface chemistry, while at the same time compatible with switching between ferroelectric states.

As proposed in this thesis, an interesting kind of molecules that could accomplish posed requirements are aromatic benzene derivatives such as para-aminobenzoic acid (pABA), characterized by delocalized electronic system mediated by the electronegativity of benzene-substituent groups.

Research of this kind would not have been possible without advanced instrumentation and different types of nanotechnology. Firstly, it enabled me to synthesize high quality ferroelectric thin films of $BaTiO_3$ by Pulsed Laser Deposition (PLD) technique, which was used as the main ferroelectric material throughout this thesis, from bare thin film surfaces to hybrid ferroelectric/organic/2D materials capacitors, prepared from $BaTiO_3$ thin films functionalized by microcontact printing method. For the surface chemical characterization, I employed mainly XPS measurements in laboratory or synchrotron based sources, which enabled me to go beyond standard working conditions in vacuum and perform experiments in water vapor atmosphere by near Ambient Pressure XPS (AP-XPS). Surface chemistry was further investigated by AFM in different modes, often accompanied by temperature and RH control, allowing me to distinguish between chemically different regions based on their work functions or Young's modulus. Finally, PFM was used as the main tool for the nanocharacterization of ferroelectric domain structure and its manipulation. While some of the techniques (e.g. PFM) have by now become standard in most ferroelectrics laboratories, the specific conditions in which my experiments have been done are unique. For this reason, besides the results, this thesis will dwell on the discussion of the experimental details.

Synopsis

The structure of this thesis is as follows. After the present brief introduction and motivation, **Chapter 1** sets out the scientific context in which this work is situated. Fundamentals of ferroelectric materials and their surface chemistry, driven by the depolarizing field screening, are explained with a focus on polarization-selective surface chemical composition and catalytic processes. Additionally, properties of archetypal ferroelectric material $BaTiO_3$ are briefly discussed.

Chapter 2 is dedicated to the experimental methods used in this thesis, with the focus placed on XPS, PFM, Kelvin Probe Force Microscopy (KPFM) and PLD. Additionally, preparation of $BaTiO_3$ thin films with $SrRuO_3$ bottom electrode on different titante- and scandate- based single crystalline substrates by PLD method, as well as their structural and functional properties, as studies by XRD and PFM, are presented.

In **Chapter 3,** the evolution of surface chemical compositions of $BaTiO_3$ thin films as a function of time exposure to ambient conditions and polarization direction is explored by XPS and related with possible polarization-driven oxidation processes. Additionally, the effect of frequently employed sample treatments (annealing in vacuum/O_2 atmosphere or exposure to radiation) has been addressed.

In the **Chapter 4,** we will delve into the surface chemistry of $BaTiO_3$ (100) single crystal upon pyrocatalytically driven redox reactions across Curie temperature. Evolution of surface chemical species and polarization screening dynamics in water vapor atmosphere, coupled to the appearance of polarization at the phase transition upon sample cooling, has been studied by combined use of AP-XPS, PFM and X-Ray Reciprocal Space Mapping (XR-RSM). The obtained results evidence how the appearance of down-oriented polarization during paraelectric-to-ferroelectric phase transition triggers water dissociation. Additionally, the coexistence between ferroelectric screening dynamics, mediated by surface chemical reactions, and emergence of polarization below the Curie temperature, was characterized as a function of time by the fast mapping of AP-XPS spectra over the phase transition.

In the following **Chapter 5**, dynamic ferroelectric lithography experiments performed in controlled RH conditions were set to investigate the impact of RH on the critical writing speed and polarization switching dynamics in $BaTiO_3$ thin film samples. It was found that RH has a

positive effect on the critical speed for ferroelectric domain writing, whereby it increases non-monotonically with RH. Experiments studying the mutual effect of RH and writing speed on the ferroelectric domain size, underscore the impact of adsorbed water layer thickness on the observed domain sizes and longitudinal domain wall dynamics, possibly mediated by the evolution of adsorbed water structure as a function of RH and its associated relative dielectric constant and ionic mobility.

In **Chapter 6**, the ferroelectric surface of $BaTiO_3$ is chemically modified in a controlled way by its functionalization with para-aminobenzoic acid (pABA) molecules. The ferroelectric properties of this hybrid organic-inorganic heterostructure are investigated by PFM. In the first study of its kind, it has been shown that aromatic pABA molecules couple to the bulk ferroelectric polarization by increasing the coercive voltage of the $BaTiO_3$ thin films, suggesting an improved stability of both ferroelectric states. These molecules demonstrate to play an active role by i) providing efficient ferroelectric polarization screening, which could emerge from the different conformations of delocalized electrons in pABA molecules imposed on-demand, by the polarization state of underneath ferroelectric, and ii) as the active capping layers protecting the ferroelectric polarization from uncontrollable environmental impact.

Finally, **Chapter 7** is dedicated to the overall conclusions of the thesis and future perspectives.

Table of Contents

List of Figures

List of Tables

List of Acronyms

Acronym	Definition
AFM	Atomic force microscopy
AM-FM AFM	Amplitude modulated frequency modulated AFM
AP-XPS	Ambient pressure X-Ray photoelectron spectroscopy
AR-XPS	Angle resolved X-Ray photoelectron spectroscopy
ATR-IR	Attenuated total reflection infrared spectroscopy
B.E.	Binding energy
BFO	Bismuth ferrite
BTO	Barium titanate
CPD	Contact potential difference
DART	Dual Amplitude Resonance Tracking
DPN	Dip Pen nanolithography
DSO	Dysprosium scandate
EELS	Electron energy loss spectroscopy
ESCA	Electron spectroscopy for chemical analysis
ESEM	Environmental scanning electron microscopy
FE	Ferroelectric
FT-IR	Fourier transform infrared spectroscopy
FTJ	Ferroelectric tunnel junction
GBL	Gamma-butyrolactone
GSO	Gadolinium scandate
HER	Hydrogen evolution reaction
IMFP	Inelastic mean free path
K.E.	Kinetic energy
KPFM	Kelvin Probe Force Microscopy
LGD	Landau-Ginzburg-Devonshire
LNO	Lithium niobate
lPFM	Lateral piezoresponse force microscopy
LSMO	Lanthanum strontium manganite

Acronym	Definition
mABA	Meta-aminobenzoic acid
MF-AFM	Multifrequency atomic force microscopy
ML	Monolayer
oABA	Ortho-aminobenzoic acid
pABA	Para-aminobenzoic acid
PDMS	Polydimethylsiloxane
PE	Paraelectric
PFM	Piezoresponse force microscopy
PLD	Pulsed laser deposition
pO_2	Partial oxygen pressure
PZT	Led zirconate titanate
RH	Relative humidity
R_{rms}	Root mean square roughness
SRO	Strontium ruthenate
SSO	Samarium scandate
SS-PFM	Switching spectroscopy piezoresponse force microscopy
STEM	Scanning transmission electron microscopy
STO	Strontium titanate
T_c	Curie temperature
TER	Tunneling electroresistance
TPD	Temperature programmed desorption
vPFM	Vertical piezoresponse force microscopy
XPS	X-Ray photoelectron microscopy
XR-RSM	X-Ray reciprocal space maps
μCP	Microcontact printing
μ	Dynamical coefficient
OH	Hydroxyl group
NH_2	Amino group
COOH	Carboxylic group
H_3O^+	Hydronium ion

CHAPTER 1

Introduction

The aim of this introductory chapter is to approach the reader to the basic concepts of ferroelectricity, boundary conditions and associated depolarizing fields. Different screening strategies that ferroelectric materials use to compensate depolarizing stray electric fields are discussed, with the special focus on external screening of bare ferroelectric surfaces by adsorbates species. It will be discussed how the interaction of ferroelectric surfaces with external adsorbate species reveals polarization-specific surface chemistry and how certain surface chemical states impact ferroelectricity. Finally, this chapter describes the coupling between ferroelectric and pyroelectric properties in the light of water splitting reactions, and how this leads to the concepts of pyrocatalysis and ferrocatalysis.

1.1 Ferroelectricity

Student Josep Valasek discovered ferroelectricity about a century ago (1921) in a material potassium sodium tartrate tetrahydrate ($KNaC_4H_4O_6 \cdot 4H_2O$), also known as Rochelle salt.[1] He claimed that "*there is a parallelism between the behavior of Rochelle salt as a dielectric and steel, for example, as a ferromagnetic substance.*" In the decades after this discovery, scientists put effort in finding and integrating different ferroelectric materials in devices used for medical, industrial and military purposes. A ferroelectric is an insulating material with two or more discrete stable or metastable states of different nonzero electric polarization in zero applied electric field, referred to as "spontaneous" polarization.[2] For a system to be considered ferroelectric, it must be possible to switch between these states by the application of the electric field of proper magnitude and orientation. This definition contains several different aspects important for the existence of ferroelectricity. In crystallographic terms, out of 32 crystalline point groups, only 21 are non-centrosymmetric. From those, 20 groups can exhibit *piezoelectricity*: appearance of the electric charge in response to the applied mechanical stress. Among those, only 10 can show *pyroelectricity*: temperature dependent spontaneous polarization, which enables creation of temporary voltages across the material as it is heated or cooled. Only some of pyroelectric materials will also be *ferroelectric*. In order to be ferroelectric, as by definition, a material's spontaneous polarization P_s should be switchable from one polar state to another by the application of the electric field above some threshold value, called the coercive field E_c. In general, in ferroelectric materials can coexist regions with different orientation of polarization vector, known as *ferroelectric domains*.

Polarization evolution as a function of an external applied electric field takes the form of the *hysteresis loop* as shown in **Figure 1.1**. Hysteresis loops are starting from P = 0 net polarization value in the absence of electric field, when the sample has domains with polarization oriented in such a way that they compensate each other. When an electrical field is applied, a gradual increase of the polarization can be observed, which finally reaches the plateau at the value of P_{s+}, corresponding to the value of polarization saturation. At this point dipole moments in all the domains are oriented parallel to the direction of applied electric field. If the electric field decreases, polarization will slightly decrease, however it will not follow the same path as before. The value of the polarization at zero electric field P_{r+} is called remanent polarization.[3]

Similar changes happen as the negative voltage is applied to the ferroelectric material, completing the hysteresis loop cycle.

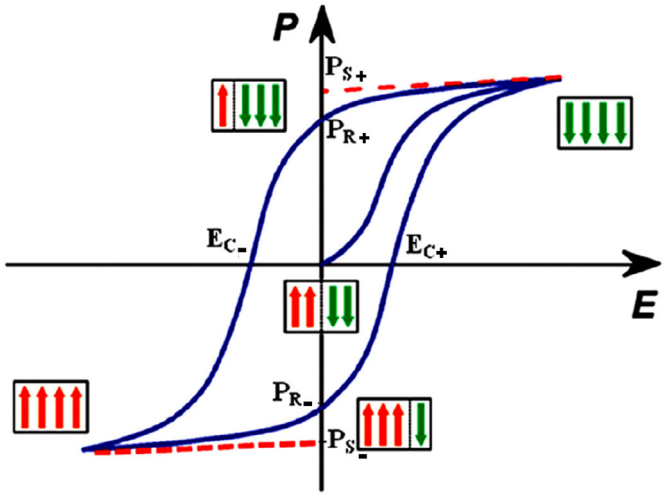

Figure 1.1 *Schematic representation of ferroelectric hysteresis loop, which defines polarization vs. electric field response of ferroelectric material. Image adapted from [3].*

As a subfamily of pyroelectric materials, ferroelectric properties are intrinsically temperature dependent; as the temperature is increased above some critical temperature T_c called *Curie point*, a phase transition occurs between the low symmetry distorted ferroelectric phase and a high symmetry prototypic paraelectric phase.

Beside different families of ferroelectrics such as hydrogen bonded systems or polymers, ferroelectricity has predominantly been studied in oxide perovskites with the general formula ABO_3, where A site is occupied by mono-, di- or tri- valent cation (e.g. Li^+, Pb^{2+}, Ba^{2+}, Bi^{3+}) and B site by penta-, tetra- or tri- valent cation (e.g. Nb^{5+}, Ti^{4+}, Zr^{4+}, Fe^{3+}), respectively. Among those, one of the most studied ferroelectric perovskites is barium titante with the formula $BaTiO_3$ (BTO), which is indeed the main ferroelectric material studied in this thesis.

1.2 Barium titanate

The discovery of barium titante is somewhat obscured by the events of the World War II. It was discovered independently in 1941 and 1944 in United States, Russia and Japan.[4] In that time, mica was the most used dielectric material in capacitors, but due to shortage of supplies coming from South America, researchers were trying to develop new type of high permittivity

materials by doping TiO_2 with BaO. Later on, in 1945 and 1946, von Hippel[5] and Wul and Goldman[6] demonstrated ferroelectric switching in BTO. This was of huge importance, because it showed that ferroelectricity can exist in oxides with simple structure, which was thought to be impossible at that point since ferroelectricity, following its discovery in KH_2PO_4, was initially associated with the presence of hydrogen bonding. Nowadays, BTO is the most widely used lead-free ferroelectric material, with a broad range of applications as capacitors, memory devices, sensors, energy-harvesting materials or catalytic platforms.

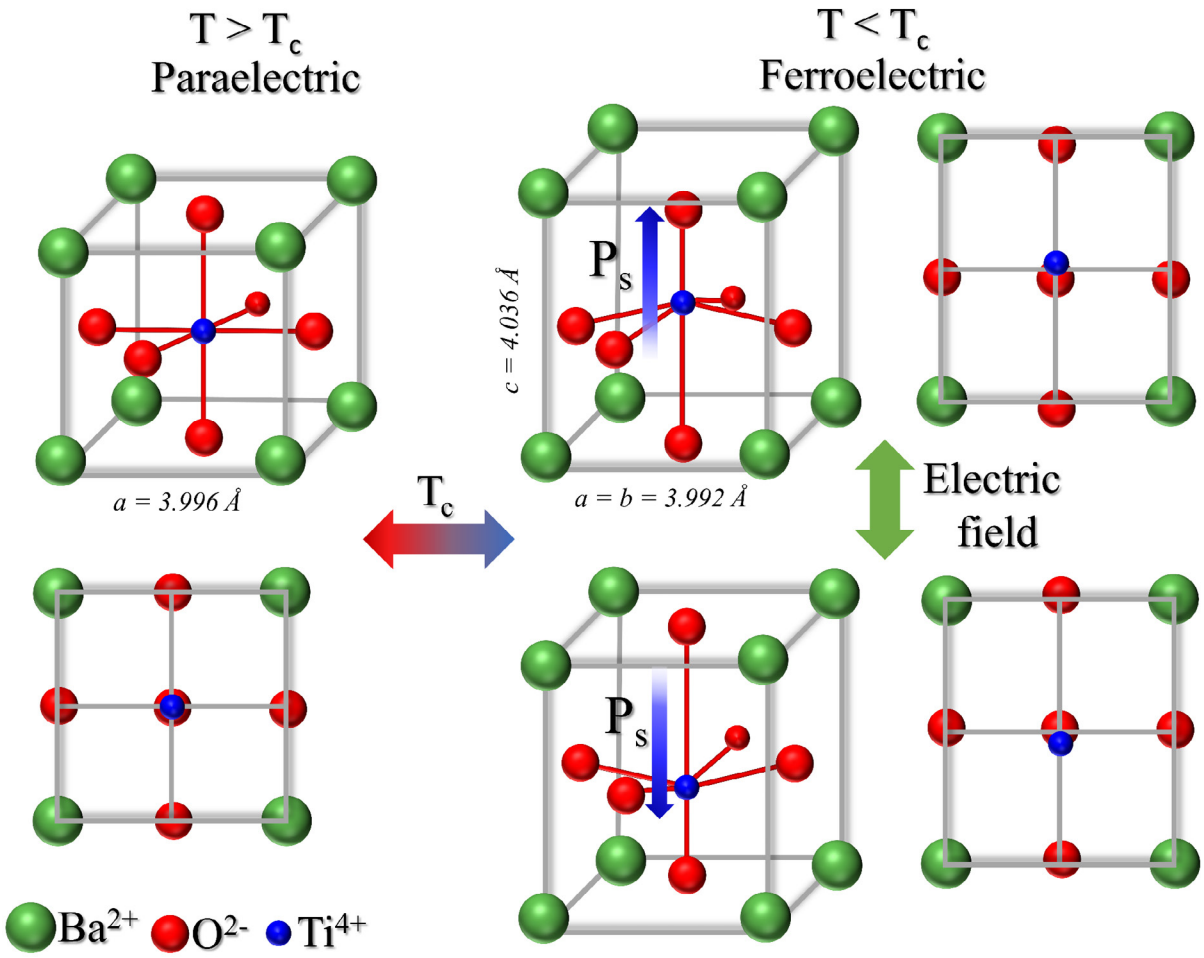

Figure 1.2 *Schematic representation of $BaTiO_3$ unit cell at paraelectric-ferroelectric phase transition between high symmetry cubic and low symmetry tetragonal phase at the Curie temperature (T_C). At the phase transition, there is a small shift of Ti^{4+} ions along one of the cubic axis (upward or downward), while the oxygen atoms shift it opposite direction, resulting in the formation of electric dipole moment pointing up or down, respectively. Switching between the states of opposite polarity can be achieved by the application of electric field.*

Barium titante belongs to the family of perovskites described by the general formula of ABO_3. In the cubic phase Ba^{2+} ions are located in the A sites, i.e., at the corners of the unit cell and

Ti^{4+} occupies the B site at the center of it. The O^{2-} anions are located at the face centers of the of the unit cell and form BO_6 octahedra with Ti^{4+} ions. During the cooling, single crystals transform from cubic to the tetragonal phase through distortive-displacive phase transition at the Curie temperature *(T_c)*, which lies between ≈ 120 and 130 ºC, depending on the crystal growth procedure.[7,8] The emergence of ferroelectric dipoles can be explained by taking microscopic considerations into account: if the position of Ba^{2+} is taken as the reference position, then the phase transition can be viewed as the small shift of Ti^{4+} ions along one of the cubic axis (upward or downward), while the oxygen atoms shift in opposite direction, resulting in the formation of an electric dipole moment pointing up or down, respectively (**Figure 1.2**). The mentioned shifts cancel several symmetry operations of the original cubic cell (e.g. center of symmetry, mirror plane (001), etc.), meaning that the overall symmetry of the system must be lowered from cubic to tetragonal. In the case of a uniaxial ferroelectric, the material can turn into any of the two equivalent states, with the net dipole moment pointing up or down, whereby one can reversibly switch between the states by the application of the electric field of proper magnitude and orientation. (**Figure 1.2**).

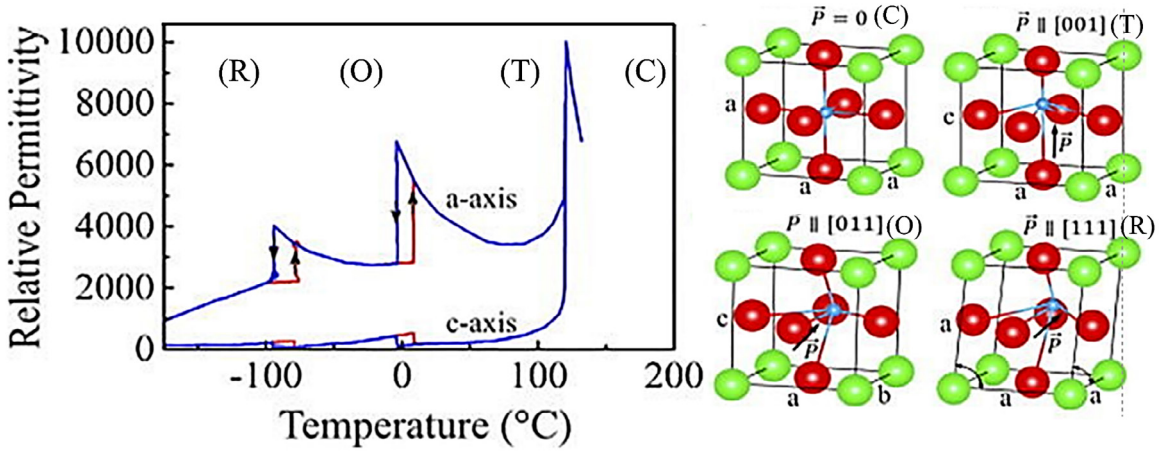

Figure 1.3 *Relative permittivity as a function of temperature during the sequence of phase transitions in BTO. Labels correspond to cubic (C), tetragonal (T), orthorhombic (O) and rhombohedral (R) crystalline structure whose schematic unit cells are shown on the right. Adapted from [4].*

Besides the paraelectric-ferroelectric phase transition, BTO undergoes two more phase transitions when further cooled down: i) it shows a phase transition from tetragonal to orthorhombic structure around $T \approx 0$ ºC, whereby polarization becomes parallel to the edge of the tetragonal unit cell and ii) from orthorhombic to rhombohedral structure between $T \approx -70$ and $T \approx -90$ ºC (**Figure 1.3**), whereby polarization is oriented along the body diagonal. The exact phase transition temperatures can vary upon growth methods employed and single crystal

purities. These phase transitions are known as inter-ferroelectric transitions, since they do not involve appearances/disappearance of ferroelectricity.[4] All the mentioned phase transitions are of first order in BTO and are typically followed by the strong changes in the dielectric constant at the transition as shown in **Figure 1.3**.

The lattice parameter of single-crystalline cubic BTO is 3.996 Å. In the tetragonal phase, where the unit cell is being elongated along the polar axis and shrunk along the axis perpendicular to it, the lattice constants have values of a = b = 3.992 Å and c = 4.036 Å, respectively. However, when BTO is grown as an epitaxial thin film over single crystalline substrate, compressive or tensile strain can be induced inside of the film, depending on the lattice mismatch between the substrate material and the BTO.[9] As a result, the properties of the strained thin films can be extraordinarily different from those stemming from bulk single crystals or relaxed thin films. This can be understood through the concept of "strain engineering", whereby strain is used as a tool to enhance particular properties of ferroelectric materials such as the polarization stability or the Curie point. Choi et al.[9] showed that, if BTO is grown on substrates which induce compressive strain, such as $DyScO_3$ (DSO) or $GdScO_3$ (GSO), both the Curie temperature and the remnant polarization are raised considerably according to the biaxial strain induced in the films. (**Figure 1.4 a,b**).

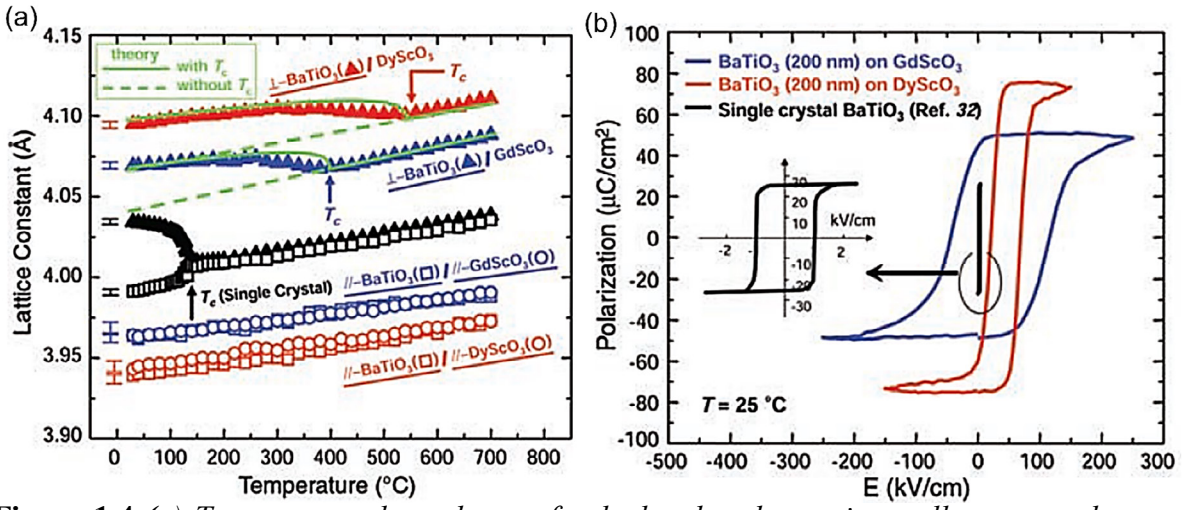

Figure 1.4 *(a) Temperature dependence of calculated and experimentally measured out-of-plane (⊥) and in-plane (//) lattice parameters of BTO thin films grown on DSO (red symbols) and GSO (blue symbols) substrates. Change in the slope at high temperatures marks the phase transition. Black squares denote the change of lattice parameters for the BTO single crystal and associated Curie temperature, which is several hundreds of degrees lower compared to the strained BTO thin films. (b) Polarization-electric field hysteresis loop for BTO capacitors on GSO and DSO substrates, sandwiched between top and bottom SRO electrodes. Inset shows hysteresis loop of unstrained BTO single crystal. Panels (a) and (b) are adapted from [9];*

In this thesis, two types of BTO samples are studied: single crystals with as grown (100) polarization and thin films grown under compressive strain on SRO-buffered STO (001) single crystal substrates.

1.3 Depolarizing fields and screening

As the physical size of the system decreases, the ratio between atoms located at the surface/interface to those in the bulk increases, making the effects of the surface on the bulk ferroelectric properties unavoidable. The emergence of ferroelectricity is related to the collective phenomenon of atomic displacements, resulting from the competition between long range dipole-dipole Coulomb interactions and short range covalent repulsions.[10] If the thickness of the ferroelectric is decreased, as in the case of thin films, it can be expected that the delicate balance between short and long range interactions will be affected. Dipole-dipole interactions will be diminished due to the lower number of interacting dipolar units in the truncated volume of the thin film,[10] while at the same time interactions present at the surface layers and interfaces will be enhanced, therefore modifying the short range interactions interpreted in terms of chemical and electric boundary conditions.

At surfaces, translational symmetry in the direction perpendicular to them is broken. This means that atoms in the top surface layers will feel the absence of the neighboring atoms, thereby creating energetically unstable dangling bonds. In order to minimize the surface energy, the free surface will tend to change its structure or atomically reconstruct by releasing/binding extra atoms into its structure, which can significantly affect physical properties of ferroelectric material. In the same way, strong chemical bonding between ferroelectric surfaces and either external chemical species or atoms in metallic electrodes will contribute to short range interactions.

Besides surface-bonding contributions, electrostatic effects are of particular importance. Discontinuity of polarization normal to the surface gives rise to bound polarization charge and depolarizing stray electric fields E_d.[11,12] The later are always opposing the polarization and in the most of the cases are high enough to completely suppress the polarization in the absence of adequate screening mechanisms. There are several strategies that a ferroelectric material can employ in order to screen depolarizing fields[10,13] and ensure ferroelectric stability. Screening charge can be supplied i) internally in form of charges (electrons/holes) or defects existing in

(wide band gap) semiconductive ferroelectric films, which create gradient concentration profiles in the vicinity of the surface and ii) externally, by charges coming from conductive metallic electrodes sandwiching the ferroelectric or by atmospheric adsorbates in the form of dipoles and/or ionic species.

In practice, both processes might happen simultaneously, whereby the relative contribution of each will be determined by the experimental boundary conditions (such as temperature, solid-gas or solid-vacuum interface or relative humidity), surface reactivity, as well as by the kinetics and the thermodynamics of the available screening mechanisms. For instance, it is expected that the screening of bare ferroelectric materials without top electrodes, once exposed to ambient conditions, is mediated by the water dipoles and ionic species coming from the atmosphere in intermediate to high humidity conditions. However, if the surface is inserted in a high vacuum chamber and stripped off atmospheric adsorbates, the materials will need to seek other internal ways of screening, e.g. localization of internal charges in the near surface region by band-bending[13] or surface reconstruction. Finally, in order to preserve the ferroelectric state, a material can divide into domains of opposite polarization or rotate the polarization in the plane of ferroelectric layer. Possible screening strategies are schematically shown in **Figure 1.5.**

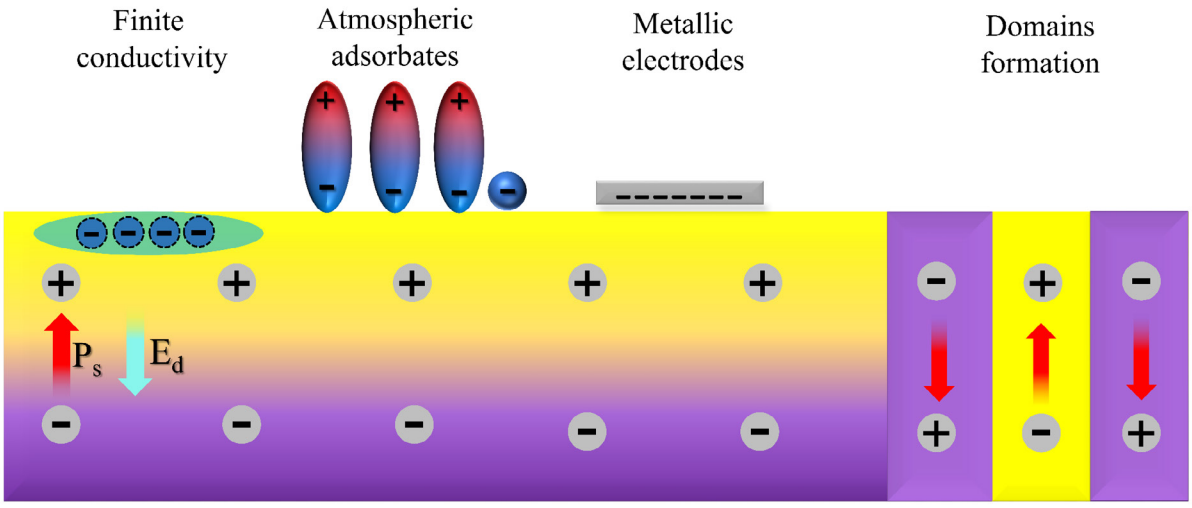

Figure 1.5 *Schematic representation of the screening mechanisms that can be employed for depolarizing field (E_d) compensation. From left to right: Internal screening induced by the finite conductivity of the thin film; External screening by atmospheric adsorbates (dipoles or ionic charges) or by electrons from conductive electrode. In the latter, screening depends on the effective screening length λ_{eff} which is the interface property of the electrode-ferroelectric system; Formation of 180 deg domains, whose size is determined by Kittel's law.*

In general, it is a still matter of debate when a material will finally lose its ferroelectric properties as the thickness is decreased under some critical value.[12,14,15] It has been established[16] that size effects will determine the absolute number of unit cells necessary in order to have stable ferroelectric phase. This number is of the order of few unit cells for different perovskite ferroelectrics in form of thin films, whereby the decrease of the thickness is followed by the reduction of polarization and other properties related to it as the critical thickness is approached.[16] However, in reality, many extrinsic effects (not inherent to the crystal) such as electric boundary conditions and depolarization fields, surface chemistry and bonding, strain induced by the substrate, or the presence of crystal imperfections and defects will shift the critical thickness towards higher values.

1.3.1 Internal screening mechanisms

In ferroelectrics, internal screening of polarization can be performed by the redistribution of mobile charge carriers and charged defects in the vicinity of surfaces and interfaces, creating the surface dipole and consecutive band bending. For example, from the surface with negative bound polarization charge, electrons will be depleted, giving rise to a positively-charged depletion region with upward band bending. Reversely, surfaces with positive bound polarization charge will be screened by the accumulation of electrons causing downward band bending.

Furthermore, the crystal structure of a ferroelectric can contain different kind of defects. One of the most common in perovskite oxides are oxygen vacancies, which are present in the electronic structure of a material as defect donor levels within the bandgap, situated below the conduction band and therefore causing n-type semiconductivity.[17]

Taking into account that ionized oxygen vacancies bear positive charge and that their location within material can be manipulated by the application of electric field,[18] they are often considered as active screening agents of ferroelectric polarization. Borisevich et al.[19] demonstrated, by scanning tunneling electron microscopy (STEM) and electron energy loss spectroscopy (EELS), vacancy-controlled screening at the BFO/$LaSrMnO_3$ (LSMO) interface. It was shown that if the polarization is pointing away from the LSMO/BFO interface (inducing a negative polarization charge), significant lattice expansion and reduction of Mn^{3+} to Mn^{2+} state could be observed locally at the interface, indicating screening by oxygen vacancies. In the case of polarization pointing towards the interface (inducing positive polarization charge),

no changes in the valance state of atoms or lattice spacing were detected, suggesting electronic screening instead of ionic one.

Combined experimental STEM and theoretical studies of led zirconate titanate (PZT) thin films grown on STO substrates with and without bottom SRO electrode also identified different screening mechanisms depending on the electric boundary condition.[20] PZT thin films grown on SRO bottom electrode compensated depolarization fields by the electronic screening stemming from metallic SRO electrode, as expected, and also by extending the ionic displacement of ferroelectric layer inside of the SRO electrode. In contrast, PZT grown directly on insulating STO lacks metallic screening and therefore accumulates oxygen vacancies at the STO/BFO interface which stabilize monodomain ferroelectric state.

It must be mentioned, however, that oxygen vacancies have a finite mobility at room temperature and thus a limited capacity to compensate polarization switching in PFM experiments.

1.3.2 Screening by metallic electrodes

Screening by metallic electrodes is of particular importance in the case of ferroelectric capacitors, where ferroelectric thin films are sandwiched between two metallic electrodes. It has been found that even structurally ideal electrode-ferroelectric interfaces are not able to provide perfect screening of the surface bound charges.[21] This imperfect screening was initially characterized by the finite Thomas-Fermi screening length, which gives rise to the layer of spatially separated screening and bound polarization charges that acts as capacitor in series with the ferroelectric layer.[22] However, at the microscopic scale this was not the best solution, since it would imply that the screening would occur very close to the electrode interface (typical screening lengths are of 0.5 Å or less). In this region the physical and chemical properties of the electrode are different from those in the bulk and therefore the use of a bulk screening length would not be appropriate. First principle calculations showed that instead of the Thomas-Fermi screening length, another parameter called effective screening length can be predicted, which depends on the ferroelectric-electrode choice, termination of the ferroelectric layer and chemical bonding at the surface. The effective screening length λ_{eff} is therefore an interface property of the electrode-ferroelectric system,[23] which gives rise to the screening charges that are spread across the short finite length and hence are not able to

fully compensate the depolarization field, which is always present. The residual depolarizing field of ferroelectric materials in capacitor geometry can be expressed by the equation (1)[10]:

$$E_d = \frac{2\lambda_{eff} P_0}{\varepsilon_0 t} \qquad (1)$$

where P_0, ε_0 and t are polarization, vacuum permittivity and film thickness. As already said, the effective screening length comprises both: electronic effects and chemical bonding effects which always need to be taken into account.

1.3.3 Formation of domains

Domains are regions in which electric dipole moments are oriented in the same direction, while the boundaries that separate them are called domains walls. If the system splits into 180 º domains, then the net surface charge in average is zero and the depolarization fields are considerably diminished throughout the biggest part of the film. The number and size of the domains formed in the thin film depend on the electrostatic energy of stray electric fields coming from the antiparallel arrangement of domains, energy cost for the domain wall formation, as well as on elastic energies. By minimizing the total energy with respect to the domain width, famous Kittel law[24] can be obtained, stating that the size of the domain scales as the square root of the material thickness following equation (2).

$$w \sim \sqrt{t} \qquad (2)$$

This means that the domains bigger than some equilibrium size will not be stable because of stray electric field contribution, while the smaller ones will not be energetically favorable due to the high cost needed for their formation.

Kittel's law implicitly assumes that the depolarization energy of the domains has not been screened by any other mechanism, hence their impact on the domain size reduction, but the formation of such spontaneous domains is generally prevented when there are enough efficient screening mechanisms such as it is the case for the most of the work that will be shown here.

In this thesis, the studied BTO thin films have thicknesses between 15 nm and 20 nm, and in all cases presented a single domain ferroelectric state. It is also worth mentioning that surface boundary conditions can determine not only if polarization will exist in a monodomain or

polydomain state, but also its preferential polarization orientation in the case when a single domain state is established.[25,26]

1.4 External screening by adsorbates

Even when a ferroelectric is split into domains of opposite polarity, the depolarizing field can be further reduced by adsorption of atmospheric adsorbates in ambient conditions. Surface-adsorbed polar molecular or ionic species can modify chemical boundary conditions and consequently influence the distribution of the polarization in the bulk. Among all possible molecules available in the atmosphere, water molecules play the most critical role in the generation of screening adsorbates due to two main factors: (i) water is itself a dipolar molecule which is able to align with stray ferroelectric fields and (ii) the magnitude of stray electric field and generated surface potential produced by uncompensated polarization charges in archetypal ferroelectric is sufficient to cause water splitting[27,28] and trigger water dissociation[29,30] on charged ionic species, altogether playing important role in screening process.

1.4.1 The role of water in ferroelectric screening

One of the first works experimentally demonstrating the role of water as surface adsorbate on the polarization screening of BTO (100) single crystals was performed by Kalinin et al.[31] by measuring the surface potential difference between up- and down- polarized domains by Kelvin Probe Force Microscopy (KPFM). The surface potential measured by KPFM was attributed to the formation of double layer, consisting of bound polarization charges and screening charges. The results indicated that the polarization bound charge is completely screened and that the domain potential is opposite to that expected from domain polarity, in a way that down domains show positive surface potential and vice versa. Further on, by relating the difference in the surface potential with variables such as surface charge, thickness and dielectric constants of ferroelectric and double layer, it was concluded that the latter corresponds to the thickness of 0.25 monolayers (ML) of water with a relative dielectric constant of 80.[31] Similar studies of surface potential as a function of temperature and relative humidity (RH) have revealed an

interplay between the dynamics of polarization switching and screening charge supply [32,33] in single crystals and thin films.

Water molecules can physisorb on ferroelectric surfaces, or dissociate forming hydroxyl OH^- and proton/hydronium ions H^+/H_3O^+ and further chemisorb on them. These processes are known to depend on the ferroelectric polarization direction, water content (relative humidity) and surface termination.[34,35] Conversely, this can also lead to distinct changes in the ferroelectric properties. Results of combined experimental and theoretical studies on 4 nm up-polarized and BaO terminated BTO thin film exposed to water[36] indicate that exposure to low water vapor doses led to a reversible physisorption process, which has no effect on its ferroelectric properties. In contrast, exposure to high water partial pressures is suggested to cause the formation of chemisorbed OH groups which influence the surface dipoles, affect associated electrostatic energies and therefore depolarization field, leading to the polarization switching from up to down state throughout the thin film. This study also points out that observed effect might be dominant only in the surface region of thicker films. Similar studies performed on 8 nm thin, up-polarized and TiO_2 terminated BTO thin films, showed somewhat different results.[37] In the absence of water molecules, bulk of the sample was up-polarized, while the rumpled top TiO_2 layer had a downward pointing electric dipole created in order to compensate the surface bound polarization charge. In contrast, after dissociative water adsorption, whereby OH^- ions tend to attach to Ti sites, surface TiO_2 dipole switched back in the direction of the bulk polarization, demonstrating that the screening is more efficient than the ionic rumpling. By the third layer, atomic distortion had the same direction as in bulk and corresponds to the up-polarized state, contrary to the results on the BaO terminated BTO film. These studies showed that presence of surface OH groups stemming from dissociation of adsorbed water molecules, is able to change ionic positions of surface as well as subsurface layers. Besides, it also points out to the difficulties in studying clean, adsorbates-free surfaces[13]:surface sensitive XPS measurements of O 1s edge show some hydroxylation percentage of the as-grown native sample, suggested to stem from the uptake of residual hydrogen already during the sample growth. On the other hand, presence of the significant peak in Ba 3d edge at higher binding energies has not been elucidated.

These results highlight the high sensitivity of (surface) polarization state to the chemical modification of surfaces upon water adsorption, which was the motivation for the coming studies in the field.

1.4.2 Polarization dependent adsorption and dissociation of molecules

Driven by the need of depolarizing field screening and surface energy minimization, ferroelectricity can induce domain-orientation-specific surface chemical states, which may include distinct surface stoichiometry, charge carrier concentration or structure and can further lead to the difference in surface chemical activities (e.g. adsorption energies, desorption rates, energy barriers for dissociation reactions, binding geometries etc.) of precursor molecules on the oppositely polarized ferroelectric surfaces. This causes overall difference in surface chemistries of oppositely-polarized ferroelectric surfaces. Importantly, water adsorption and dissociation processes entangled with ferroelectric stray fields and participating in polarization screening will necessary depend on the polarization state of the sample. In other words, water-induced adsorbate layers are expected to be different as a function of the ferroelectric polarization underneath at the time they were created.

AP-XPS measurements and theoretical studies on $LiNbO_3$ (LNO) showed a remarkable difference in surface hydroxylation and water coverage trends as a function of partial water vapor pressure on up and down polarized domains, as well as distinct desorption temperatures, suggesting different affinities and sticking coefficients of these species.[35,38]

Various temperature programmed desorption (TPD) measurements of different polar and non-polar molecules such as methanol, ethanol, acetic acid, iso-propanol, dodecane and CO_2 from oppositely polarized surfaces of BTO, LNO and PZT have been performed, all showing important influence of the polarization state on the energetics of adsorption/desorption, defined by distinctive desorption temperatures and reactive sticking coefficients.[39–41] However, these studies need to be interpreted with caution, since determining the kinetic parameters from the variation in TPD peak temperature relies on the assumption that the desorption activation energy is independent of temperature. In the frame of the TPD experiment as the temperature is increased, ferroelectric materials will exhibit pyroelectric effect, which gives rise to the extra surface charge and therefore changes the surface dipole. If molecular interactions with ferroelectric surfaces are purely electrostatic, then this continuous change of the surface dipole i) would have strong impact on the interaction of ferroelectric with polar molecules, having negligible effect on the non-polar ones and ii) it could affect determination of desorption energies. Taking into account entanglement with pyroelectric effect, results of such experiments could not univocally explain effects of intrinsic polarization orientation on the molecular adsorption. Isothermal adsorption studies of polar D-cysteine molecules from the

solution on periodically poled LNO[42] confirmed that the difference in adsorption energies indeed exists, which in this case could not be prescribed to the changes in the surface dipole due to the pyroelectric charge, but rather to the polarization dependent dipolar interaction between ferroelectric surface dipole and the polar molecules. Importantly, results of the same study pointed out to the changes in the surface stoichiometry related to polarization-dependent variation in Li/Nb ratio, which could also be responsible for observed effect.

This was further investigated in a work by the same authors,[43] where two isomers of diiodobenzene with different dipole moments were used for adsorption studies on the ferroelectric copolymer substrates with opposite polarization orientation. Isomers were chosen so that the para isomer would have zero dipole moment (non-polar), while the orto isomer had the highest dipole moment. They showed that both, polar and non-polar isomers were affected by the polarization orientation and concluded that polarization induced surface chemistry (e.g. termination, stoichiometry, charge carrier concentration close to the surface, etc.) and not simply dipolar interactions between surface and adsorbates matter in the adsorption process.

1.4.3 Electrochemical reactions on ferroelectric surfaces

Ferroelectric surfaces can also be screened internally, to some extent, by band bending, in which electrons from conduction band and holes from valence band are localized in the near surface region of up- and down-polarized surfaces, respectively. These charges make ferroelectric surfaces electrochemically active: electrons screening up-polarized surfaces can take part in reduction reactions, while holes screening the down polarized surfaces will drive oxidation reactions. This means, that beside molecular water and hydroxyls, we can expect some more complex chemical species at ferroelectric surfaces, stemming from the electrochemical reactions at the solid-vapor interface. AP-XPS measurements demonstrated that after dissociation process, Ti bonded -OH groups $(Ti\text{-}OH)^-$ can be further oxidized and form different kinds of Ti-peroxo complexes in the process of oxidative water adsorption.[44–46] Initially this was demonstrated on non-ferroelectric $SrTiO_3$ single crystalline surfaces (STO), however much higher peroxidation levels were detected in the same study on ferroelectric thin film surfaces of PZT and BTO, which also scaled with the nominal ferroelectric polarization of these films.[44]

Oxido-reductive processes at ferroelectric surfaces may also be exploited in photocatalytic reactions, whereby electron-hole pairs are created and separated due to the internal electric

field. These photocarriers can be exploited in spatially separated redox process happening at the opposite ferroelectric surfaces, as it has been demonstrated by various studies in which metal ions were reduced into elemental metals (e.g. Au, Ag or Pd).[47,48] Furthermore, it has been shown that this method can be used for the nano-patterning of surfaces by molecules[47,49] in three steps which includes: i) electric poling of up-polarized domains, ii) local reduction reaction of metal ions using photocatalytic charge carriers on predefined domains whereby metallic nanoparticles are formed and iii) attachment of molecules, functionalized by chemical groups that react preferentially with the metal nanoparticles.

1.4.4 Chemical control of ferroelectric polarization

As mentioned earlier, polarization affects water (and other molecules) adsorption. Conversely, dissociative water adsorption can change the surface dipole, which further affects associated electrostatic energies and consecutively depolarization field. Several works have evidenced that effect of surface chemistry and in general environmental conditions on ferroelectrics is particularly striking. Zhang et al.[50] demonstrated that the treatment of $BiFeO_3$ (BFO) thin films with solutions containing different concentrations of H^+ or OH^- ions (acidic vs. alkaline ones) led to thin film polarization reversal through chemically-assisted polarization switching. It has also been shown by Stephenson et al.[51] that due to the chemical equilibrium between a polar surface and the environment, overall change of O_2 partial pressure (pO_2) can lead to the reversible polarization switching of PTO thin films. Additionally, the same group studied equilibrium polarization state in these films as a function of pO_2 and temperature.[25] They found that Curie temperature varies with pO_2 and thickness and actually has a minimum at intermediate pressures. Under the Curie point, a ferroelectric material could exist in up or down monodomain state or create 180 º domains as a function of the pO_2. It means that depending on the choice of temperature/thickness, the change of pO_2 can cause ferroelectric switching via two different mechanisms: either through the formation of oppositely polarized domains or, alternatively, by a continuous mechanism in which polarization magnitude goes through zero.[25,52] Kalinin et al.[53,54] studied the coupling between ferroelectricity and surface chemical states in thin films and demonstrated that interplay between surface ionic species (controlled by gas pressure and surface potential) and surface-charge controlled polarization can give rise to the continuum of mixed electrochemical-ferroelectric states. Temperature-film thickness phase diagram calculated for different values of pO_2, also suggests existence of non-ferroelectric (i.e. electrochemical states) with irreversible polarization at very low thicknesses

and high temperatures in the absence of externally-applied electric field, caused by screening ions-associated polarizing field.

On the other hand, Eom et al.[55] reported that water treated BTO thin films with as grown down polarization form a surface layer in which ferroelectric polarization is pinned at an upward orientation thereby reducing the imprint and enhancing the polarization bistability. This aspect, besides its fundamental interest can indeed become very relevant due to its impact on the implementation of ferroelectric thin films in practical devices, whereby stability of both polarization states is prerequisite. In this sense, a novel study by Gruverman et al.[56] revealed that the change of electric boundary conditions by the use of graphene top electrode and NH_3 molecules as the buffer layer deposited at the ultra-thin BTO/graphene interface in ferroelectric tunnel junction (FTJ) devices, can increase the polarization stability and enhance tunneling electroresistance (TER) effect. It was also reported that adsorbates trapped between ferroelectric BTO surface and Pt electrodes exposed to blue laser illumination can modify remanent polarization of these films.[57]

Finally, besides having profound effects on ferroelectric properties in static conditions, adsorbates are also governing ferroelectric switching dynamics,[58,59] domain size[58,60–63] and shape[63,64] as demonstrated by local PFM studies. Local switching of ferroelectric phase by biased AFM tip, requires stabilization of the newly formed domain state, which strongly depends on the availability of screening charges and their mobilities. In that sense, ferroelectric switching can be understood as coupled physico-electrochemical process. Beside the pulse length and the amplitude of applied voltage,[65] several studies showed that domain size depends also on the relative humidity conditions.[58,60–63] It was demonstrated that the presence of a water meniscus between the AFM tip and ferroelectric surface modulates the strength of the electric field at the tip-sample contact and also extends lateral dimensions over which electric field is applied. However, this effect is very local and extends only tens of nanometers around the contact point, predominantly affecting the domain nucleation. On other hand, the size of the written domains clearly exceeds not only the contact area but also the water neck diameter, thus suggesting that the further growth of domains must depend on the long range screening conditions provided by the ionic charge.

From everything explained, it is clear that the physics of ferroelectrics is tightly entangled with their surface chemical compositions. Any change in surface chemistry leads to the modification of electrical boundary conditions, surface dipoles and consecutively depolarization fields, that

altogether may have profound effects on the bulk dipolar interactions and ferroelectric properties. By the same token, ferroelectric polarization affects adsorption, desorption, dissociating energies and redox processes at the surface. This interplay between physics and surface chemistry of ferroelectric materials can be exploited in various ways, e.g. for the chemical tunability of ferroelectric properties and in (ferro)catalytic processes beyond limitations imposed by traditionally considered "fixed" catalytic surfaces, whose activity is described the Sabatier principle.

1.5 Ferroelectrics as catalysts

Nowadays, we are living an era of drastic climate change and global warming caused by the burning of the fossil fuels and emission of the greenhouse gasses such as carbon dioxide (CO_2). This pushes the society to start to explore alternative sources of energy. One such promising alternative would be the use of hydrogen fuel due to its high density of energy and low emission of greenhouse gases. Nowadays hydrogen is mostly produced via the reforming of fossil fuels such as natural gas, coal or biomass, and by the electrolysis of water. Both leave hefty environmental and ecological footprints, and the latter requires the injection of electrons from an external source to stimulate the necessary redox reactions, in turn incurring high costs, although electricity needed for the processes can be supplied by harvesting solar, vibrational, geothermal or wasted industrial energy in form of the heat.[27,66–70]

One existing approach is photocatalytic water splitting, a process of artificial photosynthesis that generates hydrogen (and oxygen) from water and light. It employs catalysts that absorb light from the sun and use this energy to activate redox reactions, i.e., converts photonic energy into chemical energy stored in the chemical bonds of hydrogen molecules. Photocatalytic water splitting (directly converting solar energy into H_2) is a promising way of reducing the costs associated with the electricity consumption. However, it is still in the early research and development stage, and progress is hampered by several strong requirements: i) modulation of the bandgap energy for optimal photon absorption or ii) appropriate band edge position matching with the water redox potentials. Inorganic perovskites possess unique photovoltaic and charge transport properties that boost their performance as photocatalysts for water splitting.[71,72] On the front line, TiO_2[73] is a wide-bandgap semiconductor that efficiently absorbs ultraviolet radiation, and it is the prototypical photocatalyst for water oxidation used

to study the O_2 evolution reaction (OER). However, due to its small effect on driving the hydrogen evolution reaction (HER), it is typically used with a co-catalyst such as Pt to increase the rate of H_2 production.

One of the main hindrances to improve efficiency of photocatalytic water splitting lays in the recombination of photogenerated electron–hole pairs, together with the back reaction of intermediate species, as the rate-limiting parameters for surface redox reactions. Internal electric fields can be used to mitigate some of these effects e.g., by inducing charge carrier separation and thus improving photochemical reactivity. Although often arising from interfaces and p–n junctions,[74] the internal electric fields arising from the polarization of ferroelectric materials (also known as wide-bandgap semiconductors) made them interesting photocatalyst candidates,[75] improving charge carrier separation even in heterostructures made up of TiO_2 and FE materials.[76] The ferroelectric fields can also be used to modulate the activity of a catalytic layer nearby by deforming its electronic band structure.

In addition, ferroelectrics also exhibit pyroelectric and piezoelectric properties, which makes them good candidates to harness not only solar but also thermal and mechanical energy for catalysis.[77] In this sense, ferroelectric materials, have already been implemented as charge sources in a variety of catalytic processes, from water splitting to decomposition of poisonous nitrogen oxides (NO_x), water remediation, disinfection and dye degradation.[70,78–83]

Moreover, ferroelectric materials possess distinct surface states,[84,85] which spur different chemical activities of oppositely polarized surfaces.[39–43] This allows to exploit ferroelectric materials directly in catalytically driven reactions, whereby periodical modification of polarization by temperature (pyroelectricity),[70,80,86–88] pressure (piezoelectricity)[66,78,89] or electric field enables tuning of surface chemical activities, needed for the chemical reaction of interest.

The tunability of ferroelectric surfaces distinguishes them from the more typical catalytic materials with so-called “fixed” surfaces, which require optimum adsorbate-surface interaction, as determined by the Sabatier principle: if interaction is too weak, the adsorbate will not stick to the catalyst’s surface and they will fail to react, while if it is too strong the product of the reaction will not desorb (they will poison the surface). This principle can be shown graphically by plotting the reaction rate or activity against the heat od adsorption of reactants on catalyst surface, which is in catalytic literature called volcano plot.[90] Apex of the volcano plot represent the mentioned optimum interactions. However, on this way maximum

activity of catalytic processes is restrained due to the competing nature of adsorption/desorption processes. The situation drastically changes when ferroelectric (non-fixed) surfaces are used, since by changing the polarization orientation, one could actually cycle between states with different adsorbate-catalyst interaction strengths. This is highly beneficial since this would enable one to move beyond limitations imposed by Sabatier principle (i.e. single optimized interaction strength) and therefore periodically enhance adsorption/desorption processes and overall catalytic activity upon the switching process.[81]

Kakekhani et al.[81,91] proposed a way of exploring the cyclical switching between polarization states, in which one polarization state exhibits strong adsorption and dissociation properties of reactant molecules, while the opposite state exhibits strong desorption properties of the catalytic products. They also envisioned deposition of the very thin metal-oxide layer at the surface of ferroelectric, proven to enhance specific reaction of interest, while at the same time "transmitting" influence of the ferroelectric substrate. Reactions in focus were direct decomposition of NO_x compounds into N_2 and O_2 and CO oxidation into CO_2, both of high interest in the control of emissions in automotive industry. By first-principles theory they calculated polarization-dependent binding energies for intact and dissociated molecules on metal oxide-ferroelectric surfaces, as well as energy barriers for the key reactions involved in the process and predicted successful catalytic degradation of NO_x compounds and product desorption through polarization switching. Similar cycling procedures have been proposed for SO_2 and methane oxidation.[91]

Spaldin et al.[29] calculated adsorption energies of water molecules on neutral and charged FeO_2 and BiO terminated $BiFeO_3$ (BFO) slabs. The results of their study showed that water adsorption on both charged terminations proceeds by dissociation and subsequent desorption of ions hindering the screening, while it stays in a molecular state in the case of neutral surfaces. This enabled them to envision catalytic processes for water splitting through the cyclical reversal of polarization direction, during which exposed charged and neutral surfaces drive dissociative and molecular adsorption, respectively.

1.5.1 Pyrocatalysis

Spontaneous polarization of ferroelectric is a function of temperature. Therefore, change in temperature of the ferroelectric sample is followed by the decrease/increase of ferroelectric

polarization, whereby surface screening charge will be temporary in deficit/excess compared to the bound polarization charge, creating a voltage or flow of current.

The pyroelectric charge displaced upon a change of temperature within the ferroelectric phase is equal to[92]:

$$Q = p\,A\,\Delta T \qquad (3)$$

where A and ΔT are the surface active area of the material and the change of the temperature, respectively. p is the pyroelectric coefficient ($Cm^{-2}K^{-1}$), defined as the change in the spontaneous polarization vector with temperature:

$$p = \frac{dP_s}{dT} \qquad (4)$$

The pyroelectric coefficient increases with temperature and reaches a maximum at the phase transition where $T=T_c$. This means that also a maximum amount of displaced charge Q and consecutively the highest pyrocatalytical surface activity should be expected around the T_c.[88] Above T_c polarization and pyroelectric coefficient are equal to zero (**Figure 1.6**).

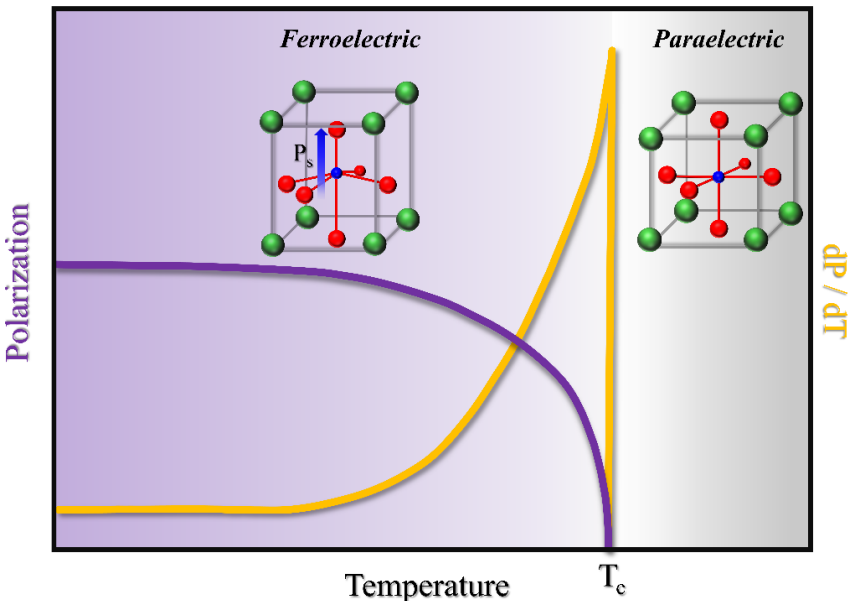

Figure 1.6 *Sketch of the spontaneous polarization and pyroelectric coefficient dP/dT dependence as a function of temperature for the ferroelectric material.*

Since ferroelectric polarization can be tuned by changing the temperature, it can be exploited for pyro-electrochemical reactions.[80,88,92] If a ferroelectric material with uniaxial polarization

P_s is at constant temperature T_1 below T_c, surface bound charges are compensated by the screening charges of the opposite sign (**Figure 1.7 a**). When the material is heated to T_2 so that $T_1<T_2<T_c$, spontaneous polarization decreases due to the loss of dipolar interaction caused by the thermal oscillations. This means that, at one point, screening charge will be in excess compared to the bound polarization charge. In short-circuit conditions this leads to the current flow, while in open-circuit conditions there will be a potential difference across the surface (electric field), which could be potentially used to drive redox processes. Excess of positive surface charge can be neutralized by the supply of negative charge created during surface oxidation reactions, while the excess of negative surface charge on the opposing surfaces can be utilized in reduction reactions, both of which involve surface adsorbed molecules (**Figure 1.7 b**). If the material is left to thermalize, an equilibrium state will be achieved after some time (**Figure 1.7 c**) Similarly, in the case of cooling, decreasing of the temperature leads to the arrangement of dipole moments and an increase of polarization. This also perturbates charges at the surface, which now need to be supplied towards the ferroelectric surface in order to account for increasing screening demands, leading to the current flow or electric field in reverse direction. Potentially, redox reactions can take place again, but with oxidizing and reducing surfaces in reverse. (**Figure 1.7 d**).

The total amount of charge generated in this processes is one of the important factors needed to drive redox reactions. Faraday law of electrolysis[93] states that the amount of substance produced/released at each electrode is directly proportional to the quantity of charge flowing through the cell and can be expressed as:

$$m = \frac{Q\ M}{F\ z} \qquad (5)$$

Where Q is total electric charge, m and M are the mass and molar mass of the substance, F is the Faraday constant and z is the valence of the ions.

On another side, in order to trigger any processes, the potential difference between the anode and the cathode is needed. In the case of, for instance, water splitting, a potential difference of at least 1.23 V is needed, although some over potential should be accounted for. The pyroelectric voltage ΔV created across the materials of thickness h can be calculated as[92]:

$$\Delta V = \frac{p\ h\ \Delta T}{\varepsilon_{33}^{T}\varepsilon_0} \qquad (6)$$

where $\varepsilon_{33}{}^{T}$ is the material permittivity at a constant stress and h is the material thickness.

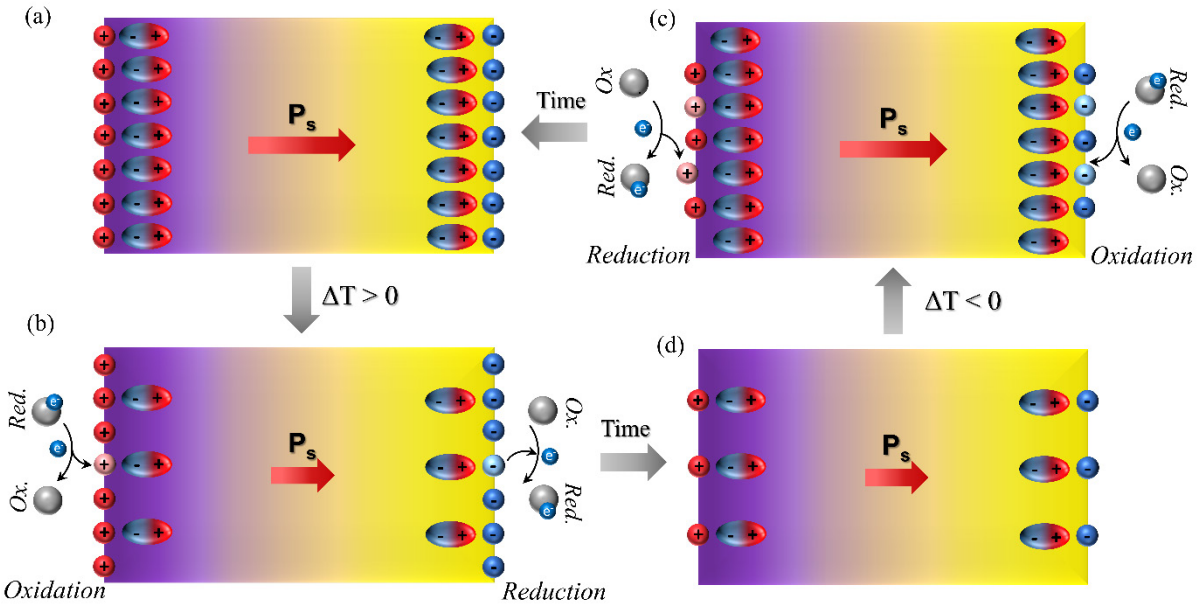

Figure 1.7 *Pyrocatalytical cycle driven by the heating/cooling of ferroelectric material. (a) Charge-balance between bound polarization (dipoles) and surface screening charge (blue and red balls) at thermal equilibrium; (b) Heating of the material, decreases the net spontaneous polarization P_s, causing appearance of excess positive/negative charges at the surface, which are neutralized by the supply/consumption of electrons during oxidation/reduction processes involving surface adsorbed species. After some time, system achieves thermal equilibrium state (c), which can be disrupted by cooling of the sample (d). Cooling reestablishes spontaneous polarization, whereby new bound charges are being compensated by the consumption/supply of electrons from redox processes, happening at the opposite surfaces compared to the ones shown in panel (c).*

Up to now, several experimental works showed successful implementation of pyro-electrocatalytic concept for water splitting and H_2 production in different configurations. The ferroelectric materials were either used as an i) external source of electrons, whereby created pyroelectric charge under temperature variations was used to drive redox reactions at anode/cathode in the separate catalytic cell [86,92] or ii) active catalytic surfaces, in the form on nano objects (i.e. nanoparticles, nanopowders, nanorods, etc.) directly dispersed inside of the water medium during the cyclical temperature variations.[87,94,95] Albeit the wide range of experimental evidences, in most cases it is not clear which are the fundamental mechanisms behind these observations. On one hand, the catalytic mechanism proposed in some of these works is a direct reaction between H^+ ions and electrons, whereby H_2 is produced. However, there is a substantial number of experimental works which successfully use the same pyro-electrocatalytic concept for water remediation (degradation of pollutants such as organic dyes) and disinfection of bacteria. In these works, explanations of the process are mainly attributed

to the creation of reactive oxygen species (ROS) and radicals, which arise when pyroelectric charges interact with adsorbed molecules. These species might then further oxidize dye pollutants and neutralize bacteria,[80,82,96] or potentially also react with surface adsorbed water molecules in the process of water splitting.

It is particularly useful to operate pyrocatalytically-driven reactions near the Curie temperature. By heating/cooling the sample across the Curie temperature, pyroelectric coefficients are maximized, since the change of the polarization with temperature (dP_s/dT) is large in this region (**Figure 1.6**). This will influence the amount of charge produced, since the latter is directly proportional to pyroelectric coefficient. Some of the benefits of working close to Curie temperature have been demonstrated in hybrid approach, were both piezoelectricity and pyroelectricity were coupled in order to drive electrochemical reactions.[88,95,97]

On the other hand, theoretical work by Kakekhani et al.[98] showed that by cycling between ferroelectric and paraelectric state, one can leverage the differences in thermodynamically preferred surface chemical states of paraelectric and ferroelectric phase, in order to drive part of H_2O splitting reactions into O_2 and H_2. In this work it was calculated that water readily dissociates on down polarized ferroelectric surfaces, whereby surface covered by H atoms is created. When ferroelectric transits into the paraelectric phase, H atoms recombine to form H_2, which are then desorbed from the surface leaving the bare stoichiometric surface, corresponding to the preferred thermodynamic state of paraelectric phase. However, in this work pyroelectrically-driven surface chemical reactions were not considered.

Finally, even though water splitting through pyrocatalytically-driven reaction has been reported by measuring the concentration of produced H_2 at the end of temperature cycles, less is known about the dominant chemical species at the surface and their evolution during the catalytic processes. This is partially caused by the selection of employed materials, which are typically in the form of nanoparticles suspended inside of the electrolytes due to the greatly improved surface areas compared to surfaces of thin films. Since the nanoparticles are in the direct contact with the electrolyte, pyroelectricity, rather than polarization orientation plays the dominant role. However, it is known that in the case of ferroelectric thin films/single crystals with surface adsorbed water, the direction of polarization plays a crucial role by determining type of surface redox processes taking place.

Therefore, in-situ studies of the surface chemistry evolution during cyclical temperature changes, performed on ferroelectric surfaces with known domain structures, would enable to

gain fundamental insight into the catalytic processes and shine some light onto the main chemical species and dynamical processes taking place. That is one of the topics explored in this thesis.

References

[1] J. Valasek, *Phys. Rev.* **1921**, *17*, 475.

[2] K. M. Rabe, M. Dawber, C. Lichtensteiger, C. H. Ahn, J.-M. Triscone, in *Phys. Ferroelectr. Mod. Perspect.*, Springer Berlin Heidelberg, **2007**, pp. 1–30.

[3] I. H. Lone, J. Aslam, N. R. E. Radwan, A. H. Bashal, A. F. A. Ajlouni, A. Akhter, *Nanoscale Res. Lett.* **2019**, *14*, 142.

[4] M. Acosta, N. Novak, V. Rojas, S. Patel, R. Vaish, J. Koruza, G. A. Rossetti, J. Rödel, *Appl. Phys. Rev.* **2017**, *4*, 041305.

[5] A. von Hippel, R. G. Breckenridge, F. G. Chesley, L. Tisza, *Ind. Eng. Chem.* **1946**, *38*, 1097.

[6] B. Wul, I. M. Goldman, *C.R. Acad. Sci. U.R.S.S.* **1946**, *51*.

[7] A. Von Hippel, *Rev. Mod. Phys.* **1950**, *22*, 221.

[8] S. H. Oh, J. H. Ko, H. Y. Lee, I. Lazar, K. Roleder, *Molecules* **2018**, *23*, 1.

[9] K. J. Choi, M. Biegalski, Y. L. Li, A. Sharan, J. Schubert, R. Uecker, P. Reiche, Y. B. Chen, X. Q. Pan, V. Gopalan, L.-Q. Chen, D. G. Schlom, C. B. Eom, *Science* **2004**, *306*, 1005.

[10] C. Lichtensteiger, P. Zubko, M. Stengel, P. Aguado-Puente, J.-M. Triscone, P. Ghosez, J. Junquera, in *Oxide Ultrathin Film.*, Wiley, **2011**, pp. 265–230.

[11] C. Lichtensteiger, S. Fernandez-Pena, C. Weymann, P. Zubko, J. M. Triscone, *Nano Lett.* **2014**, *14*, 4205.

[12] L. Mitoseriu, L. P. Curecheriu, in *Nanoscale Ferroelectr. Multiferroics*, John Wiley & Sons, Ltd, **2016**, pp. 473–511.

[13] S. V. Kalinin, Y. Kim, D. D. Fong, A. N. Morozovska, *Reports Prog. Phys.* **2018**, *81*, 036502.

[14] J. Junquera, P. Ghosez, *Nature* **2003**, *422*, 506.

[15] D. D. Fong, G. B. Stephenson, S. K. Streiffer, J. A. Eastman, O. Aucielo, P. H. Fuoss, C. Thompson, *Science* **2004**, *304*, 1650.

[16] J. F. Ihlefeld, D. T. Harris, R. Keech, J. L. Jones, J. P. Maria, S. Trolier-McKinstry, *J.*

Am. Ceram. Soc. **2016**, *99*, 2537.

[17] D. C. Lupascu, I. Anusca, M. Etier, Y. Gao, G. Lackner, A. Nazrabi, M. Sanlialp, H. Trivedi, N. Ul-Haq, J. Schröder, in *Ferroic Funct. Mater. Exp. Model. Simul.*, Springer International Publishing, **2018**, pp. 97–178.

[18] Y. Heo, D. Kan, Y. Shimakawa, J. Seidel, *Phys. Chem. Chem. Phys.* **2016**, *18*, 197.

[19] Y. M. Kim, A. Morozovska, E. Eliseev, M. P. Oxley, R. Mishra, S. M. Selbach, T. Grande, S. T. Pantelides, S. V. Kalinin, A. Y. Borisevich, *Nat. Mater.* **2014**, *13*, 1019.

[20] M. F. Chisholm, W. Luo, M. P. Oxley, S. T. Pantelides, H. N. Lee, *Phys. Rev. Lett.* **2010**, *105*, 197602.

[21] M. Stengel, N. A. Spaldin, *Nature* **2006**, *443*, 679.

[22] C. T. Black, J. J. Welser, *IEEE Trans. Electron Devices* **1999**, *46*, 776.

[23] M. Stengel, D. Vanderbilt, N. A. Spaldin, *Nat. Mater.* **2009**, *8*, 392.

[24] C. Kittel, *Phys. Rev.* **1946**, *70*, 965.

[25] M. J. Highland, T. T. Fister, D. D. Fong, P. H. Fuoss, C. Thompson, J. A. Eastman, S. K. Streiffer, G. B. Stephenson, *Phys. Rev. Lett.* **2011**, *107*, 1.

[26] C. Weymann, C. Lichtensteiger, S. Fernandez-Peña, A. B. Naden, L. R. Dedon, L. W. Martin, J. M. Triscone, P. Paruch, *Adv. Electron. Mater.* **2020**, *6*, 2000852.

[27] Y. Zhang, M. Xie, V. Adamaki, H. Khanbareh, C. R. Bowen, *Chem. Soc. Rev.* **2017**, *46*, 7757.

[28] D. Zhao, T. Lenz, G. H. Gelinck, P. Groen, D. Damjanovic, D. M. de Leeuw, I. Katsouras, *Nat. Commun.* **2019**, *10*, 1.

[29] I. Efe, N. A. Spaldin, C. Gattinoni, *J. Chem. Phys.* **2021**, *154*, 024702.

[30] N. Domingo, I. Gaponenko, K. Cordero-Edwards, N. Stucki, V. Pérez-Dieste, C. Escudero, E. Pach, A. Verdaguer, P. Paruch, *Nanoscale* **2019**, *11*, 17920.

[31] S. V. Kalinin, D. A. Bonnell, *Phys. Rev. B - Condens. Matter Mater. Phys.* **2001**, *63*, 1.

[32] S. V. Kalinin, C. Y. Johnson, D. A. Bonnell, *J. Appl. Phys.* **2002**, *91*, 3816.

[33] J. J. Segura, N. Domingo, J. Fraxedas, A. Verdaguer, *J. Appl. Phys.* **2013**, *113*, 0.

[34] G. Geneste, B. Dkhil, *Phys. Rev. B - Condens. Matter Mater. Phys.* **2009**, *79*, 1.

[35] K. Cordero-Edwards, L. Rodríguez, A. Calò, M. J. Esplandiu, V. Pérez-Dieste, C.

Escudero, N. Domingo, A. Verdaguer, *J. Phys. Chem. C* **2016**, *120*, 24048.

[36] J. Shin, V. B. Nascimento, G. Geneste, J. Rundgren, E. W. Plummer, B. Dkhil, S. V. Kalinin, A. P. Baddorf, *Nano Lett.* **2009**, *9*, 3720.

[37] J. L. Wang, F. Gaillard, A. Pancotti, B. Gautier, G. Niu, B. Vilquin, V. Pillard, G. L. M. P. Rodrigues, N. Barrett, *J. Phys. Chem. C* **2012**, *116*, 21802.

[38] S. Sanna, R. Hölscher, W. G. Schmidt, *Phys. Rev. B - Condens. Matter Mater. Phys.* **2012**, *86*, 1.

[39] M. H. Zhao, D. A. Bonnell, J. M. Vohs, *Surf. Sci.* **2008**, *602*, 2849.

[40] D. Li, M. H. Zhao, J. Garra, A. M. Kolpak, A. M. Rappe, D. A. Bonnell, J. M. Vohs, *Nat. Mater.* **2008**, *7*, 473.

[41] Y. Yun, E. I. Altman, *J. Am. Chem. Soc.* **2007**, *129*, 15684.

[42] Z. Zhang, P. Sharma, C. N. Borca, P. A. Dowben, A. Gruverman, *Appl. Phys. Lett.* **2010**, *97*, 243702.

[43] Z. Zhang, R. González, G. Díaz, L. G. Rosa, I. Ketsman, X. Zhang, P. Sharma, A. Gruverman, P. A. Dowben, *J. Phys. Chem. C* **2011**, *115*, 13041.

[44] N. Domingo, E. Pach, K. Cordero-Edwards, V. Pérez-Dieste, C. Escudero, A. Verdaguer, *Phys. Chem. Chem. Phys.* **2019**, *21*, 4920.

[45] I. Spasojevic, G. Sauthier, J. M. Caicedo, A. Verdaguer, N. Domingo, *Appl. Surf. Sci.* **2021**, *565*, 150288.

[46] N. Domingo, I. Gaponenko, K. Cordero-Edwards, N. Stucki, V. Pérez-Dieste, C. Escudero, E. Pach, A. Verdaguer, P. Paruch, *Nanoscale* **2019**, *11*, 17920.

[47] S. V. Kalinin, D. A. Bonnell, T. Alvarez, X. Lei, Z. Hu, R. Shao, J. H. Ferris, *Adv. Mater.* **2004**, *16*, 795.

[48] L. Fang, L. You, J.-M. Liu, in *Ferroelectr. Mater. Energy Appl.*, Wiley-VCH Verlag GmbH & Co. KGaA, **2018**, pp. 265–309.

[49] S. V. Kalinin, D. A. Bonnell, T. Alvarez, X. Lei, Z. Hu, J. H. Ferris, Q. Zhang, S. Dunn, *Nano Lett.* **2002**, *2*, 589.

[50] Y. Tian, L. Wei, Q. Zhang, H. Huang, Y. Zhang, H. Zhou, F. Ma, L. Gu, S. Meng, L.-Q. Chen, C.-W. Nan, J. Zhang, *Nat. Commun.* **2018**, *9*, 3809.

[51] R. V. Wang, D. D. Fong, F. Jiang, M. J. Highland, P. H. Fuoss, C. Thompson, A. M.

Kolpak, J. A. Eastman, S. K. Streiffer, A. M. Rappe, G. B. Stephenson, *Phys. Rev. Lett.* **2009**, *102*, 2.

[52] M. J. Highland, T. T. Fister, M. I. Richard, D. D. Fong, P. H. Fuoss, C. Thompson, J. A. Eastman, S. K. Streiffer, G. B. Stephenson, *Phys. Rev. Lett.* **2010**, *105*, 1.

[53] A. N. Morozovska, E. A. Eliseev, N. V. Morozovsky, S. V. Kalinin, *Phys. Rev. B* **2017**, *95*, 1.

[54] S. M. Yang, A. N. Morozovska, R. Kumar, E. A. Eliseev, Y. Cao, L. Mazet, N. Balke, S. Jesse, R. K. Vasudevan, C. Dubourdieu, S. V. Kalinin, *Nat. Phys.* **2017**, *13*, 812.

[55] H. Lee, T. H. Kim, J. J. Patzner, H. Lu, J. W. Lee, H. Zhou, W. Chang, M. K. Mahanthappa, E. Y. Tsymbal, A. Gruverman, C. B. Eom, *Nano Lett.* **2016**, *16*, 2400.

[56] H. Lu, A. Lipatov, S. Ryu, D. J. Kim, H. Lee, M. Y. Zhuravlev, C. B. Eom, E. Y. Tsymbal, A. Sinitskii, A. Gruverman, *Nat. Commun.* **2014**, *5*, 1.

[57] F. Liu, I. Fina, G. Sauthier, F. Sánchez, A. M. Rappe, J. Fontcuberta, *ACS Appl. Mater. Interfaces* **2018**, *10*, 23968.

[58] C. Blaser, P. Paruch, *New J. Phys.* **2015**, *17*, 13002.

[59] B. J. Rodriguez, S. Jesse, A. P. Baddorf, S. H. Kim, S. V. Kalinin, *Phys. Rev. Lett.* **2007**, *98*, 1.

[60] A. V Ievlev, A. N. Morozovska, V. Y. Shur, S. V Kalinin, A. V Ievlev, A. N. Morozovska, V. Y. Shur, S. V Kalinin, *Appl. Phys. Lett.* **2014**, *104*, 1.

[61] S. M. Neumayer, E. Strelcov, M. Manzo, K. Gallo, I. I. Kravchenko, A. L. Kholkin, S. V. Kalinin, B. J. Rodriguez, *J. Appl. Phys.* **2015**, *118*, 1.

[62] D. Dahan, M. Molotskii, G. Rosenman, Y. Rosenwaks, *Appl. Phys. Lett.* **2006**, *89*, 1.

[63] K.-W. Park, H. Seo, J. Kim, D. Seol, J. Hong, Y. Kim, *Nanotechnology* **2014**, *25*, 355703.

[64] A. V. Ievlev, S. Jesse, A. N. Morozovska, E. Strelcov, E. A. Eliseev, Y. V. Pershin, A. Kumar, V. Y. Shur, S. V. Kalinin, *Nat. Phys.* **2013**, *10*, 59.

[65] P. Paruch, T. Tybell, J. M. Triscone, *Appl. Phys. Lett.* **2001**, *79*, 530.

[66] W. Qian, W. Yang, Y. Zhang, C. R. Bowen, Y. Yang, *Piezoelectric Materials for Controlling Electro-Chemical Processes*, Springer Singapore, **2020**.

[67] H. Li, C. R. Bowen, Y. Yang, *Adv. Funct. Mater.* **2021**, *31*, 1.

[68] M. Xie, D. Zabek, C. Bowen, M. Abdelmageed, M. Arafa, *Smart Mater. Struct.* **2016**, *25*, 1.

[69] T. Zhang, T. Yang, M. Zhang, C. R. Bowen, Y. Yang, *iScience* **2020**, *23*, 101689.

[70] D. Zhang, H. Wu, C. R. Bowen, Y. Yang, *Small* **2021**, *17*, 2103960.

[71] M. Moniruddin, B. Ilyassov, X. Zhao, E. Smith, T. Serikov, N. Ibrayev, R. Asmatulu, N. Nuraje, *Mater. Today Energy* **2018**, *7*, 246.

[72] Y. F. Li, Z. P. Liu, *Wiley Interdiscip. Rev. Comput. Mol. Sci.* **2016**, *6*, 47.

[73] A. Fujishima, K. Honda, *Nature* **1972**, *238*, 37.

[74] L. Li, P. A. Salvador, G. S. Rohrer, *Nanoscale* **2014**, *6*, 24.

[75] S. Kim, N. T. Nguyen, C. W. Bark, *Appl. Sci.* **2018**, *8*, 1526.

[76] G. Liu, L. Ma, L. C. Yin, G. Wan, H. Zhu, C. Zhen, Y. Yang, Y. Liang, J. Tan, H. M. Cheng, *Joule* **2018**, *2*, 1095.

[77] K. Zhao, B. Ouyang, C. R. Bowen, Y. Yang, *Nano Energy* **2020**, *77*, 105152.

[78] M. Wang, B. Wang, F. Huang, Z. Lin, *Angew. Chemie - Int. Ed.* **2019**, *58*, 7526.

[79] C. Wang, T. Ma, Y. Zhang, H. Huang, *Adv. Funct. Mater.* **2022**, *32*, 2108350.

[80] C. Wang, N. Tian, T. Ma, Y. Zhang, H. Huang, *Nano Energy* **2020**, *78*, 105371.

[81] A. Kakekhani, S. Ismail-Beigi, *ACS Catal.* **2015**, *5*, 4537.

[82] Y. Xia, Y. Jia, W. Qian, X. Xu, Z. Wu, Z. Han, Y. Hong, H. You, M. Ismail, G. Bai, L. Wang, *Metals (Basel).* **2017**, *7*, 122.

[83] Q. Liu, D. Zhai, Z. Xiao, C. Tang, Q. Sun, C. R. Bowen, H. Luo, D. Zhang, *Nano Energy* **2022**, *92*, 106702.

[84] A. Kakekhani, S. Ismail-Beigi, E. I. Altman, *Surf. Sci.* **2016**, *650*, 302.

[85] K. Garrity, A. Kakekhani, A. Kolpak, S. Ismail-Beigi, *Phys. Rev. B - Condens. Matter Mater. Phys.* **2013**, *88*, 1.

[86] Y. Zhang, S. Kumar, F. Marken, M. Krasny, E. Roake, S. Eslava, S. Dunn, E. Da Como, C. R. Bowen, *Nano Energy* **2019**, *58*, 183.

[87] X. Xu, L. Xiao, Y. Jia, Z. Wu, F. Wang, Y. Wang, N. O. Haugen, H. Huang, *Energy Environ. Sci.* **2018**, *11*, 2198.

[88] Y. Zhang, P. T. T. Phuong, E. Roake, H. Khanbareh, Y. Wang, S. Dunn, C. Bowen, *Joule* **2020**, *4*, 301.

[89] Y. Zhang, H. Khanbareh, S. Dunn, C. R. Bowen, H. Gong, N. P. H. Duy, P. T. T. Phuong, *Adv. Sci.* **2022**, *9*, 2105248.

[90] P. Quaino, F. Juarez, E. Santos, W. Schmickler, *Beilstein J. Nanotechnol.* **2014**, *5*, 846.

[91] A. Kakekhani, S. Ismail-Beigi, *Phys. Chem. Chem. Phys.* **2016**, *18*, 19676.

[92] M. Xie, S. Dunn, E. Le Boulbar, C. R. Bowen, *Int. J. Hydrogen Energy* **2017**, *42*, 23437.

[93] M. Faraday, *Philos. Trans. R. Soc. London* **1834**, *124*, 77.

[94] R. Belitz, P. Meisner, M. Coeler, U. Wunderwald, J. Friedrich, J. Zosel, M. Schelter, S. Jachalke, E. Mehner, *Energy Harvest. Syst.* **2017**, *4*, 107.

[95] P. T. Thuy Phuong, Y. Zhang, N. Gathercole, H. Khanbareh, N. P. Hoang Duy, X. Zhou, D. Zhang, K. Zhou, S. Dunn, C. Bowen, *iScience* **2020**, *23*, 101095.

[96] E. Gutmann, A. Benke, K. Gerth, H. Böttcher, E. Mehner, C. Klein, U. Krause-Buchholz, U. Bergmann, W. Pompe, D. C. Meyer, *J. Phys. Chem. C* **2012**, *116*, 5383.

[97] Y. Zhang, P. T. Thuy Phuong, N. P. Hoang Duy, E. Roake, H. Khanbareh, M. Hopkins, X. Zhou, D. Zhang, K. Zhou, C. Bowen, *Nanoscale Adv.* **2021**, *3*, 1362.

[98] A. Kakekhani, S. Ismail-Beigi, *J. Mater. Chem. A* **2016**, *4*, 5235.

CHAPTER 2

Experimental methods

In this chapter, the principal experimental methods used for the investigation of ferroelectric surface chemistry and their properties at the nanoscale, with special focus on X-Ray Photoelectron Spectroscopy and Atomic Force Microscopy-based techniques, will be presented. Additionally, the procedure for $BaTiO_3$ thin films' preparation by Pulsed Laser Deposition technique will be explained, accompanied by their basic functional and structural characterization.

2.1 Thin film growth by Pulsed Laser deposition (PLD)

Pulsed Laser Deposition (PLD) is a physical vapor deposition technique that uses a high-power pulsed laser to ablate a target material which gets evaporated creating the plume directed towards the substrate where material gets deposited.

A PLD system consists of i) higher power laser and the associated laser optics system (i.e. lenses, mirrors, apertures, etc.), necessary for the guidance of the laser beam and its focus on the target surface and ii) vacuum-chamber consisting of the substrate holder with the heater, carrousel housing different targets (which can be exchanged during the growth, without breaking the vacuum, enabling growth of multilayer materials in a single run) and iii) positioning system which allows control distance between the substrate and the target. Besides, each target can be rotated and/or toggled during the growth in order to ensure uniform composition of the deposited film and avoid emission of big particulates. A schematic representation of PLD system in shown in **Figure 2.1**.[1]

The interaction of the laser with the target and growth of the thin film during PLD is a complex process, however in general it can be said that it involves three principle steps: i) absorption of the laser by the target ii) ejection of the ionized species/creation of the plasma plume and iii) deposition of the material onto the desired substrate kept at high temperature to ensure a good level of ionic mobility on the surface. The atoms of the target material absorb the UV energy of the laser (typically excimer) leading to the conversion of internal thermal and ionization energies into the kinetic energy of the ablated particles and the creation of the plume. The plasma plume can contain different species, such as electrons, excited /neutral atoms, ions, molecules or clusters of the target material that condense on the substrate where the thin film grows.

PLD growth can be done in vacuum or in the atmosphere of some background gas, such as O_2 used for the synthesis of the oxides. The background gas can contribute to the formation of the plume where oxygen and atoms of target material react physically and chemically producing oxygen molecular species. On the other hand, the presence of a background gas reduces to some extent the kinetic energy of the target-expulsed species, which can cause re-sputtering of the atoms from the already deposited thin film and therefore create defects or non-stoichiometric composition of the film. Beside background pressure, factors such as laser fluency and laser energy density, temperature of the substrate, distance between the target and

the substrate, repetition rate, as well as physical and chemical properties of the chosen substrate and target, will influence the structural properties and stoichiometry of the grown films. Although this is useful, since one could modify some of parameters in order to grow thin films for desired applications, in reality the growth of thin films requires previous optimization of the growth parameters. In this thesis, work was done to optimize the synthesis of $BaTiO_3$ ferroelectric thin films with optimal functional properties on SrRuO3 buffer layers grown on $SrTiO_3$ single crystals used as substrates, which were used all over the thesis for the different targeted experiments.

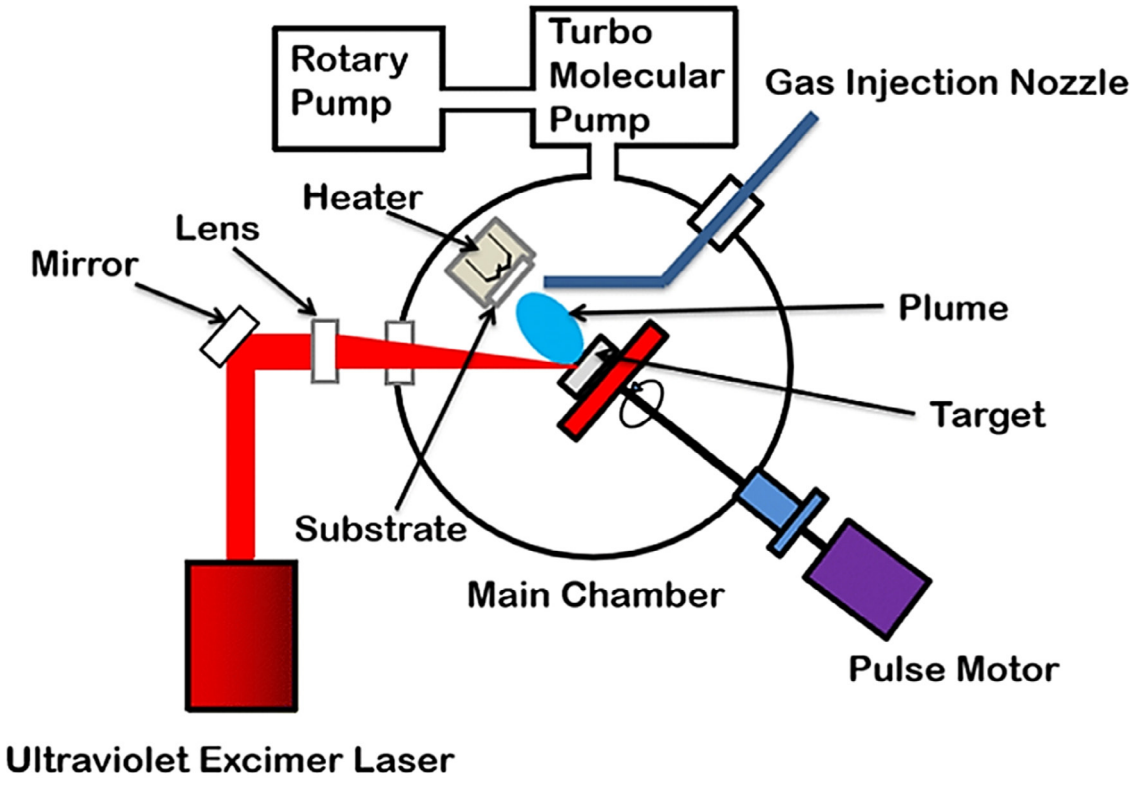

Figure 2.1 *Schematic representation of the main components of the PLD system. Adapted from [1].*

2.1.1 Growth of $BaTiO_3$ thin films by PLD

Optimized growth of epitaxial ferroelectric $SrRuO_3/BaTiO_3$ (SRO/BTO) bilayers by Pulsed Laser Deposition (PLD) technique on $SrTiO_3$ (STO) substrates was achieved using the following set up and conditions. A KrF excimer laser (λ = 248 nm, fluence 5.4 J/cm^2, 2 Hz repetition rate) was used to ablate stoichiometric ceramic targets of $SrRrO_3$ and $BaTiO_3$. As received (001) oriented STO single crystals (CrysTec GmbH) were used as substrates in all

depositions. Target-substrate distance was fixed at 8 cm. Prior to the growth of BTO layer, we firstly grow SRO layer which serves as a bottom electrode for PFM measurements. Both SRO and BTO layer were deposited in O_2 atmosphere with partial oxygen pressure pO_2 = 100 mTorr and at deposition temperatures of 635 °C and 700 °C, respectively. After the deposition sample was cooled down slowly to the room temperature with the rate of 3 °C/min in saturated O_2 atmosphere ($pO_2 = 10^4$ mTorr) in order get rid of any present oxygen vacancies. All the thin films grown in this thesis were prepared and characterized at the Nanomaterials Growth Unit located at ICN2.

2.1.2 Structural characterization of $BaTiO_3$ thin films by X-Ray diffraction

The structural properties of as grown BTO thin films were studied by X-Ray diffraction in theta-2theta (θ-2θ) geometry, whereby θ is the incident angle with respect to the surface and 2θ is the diffracted angle with respect to the incident beam, respectively. High resolution θ-2θ coupled scan recorded around the perovskite (002) reflection in the $39^0 - 49^0$ range shows three peaks belonging to BTO, SRO thin films and STO substrate (**Figure 2.2 a**). The out-of-plane lattice parameters have values of c_{SRO} = 3.955 Å for $SrRuO_3$ and c_{BTO} = 4.149 Å for BTO thin film. These values are in agreement with the values reported in the literature for the fully strained SRO/BTO bilayers grown on STO (001) substrates.[2] The results from reflectivity measurements (**Figure 2.2 b**) were analyzed by X'Pert Reflectivity Software (Malvern-Panalytical) and common Fourier method from which we obtained a thickness of 33 nm for the $SrRuO_3$ and 21 nm for the BTO layer.

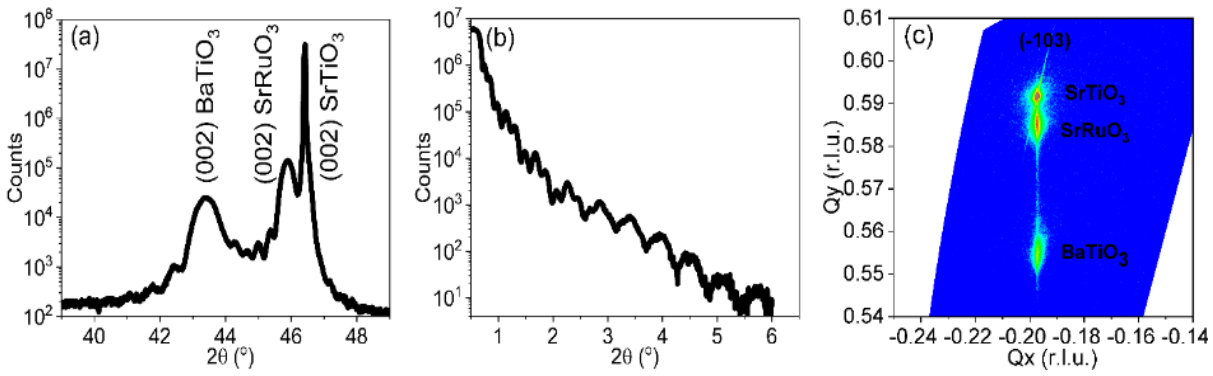

Figure 2.2 *Results of X-ray diffraction analysis of SRO/BTO bilayers grown on STO substrate. (a) θ-2θ coupled scan around the (002) reflection of the STO substrate, SRO buffer electrode and BTO thin film; (b) X-Ray reflectivity measurements and (c) Reciprocal space maps (RSM) around (103) Bragg peak, showing that SRO and BTO films are coherent and fully strained to STO substrate.*

In order to confirm the strain state of epitaxial SRO/BTO bilayers we have recorded X-Ray reciprocal map (XR-RSM) around (103) STO Bragg reflection. From this measurement is evident that SRO and BTO films are coherent and fully strained to the single crystal STO substrate (**Figure 2.2 c**). The in-plane lattice parameter of both layers is 3.905 Å and it is equal to the in-plane lattice parameter of STO substrate. c/a ratio for BTO thin film is 1.06, therefore showing that the BTO film is single-domain, tetragonal and c-oriented.

2.1.3 Growth of $BaTiO_3$ thin films on scandate substrates

Besides on STO substrates, the same growth parameters explained in Section 2.1.1 were used for growing SRO/BTO bilayers on different scandate substrates. High resolution 2theta-omega profiles of $SrRuO_3$ (SRO) - buffered BTO thin films grown on STO (001), $DyScO_3$ (DSO 110), $GdScO_3$ (GSO 110) and $SmScO_3$ (SSO 110) substrates are shown in **Figure 2.3 a**. Thickness of SRO layer was always ≈ 25 nm, while the thickness of BTO was changed from ≈ 15 to ≈ 35 nm, depending on the substrate as indicated in **Figure 2.3 a**.

Reciprocal space maps of SRO/BTO bilayers grown on DSO, GSO and SSO substrates shown in **Figure 2.3 b,c,d** evidence that both SRO and BTO layer are fully strained to the substrates. Since the in-plane lattice parameter of SRO is bigger than that of STO, but smaller than those of DSO, GSO and SSO, compressive or tensile strain are induced inside of the SRO layer on titanates or scandates respectively. This is observed in θ-2θ profiles as a shift of SRO peak towards the higher 2θ angles, as well as in Q_xQ_z RSMs as a shift of SRO peak towards higher Q_z values, indicating the decrease of the *c* out-of-plane lattice parameter. On the other hand, compressive strain induced inside in BTO layer is decreasing going from STO to SSO, whereby on SSO substrate BTO grows almost strain-free due to their very similar in-plane lattice parameters.

Similarly, a decrease of in-plane compressive strain leads to the reduction of the elongated out-of-plane *c* lattice parameter, observable as a shift of the BTO peak towards higher 2θ angles or correspondingly higher Q_z values. The calculated values of the in-plane *a* and out-of-plane *c* lattice parameters of BTO (full circles) and SRO layers (empty squares) are shown in **Figure 2.3 e**, whereby values of *c* lattice parameters were calculated from both, 2θ positions in θ-2θ scans and from Q_xQ_z coordinates extracted from RSMs. It can be seen that calculation of *c* lattice parameter by both method gives very similar values. On the other hand, it can be seen that BTO and SRO share the same value of the in-plane *a* lattice constant, which corresponds

to *a* lattice parameter of the pseudo-cubic substrate (values of the lattice parameters not shown here).

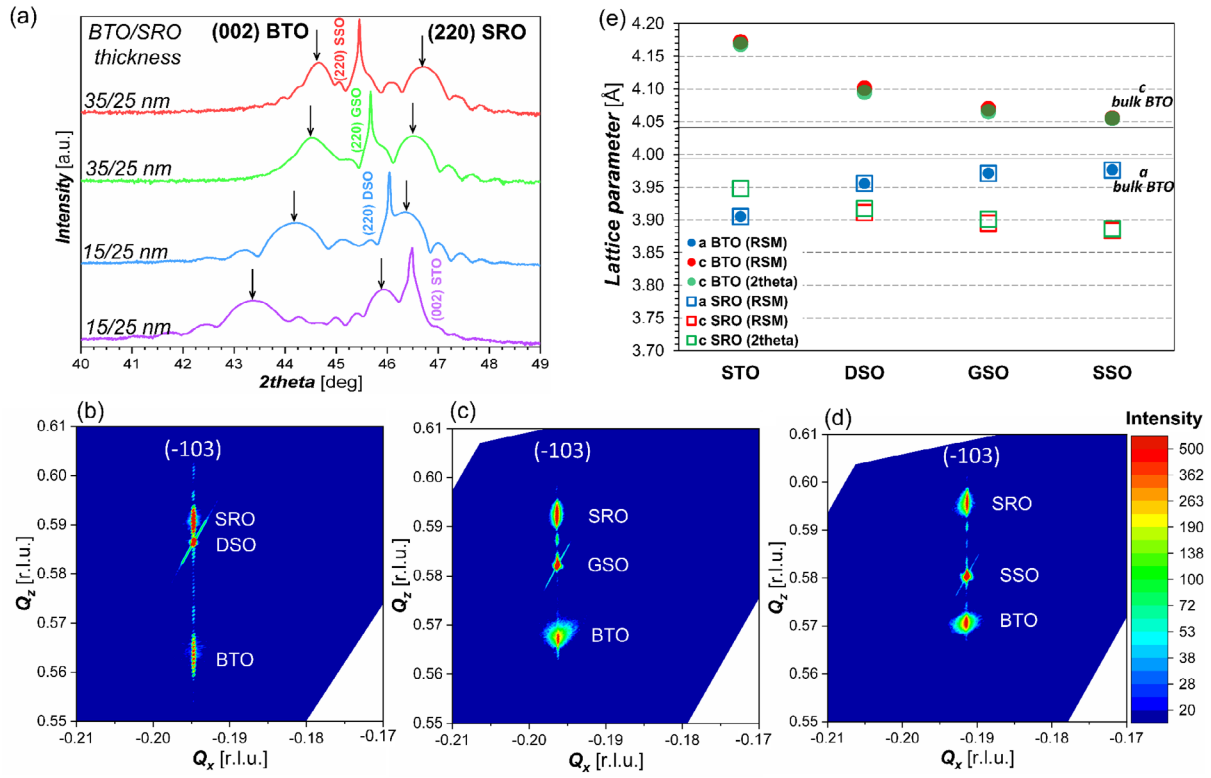

Figure 2.3 *XRD characterization of SRO/BTO bilayers grown on different scandate substrates;(a) θ-2θ coupled scans of SRO/BTO bilayers grown on DSO, GSO and SSO substrates. SRO/BTO bilayer grown on STO is also shown for a comparison. Thickness of the SRO layer is maintained constant, while thickness of BTO layer varied between 15 and 35 nm, depending on the substrate; X-Ray reciprocal space maps recorded around -103 reflection on (b) DSO, (c) GSO and (d) SSO substrates, showing coherent and strained SRO/BTO bilayers in all the cases; (e) Calculated in-plane (blue circles /squares) and out-of-plane (red and green circles/squares) of BTO and SRO layers, respectively. Out-of-plane lattice parameters were calculated from both, Q_xQ_z coordinates (red symbols) and 2theta angles (green symbols) for comparison.*

Even though all the thin films exhibited well defined ferroelectric properties as studied by PFM, in this thesis only the surface chemistry of BTO/SRO bilayers grown on STO (001) substrates was investigated, due to their highest and probably most stable polarization. The other films were used in a collaboration with Dr Giuseppe Mercurio, to investigate ultra-fast switching processes in these films in the European X-Ray Free-Electron Laser Facility (XEFL, Schenefeld), which is still undergoing. As a side note, the investigation of possible surface chemistry or structural differences in these films represents an interesting topic for future work.

2.2 Surface characterization by Atomic Force Microscopy

Atomic force microscopy (AFM) is a surface sensitive technique that allows to study from topography to all types of functional properties at the nanoscale, down to atomic spatial resolution. Invented in 1986 by the same fathers of Scanning Tunneling Microscopy Gerd Binning, Calvin Quate and Christoph Gerber,[3] it expanded the scope of materials and properties to investigate well beyond conductive samples and electronic states, becoming one of the enabling nanotechnology tools for the development of nanoscience.

In AFM, a micrometric cantilever with a sharp ended tip with characteristic radius of few nm is used to sense interactions forces with a surface down to femto-Newtons, while its movement is sensed by some electro-optical based setup (typically based on a laser reflected at the back side of the cantilever). The detected forces range from short-range repulsive van der Waals interactions to long range electrostatic and magnetostatic interactions, embracing all types of chemical, capillary and all sorts of short-range interactions in between. Then, a feedback loop acts on a z-piezo scanner that adjusts the sensed tip-sample force interactions, while the cantilever is scanned over a surface with an x-y piezo scanner.

There are essentially two modes to use the AFM based on how the cantilever is operated: contact AFM or constant force mode, and dynamic AFM. In contact AFM, the tip is brought into strong repulsive contact with the sample and the deflection of the cantilever is measured. The applied force between the tip and the sample will be proportional to the deflection of the cantilever following a Hook's law mainly defined by the cantilever stiffness. This force is meant to be kept constant during the scan by using the deflection as the control magnitude for the topography feedback loop. On the other hand, in dynamic AFM the cantilever is vibrated (using different techniques) close to the surface, and used as a damped single harmonic oscillator. In this configuration, the tip-sample interacting forces affect the dynamics of the cantilever by changing its resonance frequency, amplitude of vibration and phase. In ambient conditions, a commonly used dynamic AFM mode is Amplitude Modulation AFM (AM-AFM) in which the cantilever is mechanically excited close to its resonance frequency while the amplitude is measured and used as the control parameter of the feedback loop: in this case, the amplitude decreases when the cantilever is approached to the surface, so an amplitude setpoint

$A_{sp} < A_0$ has to be chosen to drive the feedback loop and keep the tip-sample distance constant over the scan.

From these basics, a myriad of operation modes have been developed that allow to distinguish among all possible tip-sample interaction forces as well as characterize all types of functional properties sensed through the surface. The most relevant ones for this thesis are Piezoresponse Force Microscopy and Kelvin Probe Force Microscopy.

2.2.1 Piezoresponse Force Microscopy (PFM)

Piezoresponse force microscopy (PFM) is the main technique used throughout this thesis for the electromechanical characterization of ferroelectric samples. PFM is a contact AFM based technique in which a conductive AFM tip is used both as a top mobile electrode to scan over the sample surface and as a mechanical deflection sensor.

At the core of PFM technique lies the inverse piezoelectric effect, which describes the deformation of a piezoelectric as a response to an applied electric field. If an *ac* voltage applied to the AFM tip in contact with ferroelectric material has the form given by the equation (1)[4,5]:

$$V_{tip} = V_{ac}\cos(\omega t) \qquad (1)$$

where ω is frequency and V_{ac} is the amplitude of the applied *ac* voltage, it will induce an oscillatory mechanical deformation of the sample through the inverse piezoelectric effect, which will cause a deflection of the cantilever that can be expressed as:

$$d = d_0 + A\cos(\omega t + \varphi) \qquad (2)$$

where d_0 is the equilibrium position of the cantilever. A is the amplitude and φ is the phase of the electromechanical response, which are directly related to the magnitude and the direction of the polarization in the sample. In this case, the cantilever deflection is usually detected indirectly, by following the reflection of the laser spot focused on the cantilever on a light-sensitive diode. On this way, oscillating surface displacement is converted into an oscillating voltage signal, which is analyzed by a lock-in amplifier.

If the polarization of the sample has a direction normal to the sample surface (i.e. out-of-plane) then the polarization direction can be determined by vertical (vPFM) measurements as described below. In the case when applied electric field and the underneath polarization are

pointing in the same direction, sample will locally expand. Conversely, if the electric field applied locally by the biased AFM tip and underneath polarization have opposite directions, the sample will contract. In both cases, this leads to the cantilever deflection, as defined by equation (2). The phase φ will be equal to 0° or 180° if the electromechanical response and driving *ac* voltage are in phase or out of phase, respectively. Schematic representations of both case scenarios are shown in **Figure 2.4**.

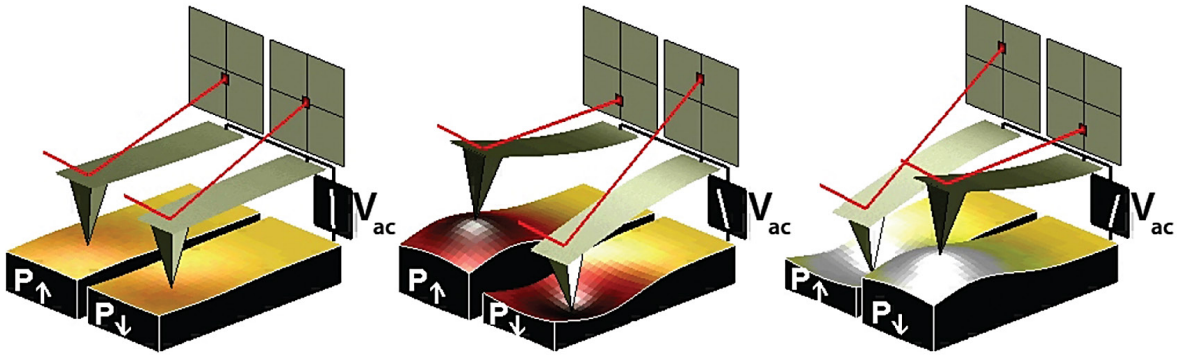

Figure 2.4 *Schematic representation of the PFM operating principle. If the sample is down-polarized and the positive voltage is applied to the tip, it will locally expand. If the sign of voltage is changed to negative, sample locally contracts. The opposite happens in the case of up-polarized domains. In the other words, if the polarization and the electric field are pointing in the same direction, electromechanical response and driving AC voltage are in phase. Image taken from [4].*

On the other hand, the amplitude of the electromechanical response A is directly proportional to the piezoelectric tensor d_{ijk} and applied *ac* voltage magnitude V_{ac}. In the case of vertical PFM measurements, the most important component of this tensor is the d_{33} piezoelectric coefficient, and therefore the amplitude A can be expressed as:

$$A \backsim d_{33} V_{ac} \qquad (3)$$

The value of the d_{33} piezoelectric coefficient can vary between 0.1 pm/V for weak and 500 pm/V for the strongest piezoelectrics, meaning that usual cantilever deflection will be in the order of pm. Therefore, for weak piezoelectrics and very thin films, such small deflection amplitudes are difficult to be detected. In order to increase them, one might use higher driving amplitudes as long as it doesn't surpass the coercive voltage of the sample, or causes some other changes such as irreversible electrochemical modification of the surface, electrical breakdown or complete surface damage.

Another way to increase the signal-to-noise ratio is to take advantage of the contact resonance frequency of the cantilever mechanically coupled to the sample, whereby the amplitude A can be enhanced by the factor Q, called the quality factor. However, working at the contact resonance frequency can lead to topographic crosstalk and artifacts due to the contact-stiffness dependent changes in the contact resonance frequency caused by the sample surface roughness. Rodriguez et al.[6] found a way to track the position of the resonance frequency during the contact PFM measurements, and therefore adjust the drive frequency in order to keep it always at the contact resonance, called Dual Amplitude Resonance Tracking (DART). Schematic illustration of DART PFM mode is shown in **Figure 2.5 a**.

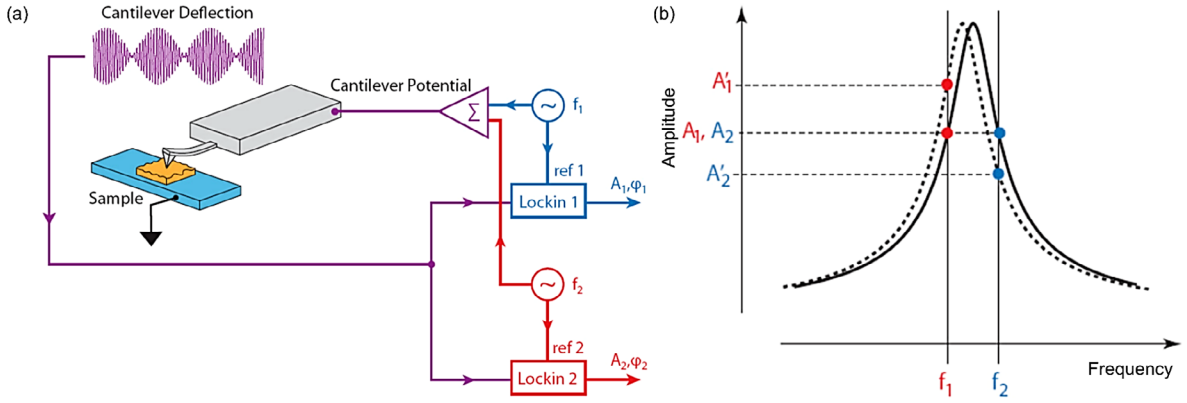

Figure 2.5 *Principle of Dual Amplitude Resonance Tracking (DART) PFM operation mode. Adapted from [6].*

Here, the cantilever is excited by two oscillating voltages at frequencies separated by small frequency window, being close to the contact resonance one, namely f_1 and f_2. Resulting cantilever deflection is sent two to separate lock-in amplifiers, referenced to the input drive signals, and the information about amplitudes A_1 and A_2 and phases φ_1 and φ_2 at both frequencies can be obtained. Decrease or increase of the resonance frequency leads to the consequential decrease or increase of the amplitude difference signal $A_2' - A_1'$, respectively (**Figure 2.5 b**). This amplitude difference signal is then used as the input to the feedback loop, which enables compensation of any contact resonance frequency shift, by adjusting the frequencies f_1 and f_2 to straddle the new contact resonance frequency peak by making $A_2' - A_1' = 0$.

2.2.2 Ferroelectric lithography and switching spectroscopy PFM (SS-PFM)

The application of *dc* bias higher than the coercive voltage to the AFM tip while being statically or dynamically in contact with ferroelectric surfaces enables local modification of polarization

through the process of polarization switching. In this process one can artificially create individual domains, domain arrays or complex patterns. In the case of ferroelectric thin film samples, used in this thesis, polarization switching can occur through the application of voltage in different configurations, whereby emergence of domains and their subsequent growth will follow different paths as explained bellow.[7]

When a ferroelectric thin film is sandwiched between two metallic electrodes in a capacitor geometry (**Figure 2.6 a**), a voltage can be applied directly by the AFM tip in the case of µm-sized capacitor, or alternately, through the external wire attached to the top electrode, whereby a homogenous electric field is created throughout the sample. Ferroelectric switching starts by the generation of many reversed domains at particular nucleation sites at the electrode, usually corresponding to the presence of defects.[8–10] Nucleated domains continue to grow by the fast forward propagation of domains across the film and subsequent slower lateral expansion. In this configuration, an AFM tip can be used for the imaging through the top electrode of ferroelectric domains created after voltage pulses,[9] or the measurement of hysteresis loops by switching spectroscopy PFM (SS-PFM), which is this case would reflect switching behavior averaged along the whole sample volume under the electrode.

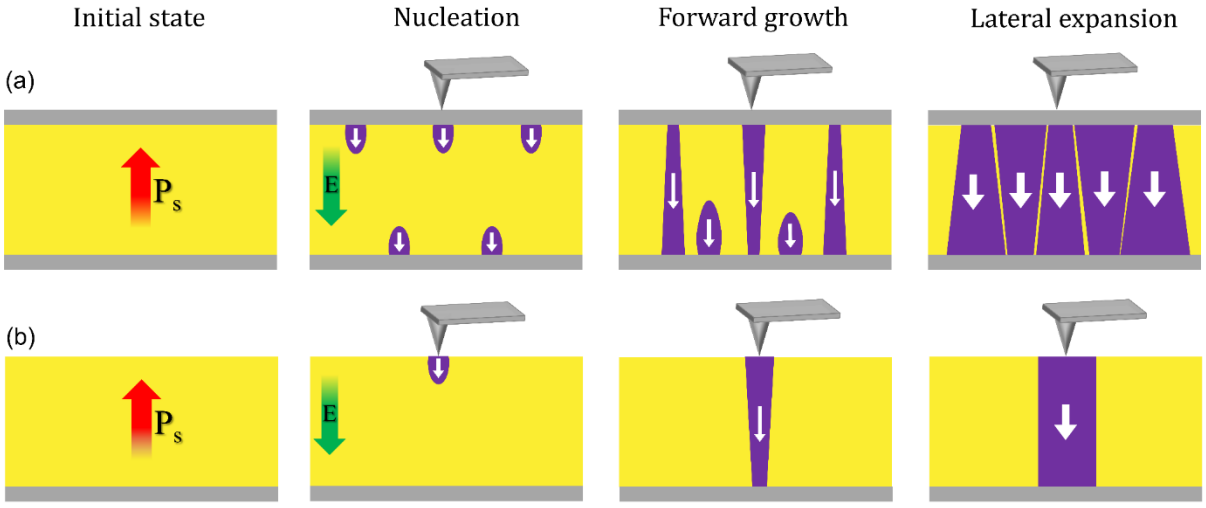

Figure 2.6 *Scheme of domain nucleation and growth in (a) bottom electrode-ferroelectric-top electrode capacitor structure, whereby voltage is applied over the whole top electrode by the biased AFM tip and (b) in bottom electrode-bare ferroelectric structure, whereby voltage is applied locally by the biased AFM tip. Yellow and purple color indicate up- and down-polarization of the thin film and created domains, respectively.*

In contrast, in the case of a bare ferroelectric (i.e. top electrode-free) surfaces, the metallic AFM tip can be used as the movable top electrode instead (**Figure 2.6 b**). In this case, the

electric field created between the biased AFM tip and bottom electrode is highly inhomogeneous, with the maximum strength achieved at the tip-surface contact. This leads to the formation of a single ferroelectric nucleus just below the tip with the opposite polarization direction to its surrounding. By increasing the magnitude or the duration of the voltage pulse, the nucleus first grows forward along the thickness of the sample until reaching the opposite interface, and then starts to expand in lateral direction by the sideways growth.[5]

The development of the PFM technique enabled the study of ferroelectric switching locally in a spectroscopy mode (SS-PFM) at a location defined by the position of the tip in contact with the bare ferroelectric surface.[11] This brought great advantages in the field of study of nanoferroics, where local switching could be investigated in inhomogeneous or polycrystalline ferroelectric materials at scales smaller than the grain size or inhomogeneity region, and reveal spatial variation of the switching properties. In SS-PFM spectroscopy, the electromechanical response of the sample to the small oscillatory *ac* bias is measured between each increasing *dc* voltage steps whose form is shown in the inset of **Figure 2.7 a**, yielding a piezoelectric hysteresis loop. A scheme of SS-PFM acquired hysteresis loop, together with the main processes happening inside of the ferroelectric sample during the voltage pulse applications marked by numbers are shown in **Figure 2.7 a,b**, respectively.

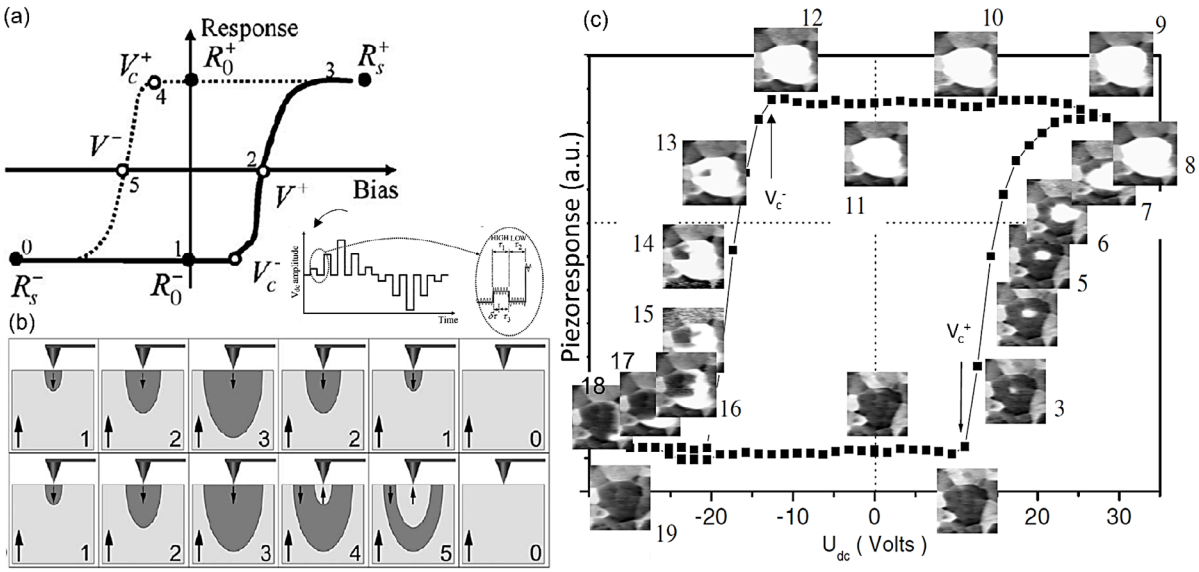

Figure 2.7 *(a) Schematic representation of SS-PFM electromechanical hysteresis loop acquired on the top of bare ferroelectric surface with the main events of domain nucleation and growth marked by numbers in panel (b). Inset at the bottom right in panel (a) shows the form of the voltage signal applied to the AFM tip during SS-PFM measurements; (c) Piezoresponse of polycrystalline PZT film, measured at the single uniformly down-polarized grain. Image adapted from [11,12].*

If the bias pulse is applied to the AFM tip, the electromechanical responses from the down-domain nucleated under the tip and the surrounding up-polarized matrix will partially compensate (1), leading to the change in the piezoresponse. The point at which this happens corresponds to the nucleation voltage (V_c^+). If the tip bias is raised, the domain grows further and at the coercive voltage (V_c^+) electromechanical signal from the created domain and the surrounding matrix compensate each other (2). When the size of the domain becomes bigger than the penetration depth of the imaging field, tip will sense the piezoresponse coming only from the inversed domain and will saturate (R_s^+) (3). If bias is decreased, two different scenarios are possible. A domain can start to reversibly shrink in lateral direction following the path (3→2→1), or the domain of opposite polarization (equal to those of the matrix) can nucleate inside of the existing domain once the negative nucleation voltage (V_c^-) is achieved (4). By further increasing of the negative voltage, antiparallel domain walls annihilate and system is back to the initial state (0).

The appearance of the local hysteresis loop can be understood if the PFM phase of the area surrounding the tip is imaged after every voltage increasing step, as show in the **Figure 2.7 c**, in the case of polycrystalline ferroelectric $PbZr_{1-x}Ti_xO_3$ (PZT) thin film, whereby polarization switching was followed in the uniformly down-polarized single grain.[12] Previously explained processes, such as nucleation of domains and their growth can be observed at the inset images, which correspond to the PFM phase images of domain structures at marked points of hysteresis.

2.2.3 Kelvin Probe Force Microscopy (KPFM)

Kelvin Probe Force Microscopy (KPFM) is a non-contact AFM based mode used for the characterization of the materials' work function at the nanoscale. When a biased AFM tip is placed at some distance from the surface, the system can be considered as a capacitor, and the existing electric capacitive force (resulting from coulombic attraction) between the tip (top electrode) and the sample surface can be expressed as the gradient of capacitor's potential energy[13–15]:

$$F_c(z,V) = \frac{-\partial E}{\partial z} = -\frac{1}{2}\frac{\partial C}{\partial z} V^2(t) \qquad (4)$$

If the tip scans across the surface at the same height *z*, then the capacitive force will only depend on the voltage drop *V* existing between the tip and the sample. In the KPFM measurements this voltage drop will depend on the:

i) contact potential difference (CPD) between the tip and sample, equal to the difference in their work functions $\Delta\phi$, such that $eV_{CPD} = \Delta\phi$;

ii) *dc* voltage applied to the tip V_{dc};

iii) modulating *ac* voltage applied to the tip in the form $V_{ac} = V_{mod}\cos(\omega_{mod} t)$.

Therefore, the total voltage can be expressed as:

$$V(t) = V_{CPD} - V_{dc} + V_{mod}\cos(\omega_{mod}t) \quad (5)$$

By changing the V^2 in equation (4) by expression (5), tip-sample force can be expressed as:

$$F_{el}(V,t) = -\frac{1}{2}\frac{\partial C}{\partial z}[V_{CPD} - V_{DC} + V_{mod}\cos(\omega_{mod}t)]^2 \quad (6)$$

$$F_{el}(V,t) = -\frac{1}{2}\frac{\partial C}{\partial z}[(V_{CPD} - V_{DC})^2 + 2(V_{CPD} - V_{DC})V_{mod}\cos(\omega_{mod}t) + V_{mod}^2 cos^2(\omega_{mod}t)] \quad (7)$$

From equation (7) it can be seen that tip-sample force can be separated in 3 terms, whereby for the KPFM measurements we can focus only on the middle term which depends on all voltage components and electrical frequency of cantilever oscillation ω as:

$$F_{el,\omega} = 2(V_{CPD} - V_{DC})V_{mod}\cos(\omega_{mod}t) \quad (8)$$

Scheme of the main steps in KPFM measurements in shown in **Figure 2.8**.

In KPFM measurements, due to the tip-sample electrostatic interaction, the cantilever will be attracted/repelled from the surface at the same frequency of the modulating voltage. Such oscillation can be detected by the photodiode and analyzed by a lock-in amplifier, whereby frequency and amplitude of the oscillating signal are obtained. The amplitude of this osculating behavior is, by equation (8), directly proportional to the voltage difference V_{CPD}-V_{dc}. In order to cancel such oscillatory movement of the cantilever, a DC voltage is applied to the tip, whereby $F_{el,\omega}$ component becomes zero. Such compensating voltage is equal to the contact potential difference between the sample and the tip:

$$V_{CPD} = V_{dc} = \frac{1}{e}\Delta\phi \qquad (9)$$

The work function of the tip can be obtained by calibration, measuring the V_{CPD} between the tip and a material with a known work function. In practice, KPFM measurements are performed in a two-pass mode, which implies: i) scanning of the surface topography in tapping mode in the first pass and ii) subsequent scanning with the tip lifted at some constant distance above the surface, while the electrostatically driven oscillation of the cantilever created by applying an *ac* voltage to the tip is cancelled by the application of a *dc* voltage, which accounts for the contact potential difference between the tip and the sample surface. Thus, the surface potential -itself related to the charge of the adsorbate species on the ferroelectric surface- can be mapped.

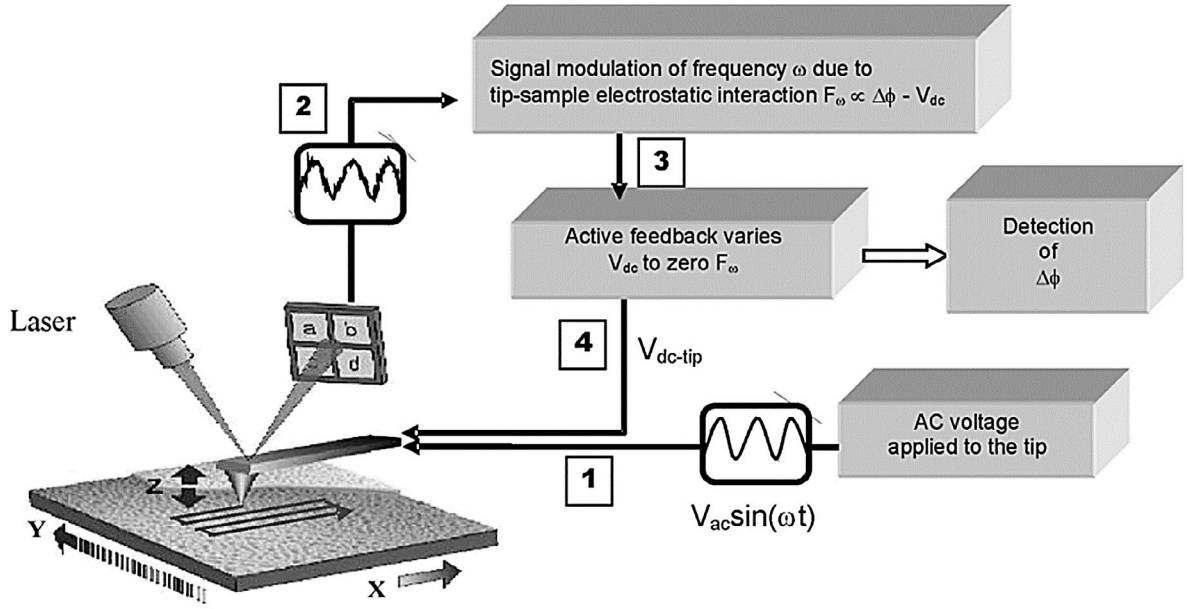

Figure 2.8 *Principle of Kelvin Probe Force Microscopy (KPFM) operation. Oscillating AC voltage applied to the tip not in contact with the surface (1), gives rise to the electric capacitive force, whose component $F_{el,\omega}$ is proportional to the ($V_{CPD} - V_{DC}$) (2). Feedback loop minimizes the $F_{el,\omega}$ (3) by applying the compensating DC voltage to the tip (4), which allows direct calculation of V_{CPD} between the tip and the sample. Image taken from [15].*

2.2.4 Functional characterization of $BaTiO_3$ thin films

AFM characterization was extensively used in this thesis for the study of surface and functional properties of $BaTiO_3$ thin films under different conditions. Details of the obtained results will be shown and discussed in the following chapters. In addition, AFM was also used as one of

the routine characterization tools to check surface roughness and ferroelectric properties of the samples grown by PLD.

The topography of the as-grown $BaTiO_3$ thin film described in section 2.1.1 was imaged by AFM tapping mode (**Figure 2.9 a**). In all the experiments, PPP-EFM tips (Nanosensors), coated with $PtIr_5$ and with a stiffness constant k = 2.8 N/m were used. On the surface of the film some atomic step-terrace structures are visible, characteristic of layer-by-layer growth, but also some holes. The root-mean square surface roughness (R_{rms}) is about 0.4 nm, which is comparable with the height of the perovskite unit cell. Ferroelectric characterization of the sample was performed by PFM in DART mode. In order to check the as-grown polarization state, we first performed ferroelectric lithography by polarizing two squares to the opposite polarization state by applying a voltage to the tip of V_{tip} = + 8 V (forcing the polarization down) and V_{tip} = – 8 V (forcing the polarization to switch up), while scanning in contact over an area of 3.5 x 3.5 μm^2 and 1 x 1 μm^2 respectively. The PFM phase and amplitude image of as-grown and electrically written ferroelectric area are presented in **Figure 2.9 b** and **Figure 2.9 c**, respectively. Amplitude image shows decrease of amplitude (black lines) in the location of the domain walls separating the domains of opposite polarity.

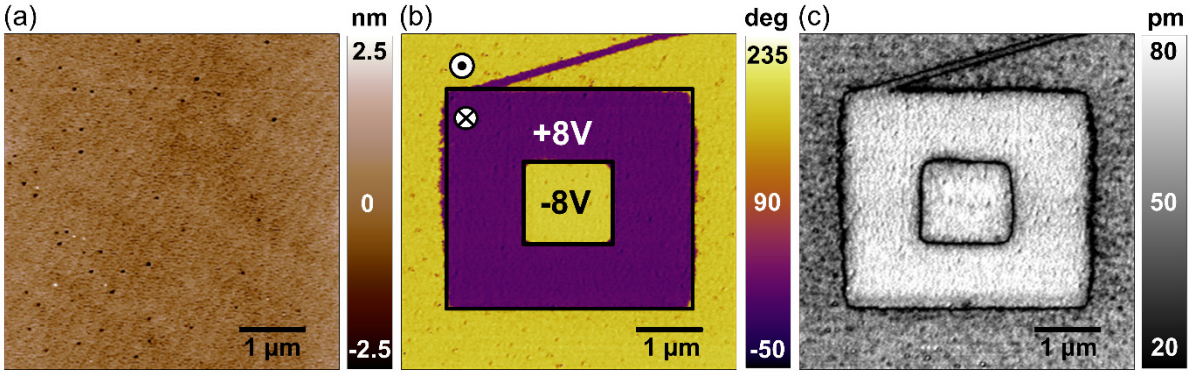

Figure 2.9 *(a) AFM topography of a 5x5 µm2 area showing the atomic steps of a perfectly layered sample; (b) PFM Phase image of the as-grown up polarized area, where a square pattern of 3.5 x 3.5 μm^2 has been switched to down polarization (purple area) by applying a positive voltage of V_{tip} = 8 V and switched back to up polarization by a reversed voltage of V_{tip} = - 8V (yellow squared inset); (c) PFM amplitude of electrically poled areas, showing the presence of domain walls separating areas of opposite polarity.*

In the PFM phase image it can also be seen that the phase contrasts of the inner square polarized with – 8 V and that of the background are the same, indicating that the as-grown $BaTiO_3$ thin film is out-of-plane up-polarized, as expected for BTO thin films grown on SRO electrodes.[2]

It should be noted that the thin film samples were prepared by the same procedure and of the same or similar thickness for all the experiments in this thesis, except in Chapter 4, where BTO (100) single crystals were used instead.

2.3 Environmentally-controlled AFM

In some of the experiments performed in this thesis, there was the need to precisely control the environmental conditions in which AFM studies were performed, mainly the temperature of the sample and the relative humidity (RH) of the surrounding gas.

2.3.1 Temperature control in AFM

In order to control the temperature, a PolyHeater stage, compatible with MFP-3D AFM (Asylum Research) was used. The polyheater stage allows heating the sample up to 300 ºC with different rates and maintain the desired temperature within ±0.2 ºC in precision, thanks to a separated environmental controller. A schematic of the polyheater assembly is shown in **Figure 2.10 a**. The center of the polyheater stage is magnetic, allowing practical mounting of samples attached to the magnetic disks.

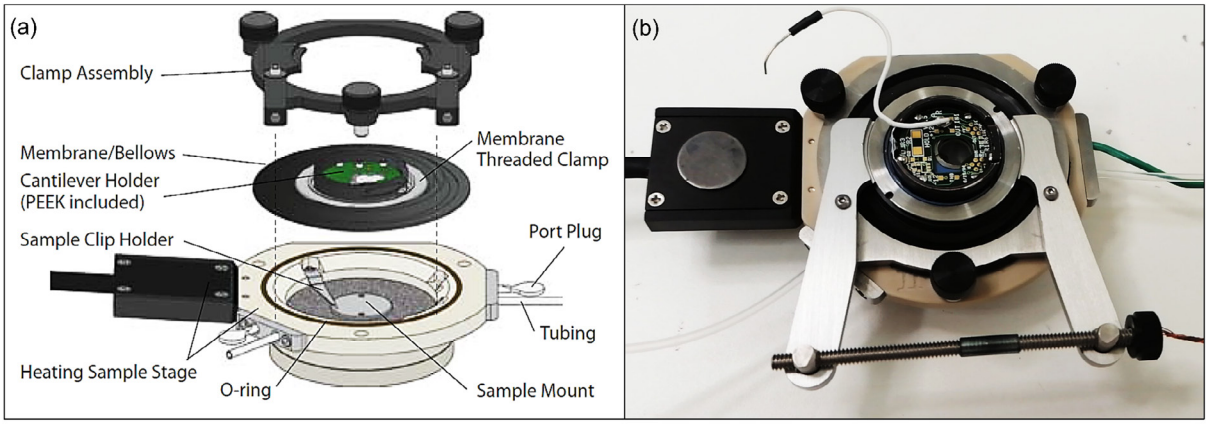

Figure 2.10 *(a) Schematic representation of the PolyHeater assembly; (b) Photograph of the hermetically closed environmental cell, with tubing elements used for injection and exhaust of N_2 gas of distinct RH, controlled by the RH controller (***Figure 2.11***). Panel (a) has been taken from Asylum Research.*

The Polyheater stage has four ports, used as inlets for the tubing, through which gases could be supplied to the hermetically closed system in our experiments. In order to achieve a

hermetically-closed cell, the cantilever holder with the tip has to be mounted together with the membrane, held by the threaded clamp. The cantilever holder with attached membrane is then carefully mounted to the assembly clamp and the latter is screwed onto the heating sample stage. Fully assembled, the hermetically closed environmental cell is shown in **Figure 2.10 b.**

2.3.2 Humidity control in AFM

The RH in the environmental cell was controlled by a low-noise continuous flow RH controller developed by Gaponenko et. al,[16,17] which, by mixing N_2 gas with the distilled water, allows control of RH in the broad range of values with high precision and stability. A schematic representation and a photograph of the humidity controller are shown in **Figure 2.11 a,b**, respectively. Upon entering the controller, dry N_2 gas flow is split into the two pathways and regulated by two mass controllers. One of the flows passes through the humidifier, whereby it gets fully saturated by the water (blue line), and gets subsequently mixed in determined ratio with the dry air in the injection chamber (mix_inj).

At this point, the temperature and RH of the mixed gas are measured, just before its dosing into the AFM cell. The RH of the N_2 leaving the AFM cell is again supplied into the exhaust chamber (mix_exh), whereby temperature and RH of the N_2 are again measured before it finally leaves the system. Humidifier used is this system is atomizer, which operates thanks to the piezoelectric element excited at ultrasonic frequencies, thereby allowing the formation of small water droplets in the form of an aerosol able to fully saturate the N_2 gas.

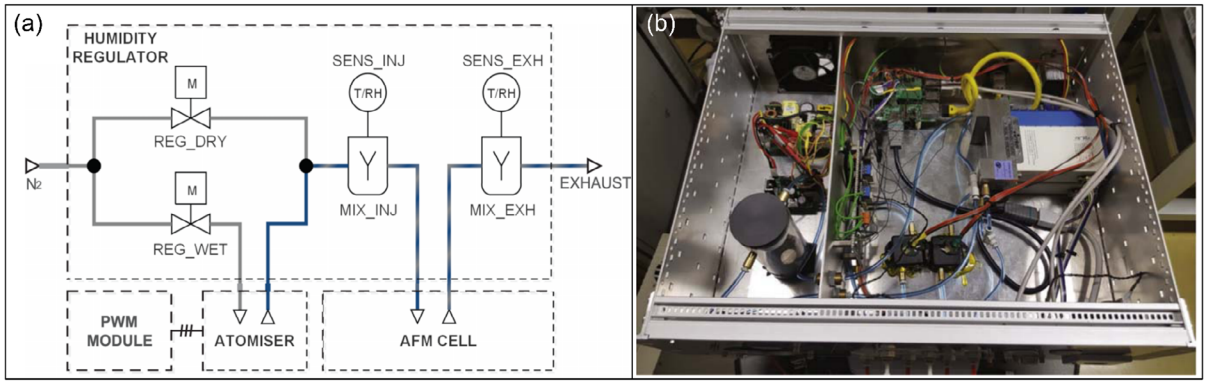

Figure 2.11 *(a) Scheme of RH controller working principle. (b) Photograph of the RH controller. Images adapted from [16,17].*

2.4 X-Ray Photoelectron Spectroscopy (XPS)

X-Ray Photoelectron Spectroscopy (XPS) or Electron Spectroscopy for Chemical Analysis (ESCA) is a surface sensitive technique that allows to determine the type and concentration of elements existing in the surface region of the sample. Beside showing which kind of elements are present in the sample, XPS allows determination of their electronic environment, i.e. to which other elements they are bound to, forming a compound.[18] While lacking the spatial resolution provided by AFM, XPS measurements have been extensively used in this thesis to gain critical insights into the chemical properties of the surfaces, providing highly valuable information.

At the core of photoelectron spectroscopy lies photoelectric effect, which was first time explained by Albert Einstein. If the sample is irradiated by X-Ray photons, i) one part of photons will pass through the sample without any interaction, ii) other part will partially lose their energy during the scattering events and iii) some photons will transfer their total energy to electrons of the sample, leading to their photoemission due to the photoelectric effect. The kinetic energy of the ejected electrons is equal to the energy of the photons minus the binding energy, and therefore the energy spectrum of the electrons provides information about the chemical environment whence they came. The photoelectric effect was implemented to the XPS technique by the Nobel Prize winner Kai Siegbahn.[19,20]

2.4.1 XPS Instrumentation

Schematic representation of XPS setup is shown in **Figure 2.12**. During the analysis, sample in vacuum is irradiated by the X-ray photons of known energy, whereby number of electrons (intensity) as a function of their kinetic energy is measured by the analyzer. The plot of photoelectron intensity as a function of their kinetic (or binding energy) is called XPS spectrum. Typical sources used in laboratory based XPS instruments are K_α lines of Al and Mg anodes, obtained by the exposure of these materials to high energy electrons. The energy of primary K_α lines are 1253.6 eV and 1486.6 eV for Al and Mg sources, respectively. These energies are sufficiently high to probe core levels of the most of elements. However, these sources are non-monochromatic: besides being doublets, the main spectral peaks are typically superimposed over the Bremsstrahlung background, and may also contain additional unwanted

satellite lines, which can drastically affect the resolution of recorded spectra. That is whynowadays all XPS spectrometers also contain monochromatic crystals, designed to preferentially choose characteristic line, with a well-defined energy as the source.

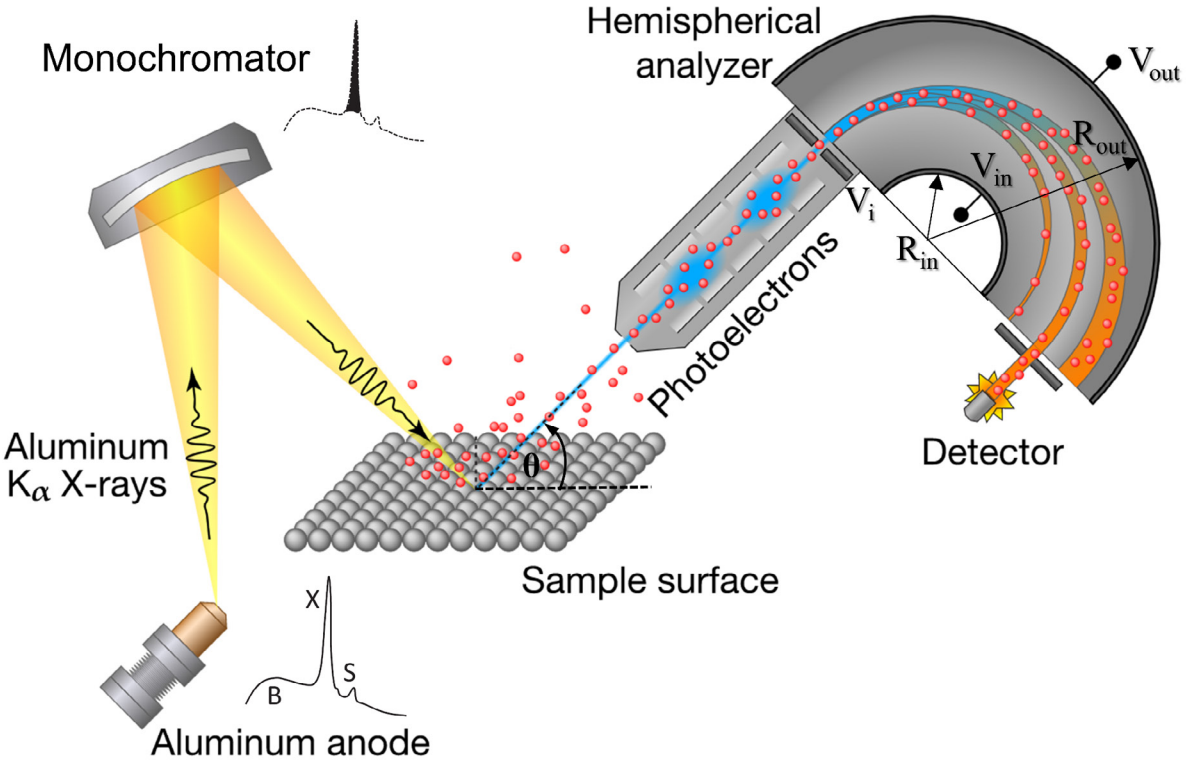

Figure 2.12 Schematic representation of the conventional vacuum-based XPS setup. Adapted from web.

Photoelectrons are collected and analyzed by an electron energy analyzer. The most common type of analyzer used in XPS spectrometers is hemispherical analyzers shown in **Figure 2.12**. As the sample arrive to the entrance slit, their kinetic energy E_i is lowered due to the bias V_i applied in the region of the slit, such that $E_i - eV_i = E_0$. Parameter E_0 is called pass energy and it is maintained constant by the application of bias to the inner V_{in} and outer hemisphere V_{out}, respectively. The kinetic energy of electrons arriving to the analyzer can be calculated by relating parameters such as pass energy E_0, decelerating voltage V_i, radii R_{in} and R_{out} and biases V_{in} and V_{out} of inner and out hemisphere, respectively. During the spectrum acquisition, parameters V_i, V_{out} and V_{in} are varied in order to probe electrons with different kinetic energies. Finally, electrons are detected by parallel multichannel detector.

2.4.2 Binding energy

The energy which needs to be supplied to electron in order to leave the sample depends on i) the binding energy of electron in particular orbital E_B^F defined relatively to the Fermi level with energy E_F and ii) the energy barrier at the surface, defined by the work function of the sample ϕ_{SA}, corresponding the energy difference between the Fermi level E_F and the vacuum level of the sample E_{VAC}^{SA} (**Figure 2.13**). In that case kinetic energy of the electron E_{kin}^{SA} can be expressed as[21]:

$$E_{kin}^{SA} = h\nu - E_B^F - \Phi_{SA} \qquad (10)$$

where *hν* represent energy of the incident photon.

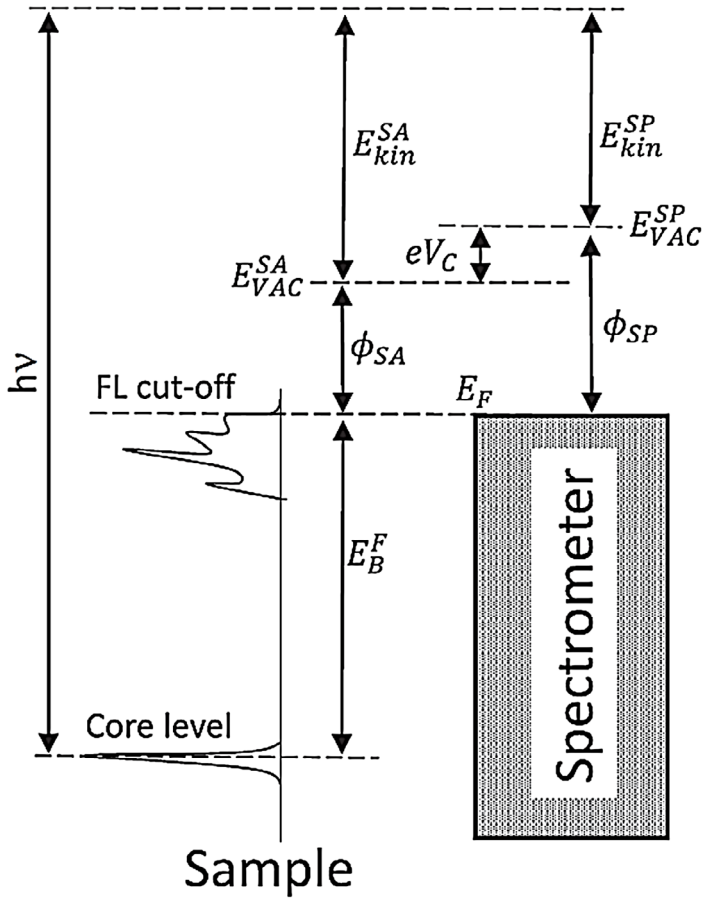

Figure 2.13 *Energy level diagram of the sample in the electrical contact with spectrometer, allowing calculation of the core electrons' binding energy E_B^F with respect to the Fermi level [21].*

In the case when there is a good electric contact between the sample and the spectrometer, their Fermi levels will align due to the electron transfer from spectrometer to the sample or vice

versa, depending on the work function of the sample ϕ_{SA} and that of the spectrometer ϕ_{SP}. This will create contact potential difference V_c between the sample and spectrometer, so that the kinetic energies of the photoelectron measured by the spectrometer E_{kin}^{SP} and of a photoelectron leaving the sample E_{kin}^{SA} will be different.

Taking into account that:

$$E_{kin}^{SA} + \Phi_{SA} = E_{kin}^{SP} - \Phi_{SP} \qquad (11)$$

Equation (10) can be rewritten as:

$$E_B^F = h\nu - E_{kin}^{SP} - \Phi_{SP} \qquad (12)$$

whereby ϕ_{SP} is spectrometer constant, determined by previous calibration. Linear relation between the kinetic energy and binding energy allows one to represent XPS spectra either on kinetic energy of binding energy scale.

2.4.3 Chemical shift in XPS

Chemical shifts are related to the change in the binding energy of a core electron of an element due to the change in its chemical bonding. A typical compound used for the explanation of chemical shifts is ethyl trifluroacetate, whose C 1s XPS spectrum and corresponding structure are shown in **Figure 2.14.**[21,22] This compound contains four C atoms with distinct chemical environment, whereby C atoms can be bound to F atoms, O atoms, other C/H atoms or something in-between that.

XPS spectra are very sensitive to their chemical environment since the valence electrons, which take part in the bond formation, can change the valence electron density in the system. In the case of C atoms bound to three F atoms, due to the high electronegativity of F atoms, electrons will be attracted to it, leaving the C atom with partially positive charge. In the system which is stripped of the negative charge, remaining electrons will be more strongly attracted to the core, leading to the lower kinetic and therefore higher binding energies of such photoelectrons. As the electronegativity of the nearest neighbors to C atoms decreases (from right to left in **Figure 2.14**), or reversely valence electronic density increases, binding energy of photoelectrons increases.

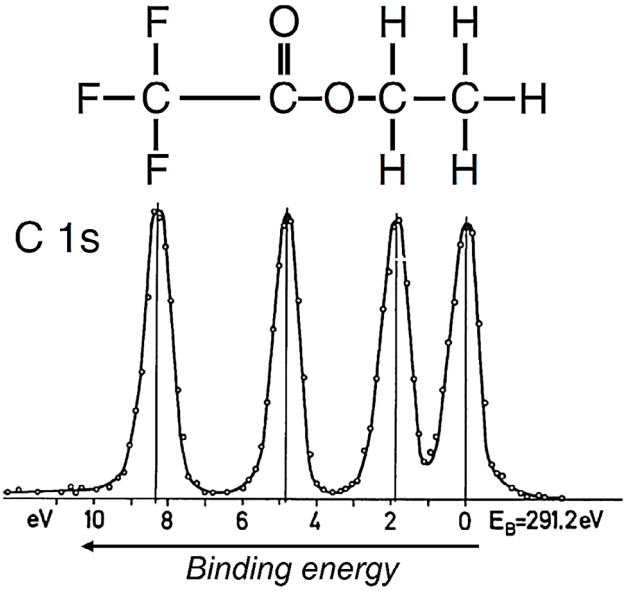

Figure 2.14 *C 1s XPS spectrum of ethyl trifluroacetate, showing the binding energy chemical shift of photoelectrons in four C atoms with different chemical environment. Adapted from [21].*

2.4.4 Sampling depth

Photoelectrons excited by the X-Rays are able to travel through the solid only short distances, due to the scattering with other electrons in the sample. Electrons originating very close to the surface will reach the detector without energy loss and will contribute to the photoemission peaks. However, photoelectrons coming from deeper in the sample will inelastically scatter with other electrons and will appear at lower kinetic (i.e. higher binding) energies in the XPS spectrum, contributing to the background signal. The intensity of the electrons I_d that reach the surface from the depth d in the sample without scattering decreases from the initial intensity I_0 following the Lambert-Beer law as[18]:

$$I_d = I_0 e^{\frac{-d}{\lambda \sin\theta}} \qquad (13)$$

whereby θ is the electron take-off angle, defined as the angle between the sample surface and photoelectron analyzer (**Figure 2.15**). The parameter λ (in $\AA$), is called inelastic mean free path (IMFP) and represents a measure of how far an electron on average travels through a solid before losing energy. It depends on the kinetic energy of the photoelectron, atomic density and composition of the analyzed material. Factor $d/sin\theta$ represents effective distance electron has passed through the sample for the take-off angle θ. The percentage of electrons coming from a

depth *d* ranging between 0 and λ, can be calculated by integrating the function I_d/I_0 in desired λ range. By solving mentioned integral for *d* between 0 and *3λ* and for $\theta = 90^o$, it can be seen that 95 % of the scattered photoelectrons' signal comes from the depth *3λ*, which is called the sampling depth $d_s = 3\lambda$. Most *λ* values are in the range of 1 to 3.5 nm for *Al* K_α line, meaning that typical sampling depth will be between 3 and 10 nm. In the case when the angle $\theta < 90^o$ then the sampling depth will be decreased as $d_s = 3\lambda sin\theta$. This is the basis of non-destructive depth profiling by angle-resolved XPS (AR-XPS),[23] where by changing the angle θ and keeping the constant incident photon energy, different sampling depths can be probed (**Figure 2.15**).

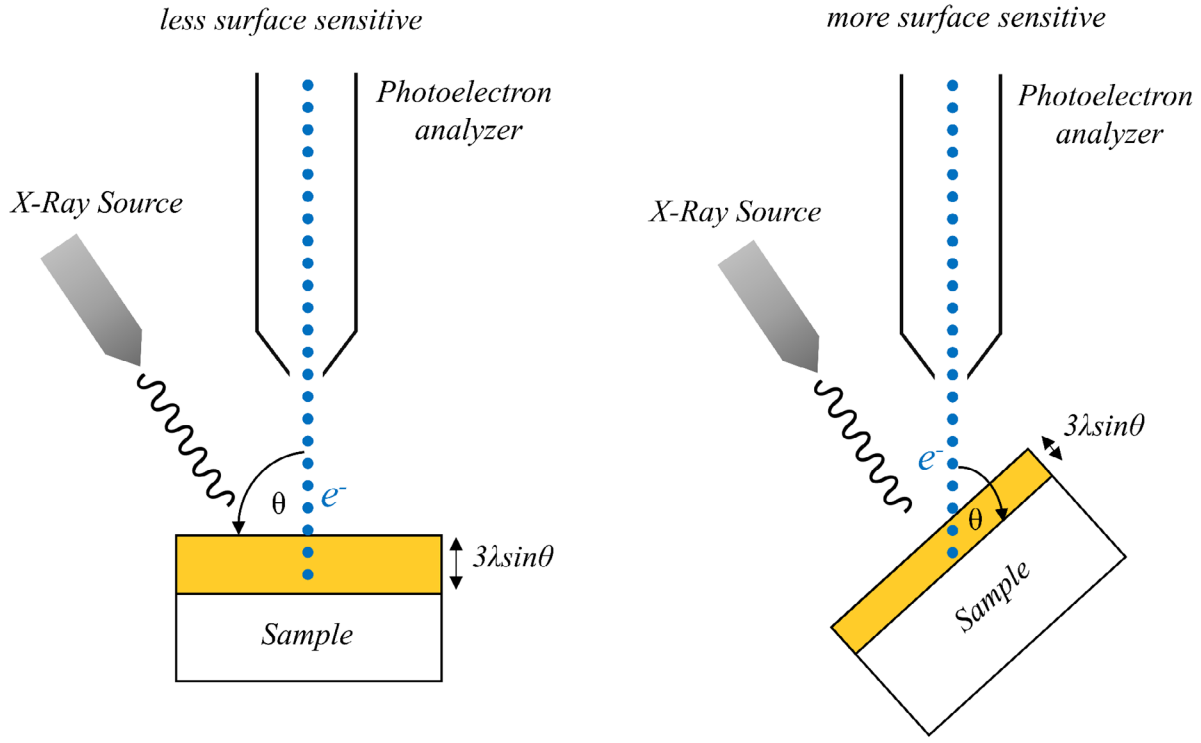

Figure 2.15 *Principle of the angle resolved XPS (AR-XPS). By decreasing the angle $\theta < 90^o$, defined as the angle between the sample surface and the photoelectron analyzer, one changes the sampling depth $d_s = 3\lambda sin\theta$, whereby the recorded XPS spectra becomes even more "surface sensitive". This method allows for the non-destructive profiling of the chemical composition along the sample's z-axis.*

From a practical point of view, this is usually achieved by tilting the sample. On the other hand, since *λ* depends on the kinetic energy of photoelectrons,[24] by changing the incident energy of X-Ray photons (i.e. in synchrotron facilities) one can also probe different depths of the sample.

2.4.5 Ambient Pressure XPS (AP-XPS)

Conventional XPS experiments, as described previously, are typically performed in the ultra-high vacuum conditions. However, if one is interested in studying the behavior of surfaces in conditions more similar to the ambient ones, several important aspects need to be considered. When the XPS chamber is not operating in the vacuum, but in a gas environment with some partial pressure, photoelectron attenuation due to the inelastic collision with atoms of surrounding gas, as well as attenuation of X-ray photons due to the absorption by gas molecules, must be taken into account. This type of XPS spectroscopy is called Ambient pressure XPS (AP-XPS).[25]

Attenuation of photoelectrons can happen through the rotational, vibrational and electronic excitation of the surrounding gas molecules or even their ionization by emitted photoelectrons, which decreases the intensity of the photoemission peak in the spectrum. If we take into account that the mass density of the gas at 1 Torr is 10^6 times smaller than that of the solid, it can be concluded that the IMFP of electrons in the gas phase will be approximately 10^6 times longer, i.e. in the order of millimeter. However, in typical XPS chambers, the distances between the sample and electron analyzer are in the order of few centimeter, making the scattering process of photoelectrons dominant. The attenuation of photoelectrons by the surrounding gas phase at pressure p and temperature T as a function of the distance z that the photoelectron has traveled can be expressed by following equation (14)[26]:

$$I_z = I_0 e^{\frac{-z\sigma p}{T}} \qquad (14)$$

Where I_0 and I_z are photoelectron signals in vacuum and at pressure p, respectively. The parameter σ is the electron scattering cross section, which, like λ, depends on the kinetic energy of the photoelectron and type of the gas. In order to keep the attenuation as small as possible, the path of electrons through the high pressure gas needs to be decreased. This is done by placing the sample surface very close to the conic aperture (nozzle),[25,26] which separates the high pressure chamber from additional part of equipment called differentially pumped stage, installed between the XPS chamber and the energy analyzer.

The role of the differentially pumped stage is to decrease pressure between the high pressure XPS chamber and the energy analyzer which operates under high vacuum conditions, as shown schematically in **Figure 2.16**. The difference in pressure between the two sides of the

differential stage aperture will depend on the size of aperture, type of gas, temperature and the pumping efficiency. If the pressure in the analysis chamber is in the order of Torr, several differential pumping stages connected in series are needed as shown in **Figure 2.16**. Sizes of the apertures connecting differential pumping stages are very important, since they determine the number of electrons that will be transmitted together with the molecules of the gas. In order to keep apertures small (and therefore not compromise the vacuum), a system of electrostatic lenses[27] can be integrated into the differential pumping stages which focuses the electrons on the aperture of the following stage as shown in **Figure 2.16. b**.

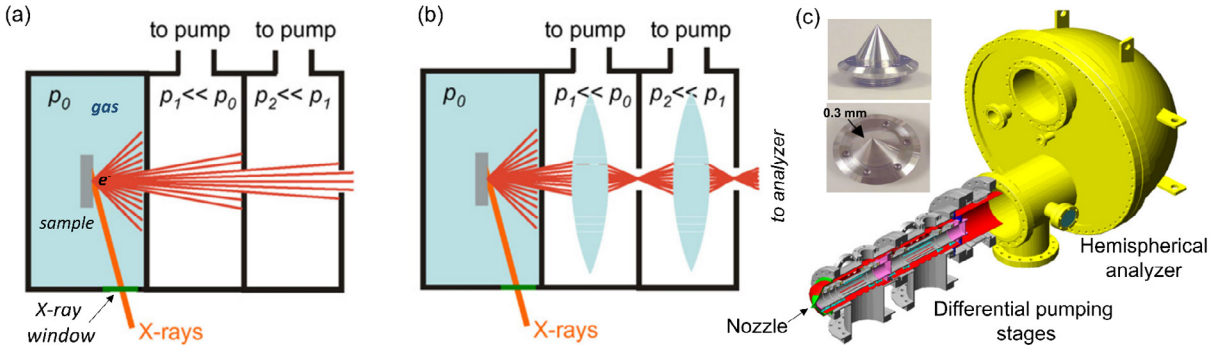

Figure 2.16 *Schematic representation of the differential pumping system. Sample in the high pressure (p_0) chamber is mounted close to the nozzle which allows passing of photoelectrons and some molecules of the gas to the first pumping stage. In order to achieve difference in pressures of 10^{-6} mbars between the high pressure chamber and analyzer several pumping stages are needed. In conventional system shown in panel (a), this also implies loss of electron depicted by red lines. In order to avoid this, set of electrostatic lenses, which refocuse electron trajectories into the apertures communicating the differential pumping stages should be installed (shown in panel b). Panel (c) shows the sketch of the differential pumping system connected with the hemispherical analyzer. Photograph of the nozzle is shown in the inset. Adapted from [25,26].*

Beside the energy analyzer, the source of X-Rays also needs to be kept under vacuum, due to the absorption of the X-rays by the gas phase. This is typically done by implementing X-Ray transparent windows in the analysis chamber or alternatively by the use of additional differential pumping stages (similar like in the case of the analyzer). A scheme of the differential pumping system connected to the hemispherical analyzer is shown in **Figure 2.16 c**, while the inset shows photograph of the nozzle placed very close to the sample in the high pressure XPS chamber. AP-XPS experiments in this work have been performed at the CIRCE beamline (BL24) of ALBA synchrotron (Cerdanyola del Vallès, Spain). Further details of the ALBA AP-XPS beamline setup can be found in reference.[28]

2.4.6 Calculation of adsorbate layers' thickness in AP-XPS

Equation (13) describes the intensity of the photoelectrons' signal for a bare substrate. However, if a substrate is covered by a layer(s) of adsorbates, the intensity of the photoelectrons' signal will be further attenuated. Following the model,[29] XPS signal intensity of a substrate covered by *n* layers above it, will be attenuated by each layer according to the Lambert-Beer law as:

$$I_s = S_s^j \lambda_s \prod_{i=1}^{n} e^{\frac{-t_i}{\lambda_i}} \qquad (15)$$

where λ_f is the effective inelastic mean free path for layer *f*. S_f^j is photoemission spectroscopy constant for layer *f* (In Eq. 15 index *s* denotes the substrate) and inner shell orbital *j* given by:

$$S_f^j = \Phi \sigma_f^j D_f N_f \qquad (16)$$

where Φ is the X-ray flux at the energy of photons, σ is the photoionization cross section of a given orbital for the given photon energy, *D* is the detector efficiency for detecting impacting photoelectrons and N_f is atomic density.

Similarly, the XPS intensity of the layer *f* attenuated by (*n-f*) layers in the multilayer system consisting of *n* layers, can be expressed as:

$$I_f = S_f^j \lambda_f (1 - e^{\frac{-t_f}{\lambda_f}}) \prod_{i=f+1}^{n} e^{\frac{-t_i}{\lambda_i}} \qquad (17)$$

In this thesis, I will study the adsorbates composition on oxide perovskites as measured at the O 1s spectral range by AP-XPS following a model recently described in our group.[30] In this model, the adsorbates stack is composed by four different types of layers at different positions: first, the substrate is covered by OH groups (1st layer), then, there is a second layer formed by two different species, that is CO_x and Surf O_2^- components (2nd layer) and finally a molecular water layer is found at the farthest position from the surface (3rd layer). This specific configuration of adsorbates has been found according to the results of depth profiling obtained after comparing O 1s spectra recorded at two different incident energies. The developed adsorbate species model will be explained in detail in Chapter 3 and Chapter 4. Nonetheless, we considered convenient to develop here the equations that will be used in these chapters to

calculate the layers' thicknesses. According to equations (15-17) the intensity of different spectral components of a multilayered system can be expressed as:

$$I_{H_2O} = S_{H_2O}\lambda_{H_2O}\left[1 - exp\left(-\frac{t_{H_2O}}{\lambda_{H_2O}}\right)\right] \quad (18)$$

$$I_{Surf\ O_2} = S_{Surf\ O_2}\lambda_{Surf\ O_2}\left[1 - exp\left(-\frac{t_{Surf\ O_2}}{\lambda_{Surf\ O_2}}\right)\right]exp\left(-\frac{t_{H_2O}}{\lambda_{H_2O}}\right) \quad (19)$$

$$I_{CO_x} = S_{CO_x}\lambda_{CO_x}\left[1 - exp\left(-\frac{t_{CO_x}}{\lambda_{CO_x}}\right)\right]exp\left(-\frac{t_{H_2O}}{\lambda_{H_2O}}\right) \quad (20)$$

$$I_{OH} = S_{OH}\lambda_{OH}\left[1 - exp\left(-\frac{t_{OH}}{\lambda_{OH}}\right)\right]exp\left(-\frac{t_{H_2O}}{\lambda_{H_2O}}\right)exp\left(-\frac{t_{Surf\ O_2}}{\lambda_{Surf\ O_2}}\right)exp\left(-\frac{t_{CO_x}}{\lambda_{CO_x}}\right) \quad (21)$$

$$I_{Ox} = S_{Ox}\lambda_{Ox}exp\left(-\frac{t_{H_2O}}{\lambda_{H_2O}}\right)exp\left(-\frac{t_{Surf\ O_2}}{\lambda_{Surf\ O_2}}\right)exp\left(-\frac{t_{CO_x}}{\lambda_{CO_x}}\right)exp\left(-\frac{t_{OH}}{\lambda_{OH}}\right) \quad (22)$$

By taking the intensity ratios, the thicknesses t_i of the species can be determined as:

$$t_{OH} = \lambda_{OH} \cdot ln(1 + R_{Ox}^{OH}) \quad (23)$$

$$t_{SurfO_2} = \lambda_{SurfO} ln\left[\frac{\left(e^{\frac{t_{OH}}{\lambda_{OH}}} + R_{Ox}^{SurfO_2} - R_{Ox}^{COx}\right) \pm \sqrt{\left(R_{Ox}^{COx} - e^{\frac{t_{OH}}{\lambda_{OH}}} - R_{Ox}^{SurfO_2}\right)^2 + 4e^{\frac{t_{OH}}{\lambda_{OH}}}R_{Ox}^{COx}}}{2e^{\frac{t_{OH}}{\lambda_{OH}}}}\right] \quad (24)$$

$$t_{COx} = \lambda_{COx} \cdot ln\left(1 + \frac{R_{Ox}^{COx}}{e^{\frac{t_{OH}}{\lambda_{OH}}} \cdot e^{\frac{t_{Surf\ O_2}}{\lambda_{Surf\ O_2}}}}\right) \quad (25)$$

$$t_{H_2O} = \lambda_{H_2O} \cdot ln\left(1 + \frac{R_{Ox}^{H_2O}}{e^{\frac{t_{OH}}{\lambda_{OH}}} \cdot e^{\frac{t_{SurfO_2}}{\lambda_{SurfO_2}}} \cdot e^{\frac{t_{COx}}{\lambda_{COx}}}}\right) \quad (26)$$

where the parameter R_j^i can be expressed as:

$$R_j^i = \frac{I_i}{I_j}\left(\frac{N_j \sigma_j \lambda_j}{N_i \sigma_i \lambda_i}\right) \quad (27)$$

The thickness of each layer can be also expressed in terms of monolayers (ML) by considering the thickness of a single layer of each specie, as reported in similar models.[29,31] The value of the ML thickness considered in the calculations for each specie is shown in **Table 1**, together with the calculated[32] values of λ (at incident energy of 700 eV) and atomic densities N. The values of ionization cross-sections σ are assumed to have minor variations for the different species, i.e. $\sigma_{Ox} \sim \sigma_{OH} \sim \sigma_{COx} \sim \sigma_{Surf\,O2} \sim \sigma_{H2O}$.

Peak	Specie	λ [nm] 700 eV	N [nm^3]	ML [nm]
Oxide	$BaTiO_3$	0.70	46.60	
OH	$Ba(OH)_2$	1.10	26.30	0.31
	$Ti(OH)_4$	0.80	60.70	
CO_x	$BaCO_3$	0.95	39.30	0.45
Surf O_2	BaO_2	0.86	40.40	0.39
Water	H_2O	1.40	33.40	0.31

Table 2.1. *Calculated values of λ and atomic densities N for different species, together with the monolayer thickness values.*

Conventional (vacuum-based) XPS, as well as AP-XPS (performed in water vapor atmosphere), described in this chapter, will be used as main techniques for the investigation of adsorbates' layer composition in this thesis.

References

[1] K. Bin Masood, P. Kumar, M. A. Malik, J. Singh, *Emergent Mater.* **2021**, *4*, 737.

[2] P. Zubko, H. Lu, C.-W. Bark, X. Martí, J. Santiso, C.-B. Eom, G. Catalan, A. Gruverman, *J. Phys. Condens. Matter* **2017**, *29*, 284001.

[3] G. Binnig, C. F. Quate, C. Gerber, *Phys. Rev. Lett.* **1986**, *56*, 930.

[4] R. Proksch, S. Kalinin, *Application Note: Piezoresponse Force Microscopy with Asylum Research AFMs*, Oxford Instruments, **2010**.

[5] A. L. Kholkin, S. V. Kalinin, A. Roelofs, A. Gruverman, in *Scanning Probe Microsc.*, Springer New York, **2007**, pp. 173–214.

[6] B. J. Rodriguez, C. Callahan, S. V. Kalinin, R. Proksch, *Nanotechnology* **2007**, *18*, 475504.

[7] S. M. Yang, Y. Kim, *J. Korean Ceram. Soc.* **2019**, *56*, 340.

[8] S. M. Yang, J. G. Yoon, T. W. Noh, *Curr. Appl. Phys.* **2011**, *11*, 1111.

[9] A. Gruverman, B. J. Rodriguez, C. Dehoff, J. D. Waldrep, A. I. Kingon, R. J. Nemanich, J. S. Cross, *Appl. Phys. Lett.* **2005**, *87*, 082902.

[10] A. Gruverman, D. Wu, J. F. Scott, *Phys. Rev. Lett.* **2008**, *100*, 3.

[11] S. Jesse, A. P. Baddorf, S. V Kalinin, *Appl. Phys. Lett.* **2006**, *88*, 062908.

[12] A. L. Kholkin, I. K. Bdikin, V. V. Shvartsman, A. Orlova, D. Kiselev, A. A. Bogomolov, S.-H. Kim, *MRS Proc.* **2004**, *838*, O7.6.

[13] B. Voigtländer, in *Scanning Probe Microsc. Force Microsc. Scanning Tunneling Microsc.*, Springer Berlin Heidelberg, **2015**, pp. 123–133.

[14] W. Melitz, J. Shen, A. C. Kummel, S. Lee, *Surf. Sci. Rep.* **2011**, *66*, 1.

[15] V. Palermo, M. Palma, P. Samorì, *Adv. Mater.* **2006**, *18*, 145.

[16] I. Gaponenko, L. Musy, S. C. Muller, P. Paruch, *Eng. Res. Express* **2019**, *1*, 25042.

[17] I. Gaponenko, L. Gamperle, K. Herberg, S. C. Muller, P. Paruch, *Rev. Sci. Instrum.* **2016**, *87*, 063709.

[18] J. F. Watts, J. Wolstenholme, *An Introduction to Surface Analysis by XPS and AES*, John

Wiley & Sons, Ltd, **2003**.

[19] U. Gelius, E. Basilier, S. Svensson, T. Bergmark, K. Siegbahn, *J. Electron Spectros. Relat. Phenomena* **1973**, *2*, 405.

[20] E. Sokolowski, C. Nordling, K. Siegbahn, *Ark. Fys.* **1957**, *12*.

[21] G. Greczynski, L. Hultman, *Prog. Mater. Sci.* **2020**, *107*, 100591.

[22] K. Siegbahn, C. Nordling, A. Fahlman, R. Nordberg, K. Hamrin, *ESCA: Atomic, Molecular and Solid State Structure Studies by Means of Electron Spectroscopy*, Almqvist And Wiksells, **1967**.

[23] R. W. Paynter, *J. Electron Spectros. Relat. Phenomena* **2009**, *169*, 1.

[24] S. Tanuma, C. J. Powell, D. R. Penn, *Surf. Interface Anal.* **2011**, *43*, 689.

[25] M. Salmeron, R. Schlögl, *Surf. Sci. Rep.* **2008**, *63*, 169.

[26] H. Bluhm, *J. Electron Spectros. Relat. Phenomena* **2010**, *177*, 71.

[27] D. F. Ogletree, H. Bluhm, G. Lebedev, C. S. Fadley, Z. Hussain, M. Salmeron, *Rev. Sci. Instrum.* **2002**, *73*, 3872.

[28] V. Pérez-Dieste, L. Aballe, S. Ferrer, J. Nicolàs, C. Escudero, A. Milán, E. Pellegrin, *J. Phys. Conf. Ser.* **2013**, *425*, 072023.

[29] J. T. Newberg, D. E. Starr, S. Yamamoto, S. Kaya, T. Kendelewicz, E. R. Mysak, S. Porsgaard, M. B. Salmeron, G. E. Brown, A. Nilsson, H. Bluhm, *Surf. Sci.* **2011**, *605*, 89.

[30] N. Domingo, E. Pach, K. Cordero-Edwards, V. Pérez-Dieste, C. Escudero, A. Verdaguer, *Phys. Chem. Chem. Phys.* **2019**, *21*, 4920.

[31] K. A. Stoerzinger, W. T. Hong, E. J. Crumlin, H. Bluhm, M. D. Biegalski, Y. Shao-Horn, *J. Phys. Chem. C* **2014**, *118*, 19733.

[32] W. H. Gries, *Surf. Interface Anal.* **1996**, *24*, 38.

CHAPTER 3

Atmospheric adsorbates on ferroelectric surfaces of $BaTiO_3$ thin films

In this chapter, I describe the investigation of adsorbate species on atmosphere-exposed surfaces of $BaTiO_3$ thin films by means of X-Ray photoelectron spectroscopy (XPS). Analyzing XPS spectra of oppositely polarized monodomain $BaTiO_3$ thin films provided information on their surface chemical composition as a function of polarization direction and atmosphere exposure time. Additionally, the effect of surface charge formed in vacuum conditions, either as a results of annealing or radiation exposure, on ferroelectric properties of thin films has been investigated.

3.1 Introduction

Ferroelectric materials display a wide range of mechanisms to screen ferroelectric polarization, as discussed in Chapter 1. Driven by a need for depolarizing-field screening and surface-energy minimization, ferroelectrics tend to change their surface chemical state, either by accumulation of electrons and holes close to the surface (electronic reconstruction) or by adsorbing/removing atoms to/from the surface (intrinsic ionic reconstruction).[1] These modifications of ferroelectric surfaces include changes in the stoichiometry, structure and electronic states close to the surface, which can lead to different surface chemical outcomes (e.g. adsorption energies, desorption rates, energy barriers for dissociation reactions, binding geometries etc.) of upcoming adsorbate molecules on oppositely-polarized ferroelectric surfaces.[2–8]

These singular properties open new opportunities to exploit ferroelectric surfaces for catalytic applications,[9,10] whereby adsorption of reactants, surface reactivity and desorption of byproducts could be selectively tuned by the ferroelectric polarization state, thereby overcoming optimal adsorbate-surface interaction strength of "fixed" catalytic surfaces defined by Sabatier principle. In this framework, ferroelectric polarization which can be controlled by several external parameters such as temperature (pyroelectricity),[11] pressure (piezoelectricity)[12] or electric field could become a dial to tune surface-adsorbate interaction strengths and surface chemical activities.

This is of particular importance for water molecules since i) they are the main external screening agents on ferroelectric surfaces, whereby their adsorption and dissociation processes will differ for oppositely polarized ferroelectric surfaces and ii) such polarization-dependent water behavior is desirable for (ferro)catalytically driven water-splitting reactions.

The change of the polarization direction also triggers the accumulation of charges/ions of opposite sign in the near-surface regions of ferroelectric, making them electrochemically active for different type of redox reactions as a function of the charge.[9,10] This means that, beside molecular water and its dissociation products,[13–16] we can expect some more complex chemical species at ferroelectric surfaces, stemming from the electrochemical reactions at the solid-vapor interface.

Redox processes on ferroelectric surfaces can be enhanced if the material is exposed to some external stimuli such as vibrations or temperature variation, which effectively changes magnitude of polarization, causing an imbalance between the bound and screening charge.[17] Such excess or lack of screening charge can be restored by driving surface reduction or oxidation reactions with surface adsorbed species. To some extent, these reactions can harvest[18] solar energy such as radiation (photocatalysis),[19–21] mechanical energy such as vibrations (piezoelectrocatalysis)[12,22–24] or thermal energy such as industrial waste heat (pyroelectrocatalysis),[12,25–30] and transform it directly into chemical energy, stored in the chemical bonds of the catalytic products. In some case even several of mentioned effects are effectively combined.[31–34]

In this chapter, I will explore which chemical species can be found on the surface of ferroelectric $BaTiO_3$ (BTO) thin films with uniaxial out-of-plane polarization, after exposure to atmospheric conditions, as studied by conventional X-ray Photoelectron Spectroscopy (XPS) measurements in vacuum. The interplay between ferroelectric polarization and surface chemical composition is assessed in terms of i) studying the effect of prolonged atmosphere exposure on the surface chemical composition as a function of polarization state and, vice versa, ii) investigating the influence of induced surface chemical states on ferroelectric properties, such as coercivity or imprint of hysteresis loops. Additionally, the effect of some commonly employed procedures, such as the annealing of samples in O_2 atmosphere, on the surface chemical composition has been addressed.

XPS measurements revealed different chemical compositions of up- and down-polarized surfaces after prolonged atmosphere exposure, reflected in their different oxidizing capacities and adsorbed water concentrations. The results indicate that down-polarized surfaces are able to enhance surface oxidation reactions, which at the same time renders them as more hydrophilic.

3.2 Surface-chemical composition of atmosphere-exposed $BaTiO_3$ thin films

Single crystalline, fully strained, epitaxial SRO/BTO thin films were grown on STO (001) oriented substrates and characterized by PFM and XRD, as described in Chapter 2. All the BTO thin films had a thickness of about ≈ 20 nm and were uniformly up-polarized in their as-

grown state. Surface characterization was performed by conventional X-Ray Photoelectron Spectroscopy (XPS) measurements in vacuum. First, we studied the surface composition of the as-grown, pristine-like sample. The sample was exposed to ambient conditions for about 20 minutes after growth, before it was transferred to the XPS chamber (Sample $A^{\uparrow}$) and is used as as a reference sample for all further XPS measurements. **Figure 3.1** shows the XPS spectra of the pristine-like Sample $A^{\uparrow}$ at the (a) Ti 2p, (b) C 1s, (c) O 1s and (d) Ba 3d regions. The Ti 2p spectrum (**Figure 3.1 a**) has been deconvoluted into the characteristic spin-orbit split doublet. The Ti $2p_{3/2}$ peak has a main component at a binding energy (B.E.) of 458.8 eV corresponding to the Ti^{4+} valence state. The presence of oxygen vacancies can be determined by existence of a shoulder in the low B.E. side of the Ti^{4+} $2p_{3/2}$ peak, corresponding to the associated presence of reduced Ti^{3+}.[16] The absence of a Ti^{3+} peak in our measurement points to the absence of oxygen vacancies close to the surface, within the limit of detection of our XPS equipment.

The C 1s region has been fitted with five well-resolved peaks as shown in **Figure 3.1 b**. The peak at lowest B.E. of 284.8 eV corresponds to C atoms attached to another C or H atom (**C**-C(H)). Components at ΔB.E. = + 1.4 eV and ΔB.E. = + 2.6 eV from the adventitious carbon peak are associated with C atoms attached by single (**C**-O) or double bond (**C**=O) to O atoms.[35] Meanwhile, the peak at ΔB.E. = + 3.65 eV can be related with C atoms in carbonate ($\mathbf{C}O_3^{2-}$), ester (C-(**C**=O)-OR) or carboxylic acid (C-(**C**=O)-OH) compounds. Finally, the peak at highest binding energy ΔB.E. = + 4.5 eV is observed only in some cases and has been related with the presence of bicarbonates ($H\mathbf{C}O_3^{-}$).[36]

The complex structure of the O 1s spectrum shown in **Figure 3.1 c** was fitted using the model previously developed in our group to explain surface chemical composition of non-ferroelectric and ferroelectric perovskite surfaces.[13] In this model, the lowest B.E. peak at 529.7 eV has been attributed to the oxide peak, while the higher BE peaks are related to different adsorbates species present on the surface. The peak at ΔB.E. = + 0.95 eV has been associated to different types of hydroxyl -OH groups on the surface bound to the metal, such as Ti- or Ba- bonded terminal -OH groups (Ti-**O**H, Ba-**O**H) and bridging hydroxyl groups (**Ox**-H) considered as H atoms bound to the lattice oxygen (also called lattice -OH groups). The peak at ΔB.E. = + 1.8 eV from the main oxide peak has been associated to different carbon-related species CO_x such as carbonates $C\mathbf{O}_3^{2-}$, ester (C-(C=**O**)-OR) or carboxylic acid (C-(C=**O**)-OH) compounds. This has been corroborated by the combined monitoring of the peak at ΔB.E. = + 1.8 eV from oxide

and the peak attributed to the same contribution in the C1s spectrum during the oxygen annealing, causing both peaks to decrease. The peak at ΔB.E. = + 2.75 eV, here named as "surface O^{2-} peak", has been mainly associated to oxidized species such as Ti-peroxo (Ti-O_2^{2-}) and -superoxo complexes (Ti-O_2^-).[13,37–39] It is worth to mention here that these species are structurally similar to the oxygen in actual metal peroxides such as Ba**O**$_2$. Finally, a peak at ΔB.E. = + 4 eV, clearly observed in AP-XPS measurements in water atmosphere, has been usually associated with physisorbed molecular water.[8,13]

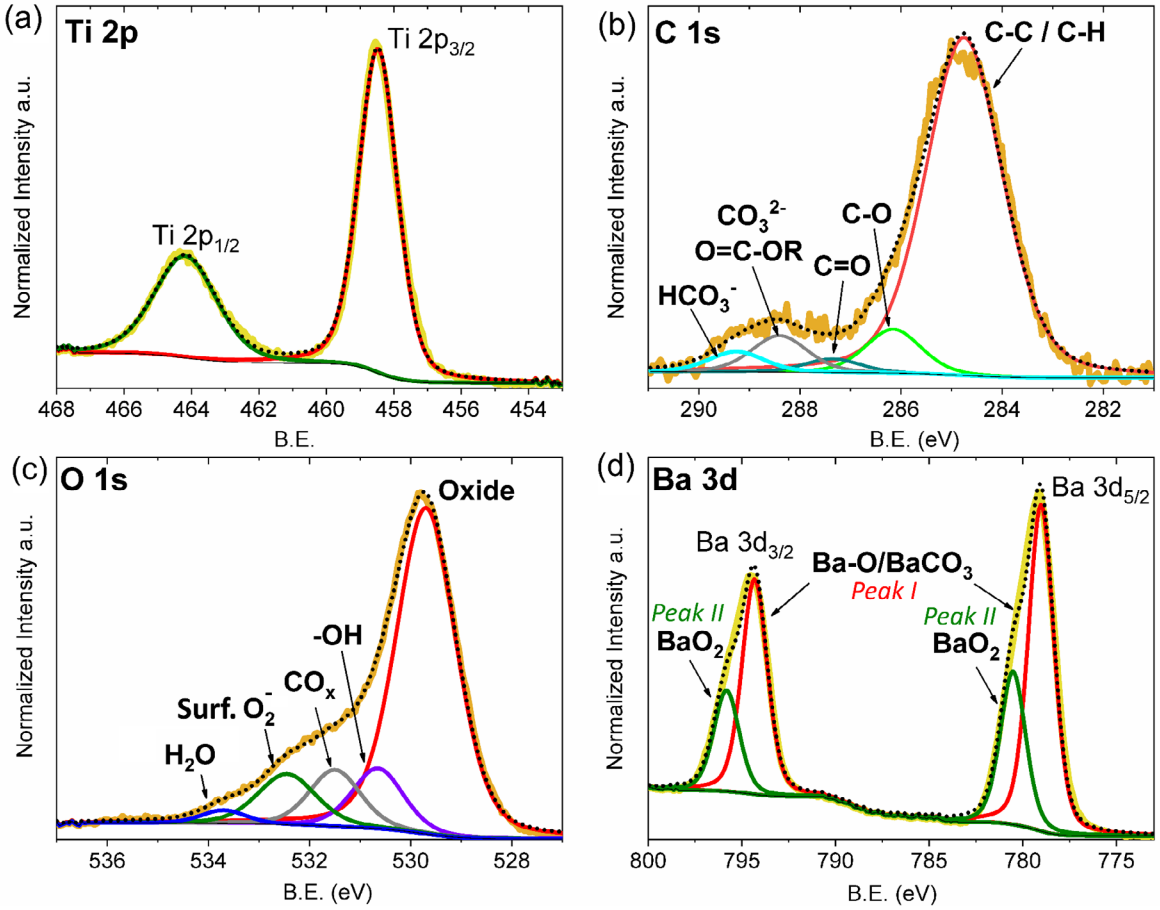

Figure 3.1 *Fitting of XPS spectra at Ti 2p (a), C 1s (b), O 1s (c) and Ba 3d (d) regions of as-grown up-polarized BTO thin film after being exposed to the air during 20 minutes, revealing contributions from undissociated water molecules, hydroxyl (OH) groups, peroxide species (Surface O_2^-) and different carbon-related species (-CO_x).*

The spectrum in the Ba 3d region (**Figure 3.1 d**) exhibits the typical $3d_{3/2}$ and $3d_{5/2}$ doublet, which can be further resolved in two different contributions. Peaks at B.E. of 779.0 eV (for the Ba $3d_{5/2}$) and 794.3 eV (for the Ba $3d_{3/2}$), hereafter labeled Peak I, belong to Ba atoms in the oxide lattice (BaO). A second peak is observed in both doublet components, shifted by ΔB.E. = + 1.5 eV from the Peak I (hereafter called Peak II). By comparing the Ba 3d spectrum taken at 0 deg with the one taken at 60 deg (thus with higher surface sensitivity) the relative intensity

of the second peak is observed to increase, pointing out the fact that this component is more superficial as compared to main Ba peak from the bulk oxide.

Hitherto, the assignment of this peak has been controversial and raised many debates: it has generally been attributed to Ba atom in surface compounds with different oxygen coordination,[40,41] barium carbonate ($BaCO_3$) or barium hydroxide $Ba(OH)_2$ compounds.[42–45] However, the two latter findings are not justified, since the peak at ΔB.E. ≈ + 1.5 eV from BaO (Peak II) is observed in many samples and in a lot of cases it exists even when carbonate species cannot be detected by XPS (i.e. in C 1s or O 1s spectra) nor by IR measurements at the surface.[16,44,46,47] Moreover, the chemical environment of Ba in $BaCO_3$ molecules should be similar to that of the bulk, so any contribution should be located close to or overlapping with the main BaO peak. Therefore, peak II cannot be univocally related to the presence of $BaCO_3$ species. On the other hand, the presence of previously proposed $Ba(OH)_2$[44] is improbable in the case of samples exposed to ambient, since CO_2 from the atmosphere would react instantaneously with $Ba(OH)_2$ forming $BaCO_3$ following the reaction[46]:

$$Ba(OH)_2 + CO_2 \rightarrow BaCO_3 + H_2O \qquad (1)$$

However, some works [48,49] show the presence of Ba $3d_{5/2}$ peak II shifted by ΔB.E. = 1.3 – 1.7 eV from the BaO, in agreement with our observations, and assign it to barium peroxide (BaO_2). Furthermore, published literature shows that the Ba $3d_{5/2}$ peak II is always followed by the presence of another peak in the O 1s spectrum at ΔB.E. = + 2.8 eV (±0.1 eV) from the main oxide peak, which is often arbitrarily (and mistakenly) associated to surface -OH groups or carbonate species.[42,44,48,50] Recent studies of oxide perovskite surfaces exposed to water vapor atmosphere demonstrated that the surface -OH peak is located within ΔB.E. = + 1.1 eV (±0.1 eV) of the oxide peak, given that its intensity uniformly increases as water is dosed into the chamber, while carbon related species (CO_x) should appear a bit further at ΔB.E. ~ +1.8 eV from the oxide peak.[8] In the same work, a peak at ΔB.E. = + 2.8 eV from the main oxide contribution (i.e., in the same position as our surface O^{2-} peak) is assigned to the Ti-peroxo complexes, arising from oxidative water adsorption process, in which adsorbed -OH groups are further oxidized to metal-peroxo complexes. Due to the resembling oxygen coordination in BaO_2 as in Ti-peroxo complex compounds, we expect that BaO_2 should contribute at similar energies in O1s spectrum.

In order to delve into the origin of Ba $3d_{5/2}$ peak II, we annealed one of our samples (Sample $B^{\uparrow}$) at 250 °C in O_2 atmosphere ($P \approx 10^4$ mTorr) and afterwards we cooled it down slowly with a rate of 3 °C/min. After such annealing treatment, the sample was transferred to XPS chamber without breaking the vacuum using a vacuum suitcase. **Figure 3.2** shows the (a) Ba $3d_{5/2}$, (b) C 1s and (c) O 1s XPS spectra of the BTO thin film measured before and after the annealing treatment. By comparing the obtained Ba $3d_{5/2}$ spectrum after annealing with the initial spectrum of this sample, it can be seen that the concentration of Ba $3d_{5/2}$ peak II has strongly increased. On the other hand, the spectra at the C 1s region show that annealing treatment diminishes the concentration of C-C, as well as **C**=O bonds, while the peak corresponding to the ($\mathbf{C}O_3^{2-}$)/(C-(**C**=O)-R) species almost doesn't suffer any change. This can be due to the simultaneous effect of $\mathbf{C}O_3^{2-}$ species decrease and (C-(**C**=O)-R) species increment. At the same time, C$\mathbf{O}_x$ peak in O1s region is decreased following the same trends observed for ($\mathbf{C}O_3^{2-}$)/(C-(**C**=O)-R) peaks in C 1s region. This simultaneous decrease of carbon related -CO_x species and increment of Ba $3d_{5/2}$ peak II proves that this component cannot be prescribed to CO_3^{2-} species, such as $BaCO_3$, since the latter follows the opposite trend in annealing experiments. We therefore believe that the origin of this component stems from the presence of barium peroxide (BaO_2), whose production is fostered as the sample is annealed in O_2 atmosphere, as follows; simultaneous decrease of CO_3^{2-} species and increment of BaO_2 can be explained by the decomposition of barium carbonate at high temperature on BaO and CO_2 as:

$$BaCO_3 \rightarrow BaO + CO_2 \qquad (2)$$

Therefore, free BaO terminations can be further oxidized to BaO_2 (while is CO_2 pumped away from the XPS chamber) following the reaction:

$$2BaO + O_2 \longrightarrow 2BaO_2 \qquad (3)$$

Figure 3.2 c shows the O1s spectra before and after O_2 annealing. It can be seen that, as expected, the formation of BaO_2 species gives rise to the surface O_2^- peak evidencing the interconnected behavior of these two peaks. It should be noted that the relative increase of BaO_2 peak (in Ba 3d spectrum) and surface O_2^- peak (in O 1s spectrum) cannot be directly compared, since the later contains total contribution from both BaO_2 and metal-peroxo complexes (due to oxidative water adsorption reactions), whose concentration also might be affected by annealing.

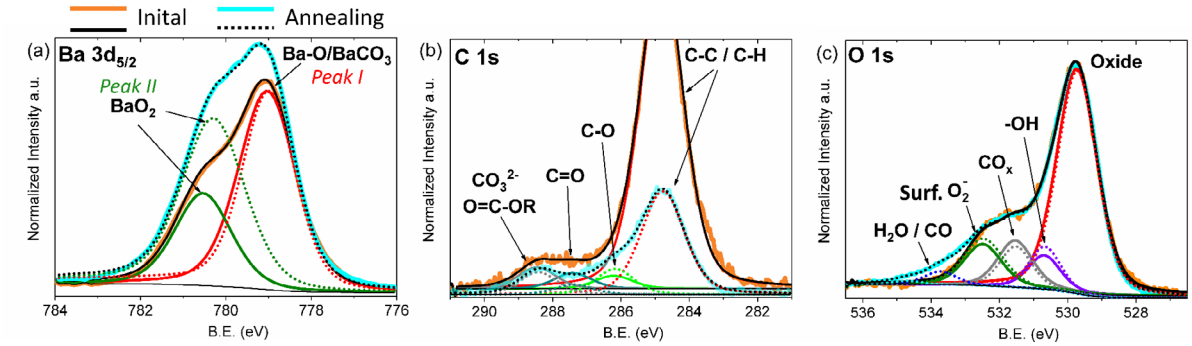

Figure 3.2 *Fitting of XPS spectra at the Ba 3d (a), C 1s (b) and O 1s (c) regions, taken in vacuum conditions at RT and with an incident angle of 60 degrees (increased surface sensitivity) of an up-polarized BTO sample (Sample B↑). The spectra are taken before (straight orange lines) and after (blue dotted lines) annealing at 250 ˚C in saturated O_2 atmosphere. Peaks are assigned to the different components identified in the figure. Ba $3d_{5/2}$ spectra shows that annealing causes an increment of the component at +1.5 eV from BaO peak (Peak II), which is in direct relation with the increment of surface O_2^- peak at +2.75 eV from main oxide peak in O 1s region and therefore can be related with the presence of BaO_2.*

This experiment confirmed that peak II in the Ba 3d region corresponds to the BaO_2 species and that its evolution is entangled to the component at ΔBE = + 2.8 eV from the main peak in the O 1s. Therefore, it can be used to specifically follow oxidation of BaO sites as a function of time and polarization. We note that considering the clear evidence of presence of $-CO_3^{2-}$ species as observed from the C1s and O1s regions spectra, we cannot neglect the presence of some $BaCO_3$. Still, as mentioned before, the position of this peak in the Ba 3d spectrum is expected to overlap the BTO peak[51,52] from the bulk contribution, making it undetectable within our energy resolution. Moreover, significant amount of BaO_2 on BTO surfaces in our case might be related with the sample preparation method: after the thin film growth at 700 ºC, the chamber is saturated with O_2 while the temperature is ramped down very slowly (3 ºC/min). These conditions of high O_2 pressure and temperature can foster the production of BaO_2 by, for example following the reaction (2), and therefore this peak might not be as relevant on samples made by other procedures.

Finally, but not the least, we note that few minutes of exposure to environmental conditions is enough for ferroelectric surfaces to react with water and hydrocarbon molecules from the atmosphere and create a layer of adsorbates: after about 20 min in ambient conditions, the surface of our as-grown up polarized BTO thin film already contains hydroxyl groups obtained after water dissociation reactions, in addition to BaO_2 and Ti-based peroxo complexes obtained after further oxidation of hydroxyl groups on the surface, as well as some contamination in the form of carbonates.

3.3 Interplay between polarization and surface chemical composition of $BaTiO_3$ thin films

3.3.1 Surface-assisted polarization switching

During some experiments performed on our BTO thin films, we found that in some cases, the polarization state of our as grown up-polarized samples was prone to reverse under specific environmental conditions or under X-Ray exposure. Spontaneous polarization switching over the whole surface was observed i) when the sample was exposed to temperatures up to 200 ºC in vacuum or ii) when irradiated with X-Rays in the frame of an XPS experiment in vacuum conditions. However, if the sample is annealed at the same temperature but in O_2 atmosphere (as in the previous experiment), the sample keeps its as-grown up-polarized state.

This spontaneous ferroelectric polarization switching was studied by ferroelectric lithography, whereby oppositely polarized domains were electrically written and subsequently scanned by PFM. Two square regions were electrically poled to opposite polarization states, by applying a voltage to the tip of V_{tip} = - 8 V (forcing the polarization up) and V_{tip} = + 8 V (forcing the polarization to switch down), while scanning in contact over a 6 x 6 μm^2 and 4 x 4 μm^2 areas respectively. The amplitude and phase PFM images of ferroelectric domains written in the case of the vacuum-annealed sample are shown in **Figure 3.3 a.b** (and similar results are available for XPS X-Ray irradiated samples)**.** Considering that the contrast of the inner square is the same as that of the background, it can be concluded that the sample annealed in vacuum possess a polarization uniformly switched from up- to down- polarized state. This switching could be attributed to the creation of a positive surface potential due to a) the formation of surface oxygen vacancies during vacuum annealing process or b) the creation of electron vacancies during the XPS measurements. In both cases, this favors ferroelectric switching from as-grown up to down-polarized state.

Polarization switching might be an inherent part of XPS experiments when the size of the X-Ray beam spot on the sample is comparable to the sample size, as high flux X-ray photons can remove photoelectrons from the sample and leave behind positively charged holes. These holes can be refilled by negative charge carriers present in the highly conductive metallic samples, but not in the case of insulating samples such as ours. In this case, surface-trapped and uncompensated positive holes would create a built-in electric field E_v, opposing the as-grown

polarization of the sample, which if sufficiently high could switch the polarization to down-polarized state. It has been reported in previous studies[53,54] that exposure of ferroelectric samples to UV or X-Ray radiation can cause entrapment of photogenerated charges in the near-surface region, observed as a drastic imprint of hysteresis loops, which in some cases persisted during months.

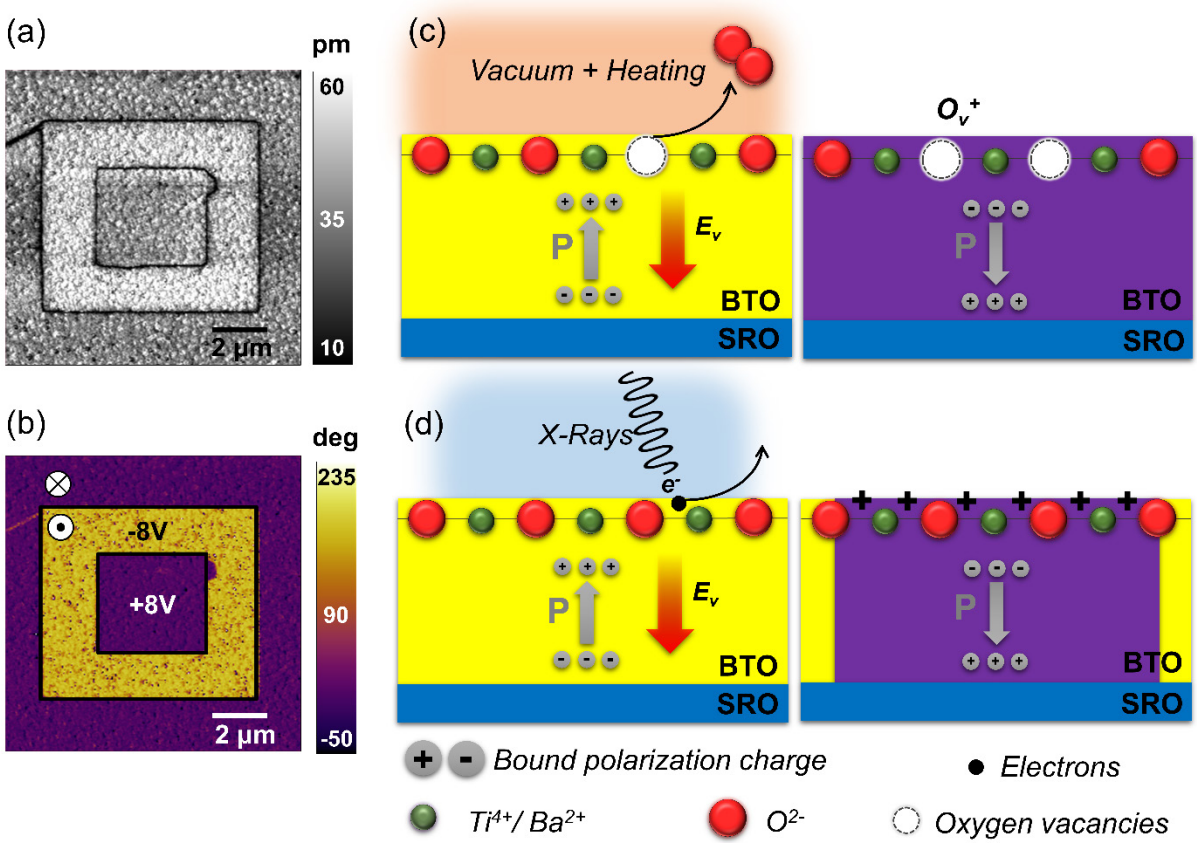

Figure 3.3 *(a) PFM amplitude and (b) PFM phase image of the BTO thin film after annealing in vacuum and ferroelectric lithography, revealing that background polarization spontaneously switched to down-polarized state; Schematic representation of polarization switching from up to down state, caused by formation of positive electric field E_v associated with the creation of (c) oxygen vacancies O_v^+ due to the vacuum annealing or (d) electron vacancies due to the X-rays photoelectric effect, leading to positive surface charging.*

In a similar way, annealing in vacuum conditions up to 200 ºC can create a positive surface voltage either by removing essential screening charges or by inducing new oxygen vacancies, typically observed in the as-grown thin films prepared in low O_2 partial pressure conditions or upon similar annealing procedures,[55–57] that can lead again to ferroelectric polarization switching. These processes are schematically depicted in **Figure 3.3 c,d**. Interestingly, samples which switched due to the exposure to high flux X-Rays in vacuum conditions preserved down-polarized state even three months after the initial measurements. It should be noted that all the

samples were stored in a desiccator equipped with a vacuum pump, except when PFM experiments in ambient conditions were performed.

Figure **3.4 a,b** show the SS-PFM hysteresis cycles of as-grown up polarized sample, which was switched down after annealing in vacuum. The as-grown sample shows a coercive voltage of $V_{c,+}$ = 1.2 V and a $V_{c,-}$ = -0.4 V, with a slightly positive bias of $V_{bias,\,up}$ = 0.4 V. This initial positive bias denotes the presence of a built-in upwards oriented electric field in the as-grown sample that nucleates the as-grown up polarization state. This field may be related to the accumulation of positive charge at the interface between the film and the bottom electrode that might be in the form of oxygen vacancies.[58] In contrast, the vacuum-annealed sample shows an increase of stability as observed by increased coercive voltages of $V_{c,+}$ = 1.5 V and $V_{c,-}$ = -1.4 V, with almost no bias. The hysteresis loops obtained on the switched samples after X-Ray exposure (not shown here) show the same trend, i.e., a slight increase of the coercive voltage and vanishing bias, pointing to an enhanced degree of polarization stability. In both cases, surface charge induced effects lead ultimately to a more robust polar material, with enhanced coercive voltage and absence of built-in bias as observed in PFM hysteresis cycles.

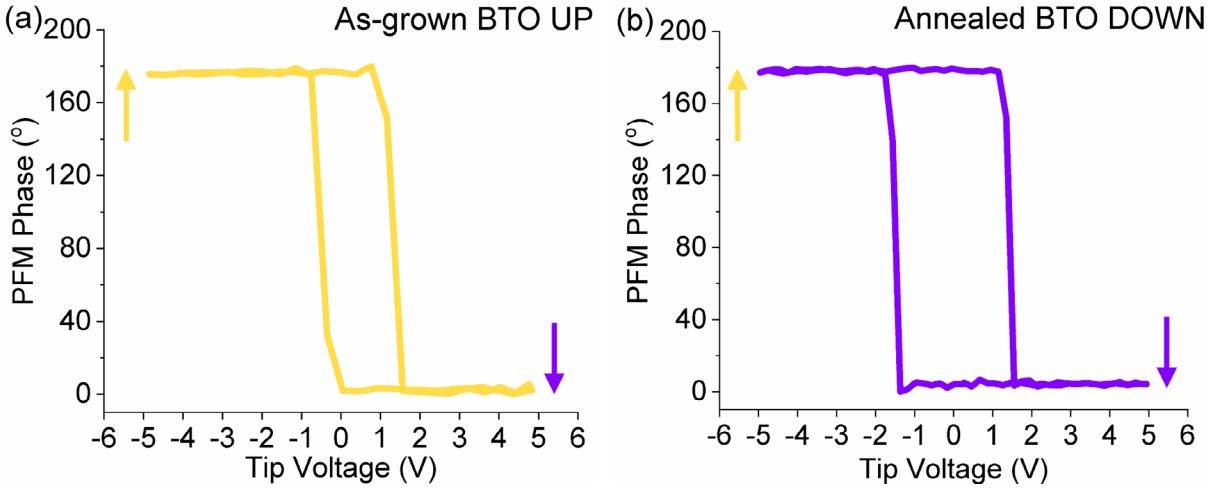

Figure 3.4 *SS-PFM hysteresis loops of (a) as-grown up-polarized BTO thin film, showing coercive voltages of $V_{c,+}$ = 1.2 V and $V_{c,-}$ = -0.4 V with a slightly positive bias of $V_{bias,\,up}$ = 0.4 V and (b) down-switched BTO thin film obtained after vacuum annealing, with increased coercive voltage of $V_{c,+}$ = 1.5 V and $V_{c,-}$ = -1.4 V and almost no bias. As a consequence of polarization switching, the internal bias disappears leading ultimately to a more robust polarization as observed by the increase of coercive voltage and absence of bias.*

From this experiment, it becomes evident that changes in the surface and interface charge of thin films can have significant effects on the polar response of ferroelectric thin films (e.g. coercivity and imprint) or even completely change the polarization direction. However, this relation is bidirectional, and therefore differences in surface chemical compositions of up- and

down- polarized surfaces should develop during prolonged exposure time to ambient conditions. This is what we focus on in the following section.

3.3.2 Polarization-dependent surface chemistry of up and down polarized $BaTiO_3$ thin films

The effect of atmospheric exposure of BTO thin film surfaces as a function of their polarization state is shown in **Figure 3.5**. The yellow lines show the XPS spectra at the (a) Ba $3d_{5/2}$, (b) C 1s and (c) O 1s regions of an as-grown up-polarized sample after three months of exposure to ambient conditions, which was *not* exposed to X-Rays previously (sample $C^{\uparrow}$). Purple lines show the XPS spectra of spontaneously switched sample $A^{\downarrow}$, taken about four months after the spectra shown in **Figure 3.1.** After the first XPS measurement on sample $A^{\uparrow}$, we could see that its polarization was switched down and thus, it remained in a down-polarized state for all the time before the second XPS measurement, performed four months later. Therefore, we will refer to this sample as $A^{\downarrow}$. If we compare pristine-like sample $A^{\uparrow}$ (**Figure 3.1**) with long-term ambient exposed BTO, apparent changes in the Ba $3d_{5/2}$, C 1s and O 1s regions can be appreciated for both polarization states.

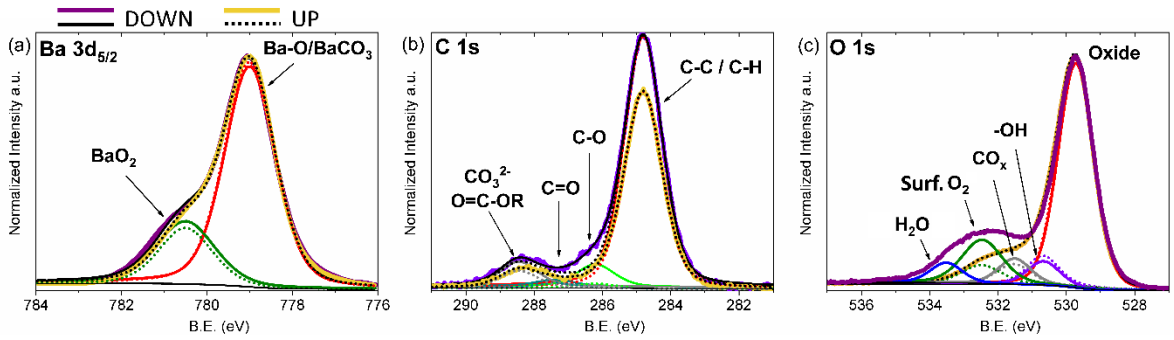

Figure 3.5 *Fitting of XPS spectra at the Ba 3d (a), C 1s (b) and O 1s (c) regions, taken in vacuum conditions at RT for down- (purple, full lines) and up- (yellow, dotted lines) polarized BTO samples after being exposed to ambient conditions during a period of several months. Compared to the spectra taken on as grown up-polarized BTO shown in* ***Figure 3.1****, long exposure to ambient conditions leads to an increase of adventitious carbon, carbonates and also surface oxygen species dominated by Ti-peroxo complexes. Importantly, this increase is more pronounced for down-polarized sample, which is represented in* ***Table 1****.*

Table 1 shows the change in the ratios of the peaks as a function of time for the different polarization states as compared to pristine-like sample $A^{\uparrow}$. For both samples, the amount of BaO_2 on the surface is increasing during time, but the down-polarized surface seems to be more reactive. The increment of $BaCO_3$ is also observable in the C 1s and O 1s region by following $-CO_3^{2-}$ and $-CO_x$ peaks, respectively, with down-polarized surface showing more intense peaks, compared to up-polarized one. The Surface O^{2-} peak in O 1s is also increasing over time for both surfaces, being the negatively-polarized surface again the one showing higher reactivity. This peak should include the contribution from both BaO_2 and Ti-peroxo complexes. In the case of complex water-assisted surface reactions, where both contributions of BaO_2 and Ti-peroxo complexes are entangled, analysis of Ba $3d_{5/2}$ region can thus provide additional information regarding oxygen atoms in Ba compounds, which is not available only from O 1s region. Since we can isolate the contribution from the increase of the BaO_2 peak in the Ba $3d_{5/2}$ spectrum, this allows us to directly monitor electrochemical reactions as a function of polarization.

Sample		O 1s			Ba $3d_{5/2}$	C 1s			
P state	Exposure to ambient	OH	COx	Surf. O_2^-	BaO_2	C-C	C-O	C=O	CO_3^{2-}
UP $C^{\uparrow}$	3 Months	2.16%	2.65%	6.64 %	7.65 %	14.13 %	-0.80%	0.36%	1.05%
DOWN $A^{\downarrow}$	4 Months	0.26 %	4.48%	20.14 %	13.68 %	20.40 %	1.20 %	0.55 %	1.89 %

Table 3.1. *Relative increase of the ratios of the species in O 1s, Ba $3d_{5/2}$ and C 1s regions of BTO thin films due to prolonged time exposure and as a function of polarization, when compared with an as-grown sample $A^{\uparrow}$. The ratio of the oxygen species is taken by dividing the areas of the peaks with the area of the main oxide peak, corresponding to bulk BaO contribution; The ratio for Ba species is taken with respect to the main Ba peak, arising from the same contribution; The ratios for carbon species are normalized with respect to the main oxide peak area, taken as constant for all the samples. The first line shows the relative increase of species for up polarized sample due to exposure to ambient conditions for three months, and the second line shows the relative increase in the species for a down polarized sample due to ambient exposure for four months, as compared to an as-grown sample.*

Surface oxidation on the different metal active sites follows distinct reactions. Ti sites in TiO_2-terminated surfaces are known to be very reactive to water.[16] They will mainly catalyze water dissociation, leading to strong surface hydroxylation. Furthermore, Ti sites are shown to be active sites for oxidative water adsorption process,[13] in which terminal -OH groups are further oxidized to Ti –peroxo and –superoxo complexes, resulting in increment of surface O_2^-

peak.[13,38] Instead, Ba sites are not able to build stable metal-peroxo complexes like Ti atoms. In this case, reaction with O_2 from atmosphere, although with much smaller reactivity rates, or O atoms from the lattice might take place, giving rise to BaO_2 and surface O_2^- peaks. In such oxidation process, oxygen atoms change valence state from -2 in BaO to -1 in BaO_2. On the other hand, segregation of surface peroxides has also been reported when an electric potential of several hundreds of millivolts is applied to the surface,[39,59] which can be considered also in our case since ferroelectric surfaces are inherently charged.

In comparison to other oxide materials, ferroelectrics have an additional degree of freedom, namely polarization, which can take different orientations and therefore affect the sign of the surface screening charge. In a simplistic model it is considered that up-polarized surfaces are able to accumulate electrons thus inducing possible surface reduction reactions. Conversely, down-polarized surfaces accumulate positive surface charge (repel the negative one), thereby inducing surface oxidation reactions.

Our results show that long exposure of BTO ferroelectric surfaces to ambient conditions leads mainly to an increment of Ti-peroxo species (as observed by a drastic increment of surface O_2^- peak), especially pronounced on the down-polarized surfaces together with some increase of BaO_2, indicating enhanced oxidation reactions on down-polarized surfaces compared to up-polarized ones. Altogether, this turns down-polarized surfaces into more hydrophilic ones, observed as additional peak at the highest binding energy in the O 1s spectrum on the down-polarized surfaces (**Figure 3.5 c**), associated to the adsorbed molecular water. This enhanced hydrophilicity of down-polarized surfaces could stem from favorable hydrogen-bond formation between water molecules and surface oxygen species and/or hydroxyl groups. It should be noted that this is in agreement with water adsorption study on ferroelectric $Pb(Zr_{0.2},Ti_{0.8})O_3$ films,[39] which shows that indeed down-polarized surfaces have more hydrophilic character as compared to up-polarized ones, rendering increased hydrophilicity as a general property of Ti-containing down-polarized ferroelectric surfaces.

3.4 Conclusions

Investigation of the BTO thin films' surface chemistry showed that surfaces exposed to ambient conditions in the order of few minutes already contain significant amount of adsorbed chemical species in the form of molecular water, but also some hydroxyl groups, surface-oxidized species (i.e. Ti-peroxo complex compounds as well as BaO_2) and various carbon-related contamination species. In addition, our findings indicate that the surface composition of atmosphere-exposed ferroelectrics varies in time over long periods, with polarization-dependent electrochemical reactions at the solid-vapor interface playing a significant role.

The formation of BaO_2 species happening in almost every BTO surface, which was neglected up to now, has been demonstrated to be enhanced by annealing processes in O_2 atmosphere. The identification of this new surface component on BTO surfaces is relevant for the study of screening mechanisms in this ferroelectric material, with potential consequences for catalytic processes.

On a different note, annealing in vacuum at not-too-high temperatures (250 ºC) evidenced how even relatively mild experimental procedures can affect surface chemical composition of ferroelectric materials and their ferroelectric properties. This was of particular importance in the case of BTO thin films annealed in vacuum conditions, which caused switching of polarization from as-grown up- to down-polarized state, presumably due to the creation of positively charged subsurface oxygen vacancies. I also observed that polarization switching can happen in the frame of XPS experiments in vacuum conditions, possibly stemming from the creation of uncompensated positively charged photoelectron holes. Additionally, polarization reversal induced by either of the aforementioned treatments, caused changes in the local hysteresis loops measured by SS-PFM, observed as an increased coercive voltage and disappearance of built-in field in the surface-induced down-switched samples.

This surface-charge-induced polarization switching which persisted during the time, enabled me to study changes in the surface chemistry of oppositely polarized BTO thin films after prolonged atmosphere exposures. Long exposure to ambient conditions of BTO surfaces leads to: i) increment of BaO_2 as observed from Ba $3d_{5/2}$ region and ii) formation of Ti -peroxo and -superoxo compounds, which are dominating the behavior of surface O_2^- peak in O 1s region. The relative increment of oxidized species is higher on down polarized surfaces and therefore

suggests that down-polarized surfaces promote oxidation processes, possibly by being able to repel electrons further from surface region, accept oxygen atoms from environment or alternatively give away lattice oxygen atoms which may interact with BaO forming BaO_2 layer. This further affects the concentration of upcoming water molecules, due to the favorable hydrogen-bond formation between upcoming water molecules and oxidized species, which therefore render down-polarized surfaces also more hydrophilic.

References

[1] A. Kakekhani, S. Ismail-Beigi, E. I. Altman, *Surf. Sci.* **2016**, *650*, 302.

[2] K. Garrity, A. Kakekhani, A. Kolpak, S. Ismail-Beigi, *Phys. Rev. B - Condens. Matter Mater. Phys.* **2013**, *88*, 1.

[3] M. H. Zhao, D. A. Bonnell, J. M. Vohs, *Surf. Sci.* **2008**, *602*, 2849.

[4] D. Li, M. H. Zhao, J. Garra, A. M. Kolpak, A. M. Rappe, D. A. Bonnell, J. M. Vohs, *Nat. Mater.* **2008**, *7*, 473.

[5] Y. Yun, E. I. Altman, *J. Am. Chem. Soc.* **2007**, *129*, 15684.

[6] Z. Zhang, P. Sharma, C. N. Borca, P. A. Dowben, A. Gruverman, *Appl. Phys. Lett.* **2010**, *97*, 243702.

[7] Z. Zhang, R. González, G. Díaz, L. G. Rosa, I. Ketsman, X. Zhang, P. Sharma, A. Gruverman, P. A. Dowben, *J. Phys. Chem. C* **2011**, *115*, 13041.

[8] K. Cordero-Edwards, L. Rodríguez, A. Calò, M. J. Esplandiu, V. Pérez-Dieste, C. Escudero, N. Domingo, A. Verdaguer, *J. Phys. Chem. C* **2016**, *120*, 24048.

[9] A. Kakekhani, S. Ismail-Beigi, *ACS Catal.* **2015**, *5*, 4537.

[10] A. Kakekhani, S. Ismail-Beigi, *Phys. Chem. Chem. Phys.* **2016**, *18*, 19676.

[11] D. Zhang, H. Wu, C. R. Bowen, Y. Yang, *Small* **2021**, *17*, 2103960.

[12] M. Wang, B. Wang, F. Huang, Z. Lin, *Angew. Chemie - Int. Ed.* **2019**, *58*, 7526.

[13] N. Domingo, E. Pach, K. Cordero-Edwards, V. Pérez-Dieste, C. Escudero, A. Verdaguer, *Phys. Chem. Chem. Phys.* **2019**, *21*, 4920.

[14] J. J. Segura, N. Domingo, J. Fraxedas, A. Verdaguer, *J. Appl. Phys.* **2013**, *113*, 0.

[15] J. Shin, V. B. Nascimento, G. Geneste, J. Rundgren, E. W. Plummer, B. Dkhil, S. V. Kalinin, A. P. Baddorf, *Nano Lett.* **2009**, *9*, 3720.

[16] J. L. Wang, F. Gaillard, A. Pancotti, B. Gautier, G. Niu, B. Vilquin, V. Pillard, G. L. M. P. Rodrigues, N. Barrett, *J. Phys. Chem. C* **2012**, *116*, 21802.

[17] Y. Zhang, M. Xie, V. Adamaki, H. Khanbareh, C. R. Bowen, *Chem. Soc. Rev.* **2017**, *46*, 7757.

[18] H. Li, C. R. Bowen, Y. Yang, *Adv. Funct. Mater.* **2021**, *31*, 1.

[19] M. A. Khan, M. A. Nadeem, H. Idriss, *Surf. Sci. Rep.* **2016**, *71*, 1.

[20] Y. Cui, J. Briscoe, S. Dunn, *Chem. Mater.* **2013**, *25*, 4215.

[21] L. Li, P. A. Salvador, G. S. Rohrer, *Nanoscale* **2014**, *6*, 24.

[22] K. S. Hong, H. Xu, H. Konishi, X. Li, *J. Phys. Chem. Lett.* **2010**, *1*, 997.

[23] W. Qian, W. Yang, Y. Zhang, C. R. Bowen, Y. Yang, *Piezoelectric Materials for Controlling Electro-Chemical Processes*, Springer Singapore, **2020**.

[24] Y. Zhang, H. Khanbareh, S. Dunn, C. R. Bowen, H. Gong, N. P. H. Duy, P. T. T. Phuong, *Adv. Sci.* **2022**, *9*, 2105248.

[25] C. Wang, N. Tian, T. Ma, Y. Zhang, H. Huang, *Nano Energy* **2020**, *78*, 105371.

[26] A. Kakekhani, S. Ismail-Beigi, *J. Mater. Chem. A* **2016**, *4*, 5235.

[27] Y. Zhang, P. T. T. Phuong, E. Roake, H. Khanbareh, Y. Wang, S. Dunn, C. Bowen, *Joule* **2020**, *4*, 301.

[28] M. Xie, S. Dunn, E. Le Boulbar, C. R. Bowen, *Int. J. Hydrogen Energy* **2017**, *42*, 23437.

[29] Y. Zhang, S. Kumar, F. Marken, M. Krasny, E. Roake, S. Eslava, S. Dunn, E. Da Como, C. R. Bowen, *Nano Energy* **2019**, *58*, 183.

[30] X. Xu, L. Xiao, Y. Jia, Z. Wu, F. Wang, Y. Wang, N. O. Haugen, H. Huang, *Energy Environ. Sci.* **2018**, *11*, 2198.

[31] Q. Liu, D. Zhai, Z. Xiao, C. Tang, Q. Sun, C. R. Bowen, H. Luo, D. Zhang, *Nano Energy* **2022**, *92*, 106702.

[32] Y. Zhang, P. T. Thuy Phuong, N. P. Hoang Duy, E. Roake, H. Khanbareh, M. Hopkins, X. Zhou, D. Zhang, K. Zhou, C. Bowen, *Nanoscale Adv.* **2021**, *3*, 1362.

[33] P. T. Thuy Phuong, Y. Zhang, N. Gathercole, H. Khanbareh, N. P. Hoang Duy, X. Zhou, D. Zhang, K. Zhou, S. Dunn, C. Bowen, *iScience* **2020**, *23*, 101095.

[34] J. Wu, N. Qin, E. Z. Lin, Z. H. Kang, D. H. Bao, *Mater. Today Energy* **2021**, *21*, 100732.

[35] J. Landoulsi, M. J. Genet, S. Fleith, Y. Touré, I. Liascukiene, C. Méthivier, P. G. Rouxhet, *Appl. Surf. Sci.* **2016**, *383*, 71.

[36] A. V. Shchukarev, D. V. Korolkov, *Cent. Eur. J. Chem.* **2004**, *2*, 347.

[37] K. A. Stoerzinger, W. T. Hong, E. J. Crumlin, H. Bluhm, M. D. Biegalski, Y. Shao-

Horn, *J. Phys. Chem. C* **2014**, *118*, 19733.

[38] J. M. P. Martirez, S. Kim, E. H. Morales, B. T. Diroll, M. Cargnello, T. R. Gordon, C. B. Murray, D. A. Bonnell, A. M. Rappe, *J. Am. Chem. Soc.* **2015**, *137*, 2939.

[39] N. Domingo, I. Gaponenko, K. Cordero-Edwards, N. Stucki, V. Pérez-Dieste, C. Escudero, E. Pach, A. Verdaguer, P. Paruch, *Nanoscale* **2019**, *11*, 17920.

[40] A. Pancotti, J. Wang, P. Chen, L. Tortech, C. M. Teodorescu, E. Frantzeskakis, N. Barrett, *Phys. Rev. B - Condens. Matter Mater. Phys.* **2013**, *87*, 1.

[41] L. T. Hudson, R. L. Kurtz, S. W. Robey, D. Temple, R. L. Stockbauer, *Phys. Rev. B* **1993**, *47*, 10832.

[42] C. C. Li, S. J. Chang, J. T. Lee, W. S. Liao, *Colloids Surfaces A Physicochem. Eng. Asp.* **2010**, *361*, 143.

[43] C. Miot, E. Husson, C. Proust, R. Erre, J. P. Coutures, *J. Eur. Ceram. Soc.* **1998**, *18*, 339.

[44] J. L. Wang, J. Leroy, G. Niu, G. Saint-Girons, B. Gautier, B. Vilquin, N. Barrett, *Chem. Phys. Lett.* **2014**, *592*, 206.

[45] R. Ayouchi, F. Martín, J. R. Ramos-Barrado, D. Leinen, *Surf. Interface Anal.* **2000**, *30*, 565.

[46] S. Kumar, V. S. Raju, T. R. N. Kutty, *Appl. Surf. Sci.* **2003**, *206*, 250.

[47] V. Craciun, R. K. Singh, *Appl. Phys. Lett.* **2000**, *76*, 1932.

[48] S. Chakrabarti, S. Ginnaram, S. Jana, Z. Y. Wu, K. Singh, A. Roy, P. Kumar, S. Maikap, J. T. Qiu, H. M. Cheng, L. N. Tsai, Y. L. Chang, R. Mahapatra, J. R. Yang, *Sci. Rep.* **2017**, *7*, 1.

[49] T. C. Droubay, L. Kong, S. A. Chambers, W. P. Hess, *Surf. Sci.* **2015**, *632*, 201.

[50] J. L. Wang, B. Vilquin, N. Barrett, *Appl. Phys. Lett.* **2012**, *101*, 1.

[51] R. P. Vasquez, *J. Electron Spectros. Relat. Phenomena* **1991**, *56*, 217.

[52] P. J. Schmitz, *Surf. Sci. Spectra* **2002**, *190*, 1.

[53] N. Menou, A.-M. Castagnos, C. Muller, D. Goguenheim, L. Goux, D. J. Wouters, J.-L. Hodeau, E. Dooryhee, R. Barrett, *J. Appl. Phys.* **2005**, *97*, 044106.

[54] A. Gruverman, B. J. Rodriguez, R. J. Nemanich, A. I. Kingon, *J. Appl. Phys.* **2002**, *92*,

2734.

[55] C. Weymann, C. Lichtensteiger, S. Fernandez-Peña, A. B. Naden, L. R. Dedon, L. W. Martin, J. M. Triscone, P. Paruch, *Adv. Electron. Mater.* **2020**, *6*, 2000852.

[56] W. Peng, J. Mun, Q. Xie, J. Chen, L. Wang, M. Kim, T. W. Noh, *npj Quantum Mater.* **2021**, *6*, 1.

[57] M. Tyunina, J. Peräntie, T. Kocourek, S. Saukko, H. Jantunen, M. Jelinek, A. Dejneka, *Phys. Rev. Res.* **2020**, *2*, 23056.

[58] Y. M. Kim, A. Morozovska, E. Eliseev, M. P. Oxley, R. Mishra, S. M. Selbach, T. Grande, S. T. Pantelides, S. V. Kalinin, A. Y. Borisevich, *Nat. Mater.* **2014**, *13*, 1019.

[59] D. Kim, R. Bliem, F. Hess, J. J. Gallet, B. Yildiz, *J. Am. Chem. Soc.* **2020**, *142*, 3548.

CHAPTER 4

Ferrocatalysis on $BaTiO_3$ single crystals

This chapter examines the surface chemistry of $BaTiO_3$ (100) single crystal upon pyrocatalytically driven redox reactions in water vapor atmosphere across Curie temperature. The evolution of adsorbates' chemical composition in water vapor atmosphere, closely related to the appearance of polarization at the paraelectric-to-ferroelectric phase transition, has been investigated by combined use of *in-situ* ambient pressure XPS, X-Ray reciprocal space mapping and piezoresponse force microscopy. Additionally, the dynamics of surface charge, during heating and cooling cycles across the Curie temperature, has been assessed by the fast-tracking of photoelectrons' kinetic energy, sensitive to the presence of unbalanced surface charge and ferroelectric polarization.

4.1 Introduction

Hydrogen (H_2) is an essential gas in the chemical industry and is widely touted as the future of clean energy in the anticipated hydrogen economy. H_2 has the highest energy density per mass of any fuel, it releases zero carbon emissions on combustion, and can be effectively used in fuel cells to store energy and produce electricity as needed. However, economically viable and green production methods are still not available. Despite being the most abundant element in the Universe, there are no natural hydrogen deposits that we can simply 'mine': instead it has to be produced. Today this is mainly performed via the reforming of fossil fuels such as natural gas or biomass, and by the electrolysis of water. Both leave hefty environmental and ecological footprints, and the later requires the injection of electrons from an external source to stimulate the necessary reaction, in turn incurring high costs.

Being a subfamily of pyroelectric materials, in ferroelectrics the polarization can be modulated by changes in temperature. The pyroelectric coefficient p is defined as[1]:

$$p = \frac{dP_s}{dT} \qquad (1)$$

where dP/dT is the change of the ferroelectric polarization with temperature, which diverges close to the Curie temperature as shown in **Figure 4.1**. Thanks to the intrinsic coupling between polarization and surface chemical composition, it can be expected that the temperature-induced polarization modification will also cause electrochemical changes on the surface,[1–4] since the change of temperature creates an imbalance between bound and screening charge, leaving the surface temporary charged. Pushing the system out of the equilibrium, leverages the surface redox reactions in which necessary charge is produced or consumed in oxidation and reduction processes involving surface adsorbed molecules.[4,5] This becomes of particular interest when experiments are performed for instance in water vapor atmosphere, in which ferroelectrics can be used as harvesters of the waste heat[3,6,7] and employed as charge sources for the production of green H_2 through water-splitting reactions.[1,3,4,8–13]

In spite of works proving the possibility of exploitation of such catalytic processes,[3,8,10,11,13,14] little is known about the dominant chemical species present at the pyroelectric surfaces and reaction mechanisms acting in operando, closely related with ferroelectrics' polarization states. The main reason for this is that materials used as catalysts are usually in form of nano entities (e.g. particles, powders, rods, etc.) dispersed in a solution of interest, whereby pyroelectricity

rather than polarization direction play a main role, given that such nano-entities are surrounded in all directions by the liquid.[12,13,15] On the other hand, in so called external systems, where pyroelectric sheet is used as a thermal energy harvester, acting as a source of charge in electrochemical cells,[8,11] the efficiency is determined by measuring the levels of produced H_2 detected during/at the end of the repeated heat-cool cycles by gas chromatography.

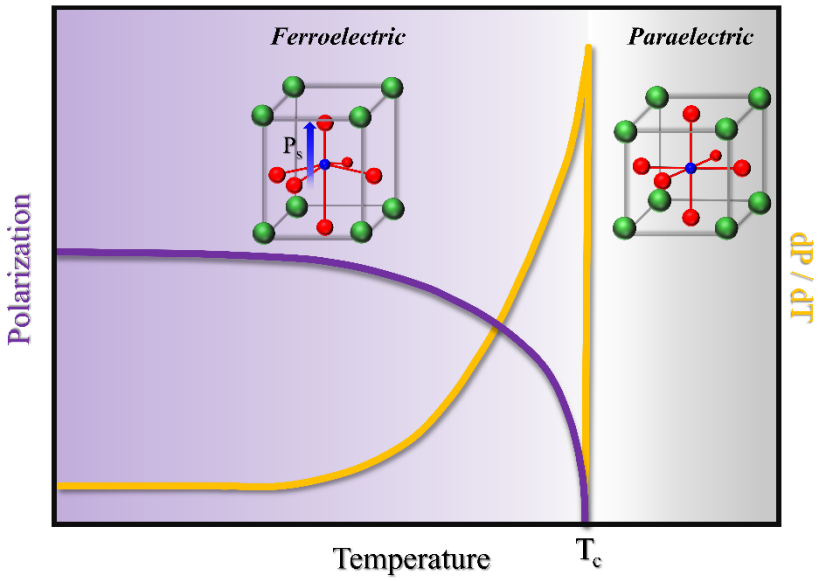

Figure 4.1 *Schematic representation of polarization and pyroelectric coefficient dependence on the temperature.*

Despite the lack of fundamental knowledge, these temperature-modulation processes have been successfully applied for disinfection or degradation of dyes and pollutants in water; in these cases, the reactions are proposed to be mediated by reactive radicals produced at the active surfaces interacting with the molecules in the solution.[1,16–19] Even though the use of nanoparticles provides increased active areas for catalysis due to maximized surface to volume ratios, the study of pyrocatalytical processes at ferroelectric thin films/single crystals with well-defined polarization state would enable to gain fundamental insight into the chemical species and main redox processes taking place.

Recent studies[10,20,21] also indicate that pyrocatalytic reactions driven across the Curie temperature of ferroelectric materials could generate higher yields due to the enhanced pyroelectric coefficient. Additionally, it has been theoretically predicted[9] that water splitting cycle is particularly efficient when the material is cycled between paraelectric and ferroelectric state. This is consistent with observation that the transition between ferroelectric and

paraelectric state changes adsorbate-ferroelectric interaction energies, enabling one to cyclically enhance the adsorptive or desorptive properties of the surface while driving reactions dictated by the most thermodynamically favorable surface state.[2,22]

However, only a few studies explore experimentally this avenue, and usually it is in combination with similar piezoelectrocatalytic effects.[20,21] Harvesting waste heat and converting it into the energy stored in the chemical bonds of molecules requires pyroelectric materials with sufficiently low T_c operating at temperature ranges close to the critical temperature.[10] $BaTiO_3$ single crystals show a T_c around 130 ºC, much lower than strained engineered thin films, and that makes them more convenient for emerging applications of pyrocatalytically-driven water splitting where fluctuations in temperature are used as a source of charge in redox reactions.

In this chapter, we delve into the surface chemistry and domain structure of $BaTiO_3$ single crystals upon pyrocatalytically-driven redox reactions in water vapor atmosphere across the ferroelectric Curie temperature. This goal is achieved by the combined use of singular operation modes of Ambient Pressure X-Ray Photoelectron Spectroscopy (AP-XPS) using synchrotron radiation, Piezoresponse Force Microscopy (PFM) and X-Ray Reciprocal Space Mapping (XR-RSM). Our as-received crystal was cut into three pieces, whereby each piece served as native crystal, used for the study of phase transition by NAP-XPS, X-Ray diffraction and PFM measurements in controlled humidity conditions. By tracking the surface chemical composition, crystallographic and domain structure evolution during the phase transition, the main redox reactions taking place and their entanglement with ferroelectric polarization was revealed. All together, we provide experimental evidence for the first time of *ferrocatalysis*, i.e., the ferroelectric activated water dissociation at the paraelectric to ferroelectric phase transition of, in this case, a $BaTiO_3$ single crystal. Additionally, the coexistence of surface chemical activity (i.e., redox reactions, ionic mobility and surface adsorption-desorption of molecules) and emergence of ferroelectric polarization below the T_c, was characterized as a function of time.

4.2 Evolution of $BaTiO_3$ (100) single crystal domain structures during the phase transition

In ferroelectric materials, the spontaneous polarization needs to be screened by the charges of the opposite sign to the bound polarization charge. During heating/cooling processes, where the polarization of ferroelectric material changes, the sign of the screening charges present in excess/lacking from on the surface (and therefore the available for redox reactions) depend on the polarization state of the ferroelectric material. Therefore, the correct determination of the polarization state of the material under study becomes crucial. Moreover, the final stable configuration of ferroelectric polarization upon a phase transition from the paraelectric state without an external applied electric field will be essentially determined by the surface chemical potential, minimization of depolarizing fields, as well as on ferroelectric and ferroelastic energies. In this sense, in some cases, the surface of ferroelectric and relaxor single crystals is observed to decouple from the bulk ferroelectric state and exhibit different domain structure and/or shifted Curie temperature of the surface "skin layer".[23,24]

Given that our heating/cooling cycles will be performed across the phase transition temperature and that both surface and bulk domain structure have an effect on the surface chemical composition, we first investigated the formation/extinction of the ferroelectric domains around the phase transition by X-Ray diffraction measurements in two geometries simultaneously. We combined grazing incidence and standard Bragg-Brentano X-ray diffraction measurements with penetration depths of < 100 nm (surface sensitive) and several microns (bulk sensitive), respectively. Given that both type of measurements needed to be performed on the native piece of BTO (100) crystal in one single round, they were performed at normal resolution (i.e. without monochromator), compatible with both geometries. All the measurements were performed in the Anton Paar DHS1100 Domed Hot stage, whereby synthetic air was continuously flushed, for which a base RH of the order of 2.5 % at room temperature is expected.

The evolution of bulk and surface sensitive x-ray reciprocal space maps is shown in **Figure 4.2 a,b**. The bulk sensitive Q_xQ_z reciprocal space maps around 303 reflection at 50 ºC show three main peaks present as doublets, stemming from $K\alpha_1$ and $K\alpha_2$ contribution of the non-monochromatic Cu source. The most and the least intense reflection have the same Q_x

coordinate consistent with the expected length of the *a*-axis parameter, while their low and high Q_z coordinates correspond to the *c* and *a* out-of-plane lattice parameters of the BTO tetragonal phase, respectively. Therefore, the highest intensity $330a_{\perp}$ reflection corresponds to the a_2 domains, while the lowest intensity $303c_{\perp}$ reflection stems from the *c* domains.

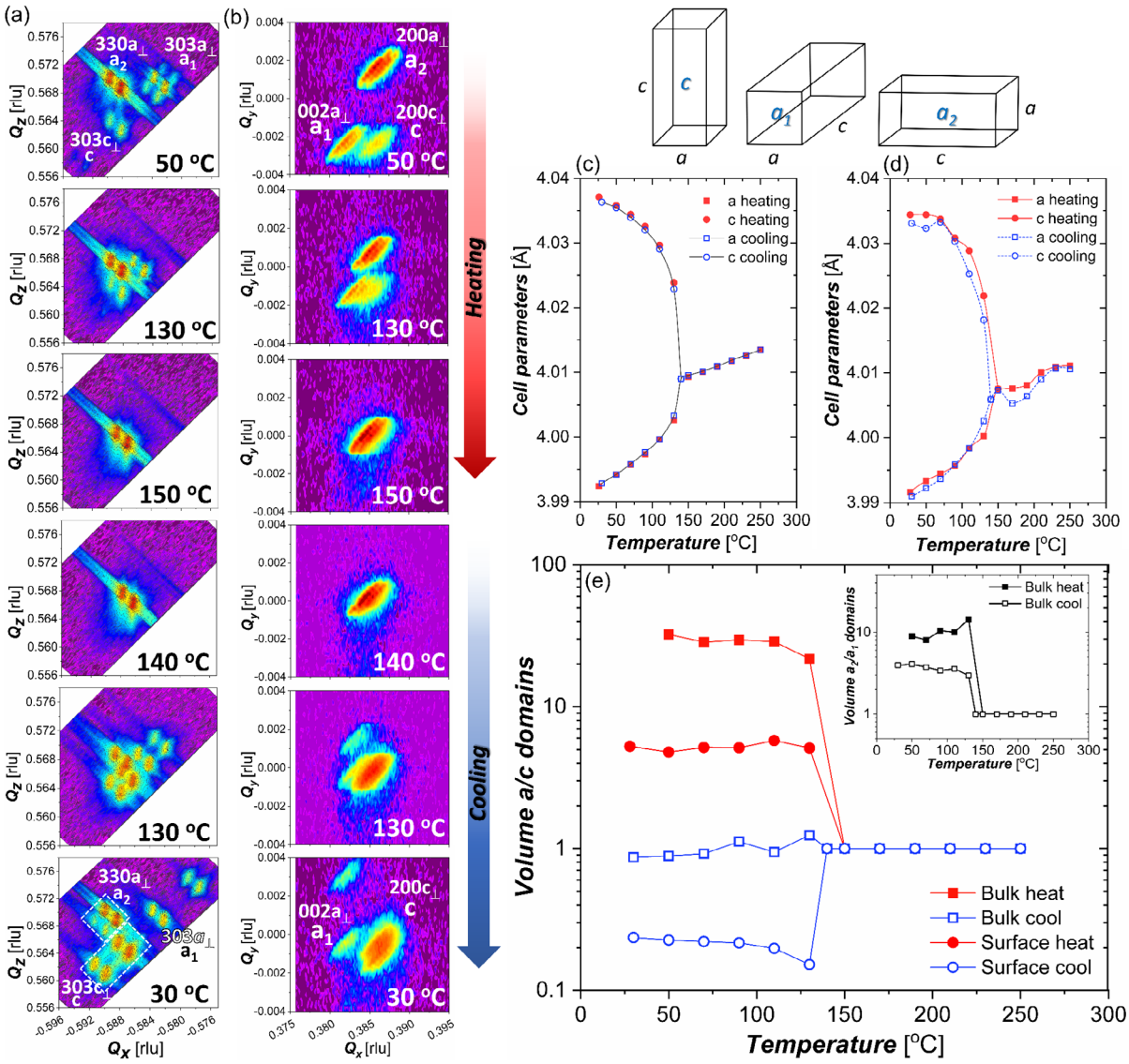

Figure 4.2 *X-Ray diffraction on the native BTO single crystal; Evolution of (a) X-Ray Q_xQ_z reciprocal space maps of the 303 region of the bulk crystal along with (b) surface sensitive grazing incidence in-plane Q_xQ_y maps around 200/002 reflection measured at different temperatures at Phi=90 deg during heating and cooling through the Curie temperature; Calculated a and c lattice parameters from (c) bulk 330 $a_{\perp}$ and 303 $c_{\perp}$ and (d) surface 002 $a_{\perp}$ and 200 $c_{\perp}$ reflections measured in whole range of temperatures, showing no difference between surface and bulk Curie temperature; e) Calculated a/c domain ratio as a function of temperature in bulk (squares) and at the surface (circles) in native state and after the first phase transition FE→PE→FE' cycle, showing difference between bulk and surface domain orientations.*

Finally, reflection $303a_\perp$ corresponds to the domains with the *c*-axis oriented in-plane (a_1 domains) orthogonal to a_2 domains. Low intensity peaks (also present as doublets) around a_1 domains, clearly observed in the cooling cycle, indicate some extent of domain tilt in the out-of-plane direction. Determination of cell parameters from Q_xQ_z coordinates at 50 ºC gives values of a = 3.992 Å and c = 4.037 Å, characteristic of the tetragonal phase. As the temperature is increased, the peaks get closer to each other as tetragonal splitting decreases and finally disappears at the Curie temperature, when the sample's crystallographic structure becomes cubic. Curie temperature lies between 130 ºC and 140 ºC as measured by our setup. RSM measurements performed up to 250 ºC (not shown here), do not show any substantial differences as compared to the RSM taken at 150 ºC. After cooling back to 30 ºC and restoration of ferroelectricity, the emerging domain structure becomes more complex and significantly different from the original state. It can be seen that although the same three types of domains (*c*, a_1, a_2) are present, the intensity of the peak related with *c* domains is higher as compared to the original state. Splitting of the peaks surrounding the main reflections (marked by dotted regions) indicate that some amount of these domains is present with a particular rotation in the bulk of the sample. Note that the secondary reflection present at lowest Q_x values might stem from the reflections coming from the edge of the sample or very tilted domains and therefore is not considered in further calculations.

Meanwhile, grazing incidence in-plane Q_xQ_y map (surface sensitive) around 200/002 reflection at 50 ºC (**Figure 4.2 b** top) also shows three main peaks. If we assume the same orientation of domains at the surface as in the bulk for the pristine crystal, the reflection $002a_\perp$ at low Q_x coordinate stems from the domains having *c*-axis oriented in-plane (a_1 domains), while the two reflections at high Q_x coordinate correspond to the domains with *a*-axis in plane, consistent with either a_2 or *c* domains. It can be seen that the reflection stemming from a_2 domains is the most intense, consistent with the bulk measurements. The fact that $200a_\perp$ and $200c_\perp$ reflections are at different Q_y value is an indication of a certain relative in-plane rotation of those domains. Changing the azimuthal ϕ angle by 90 degrees (i.e. rotating the sample around the stage normal), allows us to separate the contribution from *c* domains. The Q_xQ_y maps recorded around 200/002 reflection at ϕ=0 deg and at 50 ºC of the native crystal are shown in **Figure 4.3 a**. When the sample is rotated by 90 degrees, the main reflection belongs to a_2 domains, while the weaker reflection stems from either *c* or a_1 domains. Since the rotation of the sample doesn't affect position of *c* domains, it can be concluded that the lowest intensity $200c_\perp$ and highest intensity $200a_\perp$ reflections of the initial sample (i.e. non-rotated) belong to

c and a_2 domains, respectively. By heating the sample, we can see how also at the surface, the tetragonal splitting of surface domains disappears at temperatures between 130 ºC and 140 ºC, very similar to the observed bulk behavior. Cooling back to the ferroelectric state, shows again the presence of a_1 domains, albeit the observed splitting of the peaks along Q_y surrounding the main reflection indicates that some a_1 domains are also tilted with respect to their main orientation. On the other hand, the peak with the highest intensity might arise from the independent contribution of *c* and a_2 domains, or from their overlapped contribution. When compared with Q_xQ_y maps recorded at ϕ=0 deg and at 30 ºC after the first phase transition FE→PE→FE' cycle shown in **Figure 4.3 b**, a dominant contribution of *c* or a_1 domains and negligible contribution of a_2 domains is observed. Therefore, it can be assumed that the high intensity peak in question predominantly stems from a majority of *c* domains with a minor a_2 domains contribution.

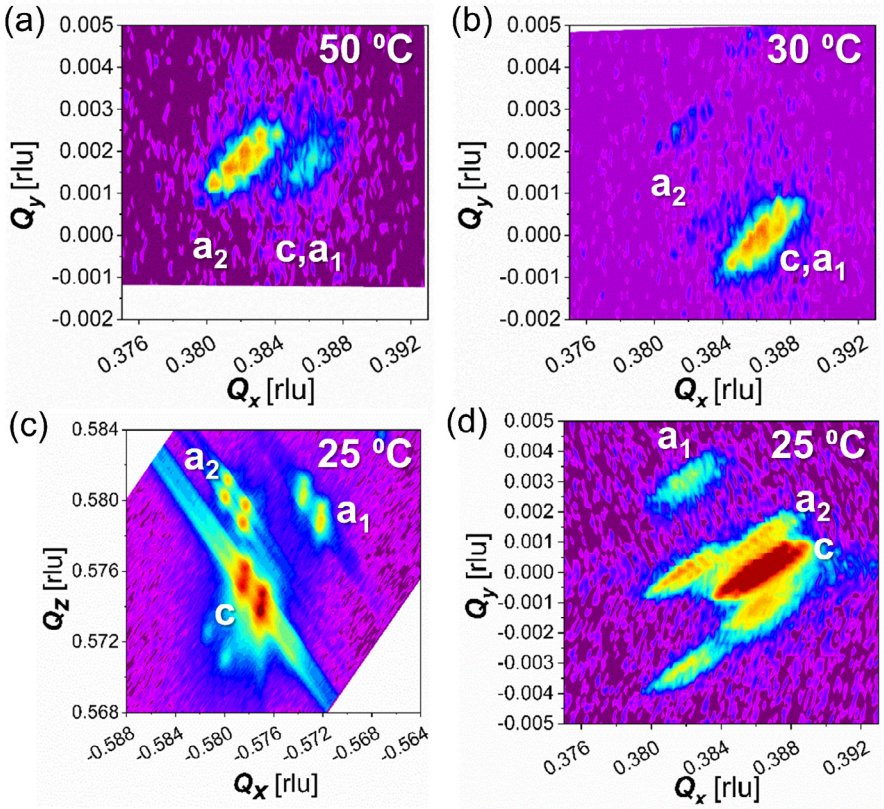

Figure 4.3 *Surface sensitive grazing incidence in-plane Q_xQ_y maps around 200/002 reflection recorded at ϕ=0 deg of (a) native BTO crystal at 50 ºC and (b) BTO crystal after its first phase transition FE→PE→FE' cycle at 30 ºC; (c) Q_xQ_z bulk sensitive RSM around 303 reflection and (d) Q_xQ_y surface sensitive RSM around 200/002 reflection, recorded at ϕ=90 deg of BTO crystal which passed several phase transitions (previously studied by AP-XPS).*

By extracting two angular positions of the observed main reflections in the measured temperature range, the evolution of *a* and *c* lattice parameters with the temperature for both bulk- and surface- sensitive measurements can be determined as it is shown in **Figure 4.2 c,d**, respectively. It can be seen that cell parameter values, as well as the transition temperature are almost identical in the bulk and at the surface. However, if we plot total *a*-to-*c* domain volume ratio (*a/c*) as shown in **Figure 4.2 e**, whereby contribution of each domain has been calculated as the integrated intensity of particular reflection from the bulk and surface RSM at each temperature, it can be seen that there is a substantial difference between bulk and surface domain orientations. Note that in this case, the volume of *a* domains corresponds to the sum of a_1 and a_2 domain contribution. The bulk pristine crystal behaves as expected: it shows *a/c* volume ratio ~ 30, with the majority of a_2 domains (see the inset), indicating mostly single in-plane orientation. Upon heating above the transition Curie temperature, the sample transforms into cubic structure, while after cooling down below the Curie temperature, a tetragonal structure is recovered with almost equivalent orientation of *a* and *c* domains (*a/c* volume ratio ~ 1). At the same time, a_2/a_1 volume ratio decreases from 10 (for the native crystal, indicating a majority of a_2 domains) to 4 (for transitioned crystal), showing that it maintains a certain prevalence of a_2 domains.

On the other hand, very different situation can be observed at the surface of the native crystal, where the observed domain orientation is already different than that of the bulk from the starting point. It can be seen that native surface *a/c* volume ratio is ~ 5, far lower than in the bulk, meaning that there is already a substantial concentration of *c* domains at the surface of the pristine crystal. After heating above T_c and cooling down again to the ferroelectric phase, the surface *a/c* volume decreases to 0.2, meaning that *c* domains are dominant at the surface after the first phase transition FE→PE→FE' cycle. These results indicate that the surface of the BTO crystals develops a "skin" with a significantly different domain arrangement as compared to the bulk which, while showing the same Curie temperature, is clearly composed predominantly by *c* domains even in a nominally (100) oriented BTO single crystal.

The results of surface sensitive diffraction measurements were further corroborated by PFM measurements in DART mode, performed under N_2 saturated atmosphere in an environmental control cell, for which the base RH is ~ 2.5% at room temperature. PFM is mainly sensitive to surface ferroelectric domains and therefore allows us to investigate the surface domain organization of our sample. Lateral (lPFM) and vertical (vPFM) imaging was performed in the

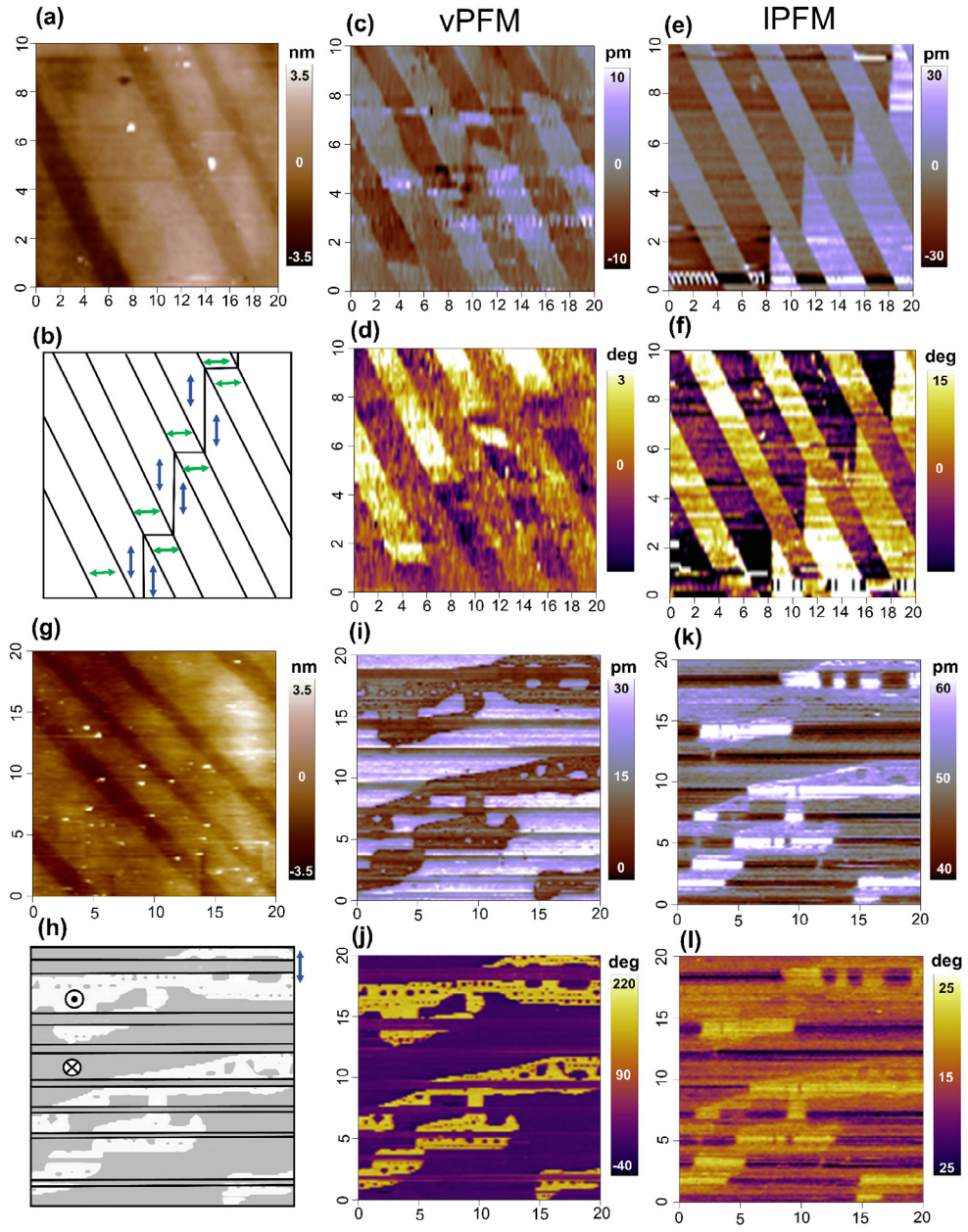

Figure 4.4 *Vertical and Lateral DART PFM imagining of the BTO single crystal;(a) AFM topography and (b) scheme of in-plane a_1/a_2 domain arrangement of native crystal, as determined from vPFM and lPFM amplitude (c, e) and phase (d, f) images, respectively; (g) AFM topography and (b) scheme of a/c domain orientation arising after the first phase transition FE→PE→FE' cycle, as determined from vPFM and lPFM amplitude (i, k) and phase (j,l) images. Green and blue arrows denote in-plane domain orientation parallel or perpendicular to the cantilever axis, respectively.*

different areas of the native and transitioned crystal and the representative results are shown in **Figure 4.4**. Figure **4.4 a** shows topography of the investigated region in the native crystal, together with PFM amplitude (**c**, **e**) and PFM phase (**d**, **f**) of vertical and lateral piezoresponse,

respectively. The scheme of the domain arrangement of the native crystal is shown in Figure **4.4 b**. Diagonal lines represent 90-degree domain walls between domains laying in the plane of the crystal (a_1/a_2 twins). It can be seen that in-plane domains lying perpendicular to the cantilever (blue) are giving lPFM piezoresponse to distinct bands, which also contain 180-degree domain wall separating regions of oppositely oriented in-plane domains. Complementary bands, which do not exhibit lPFM response, show very weak vPFM response. This response is related to the existence of in-plane domains oriented along the cantilever axis (green), which give artifactual small response in the out of plane signal due to the buckling effect. Panel **4.4 g** shows slightly broader topography region of the crystal after the first phase transition FE→PE→FE' cycle, together with PFM amplitude (**i**, **k**) and PFM phase (**j**, **l**) of vertical and lateral piezoresponse, respectively. We observe that, previously dominant in-plane a_1/a_2 domain orientation, converts into the *a*/c domain arrangement, in agreement with grazing incidence diffraction results. Complementary lPFM and vPFM piezoresponses show that almost whole investigated surface region exhibits out-of-plane domain arrangement (*c* domains), with some amount of in-plane *a* domains existing in horizontal bands. In addition, meandering 180-degree domain walls are created between regions with opposite out of plane polarization direction, observable as yellow patches on almost uniform purple background in vPFM phase images.

However, for the correct interpretation of XPS results, it is necessary to determine absolute polarization direction in this regions. **Figure 4.5 a,b,c** shows vPFM phase and amplitude image of one such region, together with corresponding contact potential difference (CPD) map acquired by Kelvin Probe Microscopy (KPFM), respectively. CPD image shows that regions with opposite out of plane polarization also exhibit different surface potential. In this case, surface potential of yellow patches (observed in PFM phase images) is for ≈ 100 mV more negative, compared to the purple background. This can be explained by the up-polarized state of yellow patches, whose positive bound polarization charge is effectively screened by negative charges, giving the opposite contrast in the CPD image.[25] In addition, we performed PFM off-resonance measurements in single frequency mode, which allowed us to ultimately distinguish between opposite polarization directions, as shown in **Figure 4.5 d**. Therefore, in our case the majority of the *c*-domains are pointing downwards, however they can also contain certain amount of up-polarized domains, which are visible as yellow patches at the vertical PFM images. Furthermore, up-polarized regions, show fine domain structure, composed of down-polarized bubble-like domains.

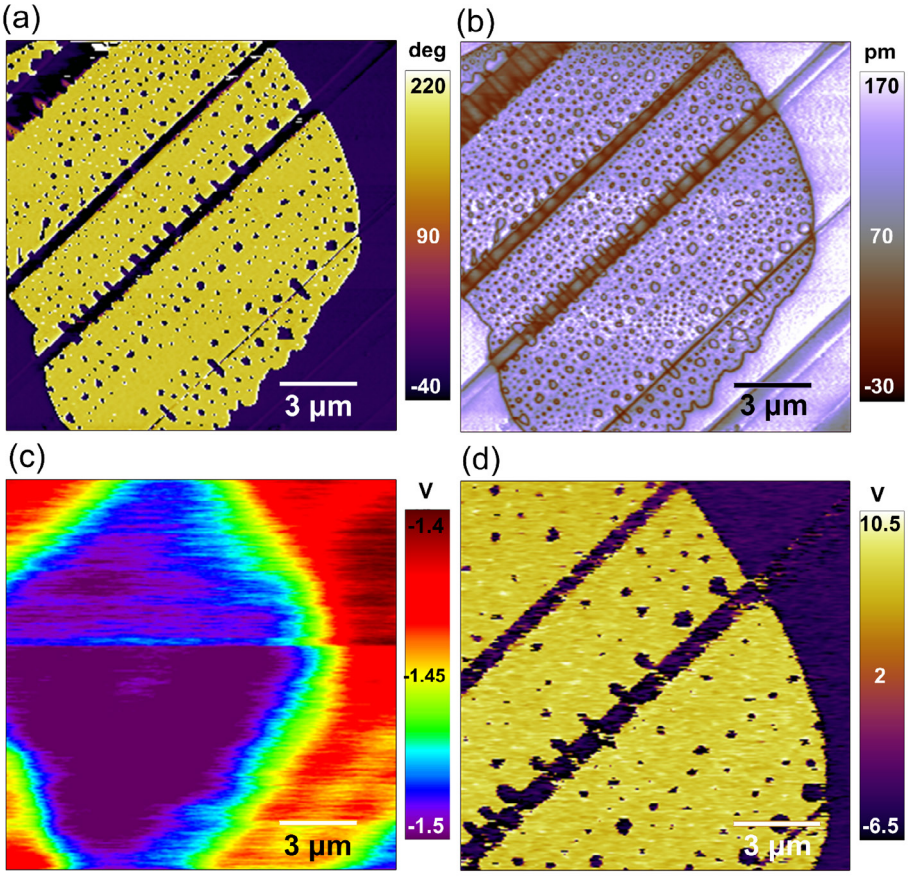

Figure 4.5 *(a) DART vPFM phase and (b) amplitude of the a/c domain region; (c) CPD map acquired by KPFM of the same region; (d) Single frequency PFM image of the magnified area, showing that yellow patches are up-polarized, compared to the predominantly down-polarized background.*

The observed prevalence of out of plane down-polarized *c* domains after the phase transition cycle (especially at the surface), can be related with previously observed (in Chapter 3) higher hydrophilicity of down-polarized $BaTiO_3$ surfaces of thin films. Since the relation between ferroelectricity and surface chemistry is bidirectional in nature, it seems that the presence of water on the surface at the phase transition preferentially stabilizes formation of downward oriented *c* domains. In this sense, we confirm the impact of the chemical surface composition on the metastability of the ferroelectric phase transition, since we can state that a paraelectric to ferroelectric phase transition in the presence of adsorbed water molecules leads to the nucleation and further stabilization of down polarization in $BaTiO_3$ single crystal.

Finally, we also performed diffraction measurements of the piece of BTO crystal which was subjected to a high number of phase transitions during synchrotron XPS measurements. RSM recorded around bulk 303 and surface 200/002 reflections at ϕ=90 deg are shown in **Figure 4.3 c,d**, respectively. It can be seen that these results closely resemble RSMs collected at 30 ºC

after the first FE→PE→FE' phase transition cycle shown in **Figure 4.2 a,b** (bottom), showing a predominance of *c* domains in the bulk and at the surface. This means that after several phase transition cycles, crystal keeps a similar domain structure to that obtained after the first phase transition cycle, characterized by the formation of a skin layer of predominantly out of plane down polarization. As it will be discussed, the preference for the down oriented polarization is crucial for the interpretation of the AP-XPS measurements due to the several reasons: i) screening charge and therefore possible pyrocatalyticaly driven redox reactions are expected to take place at the surfaces normal to the polarization direction and ii) the type of the surface redox reactions and charge involved therein is directly related with the polarization direction (i.e. up vs. down), giving that oppositely polarized surfaces will catalyze opposite electrochemical reactions. In our case, transition from paraelectric to ferroelectric state will be followed by the emergence of down-polarized *c* domains.

4.3 Surface charging/discharging dynamics during the phase transitions

In AP-XPS, measured kinetic energy of electrons emerging from a material is intrinsically sensitive to the electric stray fields present at the surface of ferroelectric materials, observed as an offset of the overall spectra and calculated apparent binding energies.[26] On the other hand, AP-XPS spectra at the O1s range measured with high resolution, such as those shown in Chapter 3, typically take up to several minutes to be recorded, so they can only track slow surface charging-discharging processes. Here, in order to track fast surface charging/discharging events on the order of seconds, we collect fast spectra with acquisition times of ~5 seconds at the O 1s edge that, although lacking enough energy resolution to identify the different components, provide clear insight in the energy shift arising from surface stray electric fields. With this operation methodology, we could track the surface-charging events by quantifying the displacement of the AP-XPS spectra at the O1s edge with respect to the measurements obtained at the charge-neutral surfaces in equilibrium.

First we used fast-acquired AP-XPS spectra to study the phase transitions between ferroelectric and paraelectric state in both directions, by recording O 1s spectra as temperature was varied between 102 ºC and 110 ºC at a constant changing rate of 1 ºC/min under 0.5 mbar of water pressure (which corresponds to a value of RH ~ 2 % at room temperature). Here we worked at

low X-Ray incident energy to enhance surface sensitivity, with expected kinetic energies of emerging electrons in the range of ~ 140 eV. The evolution of photoelectrons kinetic energies in the O 1s spectra as a function of temperature and elapsed time is shown in **Figure 4.6**. Red circles show evolution of kinetic energy during the ferroelectric-to-paraelectric phase transition (FE-PE, heating), while the blue squares show the evolution during the opposite event, i.e. paraelectric-to-ferroelectric phase transition (PE-FE, cooling). It can be seen that in the case of FE-PE phase transition, the kinetic energy first steeply shifts about 35 eV towards lower values and then it shifts back close to the initial point. In the case of PE-FE phase transition, the opposite happens: kinetic energy first quickly increases for about 7.5 eV and then it decreases more slowly towards the near initial value. Two characteristic features in the **Figure 4.6** can be observed: i) the charging/discharging dynamics is asymmetric around the phase transition, depending on whether ferroelectric polarization vanishes or emerges and ii) the absolute measured values of charging and discharging (and therefore changes in the kinetic energy) are quantitatively different.

It is not a rare observation that kinetic and calculated apparent binding energies of elements in the measured sample sometimes diverge from their expected energy. In some cases, this can be related to chemical shifts associated with atoms changing their valence state, or existing in the electronic environments different from the native one. These shifts are typically much lower than the ones observed in **Figure 4.6**. However, if all the elements in the spectra shift by a similar amount, then the main cause might be an overall charging of the sample surface.[27] The presence of positive or negative surface charge affects the electric field through which photoelectrons travel, rendering their measured kinetic energies lower or higher, respectively. Since the measured kinetic energies of photoelectrons are used to calculate the binding energies from known values of X-Ray incident energy, this turns into an apparent change of the calculated binding energies, which then includes the stray electric field offsets. This is of particular importance when one performs temperature dependent measurements on ferroelectric materials, which are also pyroelectric, i.e. they change the magnitude of their spontaneous polarization - and therefore surface charge - in response to the change of temperature before an equilibrium is reached. In order to better understand the charge dynamics around the T_c, it is more useful to plot the change of the kinetic energy $\Delta K.E.$ as a function of temperature for the heating and cooling cycles as shown in **Figure 4.7 a.**

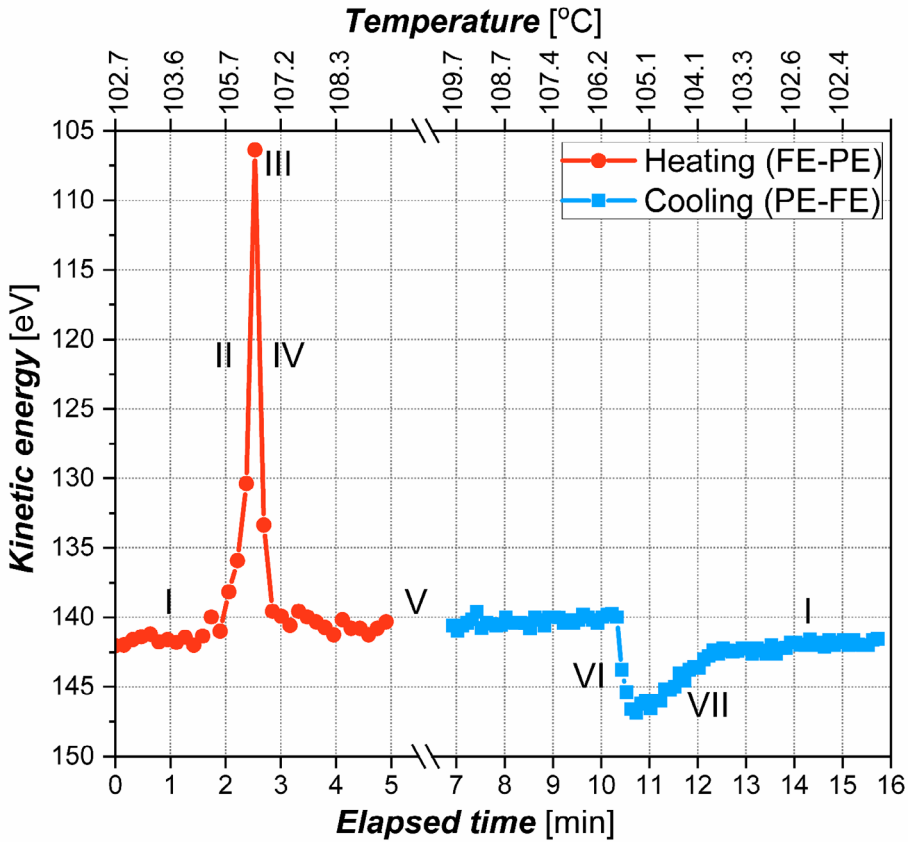

Figure 4.6 *Evolution of photoelectrons kinetic energy in O 1s spectra as a function of temperature and elapsed time during the ferroelectric-to-paraelectric (red circles, heating) and paraelectric-to-ferroelectric (blue squares, cooling) phase transition in 0.5 mbar of H_2O.*

It can be seen that while charging effects are observed below and above the transition temperature during the FE-PE phase transition, they are only present below the T_c during the cooling and associated PE-FE phase transition. If we now analyze in more detail the different stages of the process happening during the heating and cooling process as marked by numbers in **Figure 4.6** and **4.7 a**, their interpretation can be represented schematically as shown **Figure 4.7 b**. Starting from an *c/a* domain distribution with predominantly downwards oriented *c* domains, at constant temperature negative bound polarization charge needs to be screened by the same amount of the charges of the opposite sign, leading to an overall neutral impact on surface electric stray fields (I). We note that this screening charge might have internal (i.e. holes accumulated due to the band bending) or external (adsorbate species) origin. However, when temperature is increased closer to the critical point T_c, dipole moments are getting disordered and the net spontaneous polarization of the sample is decreasing, leaving the surface unbalanced with the excess of positive charge. Indeed, this is the region where the material shows the highest pyroelectric coefficient as shown in **Figure 4.1**, meaning that any small

change of temperature leads to a high degree of ferroelectric polarization change. Thus, in region II, the ejected photoelectrons are being attracted towards the electropositive surface and arrive to the detector with progressively lower kinetic (and therefore apparent higher binding) energy. During this stage - and depending on the screening mechanism in action - some of the positive screening charge now in excess will also dissipate/desorb from the surface, which is depicted by the black arrows in **Figure 4.7 b**. As the temperature further increases to the Curie point (III), the ferroelectric polarization completely disappears and the kinetic energy spikes towards lower kinetic energies. Finally, once in the paraelectric phase shown as region IV, screening charges are not needed anymore and are therefore they are released from the surface rapidly, causing a fast relaxation of the measured kinetic energies. Further increase of temperature doesn't cause almost any change of the binding energy, once the paraelectric phase is stabilized, as depicted by region V.

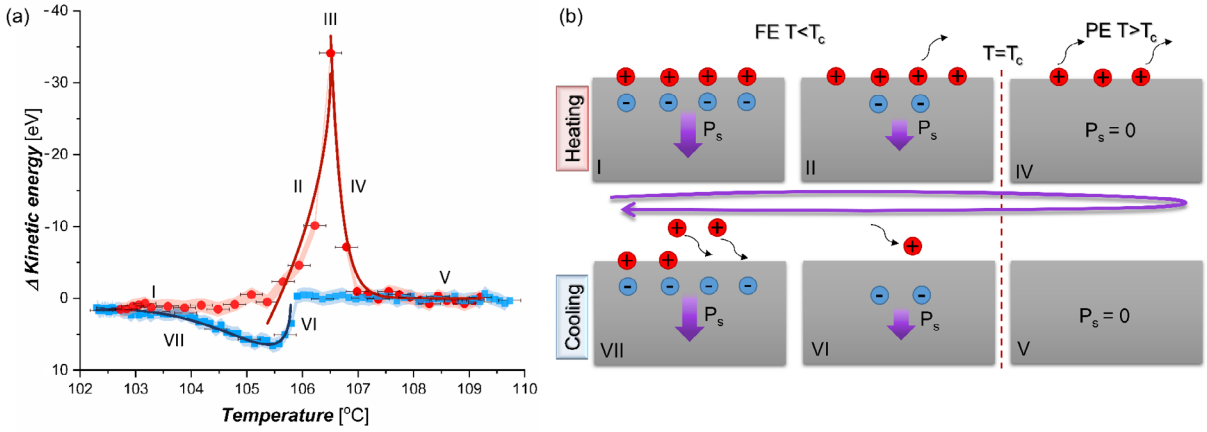

Figure 4.7 *(a) Change of photoelectrons kinetic energy Δ K.E. as a function of temperature for heating and cooling cycle. Red, gray and blue lines are fitting functions defined by equations (2)-(4) describing change of total surface charge (and therefore kinetic energy) during polarization decrease in ferroelectric phase, its disappearance above transition temperature T_c and subsequent recovery as sample is cooled down, whereby it becomes ferroelectric again bellow the T_c, respectively. Main processes involving bound polarization (blue) and screening charge (red) during the phase transitions, marked by numbers I-VII in both panels as well as in* ***Figure 4.6****, are schematically depicted in (b). Excess/lack of positive screening charge at the phase transition during the heating/cooling process causes charging of the sample and change of the photoelectron kinetic energies.*

If the sample is cooled down from the paraelectric phase (region V), nothing happens above the Curie temperature, but once the ferroelectric polarization is triggered by the phase transition at T_c, a sudden formation of negative bound polarization charges below T_c, which are almost entirely uncompensated, increases the kinetic energy of photoelectrons in the region VI. It can

be seen that further decrease of temperature, progressively compensates the surface charging effects as observed in region VII, which slowly approaches its starting value (as for the region I). The dynamics of this regime is probably the most complex, since the charging function reflects how the rhythm of ferroelectric bound charge generation dictated by the pyroelectric coefficient is progressively compensated by the activation of screening mechanisms.

A closer inspection shows that the kinetic energies of O 1s are about ~ 1.2 eV lower in the paraelectric phase as compared to the ferroelectric state, which may reflect different core level energies in these two phases. In the case of down-polarized ferroelectric surface, externally screened by positive charge, a band bending in the near surface region would cause an increase of its core binding energies (and decrease of corresponding kinetic energies), as compared to the paraelectric sample,[26] which is the opposite of what is observed from our XPS measurements. On the other side, we observed that beside O 1s spectrum, Ti 2p and Ba 3d spectra suffer by similar shifts towards higher binding energy in paraelectric state by 1.3 ± 0.2 eV, possibly suggesting different charging between these two phases as the origin of observed effect. It should be noted that by repeating heating/cooling cycles several times sequentially, we observe that in all the cases both transitions show asymmetric kinetic behaviors, with almost the same values of kinetic energy shifts. Finally, we note that observed values of T_c might be lower due to a certain temperature gradient between the crystal and the position of the thermocouple.

4.3.1 Charging dynamics around the phase transition

In order to perform a quantitative analysis of the charging dynamics around the phase transition, we can assume the change of the photoelectrons' kinetic energy is directly proportional to the sign and total amount of surface charges at constant temperature [$\Delta K.E.\ (T) \sim Q\ (T)$].[28] Thus, it is of interest to express net surface-charge as a function of temperature, and relate it to the observed kinetic energy peak-shifts as a function of temperature.

The total surface charge Q can be described by the sum of bound polarization charge Q_b and screening charge Q_s. The change of the bound charge (i.e. polarization) with temperature can be obtained from Landau-Ginzburg-Devonshire (LGD) theory.[29] In this regard, although the phase transition in $BaTiO_3$ single crystals is of the first order, it is very close to being the second order, which enabled to simplify the dependence of polarization as a function of temperature by expression derived for the second order phase transition. In the case of heating process for

T < T_c surface charge is approximated by a constant A. Therefore, the change of the surface charge during the heating can be expressed as:

$$Q\ (T) = \ A - k\sqrt{Tc - T} \qquad (2)$$

where k is the coefficient which includes Curie Weiss constant, permittivity of vacuum and Landau coefficient b, while T_c is the Curie temperature. In general, k might also depend on A (i.e. on the screening charge), however in this case we will assume k to be constant. The minus sign between the terms comes from the fact that (experimentally) our sample is down-polarized and therefore the bound charge at the top surface is negative.

The fit of the heating branch for T < T_c by equation *(2)* is depicted by the red line in region II of **Figure 4.7 a**. The reasonably good fit of the proposed function to the data suggests that screening charge has high affinity towards the ferroelectric, and stays at the surface nearly constant (though in an excess A), all the way up to the phase transition, even as the ferroelectric polarization decreases. However, once the sample becomes paraelectric, it can be expected that the affinity of screening charges towards the surface drastically decreases, thereby causing their quick dissipation/desorption from the surface, followed by the photoelectrons' kinetic relaxation in region IV. We describe this process for T > T_c by a function which is exponentially decreasing from the peak excess charge A:

$$Q = Ae^{B_1(Tc-T)} \qquad (3)$$

where $B_1 > 0$ is the exponential factor. The fit of the heating branch for T>T_c by equation (3) is depicted by a dark gray line in **Figure 4.7 a**.

The cooling process for T < T_c of regions VI-VII, cannot be modeled by one single equation, but rather by the combination of two functions, describing two coexisting processes: i) pyroelectricity, which conversely to the heating process, depicts the appearance of mainly negative bound polarization charge associated to the emergence of downwards-oriented polarization state as temperature is decreased under the T_c, described by the first term of Eq. (4) and ii) surface chemical reactivity, describing subsequent charge accumulation/adsorption of surface molecules and ions which tend to compensate the ferroelectric stray fields and bring it back to a fully screened equilibrium state, depicted by the second term of Eq. (4):

$$Q = -k\sqrt{T_c - T} + A\left(1 - e^{B_2(T_c - T)}\right) \qquad (4)$$

whereby $B_2 < 0$ is the exponential factor. The corresponding fit of the equation *(4)* is depicted by a blue line in **Figure 4.7 a**. In this case, the adsorption function takes the value 0 at the Curie temperature $T = T_c$, and it approaches its horizontal asymptote A for the values $T < T_c$. Also, the shape of our adsorption function is symmetric to the desorption function (3) used in region IV. During the cooling bellow the T_c, the coexistence of the two processes (pyroelectricity and surface-chemical reactivity) happening in this range, leads to an overall smoother function of charging dynamics for the PE-FE phase transition with a local minimum of the curve at temperature T_{min}, bellow which the adsorption process dominates the behavior of the kinetic energy shift. This means that, bellow the T_c and transition to the ferroelectric phase, the screening mechanisms respond quickly to the emergence of bound polarization charge and therefore do not allow strong surface charging, contrary to observed FE-PE phase transition on heating. In this regard both observed behaviors, i.e. difficulty to remove and an ease of binding of charged species, points out to the high affinity of surface charged species towards the ferroelectric surface: in the case of heating, their high affinity towards the surface causes high divergence of photoelectrons' kinetic energy, contrary to the cooling, where their high affinity relaxes kinetic energy effectively, leading to the observed asymmetric dynamic behavior.

On the other hand, fast desorption process (3) in paraelectric phase suggests that it is easier to get rid of screening species from paraelectric surface than to attract/adsorb them onto ferroelectric surface. This is because, while releasing screening species is dominated by desorption processes, the creation of surface charged species might be followed by water adsorption and further dissociation, as well as pyrocatalytically-driven surface electrochemical reactions expected to take place around phase transition, which are likely to strongly influence the evolution rate of the surface discharging. In the following section we will put some light on these processes by identifying and quantifying the concentration of oxygen-containing species during the phase transition, and describing the possible associated chemical reactions.

Finally, it is also necessary to underscore that the overall screening dynamics is observed to have a characteristic time window of several hundreds of seconds around the phase transition: so, while pyroelectric and ferroelectric phase-transition dynamics can be taken as nearly instantaneous from a structural point of view, the overall approach to an electrostatic equilibrium state is not.

4.4 Surface chemical composition across paraelectric to ferroelectric phase transition

In order to study evolution of surface chemical composition, we recorded high resolution spectra at O 1s edge during the PE-FE phase transition in a 0.5 mbar of water vapor, while the temperature was decreased between 120 ºC and 95 ºC at the rate of ~ 0.3 ºC/min. Overlaid O 1s spectra are shown in **Figure 4.8**, whereby different colors denote distinct temperatures at which O 1s spectra were collected. The background of the spectra has been subtracted and the spectra has been normalized to the size of the bulk oxide peak (corresponding to the peak at the lowest binding energy) in order to take into account the loss of intensity due to the electron inelastic scattering when travelling through the adsorbates layer. Finally, spectra have been offset along y axis for clarity. Similar to the previous case, we could also observe a shift of the kinetic (and therefore binding) energies during the temperature ramps due to the surface charging effects, although since the characteristic time scale of these measurements is already on the order of several minutes, the observed shifts applied to only one or two spectra around the phase transition according to the description in the previous sections. For the sake of comparison, the binding energy of oxide bulk peak have been fixed to a single value and the absolute numbers at the x axis have been omitted.

Fitting of the spectra has been performed following the same model employed for the BTO thin film sample, explained previously in the Chapter 3, also described in previously published papers.[30,31] The components of the spectra measured at 120 ºC are shown in **Figure 4.8**. In this case, taking into account that experiment was performed in near ambient pressure conditions, in the presence of water vapor and not in the ultra-high vacuum (as it was the case for the BTO thin films), a peak stemming from water in the gas phase at ΔB.E. = (5.45 ± 0.1 eV) from the oxide peak (pink Gaussian) is visible at the highest binding energies. Also, the peak coming from the adsorbed water (dark blue Gaussian) becomes more pronounced under these conditions.

At the first glance, already from the evolution of the overall spectral shape with temperature it can be seen that the concentration of oxygen-related species is changing. Beside other species, it can be seen that the concentration of OH groups and surface peroxide species (purple and

green Gaussians) increase as temperature is decreased. In order to quantify the concentration of all the species we employed a multilayer electron attenuation model,[32,33] which considers each specie as a slab in a multilayer configuration, whereby its peak intensity is characterized by its oxygen atomic density (N), photoionization cross-section (σ), thickness (t) and inelastic mean free path (λ). Details of the employed model can be found in Chapter 2.

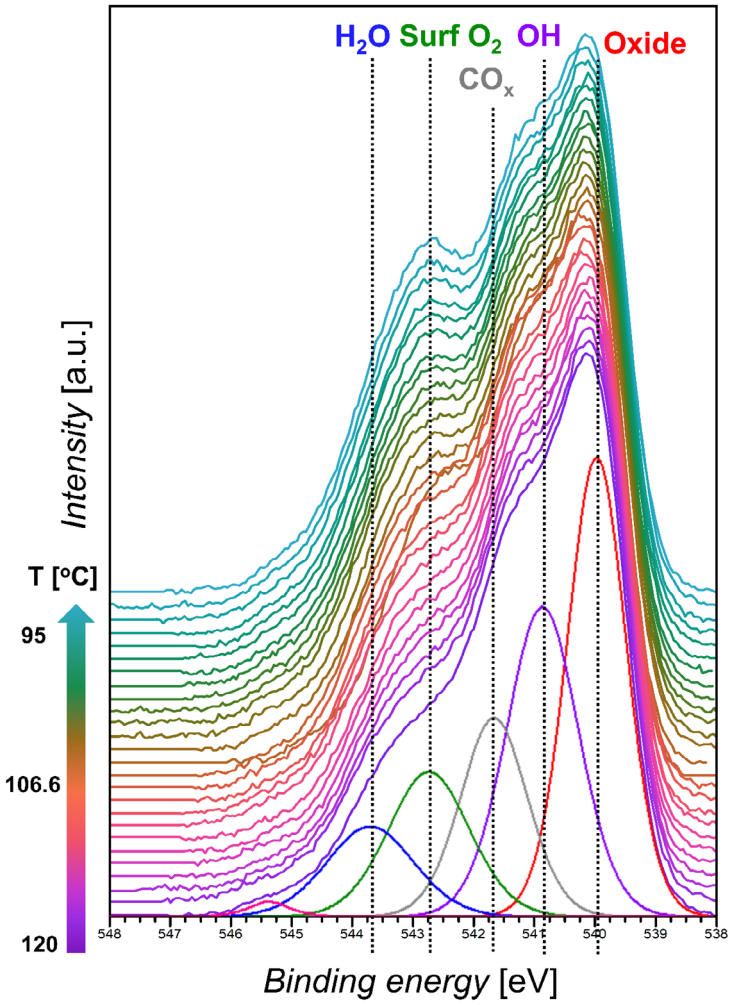

Figure 4.8 *Overlaid and along y-axis offset O 1s spectra recorded at different temperatures and in 0.5 mbar of H_2O vapor pressure at the paraelectric-to-ferroelectric phase transition. Fitting components are shown only for the spectra recorded at highest temperature and involve the same chemical species present at the surface of $BaTiO_3$ thin films discussed previously in Chapter III. The distance between two neighboring ticks on the x axis is 0.25 eV.*

However, in order to correctly express intensities of measured species accounting for the attenuation by the overlaying species, it is necessary to determine the order of the species present in the slabs. Chemical composition at different probing depths can be obtained by changing the incident energy of the photons. **Figure 4.9 a** shows two spectra taken at incident photon energies of 700 and 1000 eV, normalized to the intensity of the bulk oxide peak

(assuming that the oxide contribution should not be depth-dependent and therefore equal for both of them). It can be seen that the concentration of surface O 1s species is increased in the case of the spectrum taken at 700 eV, suggesting that all the adsorbed species are present only at the surface. In order to qualitatively determine the ordering of surface species along the axis normal to the sample surface, we plot the ratios $Y_{j,E}$ of each adsorbates' peak intensity (at given energy E) denoted as $I_{j,E}$, to the average intensity value of that peak obtained at both energies[30]:

$$Y_{j,700} = \frac{2 \cdot I_{j,700}}{(I_{j,700} + I_{j,1000})} \qquad (5)$$

$$Y_{j,1000} = \frac{2 \cdot I_{j,1000}}{(I_{j,700} + I_{j,1000})} \qquad (6)$$

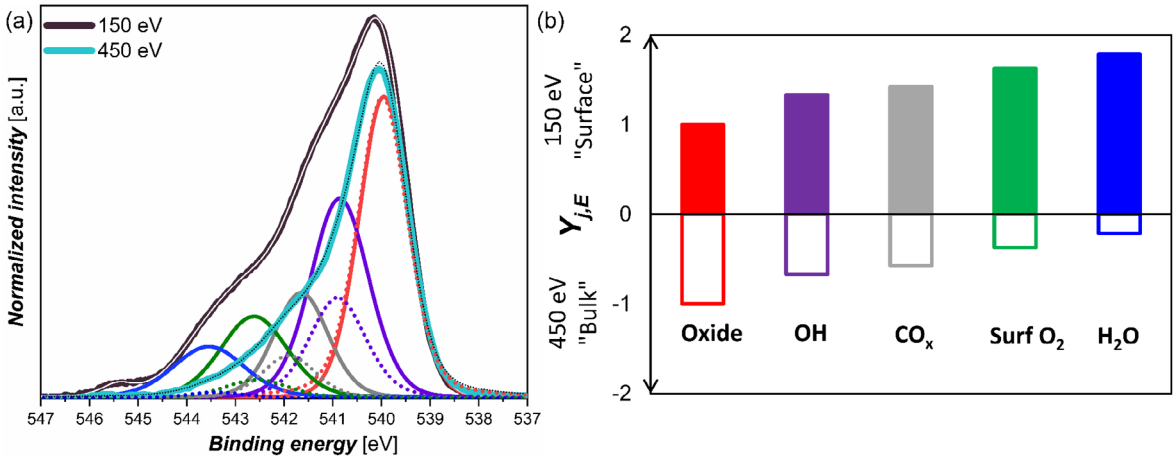

Figure 4.9.*(a) Overlaid O 1s spectra at 0.5 mbar of H_2O vapor recorded at two different photon incident and therefore photoelectrons' kinetic energies of 450 eV (cyan line) and 150 eV (black line), originating from more "bulk"-like and "surface"-like regions, respectively. Components of the "surface" and "bulk" O 1s spectrum and depicted by full and dotted lines, respectively. (b) Depth profile of surface adsorbed species.*

In this way, the calculated ratio for a single specie at constant incident photon energy represents the partial signal contribution of that specie to the total averaged signal obtained at both incident energies. The ratios for all the adsorbate species at incident energies of 700 eV and 1000 eV are graphically depicted by bars in **Figure 4.9 b** and represent the proxy for the depth profile of the out-coming electrons. Filled bars correspond to the partial contribution of each specie to the total averaged signal measured at 700 eV, while empty bars correspond to the partial contribution of the same specie measured at 1000 eV. For the species with higher full bars (i.e. higher partial contributions to the averaged signal measured at 700 eV), detected

electrons should originate closer from the external surface, rendering that specie more superficial. In this particular case, we can suppose that hydroxyl groups are the species closest to the oxide interface. This seems reasonable since terminal OH groups are expected to attach to metallic ions, while bridging OH groups consist of H atom bound directly to the lattice oxygen. CO_x and Surf O_2^- are considered as different layers that can be found at the same distance from the oxide interface. This can be because they are adsorbed above the first OH layer, or they have higher thickness, which is more probable since Surf O_2 and CO_x species need to interact with surface metallic ions. The formulas and quantification parameters used for the calculation of each adsorbates' thickness can be found in the Chapter 2. These can be further expressed in terms of surface coverage, corresponding the certain number of monolayers (ML) of each specie by considering the monolayer thicknesses of each specie.

The calculated normalized number of monolayers Δj [ML] of each specie containing oxygen as a function of time and temperature is shown in **Figure 4.10**. Since the starting number of ML for every component can slightly vary for consecutive (i.e. repeated) phase transitions, here we account only for the relative change of adsorbates thickness with respect to the starting point, and thus positive and negative Δ values indicate increase or decrease from the initial coverage value, respectively. Additional top x-axis shows the temperature for every data point of the phase transition. It can been seen that all the curves plotted in **Figure 4.10 a,b,c,d** consist of three characteristic regions corresponding to the following (range of) temperatures: i) 120 ^{o}C $\geq$ T < 108 ^{o}C which describes evolution of species before phase transition during which BTO is in paraelectric phase, ii) T = $T_c \approx$ 108 ^{o}C at which PE-FE phase transition happens and iii) 108 ^{o}C < T < T $\leq$ 95 ^{o}C, whereby BTO remains ferroelectric. In order to understand the observed trends, we have to consider the three main processes happening at the same time, therefore affecting the surface chemical composition: i) pyrocatalytically-driven surface chemical reactions, ii) molecular adsorption dynamics led by the increment of the RH locally near the sample surface as it cools down and associated chemical reactions driven by the surface active sites and iii) molecular adsorption dynamics led by the total time of exposure to water atmosphere (with characteristic times that can reach the order of tens of minutes).

In the paraelectric region, the concentration of OH groups, molecular H_2O and Surf O_2 species uniformly increases, while CO_x species are slightly diminished. Since in the paraelectric phase the crystal is non-pyroelectric, the observed effect stems from the local increment of RH as temperature is decreased at constant atmospheric water pressure, as well as redox reactions

facilitated by Ti active sites; here, the adsorption of water is followed by its dissociation on OH groups, whereby some of them can be further oxidized into Ti-peroxo ($Ti\text{-}O_2^{2}$) or Ti-superoxo ($Ti\text{-}O_2^{-}$) species, giving the rise to the Surf O_2^- peak.

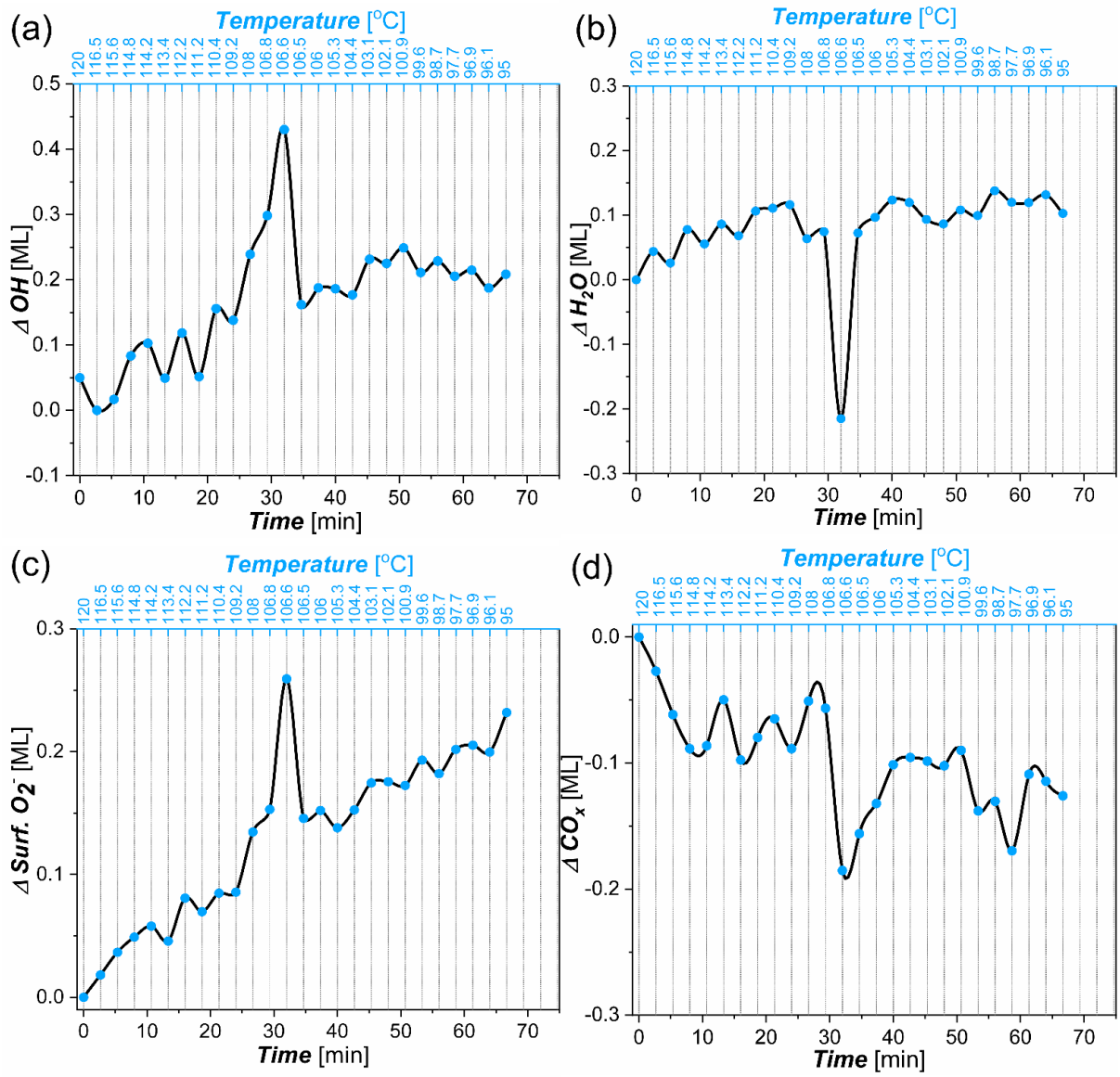

Figure 4.10 *Normalized number of monolayers Δ_j [ML] of (a) OH groups, (b) molecular H_2O, (c) Surface O_2^- species and (d) Carbon-related CO_x species as a function of time and temperature during the paraelectric-to-ferroelectric phase transition in 0.5 mbar of H_2O vapor.*

Bellow the critical Curie temperature at which the transition to the ferroelectric state happens, a sudden change of the concentration of all the species is observed. Note that the characteristic measurement time of each high resolution spectra is about 2 minutes, so in the best case scenario only one or two points can be acquired in the regions VI and VII after the PE-FE phase transition described in the previous section, lasting approximately only 3 minutes. At this point,

H_2O content at the surface decreases abruptly, while at the same time a concentration of OH groups increases. Simultaneous decrease of molecular water and an increase of hydroxyl groups demonstrates that there is a direct correlation between the emergence of ferroelectric polarization and the triggering of the water dissociation reactions on the ferroelectric surface, being the first direct evidence of *ferrocatalytically*-enhanced water dissociation obtained up to now to the best of our knowledge. Additionally, the sudden increase of surface peroxo species at the phase transition might be a consequence of strong surface hydroxylation, whereby bridging and terminal OH group are forming surface Ti-peroxo species. As demonstrated in the Chapter 3, this reaction might be particularly favorable on down-polarized surfaces, observed to emerge after the PE-FE phase transition also in this case.

The observed abrupt changes at the phase transition can be explained if we take into account that the amount of the unbalanced surface charge is directly proportional to the magnitude of the temperature change and the pyroelectric coefficient. At the PE-FE phase transition, whereby material suddenly becomes ferroelectric, change of the polarization with temperature at the constant rate is achieving the maximum value and surface becomes temporary charged, as observed from sudden shifting of kinetic energies in the **Figure 4.7 a**. Such charge-unbalanced surface is in the urgent need of screening and therefore strongest ferrocatalytic effect can be expected.

During the further cooling, polarization continues to increase and ferroelectric needs to continuously supply the charges to the surface in order to achieve charge neutrality. It can be seen that after the initial strong change of concentration close to the T_c, the adsorption of molecular H_2O and OH groups slows down and the thickness of molecular water reaches a plateau, albeit an increase of exposure time and RH should lead to an enhancement of the molecular water thickness. Thus, in this region, water concentration might be affected by the simultaneous processes of water adsorption and water dissociation happening at similarly (slow) rates, resulting finally in the net slower evolution. Similarly, in the case of OH groups, production of Ti-peroxo species, observed as continuous increase of Surf O_2^- peak, could hinder the OH evolution rate. On the other hand, albeit an increase of the carbon-related species in progressively more humid environment conditions has been typically observed during AP-XPS measurements, our results show an overall decrease of carbon-related species, which to some extent could also be related with screening activity of $BaTiO_3$ surfaces. However, in order to

be able to propose possible reactions paths for carbon-related species, detailed temperature dependent measurements on C 1s edge are needed, which is currently out of scope of this work.

Additionally, it is of interest to compare time scales during which enhanced catalytic activity can be observed. By comparing time scale of peaks observed in concentration profiles of species in **Figure 4.10**, with those of enhanced surface charging activity during PE-FE phase transition in **Figure 4.6**, it can be observed that they are of the same order of approximately 3 minutes. This supports our conclusions that relaxation of kinetic energies towards the equilibrium is caused by the adsorption and consecutive dissociation of water molecules, which tend to screen the emerging polarization. From the experimental point out few, established relaxation times directly determine the minimum rate at which repetitive thermal cycling between paraelectric and ferroelectric state can be performed in order to achieve maximum catalytic performance, with the minimum of input (thermal) energy cost.

Nevertheless, it should be pointed out that the reactions happening at ferroelectric surfaces in the investigated conditions and the observed trends are most likely the superposition of i) electrochemical reactions happening due to the interaction of adsorbed molecules and pyroelectric charge and ii) the activity of different surface sites (i.e. Ti atoms) for particular reactions. Additionally, effects of surrounding atmosphere and relative humidity, which varies in the investigated temperature range, should also be taken into account. This complex interplay, might cause competition between different processes (i.e. water molecular adsorption in increasing RH and its dissociation needed for efficient screening) or reversely, their cooperation (i.e. enhanced water dissociation on Ti- and possible vacancy-sites due to the screening of emerging polarization), altogether affecting the concentration evolution of adsorbed water and OH groups. However, hereby we showed that some of mentioned processes are clearly enhanced in extreme conditions, such as at the phase transition, whereby dissociation reactions are favored over the molecular water adsorption.

4.4.1 Implications of pyrocatalytic reactions in water splitting

Finally, we are going to discuss about other reactions beyond water dissociation which could lead to a similar chemical composition as a function of temperature. At negatively polarized surfaces in cooling conditions, the emerging negative bound polarization charge seeks to be screened by the charge of the opposite sign. The stable positive screening conditions of the ferroelectric surface could be achieved by giving away any free negative charges, which could

be further used in the redox reactions involving surface adsorbate species.[4] For instance, surface adsorbed water could accept such electrons, which would cause formation and adsorption of H_{ads} at the surface in alkaline or neutral media.[34] Besides binding to the metal, in our case it can be expected that part of produced H_{ads} will also bind to lattice oxygen. In such case, one should expect a sudden decrease of water molecules, while the binding of H atoms to the surface bridging oxygen atoms would results in the fast increment of -OH groups at the phase transition, in agreement with the observed trends of -OH and H_2O species in **Figure 4.10 a,b** at the phase transition. Indeed, it has been theoretically predicted that 1 ML of hydrogen atoms has been found as thermodynamically most stable state of down-polarized PTO surfaces.[9] Further paths of H_{ads} would depend on the thermodynamically most stable surface state and on the barriers for distinct chemical reactions, overall dictated by the polarization.

For instance, hydrogen molecules could be further produced following hydrogen evolution reactions (HER) either by electrochemical process involving other water molecule and electron or by pure chemical process in which two adsorbed H atoms form H_2 molecule as follows:

$$H_{ads} + H_2O + e^- \leftrightarrows H_2 + OH^- \quad (7)$$

$$2\,H_{ads} \leftrightarrows H_2 \quad (8)$$

From the experimental point of view, it should be taken into account that univocal detection of H_{ads} is not a straightforward task, since H cannot be directly probed in XPS measurements due to extremely low ionization cross section of its 1s orbital (i.e. 5000 lower than that of C 1s orbital), and therefore its indirect detection makes its origin sometimes unclear.

4.5 Conclusions

In this chapter**,** we delved into the surface chemistry of BTO (100) single crystals around the phase transition and its correlation with the ferroelectric state. The combined use of AP-XPS, PFM and X-Ray Reciprocal Space Mapping (XR-RSM) has enabled us to retrieve information about the evolution of surface chemical composition, crystallographic and domain structure during the phase transition, necessary to establish the presence of chemical species, the main redox reactions taking place and their entanglement with bulk ferroelectric polarization and screening.

XR-RSM analysis of a BTO (100) single crystal provides evidence of a distinct distribution of ferroelectric domains at the surface of the native single crystal as compared to the bulk, that besides characteristic a_1/a_2 domain distribution, also shows an enhanced presence of *c* domains. After the first phase transition FE→PE→FE' cycle, the surface layer of the ferroelectric single crystal shows a predominance of *c* domains. PFM characterization performed across the phase transition demonstrates that the *c* domains are predominantly down-oriented, suggesting that the presence of small amounts of water at the surface during the phase transition could promote the nucleation of down polarized domains.

Correlative AP-XPS analysis as a function of temperature has provided us with direct evidence of the chemical reactions and polarization screening dynamics, coupled to the observed changes of the domain structure during the phase transition between ferroelectric and paraelectric state in water vapor atmosphere and low RH conditions. The obtained results show how the appearance of down-oriented polarization during paraelectric-to-ferroelectric phase transition triggers water dissociation, giving the first evidence to the best of our knowledge of *ferrocatalysis*, that is, direct correlation between the emergence of ferroelectricity and enhanced surface chemical reactions.

Besides, fast mapping of AP-XPS spectra over the phase transition has enabled to monitor the coexistence between ferroelectric screening dynamics mediated by surface chemical reactions and emergence of polarization at the time scale of seconds, which take place on the surface of the single crystal until equilibrium is reached after some few minutes. With this in mind, the obtained results point out that if cycling schemes between the paraelectric and ferroelectric states are to be implemented, it should be taken into account that ferrocatalytically-enhanced reactions take place mainly while the high charge-imbalance exists on ferroelectric surfaces, which is in the order of few minutes.

References

[1] C. Wang, N. Tian, T. Ma, Y. Zhang, H. Huang, *Nano Energy* **2020**, *78*, 105371.

[2] A. Kakekhani, S. Ismail-Beigi, *ACS Catal.* **2015**, *5*, 4537.

[3] D. Zhang, H. Wu, C. R. Bowen, Y. Yang, *Small* **2021**, *17*, 2103960.

[4] M. U. De Vivanco, M. Zschornak, H. Stöcker, S. Jachalke, E. Mehner, T. Leisegang, D. C. Meyer, *Phys. Chem. Chem. Phys.* **2020**, *22*, 17781.

[5] Y. Zhang, M. Xie, V. Adamaki, H. Khanbareh, C. R. Bowen, *Chem. Soc. Rev.* **2017**, *46*, 7757.

[6] H. Li, C. R. Bowen, Y. Yang, *Adv. Funct. Mater.* **2021**, *31*, 1.

[7] T. Zhang, T. Yang, M. Zhang, C. R. Bowen, Y. Yang, *iScience* **2020**, *23*, 101689.

[8] Y. Zhang, S. Kumar, F. Marken, M. Krasny, E. Roake, S. Eslava, S. Dunn, E. Da Como, C. R. Bowen, *Nano Energy* **2019**, *58*, 183.

[9] A. Kakekhani, S. Ismail-Beigi, *J. Mater. Chem. A* **2016**, *4*, 5235.

[10] Y. Zhang, P. T. T. Phuong, E. Roake, H. Khanbareh, Y. Wang, S. Dunn, C. Bowen, *Joule* **2020**, *4*, 301.

[11] M. Xie, S. Dunn, E. Le Boulbar, C. R. Bowen, *Int. J. Hydrogen Energy* **2017**, *42*, 23437.

[12] R. Belitz, P. Meisner, M. Coeler, U. Wunderwald, J. Friedrich, J. Zosel, M. Schelter, S. Jachalke, E. Mehner, *Energy Harvest. Syst.* **2017**, *4*, 107.

[13] X. Xu, L. Xiao, Y. Jia, Z. Wu, F. Wang, Y. Wang, N. O. Haugen, H. Huang, *Energy Environ. Sci.* **2018**, *11*, 2198.

[14] C. Wang, N. Tian, T. Ma, Y. Zhang, H. Huang, *Nano Energy* **2020**, *78*, 105371.

[15] C. Wang, T. Ma, Y. Zhang, H. Huang, *Adv. Funct. Mater.* **2022**, *32*, 2108350.

[16] E. Gutmann, A. Benke, K. Gerth, H. Böttcher, E. Mehner, C. Klein, U. Krause-Buchholz, U. Bergmann, W. Pompe, D. C. Meyer, *J. Phys. Chem. C* **2012**, *116*, 5383.

[17] L. Chen, H. Li, Z. Wu, L. Feng, S. Yu, H. Zhang, J. Gao, Y. W. Mai, Y. Jia, *Ceram. Int.* **2020**, *46*, 16763.

[18] A. Benke, E. Mehner, M. Rosenkranz, E. Dmitrieva, T. Leisegang, H. Stöcker, W.

Pompe, D. C. Meyer, *J. Phys. Chem. C* **2015**, *119*, 18278.

[19] Y. Xia, Y. Jia, W. Qian, X. Xu, Z. Wu, Z. Han, Y. Hong, H. You, M. Ismail, G. Bai, L. Wang, *Metals (Basel).* **2017**, *7*, 122.

[20] P. T. Thuy Phuong, Y. Zhang, N. Gathercole, H. Khanbareh, N. P. Hoang Duy, X. Zhou, D. Zhang, K. Zhou, S. Dunn, C. Bowen, *iScience* **2020**, *23*, 101095.

[21] Y. Zhang, P. T. Thuy Phuong, N. P. Hoang Duy, E. Roake, H. Khanbareh, M. Hopkins, X. Zhou, D. Zhang, K. Zhou, C. Bowen, *Nanoscale Adv.* **2021**, *3*, 1362.

[22] A. Kakekhani, S. Ismail-Beigi, *Phys. Chem. Chem. Phys.* **2016**, *18*, 19676.

[23] N. Domingo, N. Bagués, J. Santiso, G. Catalan, *Phys. Rev. B - Condens. Matter Mater. Phys.* **2015**, *91*, 1.

[24] N. Domingo, J. Narvaez, M. Alexe, G. Catalan, *J. Appl. Phys.* **2013**, *113*, 187220.

[25] S. V. Kalinin, C. Y. Johnson, D. A. Bonnell, *J. Appl. Phys.* **2002**, *91*, 3816.

[26] N. G. Apostol, L. E. Stoflea, G. A. Lungu, C. A. Tache, D. G. Popescu, L. Pintilie, C. M. Teodorescu, *Mater. Sci. Eng. B Solid-State Mater. Adv. Technol.* **2013**, *178*, 1317.

[27] G. Greczynski, L. Hultman, *Prog. Mater. Sci.* **2020**, *107*, 100591.

[28] M. A. Brown, Z. Abbas, A. Kleibert, R. G. Green, A. Goel, S. May, T. M. Squires, *Phys. Rev. X* **2016**, *6*, 011007.

[29] A. K. Tagantsev, L. E. Cross, J. Fousek, *Domains in Ferroic Crystals and Thin Films*, Springer New York, **2010**.

[30] N. Domingo, E. Pach, K. Cordero-Edwards, V. Pérez-Dieste, C. Escudero, A. Verdaguer, *Phys. Chem. Chem. Phys.* **2019**, *21*, 4920.

[31] I. Spasojevic, G. Sauthier, J. M. Caicedo, A. Verdaguer, N. Domingo, *Appl. Surf. Sci.* **2021**, *565*, 150288.

[32] J. T. Newberg, D. E. Starr, S. Yamamoto, S. Kaya, T. Kendelewicz, E. R. Mysak, S. Porsgaard, M. B. Salmeron, G. E. Brown, A. Nilsson, H. Bluhm, *Surf. Sci.* **2011**, *605*, 89.

[33] K. A. Stoerzinger, W. T. Hong, E. J. Crumlin, H. Bluhm, M. D. Biegalski, Y. Shao-Horn, *J. Phys. Chem. C* **2014**, *118*, 19733.

[34] M. Ďurovič, J. Hnát, K. Bouzek, *J. Power Sources* **2021**, *493*, 229708.

CHAPTER 5

Effect of humidity on the ferroelectric writing speed and domain wall dynamics

In this chapter, the influence of water on the ferroelectric polarization dynamics in $BaTiO_3$ thin films has been studied in controlled relative humidity (RH) conditions. Specifically, it will be demonstrated that the RH, controlled in the wide range between 2.5 % and 60 %, has a significant effect on the maximum writing speed of ferroelectric stripe-like domains, referred to as the *critical speed*, as well as on the transversal domain wall dynamics. Moreover, I will also analyze how the size of the written domains and observed polarization dynamics are affected by water meniscus radius at the tip-sample contact, adsorbed water layer thickness and its associated structure as a function of RH.

5.1 Introduction

The continuous progress of information and communication technologies requires the development of increasingly powerful memories, i.e. devices capable of storing information more densely and more quickly. Non-volatile ultrahigh density memories can be produced by using ferroelectric oxides films, whose polarization is locally and reversibly patterned with nanometric resolution and high precision. In this framework, AFM emerges as a unique tool to study the ferroelectric switching dynamics at the nanoscale, since the tip can be used as a mobile top electrode to apply the required electric field locally.[1] The size of the patterned domains and therefore the density of stored information depend on experimental parameters such as the magnitude of the applied voltage and the pulse duration.[1–3] Furthermore, by taking into account that the screening of the depolarization field directly impacts the stability of ferroelectric polarization, relative humidity (RH) of the ambient plays an important role on bare ferroelectric surfaces (i.e. in the absence of metallic electrodes) and influences the size of the newly formed domains.[2,4–11] So far, however, studies concerning size evolution of written domains with RH are inconsistent. The majority of works demonstrate that the size of written domains at constant bias grows with RH,[2,4,5,7,8,10,12] but some authors report on nonlinear decrease of domain size at high RH.[6,13] The reason for the observed change in domain size with RH has been subject of various works, which in general account for two main factors: i) the effect of water meniscus on electric field distribution and ii) the conductivity of the surface water layer.

The electric field created by a biased AFM tip is inhomogeneous: it is strongest under the tip-surface contact and it decreases away from it. Therefore, domain growth and its dynamics will be affected by any processes which modify this spatial distribution of electric field, such as the tip shape and the presence of adsorbates or water meniscus, commonly formed between the AFM tip and sample surface.[14] It has been reported that water meniscus locally decreases the strength of the electric field at the tip-sample contact,[2] but also slightly extends lateral dimensions over which high amplitudes of electric field are applied. Decrease of electric field just under the tip-surface contact decreases the probability of the domain nucleation (which depends on the intensity of the electric field in the local region under the biased SPM tip), but on the other hand, the lateral extension afforded by the meniscus can also promote more rapid domain growth through the high field region were nucleation can occur.[2,6] However, this

effect is in theory of relatively short-range, with no significant change in the field profile at distances beyond several tens of nm from the contact point and therefore cannot explain observed domain sizes of several hundreds of nm measured for PZT[2] and similar BTO thin films in this work, as it will be shown in this chapter. This suggests that water neck size has just a partial effect on observed domain size and that other effects should be taken into account.

Beside water meniscus formed at the tip-sample contact, all surfaces (so does the ferroelectric ones) are covered with a layer of water, which extends beyond the range of the formed meniscus. Therefore, screening of ferroelectric surfaces in a humid atmosphere can rely on electrostatic interactions between water molecule dipoles and ferroelectric fields, but also on the ionic species provided after water dissociation on the surfaces, such as hydronium H_3O^+ or hydroxyl OH^- ions.[15–22] Hence, not only the availability of screening charges, but more specifically their mobilities along an adsorbed water layer, can have an important impact on the stability and size of observed domains. This means that ferroelectric switching can be understood as a coupled physico-electrochemical process, which depends on the surface reactivity and ionic mobility and therefore on the rate at which screening species can be produced or/and supplied at the top of the newly formed domains.

Up to now, almost all studies of switching dynamics were conducted in a static mode, i.e., by applying pulses of different intensities and lengths to a biased AFM tip placed in contact at a fixed point of the substrate.[1,2,4,6,7,10,23] Seminal works led by Gruverman [24,25] and Paruch et al.[1,26,27] studied the ferroelectric domain growth under static electric fields generated by an immobile AFM tip and established the exponential dependence of the lateral domain wall velocity with the field and the domain size.

However, encoding of ferroelectric bits is a dynamic process, and in some proposed setups, the speed at which information can be encoded is limited by the successfulness of switching events at a given scanning speed: as the speed of rotation of a “ferroelectric record disk” is increased, successful single-bit writing by a biased tip decreases.[28,29] This behavior might be related to the insufficient population and/or mobility of surface screening charges, incapable of stabilizing the newly formed domains at sufficient speed. Beyond the bit density, the maximum speed at which information can be encoded is of crucial importance for the application of ferroelectric materials in memory devices. Although the kinetics of domain growth can be tuned by RH, studies that concern the interplay between scanning speed and RH on domain switching dynamics are still lacking.

Moreover, most of the static-switching experiments have been conducted at high RH between 20 % and 90 %, and detailed studies at very low RH conditions (RH < 10 %)[6,8,12] are scarce. Studies of switching dynamics in the dry range are of both practical and fundamental interest. In practical terms, low RH is prevalent in many parts of the world. On a more fundamental level, studies at low humidity should shed light on important processes expected to take place, such as chemisorption of anchoring hydroxyl groups and physisorption of the first water layers, as well as their influence on the mobility of ionic compensating species.[30–32]

In this chapter, I explore the influence of RH on the critical speed for stripe-like domain writing, by driving a biased AFM tip across the ferroelectric $BaTiO_3$ thin film surface using different speeds and in distinct RH conditions. With this setup we are actually simulating the rotation of the ferroelectric disk, with the difference that here the ferroelectric medium is static, while the biased AFM tip is moving at different speeds across the surface, thus writing stripe-like domains. Two sets of experiments were performed: in one case, a constant writing speed was maintained while increasing the voltage applied to the AFM tip; in the other, the applied voltage was fixed and the writing speed varied. All measurements were performed in a wide range of writing speeds and RH, including the low-humidity range all the way down to 2.5 % RH.

I found that the maximum speed at which domains can be written (and therefore the critical speed of writing) increases as the RH rises, which can be explained by the improved screening conditions which disable polarization back-switching as the writing speed is increased. By the same token, a decrease of RH required application of higher voltages in order to achieve acceptable writing speeds.

Moreover, I assessed the domain wall dynamics in transversal direction (i.e. perpendicular to the tip scanning direction) and observed creep-like behavior of domain walls, noting that the dynamic coefficient μ, characteristic of creep-like domain wall motion in the pinning potential, is also strongly influenced by the RH conditions.

In addition, the dependence of domain size on ferroelectric writing speed and applied tip voltage, independently, in different RH conditions was studied. This enabled me to construct a map of domain size evolution as a function of these parameters and correlate the observed behavior with the dominant screening mechanisms involved, shown to be closely related to the adsorbed water thickness. Furthermore, effect of adsorbed water structure, its associated dielectric constant and ionic mobility on ferroelectric screening is discussed.

5.2 Impact of RH and voltage on the domain size

The sample used in all the experiments is a 21 nm thick BTO thin film, grown on 33 nm thick SRO, which serves as a conductive bottom electrode, necessary for PFM characterization. The BTO/SRO bilayer was grown on a (001) oriented single crystalline STO substrate by PLD technique. The same optimized preparation procedure explained in the Chapter 2 has been employed as well in here for the growth of the ferroelectric BTO thin film. The BTO film was atomically flat, fully epitaxial and uniformly *c*-axis oriented with up-polarized as-grown state, as evidenced by PFM measurements. The writing speed experiments were performed using an Asylum MFP3D AFM with an environmental cell integrated to a low-noise continuous flow humidity controller that, by combining dry N_2 gas with distilled water, allows high precision control of RH at the cell with long term stability.[33] The minimum value of RH achieved after exposure to pure N_2 gas for 60 h was 2.5 %. The temperature was held constant throughout the whole experiment. In all the experiments, a Nanosensors EFM tip ($k \sim 2$ N m^{-1}) was used at a constant force of ~100 nN.

Once the desired RH was achieved, two sets of consecutive writing experiments were performed: first by applying an increasingly positive voltage to the AFM tip at a constant writing speed, and second by setting a constant applied voltage and increasing the writing speed, respectively. All domains were written dynamically in the shape of lines, giving us the possibility to probe influence of RH on the maximum writing speed and also effect of writing speed on the domain size in different RH conditions. For each voltage/scanning speed combination, two consecutive lines were written to verify repeatability. In order to achieve stable tip-sample coupling, two extra lines were written at the beginning of each experiment at the lowest speed/voltage conditions. Successfulness of domain-writing was probed by PFM imagining of the written areas, and the line thicknesses that correspond to domain width were calculated from the average number of pixels in the PFM phase images.

In order to characterize the switching response, we apply “writing” voltages in the range from 4.5 to 7.5 V to the AFM tip while scanning straight lines in contact mode at a constant speed of 12.47 μm s^{-1} and in different RH conditions. When the voltage is sufficiently large, “line domains” appear in the tip’s wake, with a width that, like the diameter of point-domains,[2] grows proportionally to the excess voltage above coercivity. Amplitude (top) and phase

(bottom) PFM images of written line domain pattern is shown in **Figure 5.1 a**. Extracting the quantitative information from the maps, we see (**Figure 5.1 b**) that indeed domain width increases with voltage, until it reaches a saturation value. We also observe that the width of the line domains depends not only on applied voltage, but also on humidity: for any given voltage, domain width increases with increasing humidity. Moreover, the final domain width is larger, and is reached at lower voltages, as humidity is increased. The results indicate that surface water and related adsorbates facilitate switching and stabilize the switched domains by providing the requisite screening charge.

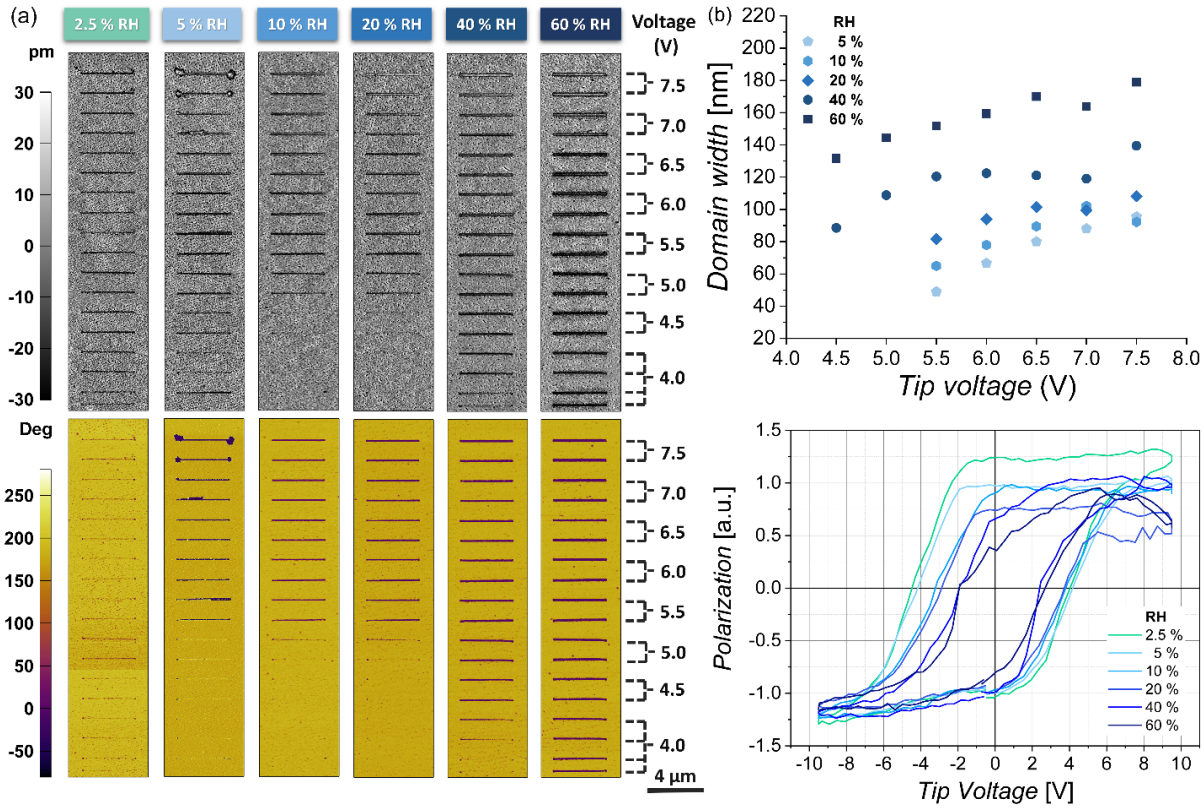

Figure 5.1 *(a) PFM amplitude and phase images of down-polarized lines written in different RH conditions by increasing writing voltage, using a Nanosensors EFM tip (k ~ 2.8 Nm^{-1}, r = 50 nm) at the constant speed of 12.47 µm s^{-1} and contact force of 100 nN. (b) Domain width evolution as a function of applied tip voltage for the constant speed of 12.47 µm s^{-1} and for different RH. Domain width increases with voltage and RH until it reaches a saturation value; (c) Hysteresis loops measured by SS-PFM at 0.2 Hz in different RH conditions showing a decrease of the coercive voltage with RH.*

This conclusion is also supported by the switching spectroscopy PFM measurements[34] on up-polarized BTO thin film as a function of RH shown in **Figure 5.1 c.** It can be seen that the coercive voltage decreases when the RH is raised from 2.5 % to 60 % RH and hysteresis loops

become narrower. The effect of screening charge on hysteresis loops measured by SS-PFM has been previously investigated in the work by Morozovska et al.[35] The rate at which electromechanical response of the cantilever changes depends on the activation energy for domain nucleation and further on the velocity at which domain wall is able to travel causing the growth of the domain. The speed of the domain wall during the switching might be influenced by the mobility of the screening charges present in the meniscus and adsorbed water layer. Taking into account that the speed of the domain walls is determined by the rate at which the ionic charges can travel through the meniscus and surface water layer to reach the screening front, domain walls are prone to move slower in low RH conditions. This is in some way equivalent to the studies of domain wall motion under top electrode with limited conductivity, where higher resistivity electrode caused decrease of domain wall velocity.[36,37] On the other hand, it can be seen from **Figure 5.1 b** that achieving higher domain radius at constant writing speed (or pulse length) and relative humidity is only possible if voltage is increased, which could explain why at low RH hysteresis loops appear broader (i.e. their coercive voltage is larger). Additionally, as the lateral mobility of screening charges rises with RH, rapid growth of domains at high RH will result in earlier saturation (at smaller voltages) of the hysteresis loops, clearly visible by comparing hysteresis loops measured at the two extremes (e.g. at 2.5 % and 60 % RH), as well as from **Figure 5.1 b**.

5.3 Impact of RH on the dynamics of ferroelectric switching

5.3.1 Effect of RH on the writing speed of ferroelectric domains

Having established that water facilitates ferroelectric switching both in point-measurements of hysteresis loops and in ferroelectric lithography of stripe domains, next we explore how humidity affects the writing speed of ferroelectric domains. To address this issue, we perform a new set of ferroelectric lithography measurements where, instead of fixing the scanning speed and increasing voltage, we fix the voltage and increase the scanning speed. **Figure 5.2** shows the PFM amplitude and phase images of down-polarized lines written in different RH conditions by using a constant bias of 6.5 V and increasing writing speeds in the range from 12.47 μm s^{-1} to 585.94 μm s^{-1}.

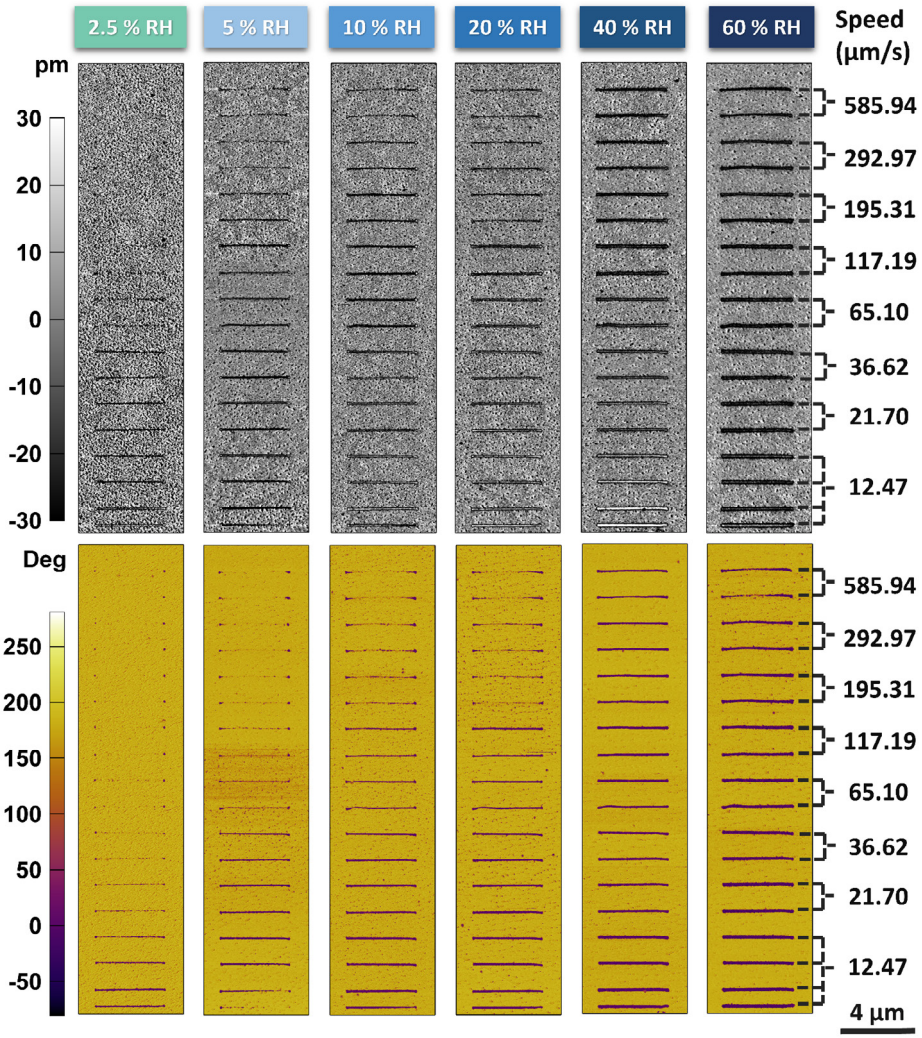

Figure 5.2 *PFM amplitude (top) and phase images (bottom) of down-polarized lines written in different RH conditions by increasing writing speeds and at a constant tip bias of 6.5 V while scanning using a force of 100 nN. Critical writing speed is shifting towards higher values as RH is increased.*

At each RH, the width of the lines decreases and gradually disappears for increasing writing speeds. We can define the critical speed of writing as the highest speed for which homogeneous writing (a continuous line domain) is observed for each RH condition. It can be seen that the critical speed shifts towards higher values as RH is increased, and at 40 % RH all the lines are written successfully, independently of the used scanning speed within our experimental range. The increase in the critical writing speed confirms that humidity facilitates switching by providing improved screening conditions as RH is raised.

5.3.2 Effect of relative humidity on transversal domain wall dynamics

In terms of ferroelectric polarization switching dynamics, two different axes can be distinguished in our experiments: i) the direction along the tip displacement, characterized by the longitudinal tip scanning speed, i.e., the writing speed *S*, and ii) the transversal axis perpendicular to the writing direction, where the domain growth speed *v* is determined by a creep process which defines the domain wall motion, and also by characteristic time, dependent on the inverse of the longitudinal tip scanning speed. Scheme of the stripe-like domain formation, together with tip scanning speed *S* and domain wall velocity *v*, directed along two perpendicular axes is shown in **Figure 5.3.**

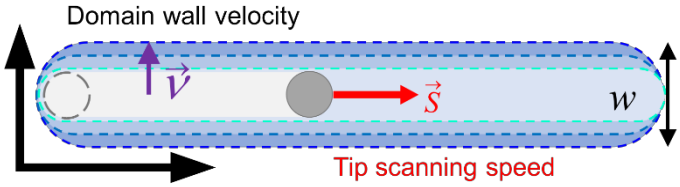

Figure 5.3 *Scheme of the stripe-like domain formation and growth; Size (width) of written domains w, depends on the transversal domain wall velocity v, proportional the pulse time and therefore to the inverse of the tip scanning speed S.*

In order to quantify the observed behavior, I first approach it from the perspective of transversal domain wall propagation, by measuring the size of domains (their line width) as a function of tip scanning speed for each RH, in order to compare the results with single point domain writing experiments.

Average growth velocity *v* of the domains perpendicular to the writing direction is proportional to the product of domain width *w* and the tip scanning speed *S* (inversely proportional to the pulse time) as $v \propto w \cdot S$. The domain growth velocity in creep regime depends on the domain wall motion, shown to be influenced by the domain wall pinning in defect sites.[27,38,39] The motion of domain walls governed by creep processes is described by the velocity of observed lateral domain expansion taking the form (1):

$$v = v_{\infty}\, exp\left[-\frac{U_a}{kT}\left(\frac{E_c}{E}\right)^{\mu}\right] \qquad (1)$$

Where μ is the dynamical exponent, U_a is the characteristic activation energy, E_c is the critical electric field, T is the temperature and k is the Boltzmann's constant. Electric field $E(r)$, varies

with the distance r from the AFM tip. It has been shown in the model[40] that when the conical part of the tip is modeled as the charged line segment near the bare surface, electric field scales with distance as $E \sim r^{-1}$. If in our case we consider that $E \sim w^{-1}$ then equation (1) can be simplified and the following relation can be obtained[41]:

$$\ln v = \ln v_{\infty} - K \cdot w^{\mu} \qquad (2)$$

Figure 5.4 a shows the fit of Equation (2) to the experimental data, with the dynamical exponent plotted in **Figure 5.4 b** as a function of the RH. In this case, a steep increase of the dynamical exponent with increasing RH from 0 to 10 % is observed, followed by an abrupt change between 10 % and 20 % of RH, until a plateau is finally reached for RH ≥ 40%.

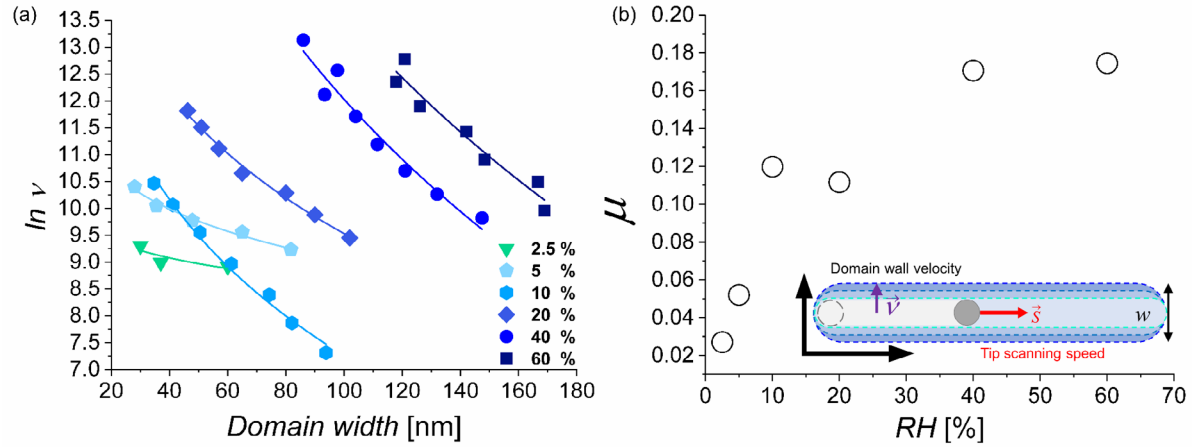

Figure 5.4 *(a) Exponential dependence of the domain growth velocity along the transversal axial direction on the domain width for different RH. The continuous lines correspond to the fits of the data by Equation (2); (b) Dynamic coefficient μ as a function of RH. The fits share the same K values for all RH. Inset: Scheme of the stripe-like domain formation and lateral expansion.*

Traditionally, the decrease of the domain growth rate and domain wall velocity has been explained in terms of domain wall pinning in defect sites during domain growth under static electric field. However, more recent works[37,42] proposed that the electrostatic field might evolve during the time and lateral distance from the biased AFM tip. This is explained by the fact that the motion of the domain wall is linked to the flow of screening charges needed to compensate the change in bound charge due to the polarization-switching, and therefore the kinetics of the domain wall must depend on the mobility of the compensating charges. Similarly, another work[43] explains the decrease of *a-c* domain-bundles velocity under a uniform electric field created between electrodes in co-planar geometry by the non-constant

driving force exerted on the domain boundary (present even in the case of nominally homogenous electric field), which fluctuates in the function of space and/or time. It is proposed that the effective driving force for domain boundary motion is strongly dependent on the rate at which the depolarization field of a newly-formed domain can be screened.

In the case when the screening charge is supplied by metallic thin film electrodes, screening capabilities and therefore domain wall kinetics will depend on their conductivity, controlled by their thickness.[36] However, in the case when experiments are performed in ambient conditions, where external screening by adsorbates is the dominant screening mechanism, RH plays a crucial role. The observed strong dependence of the dynamical exponent on RH, especially for RH < 10 %, suggests that albeit the density of defects and pinning sites can be influenced by the presence of surface water, there is a direct impact of surface conductivity on the domain wall kinetics, which rather hints to a strong dependence of the dynamics on the change of electrostatic boundary conditions modulated by the amount of surface water. The impact of not only the amount of water (i.e. water layer thickness), but also its structure on the surface conductivity is further discussed in Section 5.6 of this chapter.

5.3.3 Mutual effect of RH and writing speed on domain size

To further study the RH influence on the domain size and writing dynamics, I correlated the measured domain size with the tip scanning speed S at each RH. In **Figure 5.5 a** is plotted the logarithm of domain width in function of the writing speed logarithm, showing straight (in log-log scale) decrease of domain size width with increasing scanning speed for each RH. This indicates a power law dependence between the domain width w and the writing speed S as $w \sim S^{-\phi}$. The observed behavior is consistent with previous studies of domain wall kinetics, which observed that domain size grows following a power law as a function of the writing time t[12] as $w \sim t^{\phi}$, with the growth rate coefficient ϕ taking values $\phi < 1$.[5,8,44] Conversely, in our case, giving that pulse time at each point along the line is inversely proportional to the scanning speed ($t \sim 1/S$), domain size logarithm should decrease linearly with the logarithm of the scanning speed S, as shown by experimental results which can be fitted by the following equation:

$$\log w = K - \phi \cdot \log S \qquad (3)$$

In Equation (3) w is the line width, K is a constant, S is the scanning speed and ϕ is the growth rate coefficient. The slope of the fitting function ϕ was plotted as a function of RH in **Figure 5.5 b**.

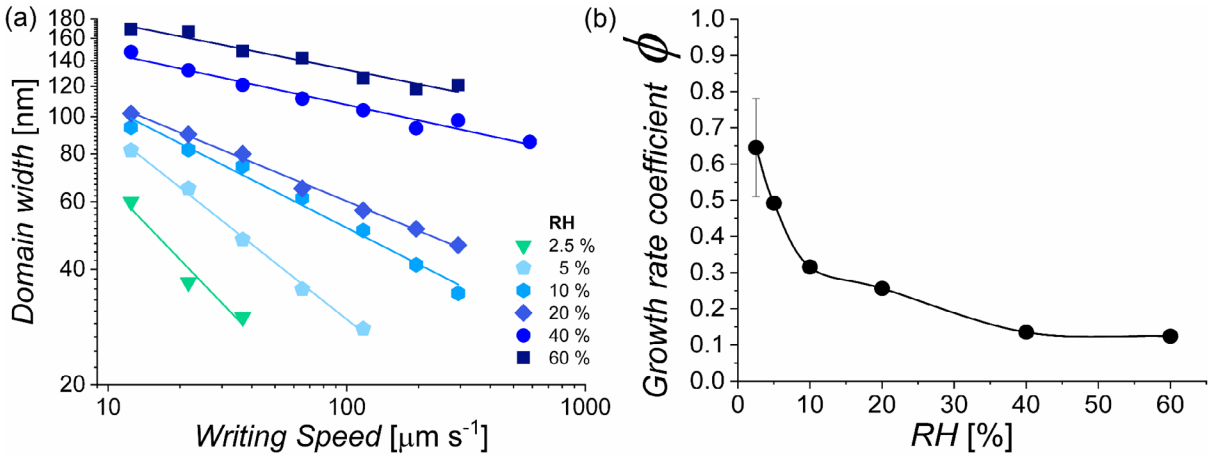

Figure 5.5 *(a) Measured domain width as a function of writing speed (in log-log scale) for different RH. Lines depict fit of the data by Eq. (3); (b) Slopes of the fitting curves shown in panel (a) as a function of RH. Absolute values of growth rate coefficient decrease with the rise of RH, achieving a plateau at high RH and revealing that the domain width is more sensitive to the writing speed in the low RH range.*

The growth-rate coefficient ϕ is observed to decrease as RH increases, i.e. $\phi = 0.64$ for 2.5 % RH and decreases to $\phi = 0.26$ for 20 % RH, achieving a plateau above 40 % RH. Higher values of the growth rate coefficient for low RH (i.e. under 10 % RH) indicate that domain width decreases faster with writing speed and is therefore more sensitive to it due to the poor screening conditions in low RH range. At some point, at sufficiently low RH and/or high writing speeds, inefficiency of screening charges fully inhibits domain switching. As we will see, inefficiency of external screening charges can be related to their scarce presence and/or low mobility. In contrast, at high RH humidity, where the screening becomes sufficiently effective, the coefficient ϕ saturates, making the behavior of domain width vs. writing speed almost independent on RH. Note that a similar trend has been observed for the dynamic coefficent μ (**Figure 5.4 c**).

The color map shown in **Figure 5.6** shows how RH and writing speed simultaneously affect size of dynamically written domains. Every symbol represents a combination of RH and writing speed for which a writing experiment has been performed. Full, half-filled and empty symbols denote conditions for which either complete, partial or unsuccessful writing has been observed, respectively. For our experiment, where we used a tip with a nominal radius of R =

50 nm, the minimal observed widths of dashed and fully written lines are 35 nm and 40 nm, respectively. Full lines represent combinations of RH and tip writing speed parameters for which the same domain width is achieved (specified for each line) and are therefore referred to as iso-width lines. These lines were calculated from the fitting parameters of **Figure 5.5 a** by choosing the desired input values of speed and then calculating predicted values of domain width at each RH. Iso-width lines are obtained by connecting the coordinates (RH, Speed) that give the same value of calculated domain width. The color scale is the whole distribution map of domain width vs. writing speed and RH. The white region denotes combinations of RH and tip scanning speed for which scanning is too fast or humidity too low for domains to be written at all, and therefore the edge of the white region represents the critical writing speed for each RH where domains disappear altogether. In the following section we set to explore parameters that influence the observed iso-width line shape.

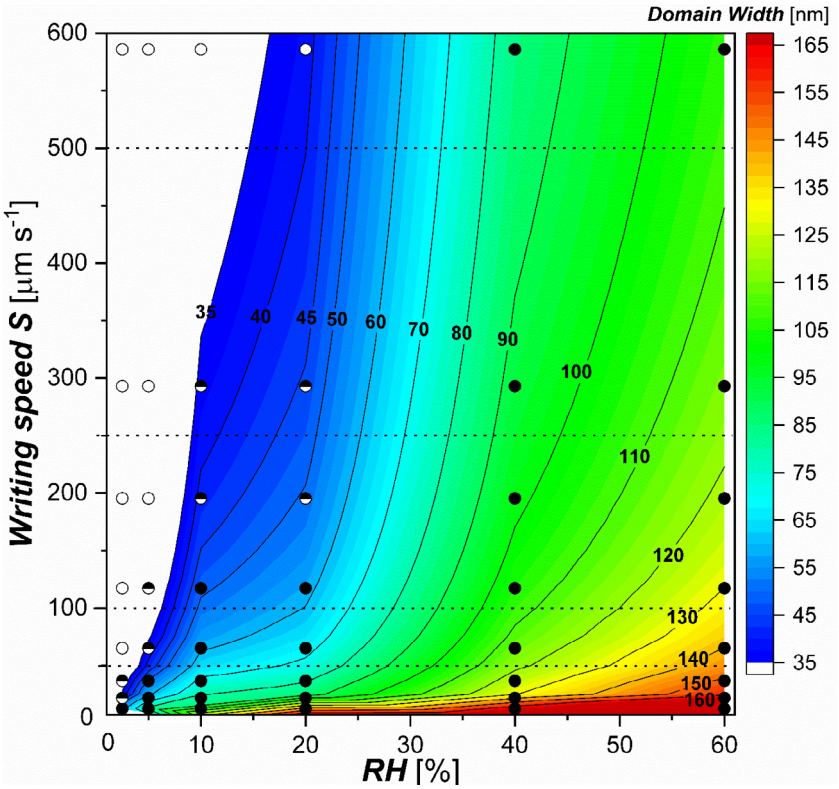

Figure 5.6 *Color map showing the dependence of domain width on the writing speed and RH. Symbols correspond to experimental points of RH and speed for which writing experiment has been performed with full, half-filled and empty symbols denoting conditions for which complete, partial and unsuccessful writing has been observed. Iso-width lines are obtained by connecting the coordinates (RH, Speed) that give the same value of calculated domain width, predicted by using fitting parameters of* ***Figure 5.5 a****.*

5.4 Evaluation of the influence of water meniscus on domain size

Cross sections along the black horizontal lines in the color map shown in **Figure 5.6** yield the dependence of domain width on RH for arbitrarily chosen writing speeds. A few such lines are plotted in **Figure 5.7**. Several interesting features emerge from this graph. Above 20 % humidity, the line width is an almost-linear function of the RH, which is in good agreement with the only reported study so far, where domain diameter was plotted as a function of RH for RH > 30 % and different pulse times.[2] However, at low RH the behavior is non-monotonic, showing a plateau of constant domain width between 10 % and 20 %, and a non-linear dependence at lower humidity that gets increasingly steeper as RH approaches 0.

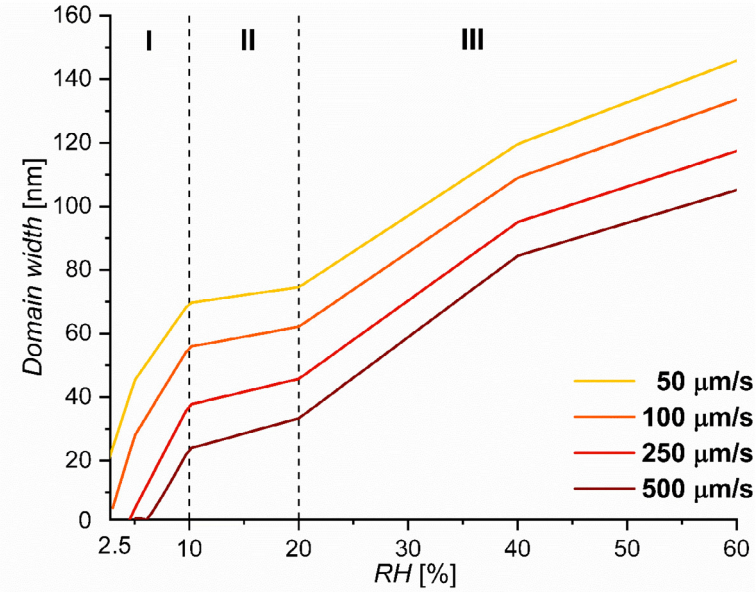

Figure 5.7 *Cross sections of domain width map shown in* ***Figure 5.6*** *at four arbitrary chosen writing speeds, denoted by black dotted horizontal lines, showing non-monotonic growth of the domain width as a function of RH at the constant writing speed.*

There are several factors that could influence domain width as a function of RH such as i) the dynamics of the water meniscus formation and growth up to its thermodynamic equilibrium and ii) thickness of the adsorbed water layer. Importantly, the latter can have a direct influence on adsorbed water structure (ice-like vs. liquid-like), dielectric permittivity and conductivity, which play crucial role in domain screening and stabilization.

In static conditions (or, in our case, at the constant writing speed), the size of the written domains, could depend on the lateral size of the water meniscus, formed by capillary condensation in the small gap between the tip and sample, which is expected to grow with

RH.[2,6] The water meniscus formed around a sphere tip in contact with a flat surface (an idealized view of the tip-surface contact in the PFM measurements) at thermodynamic equilibrium with vapor can be described by the equation (4) [45]:

$$R_m T ln\left(\frac{P}{P_0}\right) = \gamma V_m \left(\frac{1}{l} - \frac{1}{r}\right) \qquad (4)$$

where R_m is the molar gas constant, T the temperature, P_0 the saturation vapor pressure over a planar liquid surface, γ the surface tension of the liquid interface, V_m the molar volume of the liquid, and l and r are the azimuthal radius, concave with respect to the liquid, and the meridional radius perpendicular to l, respectively. A sketch of the AFM tip modeled as a sphere in contact with the surface covered with the water layer of thickness d together with mentioned radii is shown in **Figure 5.8 a**. The liquid is assumed to form a contact angle θ_1 with the spherical tip and θ_2 with the plane, whereby the sum of two radii $\Theta = r + l$ represents the lateral extension of water meniscus around the tip, i.e. water meniscus radius. Based on the[45] adapted values of azimuthal and meridional radius in our case can be calculated from equations (5) and (6) as:

$$r = \frac{R(1 - cos\beta) - d}{\cos(\beta + \theta_1) + \cos(\theta_2)} \qquad (5)$$

$$l = Rsin\beta - r[1 - \sin(\beta + \theta_1)] \qquad (6)$$

where β is the filling angle. By changing the values of β from 0 to 90 deg, we can calculate the r and l parameters and correlate the values with the corresponding RH by Equation (4). We consider a tip radius of R = 50 nm, contact angles θ_1 = 10° and θ_1 = 0° supposing a perfect wetting at tip/water and surface/water interface, respectively. In **Figure 5.8 b** is shown the corresponding meniscus radius $\Theta = r + l$ as a function of RH for different water layer thicknesses d, assuming that one monolayer of water has a thickness of 0.33 nm.[46]

In the low RH range < 10 % we expect to have < 1 ML of water coverage at the surface.[47] For RH in the range between 10 and 20 % we shall expect a stable surface water layer with thickness values between 2 and 3 ML and for RH >20 % the coverage is progressively increased. It can be seen that the water meniscus radius increases from Θ = 7 nm at RH = 2.5 % (1 ML) to Θ = 13 nm at RH = 20 % (~ 3 ML). Further increase of the water meniscus radius up to Θ = 20 nm at RH = 60 % (6 ML) is observed. This means that the calculated thermodynamic diameter of the water meniscus is between 14 nm and 40 nm for the lowest

and highest RH investigated in this work, respectively. Most importantly, calculated dependence of water meniscus radius as a function of RH exhibits very different trend compared to the measured domain size vs. RH shown in **Figure 5.7**. The calculations show a monotonical curve that grows very slowly, and takes off above 80 % RH, whereas the experimental results exhibit a rapid increase of domain size at low RH, followed by a plateau, and subsequent slower growth. For this reason, the relative increase of the water meniscus diameter with RH cannot account for the observed increase of the written domain sizes shown in **Figure 5.7**, meaning that the lateral size of the water meniscus plays a minor role.

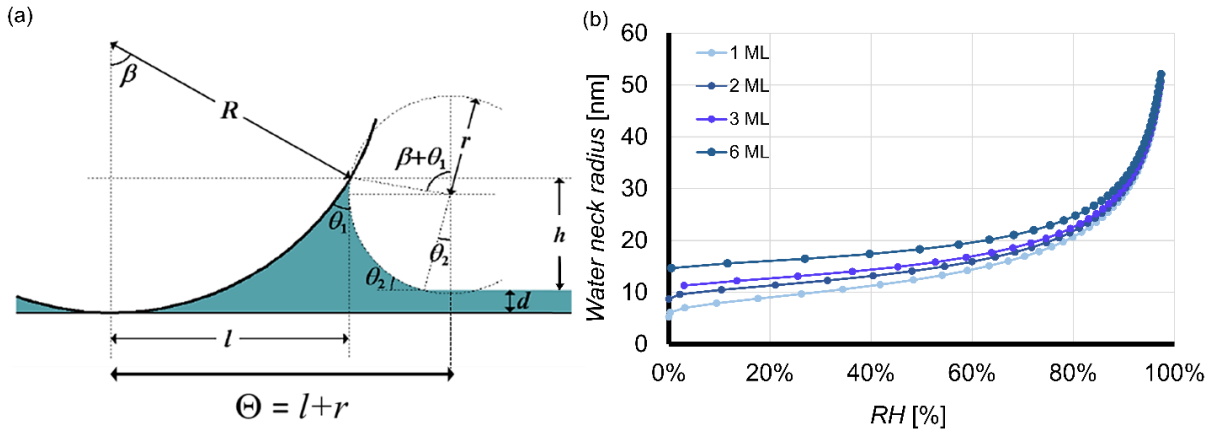

Figure 5.8 *(a) Sketch of the AFM tip modeled as a sphere of radius R, in contact with a surface covered by a water layer of thickness d. The total water meniscus volume is shown in blue, and its maximum extension over the surface is shown by the radius Θ; (b) Calculated water meniscus radius Θ as a function of RH for various thicknesses of the surface water layer d. Here we take as a reference the thickness of 1 ML of water as d = 0.33 nm.*

Another factor that could affect the observed increment of domain size at constant RH is the time constant of water meniscus growth until the thermodynamic equilibrium, happening through ambient adsorption and transport of water molecules across the surface. Overall time scale for the meniscus formation is of the order of several ms,[48] which is in the upper limit of the total time spent in our experiments to move the tip one single step of Δx = 100 nm at the lowest writing speed of 12.5 μm s^{-1}. All other writing speeds were faster and therefore the "dwell time" of the cantilever at each point was even smaller, meaning that at the higher speeds meniscus does not have time to fully form. On the other hand, further increase of water meniscus volume until its thermodynamic equilibrium in static conditions, observed by environmental scanning electron microscopy (ESEM) measurements, is reported to take up to hundreds of seconds.[14,49] However, other studies predicted much shorter equilibrium time constant of tens of ms in static conditions, which are drastically affected when instead of static

tip-sample contact, speed of the moving tip (or sample) is taken into account.[48] The later work demonstrated that meniscus cannot achieve its equilibrium size at speeds higher than 3 μm/s due to the constant change in the position of tip-sample contact caused by its lateral movement. Taking into account our estimated dwell time and mentioned dynamic effects, it can be concluded that in the frame of our experiment water meniscus will not be able to grow up to its saturation even at the lowest speed. Therefore, it can be expected that the real diameters of the water menisci will have even smaller values than those calculated in the static limit (**Figure 5.8 b**), which are at the same time significantly smaller than observed domain sizes. Hence, physical diameter of the water meniscus cannot explain observed domain sizes.

Still, the water meniscus, even if it is smaller than the domain width, can still be a source of ionic charges such as protons and hydroxyl groups among others, since a portion of water molecules will dissociate under the application of high voltages, thus becoming the closer source of screening agents. However, the efficiency of polarization screening by ions generated or concentrated at the water meniscus, similarly to Dip Pen nanolithography (DPN), will strongly depend on the transport rates of charges through the meniscus and especially on their diffusion rate at the surface. As it will be explained in the following sections, transport and diffusion rates of screening species are going to be highly influenced by the thickness of the adsorbed water layer, dictated by RH conditions.

5.5 Influence of the adsorbed water thickness on the domain size

The process of water adsorption is governed by RH conditions via the adsorption isotherm,[50] which relates the thickness of the adsorbed water layer to the relative pressure or RH at constant temperature. In order to delve into the adsorption of water on our $BaTiO_3$ thin film surfaces, we measured a set of oxygen O 1s spectra in distinct RH conditions by the means of AP-XPS. XPS measurements were conducted in the range of RH between 0 % and a maximum of ~17 % (low and intermediate RH ranges) by increasing the water vapor pressure in the XPS chamber from UHV to 4 mbar. Unfortunately, this is the highest RH which can be achieved by this technique in isothermal mode, since for higher pressures, the water adsorption is so high that it completely masks the native oxide peak, thus preventing quantification, and moreover the overall signal becomes too small to be detected due the increased collision between photoelectrons and gas atmosphere. Still, this range is significant enough to illustrate region I

and onset of region II shown in **Figure 5.7**, which are indeed of the highest interest to the present study.

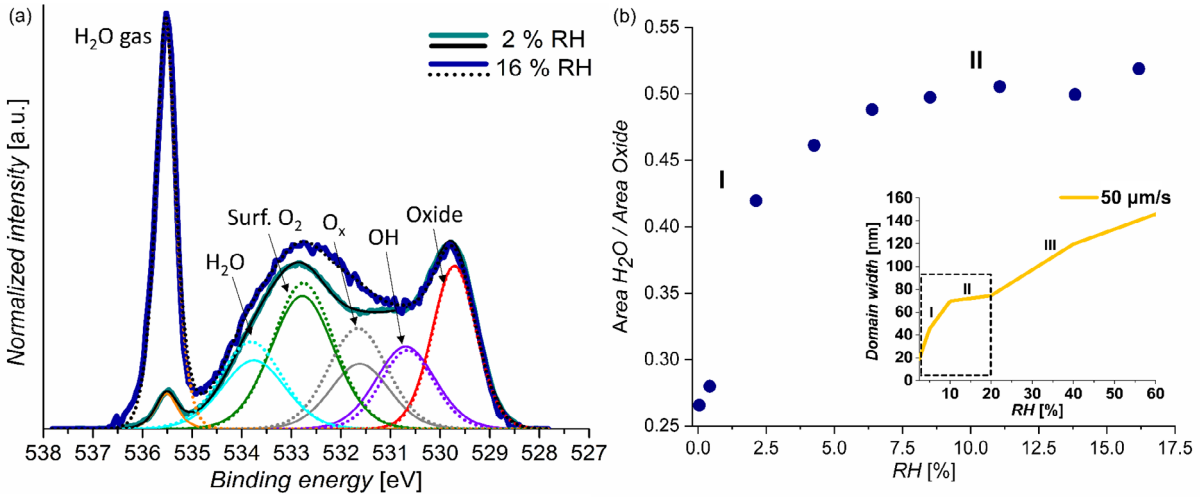

Figure 5.9 *(a) Fitting of O 1s spectra measured for BTO thin film in two different RH atmospheres by AP-XPS. Full and dotted lines denote spectral components in 2 % and 16 % RH normalized by the area of the oxide peak, respectively. Water content at the surface (cyan peak) is increasing as RH is raised. Note that the observed increment of CO_x species, corresponding to the contamination of the surface by carbon-related compounds is commonly observed during RH increase. (b) Area of the water peak normalized by the area of bulk oxide peak in O 1s spectrum as the function of RH, representing water adsorption isotherm on BTO surface in low to intermediate RH range, which closely resembles domain width vs. RH curve (**Figure 5.7**). For the comparison, in the inset is shown domain width vs. RH dependence at the scanning speed of 50 µm/s and by the black dotted line is denoted area of RH studied by AP-XPS.*

The obtained O1s spectra at ~ 2 % and ~ 16 % RH, normalized by the intensity of the main oxide peak, are shown in **Figure 5.9 a.** O 1s spectra were fitted following the peak model explained in detail in Chapter 3, which enabled us to quantify the amount of molecular water adsorbed at every RH. From the represented spectra it is evident that the peak of molecular water is increasing as RH is raised. The area of the molecular water peak normalized by the area of bulk oxide peak, which gives the quantitative information about the thickness of water isothermally adsorbed on the surface, has been plotted as a function of RH and shown in **Figure 5.9 b**. It can be seen that at low RH < 10 %, water adsorbs on BTO surface in non-linear fashion (region I), reaching a plateau of constant water content between 10 % and ~ 17 % of RH (region II). The shape of the adsorption isotherm of water on our BTO surfaces in the measured RH range (**Figure 5.9 b**), is in good agreement with the trends observed on different oxide surfaces[31,51–53] and is remarkably similar to the shape of the domain width vs. RH depicted in **Figure 5.7**, pointing out to a link between the two. In the inset of **Figure 5.9 b** is shown one

such dependence of domain width as a function of RH at the constant speed of 50 μm/s for the straightforward comparison. It can be seen that both curves consist of two regions with similar behavior corresponding to same range of RH: a first region of steep increase in domain width/water layer thickness as a function of humidity and a second region with a plateau. In the third region, domain size and presumably adsorbates layer thickness grow again linearly, similarly to the findings in the work.[2] Remarkably, these results show that the domain size is proportional to the actual thickness of adsorbed water layer. Processes which contribute to the observed characteristic shape of water adsorption isotherm and their influence on the screening of ferroelectric domains will be discussed in the following section.

5.6 Influence of the adsorbed water structure on surface conductivity

The structure that water molecules form when adsorbed on a surface strongly depend on their interaction with the surface and the thickness of the water films. Several authors investigated structure of adsorbed water on oxide surfaces in controlled RH conditions by attenuated total reflection-infrared (ATR-IR) spectroscopy. They could follow the intensity and position of the O-H bond stretching vibration in adsorbed water molecules and associate it with the presence of different water structures such as ice-like or liquid-like water.[31,51–53] A peak typically present at lower wave number was attributed to the ice-like water structure, stemming from the higher degree of hydrogen bonding which impairs stretching vibration of the O-H bond. By quantifying the evolution of mentioned peaks as a function of RH, water adsorption isotherm on the material of interest could be constructed and related with the presence of distinct water structures. Such isotherms exhibit a distinctive shape as a function of the thickness of adsorbed water, characterized by a rapid initial rise followed by the plateau and slower subsequent growth, which very closely resembles isotherm measured on BTO shown in **Figure 5.9 b.** Moreover, this isotherm navigates through different characteristic water structures, starting from ice-like organization of water molecules for the first adsorbed layers, followed by liquid-like structures as the water thickness is increased. This suggests that on our BTO surfaces, similar like on the other investigated oxides, water layers with different structure in the three depicted regions might exist. This is of particular importance in the case of ferroelectric surfaces, since the water structure can influence dielectric permittivity and ionic conductivity of adsorbed water layers, which have major effect on the ferroelectric domain screening and

therefore their size. However, the contribution of water structure, dictated by water thickness (and therefore RH conditions) on ferroelectric domain screening has not been considered up to now.

The low-humidity range in our ferroelectric dynamic lithography experiments comprises RH between 2.5 % and 10 % RH. In the Chapter 3 it has been demonstrated that the hydroxyl (OH) groups available from water-splitting reactions[16,17,20] get chemisorbed onto the surface immediately after exposing the sample to the ambient conditions from the vacuum preparation chamber. Taking into account that chemisorbed OH groups cannot be easily removed from the surface even by heating in low RH conditions,[30] it can be expected that our starting point at 2.5 % RH is already hydroxylated surface onto which upcoming water molecules will bind. Additionally, it has been shown that the water coverage in 2.5 % - 10 % RH range is discontinuous at best, with the sub-monolayer of water thickness.[47]

Water molecules in the sub-monolayer up to the first monolayer state are tightly bound to the surface OH groups (Region I in **Figure 5.7** and **Figure 5.9 b**), leading to the formation of a highly structured ("ice-like") water layer with very low dielectric constant[31,54,55] which could reach values around $\varepsilon \sim 2$, and where rotation or diffusion of water molecules is very limited.[56] Therefore, in this highly-structured water layer, dipolar screening by water molecules reorientation is negligible. Moreover, the mobility of ionic charges mediated by hoping of H^+ and OH^- through the chain of water molecules bound by H-bonds is also strongly affected by water structure and therefore RH.[57] Ab initio molecular simulations confirmed that proton transfer rate substantially decreases going from a liquid-like multilayer to the rigid monolayer coverage on a ZnO surface, following the associated change on the water structure.[58] **Figure 5.10** schematically represents different water structures that can be expected on a BTO surface as a function of increasing RH.

In this low RH regime, therefore, polarization screening mechanisms assisting ferroelectric polarization switching and stabilization, mediated by the reorientation of water dipoles and/or redistribution of ionic charges in the area of newly formed domain, will be highly inefficient. Moreover, the sub-monolayer water adsorption, leading to incomplete water layer coverage of the surface, could additionally affect the percolation paths of the already limited-mobility ionic charges over longer ranges. The experimental evidence indicates that, at sufficiently fast scanning speeds and low RH (**Figure 5.6**, empty circles), neither of these processes is fast enough to keep up with the screening demands of a switched polarization, and writing

efficiency is probably dominated by internal screening mechanisms. As the speed slows down below its critical value or RH is increased, ionic screening becomes available to cope up with the demanding screening needs of newly formed ferroelectric domains. Therefore, as shown experimentally it is expected that the size of the written domains vs. RH will change following the rate of water adsorption (**Figure 5.9 b**), according to the associated rise in the surface conductivity.[30,57]

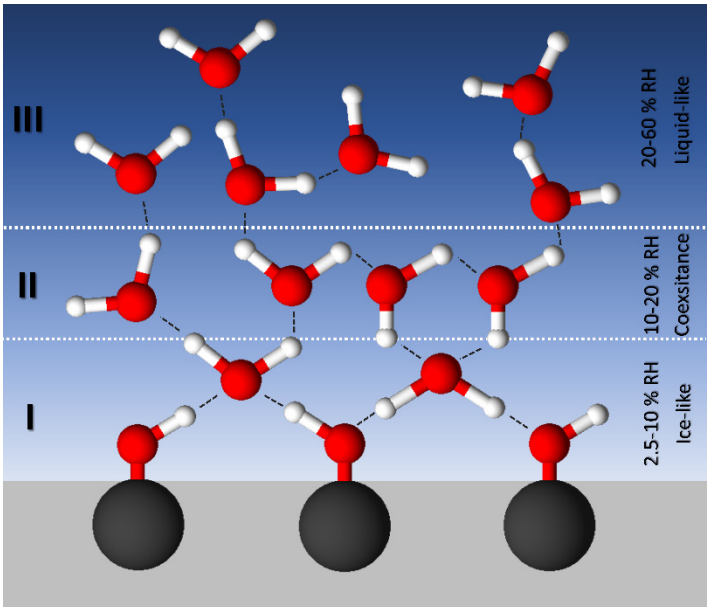

Figure 5.10 *Schematic representation of the water structures expected on BTO surface as a function of increasing RH. I. Highly structured ice-like water layer where hydrogen bonds are formed between chemisorbed OH groups and upcoming water molecules (represented by dashed lines). This immobilized ice-like water layer is characterized by low dielectric constant of water molecules and hindered mobility of water and ionic species; II. Coexistence between highly structured and liquid-like water growth structures with a higher dielectric constant and therefore higher capacity for dipolar screening but still limited ionic mobility; III. Stabilization of liquid-like water layers with maximized ionic mobility.*

The region between 10 % and 20 % RH is characterized by simultaneous stagnation of the initial growth of the water layer thickness and domain width as a function of RH (Region II, **Figure 5.7** and **Figure 5.9 b**). After the first monolayer of water is formed, subsequent water layers feel weaker influence from the hydroxylated substrate and adsorb in a less ordered manner; some water molecules become mobile on the surface and thus the water acquires a structure similar to the bulk liquid water. Therefore, the plateau between 10 % and 20 % RH is characterized by the coexistence of two water-growth structures, schematically represented in the **Figure 5.10**, with different kinetic behavior: 1) highly ordered, surface immobilized water and 2) mobile, liquid-like water molecules. Moreover, the barrier for protonic mobility by

hoping is decreasing with increasing RH in this range, giving an overall rise of the protonic conductivity of thicker water layers in this range despite the ice-like structure and associated low dielectric constant.[58,59] Therefore, a higher protonic conductivity together with increased mobility and a certain orientational freedom of water molecules in this region should assist in the polarization screening, enabling the successful writing of continuous ferroelectric stripe-like domains even when high speeds are used.

The stagnation of the water layer growth in this region has been explained by the instability of the liquid-like water molecules in this initial stage, which need higher RH in order to grow further, while at the same time the ice-like water layer becomes unsustainable.[31] Therefore, conductivity of such mixed water layer should change slowly in the mentioned RH range and so the size of the formed domains as well.

Finally, at higher RH, i.e., above 20 %, water forms a highly mobile liquid structure that characterizes region III in **Figure 5.7**. Previous studies of domain size for different pulse duration and RH show similar monotonic increase in the range of RH from 28 – 65 %.[2] The most natural explanation for this behavior is that, once a continuous layer of liquid-like water has condensed on the entire surface of the ferroelectric film, ions can easily migrate to assist the screening process. The approximately linear relationship between domain size and RH for any given scanning speed (range III in **Figure 5.7**) (or, equivalently, for any given switching time[2]) would be a direct evidence of the increasing thickness of the transport layer (the liquid), since conductivity (ionic, in this case) is linearly proportional to the thickness of the conductor. Therefore, it can be concluded that the surface conductivity and diffusivity of ions and charges needed for the domain screening is dominated not only by the thickness of surface adsorbed water determined by RH, but most notably, by the adsorbed *water structure* strongly modulating its electric and diffusion properties.

5.7 Conclusions

In this chapter I investigated the effect of water and RH on the critical writing speed of ferroelectric domains and associated polarization switching dynamics. Furthermore, mutual effect of writing speed and RH on the size of written domains was evaluated.

We find that the ferroelectric switching and the domain wall motion are governed by two different mechanisms below and above a RH ~ 10 %, characterized by one order of magnitude different dynamical coefficient μ. For RH < 10 %, screening charge might be provided by internal mechanisms due to the low surface charge mobility, and domain dynamics is characterized by a creep-like lateral motion of domain walls pinned by internal defects. For RH > 10 %, external screening by surface charges becomes more efficient for the stabilization of switched ferroelectric domains and switching dynamics is influenced by the mobility of ionic charges able to reach the screening front. Obtained results suggest that the mobility of ionic species is modulated not only by the thickness of adsorbed water, but possibly also by the water structure as a function of RH.

These findings have further impact on the study of writing dynamics of linear domains. Our measurements demonstrate that the critical speed for domain writing is highly dependent on RH. While for RH above 20 % domains can be written at speeds of 600 μm/s or faster, in dry atmospheres with RH below 5 % the critical writing speed slows down to below 60 μm/s. The width of the written linear domains shows a power low dependence on the writing speed, exhibiting higher growth rate coefficient ϕ, and therefore higher sensitivity of domain size to the writing speed for the lowest measured RH, caused by the restricted dipolar screening and/or low mobility of ionic species in these low RH conditions.

These findings have been corroborated by investigation of the observed domains' sizes as a function of RH at the constant writing speed. For a given writing speed, three distinct dynamic regimes as a function of RH can be identified: i) a low humidity regime below 10 % RH, characterized by a non-linear growth of the domain width as a function of RH; ii) a transition regime between 10 % and 20 % RH, where domain width as a function of RH meets a plateau; and iii) a high humidity regime above 20 % RH with an almost linear growth in domain width vs RH.

Once discarded the potential effects of the water meniscus diameter and its growth dynamics up to the equilibrium state on the domain size evolution, the thickness of adsorbed water as a

function of RH was measured. By fitting and quantifying O 1s XPS spectra recorded in controlled RH conditions, water adsorption isotherm on the BTO surface (corresponding to the water thickness as a function of RH) was constructed. Noting that both, the size of the written domains at the constant speed and the adsorbed water thickness follow the same behaviour as a function of RH, it can be concluded that the size of the written domains is directly proportional to the thickness of the adsorbed water layer.

Furthermore, structural measurements of adsorbed water layers on different oxide materials reported in literature show that the characteristic shape of adsorption isotherm, also observed in our BTO samples, is closely related to the existence of distinct adsorbed water structures in three mentioned RH regimes. This provides direct correlation with our BTO surfaces, where similar to other investigated oxides, water layers with different structure might exist as a function RH. This greatly influences the domain size and polarization switching dynamics, due to the different electronic conductivities, ionic diffusivity and therefore screening capabilities in the three mentioned regimes, which are proposed to be consistent with the initial presence of: i) ice-like highly structured water molecules in regime I, which besides providing low level of dipolar screening also prevent redistribution of surface charges by hopping, necessary in attending the screening demands (i.e., screening becomes slow in a nominally insulating ferroelectric film); ii) ice-like plus incomplete liquid-like water coexisting in regime II, with a higher dielectric constant and therefore higher capacity for dipolar screening but still limited ionic mobility, and iii) a complete layer of liquid-like water on the surface of the film in regime III, which provides efficient screening via fast ionic mobility along the surface.

The results presented in this chapter indicate that, if PFM-based schemes for writing ferroelectric memories are to be implemented,[28,29] their performance limits in dry-atmosphere conditions will have to be taken into account; otherwise, a ferroelectric memory record that works well in Singapore may not work so well in Helsinki. Conversely, the results also highlight how PFM studies of ferroelectric switching open another window into the complex physics of water adsorption and dissociation on ferroelectric thin film surfaces.

References

[1] P. Paruch, T. Tybell, J. M. Triscone, *Appl. Phys. Lett.* **2001**, *79*, 530.

[2] C. Blaser, P. Paruch, *New J. Phys.* **2015**, *17*, 13002.

[3] B. J. Rodriguez, R. J. Nemanich, A. Kingon, A. Gruverman, S. V Kalinin, K. Terabe, X. Y. Liu, K. Kitamura, *Appl. Phys. Lett.* **2005**, *86*, 8.

[4] D. Dahan, M. Molotskii, G. Rosenman, Y. Rosenwaks, *Appl. Phys. Lett.* **2006**, *89*, 1.

[5] V. Y. Shur, A. V Ievlev, E. V Nikolaeva, E. I. Shishkin, M. M. Neradovskiy, *J. Appl. Phys.* **2011**, *110*, 052017.

[6] A. V Ievlev, A. N. Morozovska, V. Y. Shur, S. V Kalinin, A. V Ievlev, A. N. Morozovska, V. Y. Shur, S. V Kalinin, *Appl. Phys. Lett.* **2014**, *104*, 1.

[7] K.-W. Park, H. Seo, J. Kim, D. Seol, J. Hong, Y. Kim, *Nanotechnology* **2014**, *25*, 355703.

[8] E. V Shishkina, E. V Pelegova, M. S. Kosobokov, A. R. Akhmatkhanov, P. V Yudin, A. Dejneka, V. Y. Shur, *ACS Appl. Electron. Mater.* **2021**, *3*, 260.

[9] A. Brugère, S. Gidon, B. Gautier, *J. Appl. Phys.* **2011**, *110*, 1.

[10] S. M. Neumayer, E. Strelcov, M. Manzo, K. Gallo, I. I. Kravchenko, A. L. Kholkin, S. V. Kalinin, B. J. Rodriguez, *J. Appl. Phys.* **2015**, *118*, 1.

[11] A. V. Ievlev, S. Jesse, A. N. Morozovska, E. Strelcov, E. A. Eliseev, Y. V. Pershin, A. Kumar, V. Y. Shur, S. V. Kalinin, *Nat. Phys.* **2013**, *10*, 59.

[12] A. Brugère, S. Gidon, B. Gautier, *J. Appl. Phys.* **2011**, *110*, 052016.

[13] A. V. Ievlev, S. Jesse, A. N. Morozovska, E. Strelcov, E. A. Eliseev, Y. V. Pershin, A. Kumar, V. Y. Shur, S. V. Kalinin, *Nat. Phys.* **2013**, *10*, 59.

[14] B. L. Weeks, M. W. Vaughn, J. J. DeYoreo, *Langmuir* **2005**, *21*, 8096.

[15] J. L. Wang, B. Vilquin, N. Barrett, *Appl. Phys. Lett.* **2012**, *101*, 1.

[16] J. L. Wang, F. Gaillard, A. Pancotti, B. Gautier, G. Niu, B. Vilquin, V. Pillard, G. L. M. P. Rodrigues, N. Barrett, *J. Phys. Chem. C* **2012**, *116*, 21802.

[17] X. Li, B. Wang, T. Y. Zhang, Y. Su, *J. Phys. Chem. C* **2014**, *118*, 15910.

[18] H. Lee, T. H. Kim, J. J. Patzner, H. Lu, J. W. Lee, H. Zhou, W. Chang, M. K.

Mahanthappa, E. Y. Tsymbal, A. Gruverman, C. B. Eom, *Nano Lett.* **2016**, *16*, 2400.

[19] K. Suzuki, T. Hosokura, T. Okamoto, J. Steffes, K. Murayama, N. Tanaka, B. D. Huey, *J. Am. Ceram. Soc.* **2018**, *101*, 4677.

[20] N. Domingo, E. Pach, K. Cordero-Edwards, V. Pérez-Dieste, C. Escudero, A. Verdaguer, *Phys. Chem. Chem. Phys.* **2019**, *21*, 4920.

[21] G. Geneste, B. Dkhil, *Phys. Rev. B - Condens. Matter Mater. Phys.* **2009**, *79*, 1.

[22] N. Tymińska, G. Wu, M. Dupuis, *J. Phys. Chem. C* **2017**, *121*, 8378.

[23] J. Y. Son, G. Lee, Y. H. Shin, *Appl. Phys. Lett.* **2009**, *94*, 3.

[24] B. J. Rodriguez, R. J. Nemanich, A. Kingon, A. Gruverman, S. V. Kalinin, K. Terabe, X. Y. Liu, K. Kitamura, *Appl. Phys. Lett.* **2005**, *86*, 012906.

[25] A. Agronin, M. Molotskii, Y. Rosenwaks, G. Rosenman, B. J. Rodriguez, A. I. Kingon, A. Gruverman, *J. Appl. Phys.* **2006**, *99*, 104102.

[26] P. Paruch, T. Giamarchi, T. Tybell, J. M. Triscone, *J. Appl. Phys.* **2006**, *100*, 51608.

[27] T. Tybell, P. Paruch, T. Giamarchi, J. M. Triscone, *Phys. Rev. Lett.* **2002**, *89*, 8.

[28] T. Aoki, Y. Hiranaga, Y. Cho, *J. Appl. Phys.* **2016**, *119*, 184101.

[29] Y. Hiranaga, T. Uda, Y. Kurihashi, H. Tochishita, M. Kadota, Y. Cho, *Jpn. J. Appl. Phys.* **2009**, *48*, 09KA18.

[30] K. Cordero-Edwards, L. Rodríguez, A. Calò, M. J. Esplandiu, V. Pérez-Dieste, C. Escudero, N. Domingo, A. Verdaguer, *J. Phys. Chem. C* **2016**, *120*, 24048.

[31] D. B. Asay, S. H. Kim, *J. Phys. Chem. B* **2005**, *109*, 16760.

[32] A. Verdaguer, G. M. Sacha, M. Luna, D. Frank Ogletree, M. Salmeron, *J. Chem. Phys.* **2005**, *123*, 124703.

[33] I. Gaponenko, L. Gamperle, K. Herberg, S. C. Muller, P. Paruch, *Rev. Sci. Instrum.* **2016**, *87*, 063709.

[34] S. Jesse, A. P. Baddorf, S. V Kalinin, *Appl. Phys. Lett.* **2006**, *88*, 062908.

[35] A. N. Morozovska, S. V. Svechnikov, E. A. Eliseev, S. Jesse, B. J. Rodriguez, S. V. Kalinin, *J. Appl. Phys.* **2007**, *102*, 114108.

[36] L. J. McGilly, L. Feigl, T. Sluka, P. Yudin, A. K. Tagantsev, N. Setter, *Nano Lett.* **2016**, *16*, 68.

[37] L. J. McGilly, P. Yudin, L. Feigl, A. K. Tagantsev, N. Setter, *Nat. Nanotechnol.* **2015**, *10*, 145.

[38] P. Paruch, J. Guyonnet, *Comptes Rendus Phys.* **2013**, *14*, 667.

[39] P. Paruch, T. Giamarchi, T. Tybell, J. Triscone, *J. Appl. Phys.* **2006**, *100*, 051608.

[40] N. A. Pertsev, A. Petraru, H. Kohlstedt, R. Waser, I. K. Bdikin, D. Kiselev, A. L. Kholkin, *Nanotechnology* **2008**, *19*, 375703.

[41] N. A. Pertsev, D. A. Kiselev, I. K. Bdikin, M. Kosec, A. L. Kholkin, *J. Appl. Phys.* **2011**, *110*, 052001.

[42] P. V Yudin, M. Y. Hrebtov, A. Dejneka, L. J. McGilly, *Phys. Rev. Appl.* **2020**, *13*, 14006.

[43] P. Sharma, R. G. P. McQuaid, L. J. McGilly, J. M. Gregg, A. Gruverman, *Adv. Mater.* **2013**, *25*, 1323.

[44] A. P. Turygin, M. M. Neradovskiy, N. A. Naumova, D. V. Zayats, I. Coondoo, A. L. Kholkin, V. Y. Shur, *J. Appl. Phys.* **2015**, *118*, 072002.

[45] H. J. Butt, M. Kappl, *Adv. Colloid Interface Sci.* **2009**, *146*, 48.

[46] J. T. Newberg, D. E. Starr, S. Yamamoto, S. Kaya, T. Kendelewicz, E. R. Mysak, S. Porsgaard, M. B. Salmeron, G. E. Brown, A. Nilsson, H. Bluhm, *Surf. Sci.* **2011**, *605*, 89.

[47] N. Domingo, I. Gaponenko, K. Cordero-Edwards, N. Stucki, V. Pérez-Dieste, C. Escudero, E. Pach, A. Verdaguer, P. Paruch, *Nanoscale* **2019**, *11*, 17920.

[48] L. Sirghi, *Langmuir* **2012**, *28*, 2558.

[49] B. L. Weeks, J. J. DeYoreo, *J. Phys. Chem. B* **2006**, *110*, 10231.

[50] J. U. Keller, R. Staudt, *Gas Adsorption Equilibria*, Kluwer Academic Publishers, **2005**.

[51] X. Deng, T. Herranz, C. Weis, H. Bluhm, M. Salmeron, *J. Phys. Chem. C* **2008**, *112*, 9668.

[52] L. Chen, X. He, H. Liu, L. Qian, S. H. Kim, *J. Phys. Chem. C* **2018**, *122*, 11385.

[53] T. Rakitskaya, A. Truba, G. Dzhyga, A. Nagaevs'ka, V. Volkova, *Colloids and Interfaces* **2018**, *2*, 61.

[54] L. Fumagalli, A. Esfandiar, R. Fabregas, S. Hu, P. Ares, A. Janardanan, Q. Yang, B. Radha, T. Taniguchi, K. Watanabe, G. Gomila, K. S. Novoselov, A. K. Geim, *Science*

2018, *360*, 1339.

[55] A. Calò, N. Domingo, S. Santos, A. Verdaguer, *J. Phys. Chem. C* **2015**, *119*, 8258.

[56] B. P. Dhonge, S. S. Ray, B. Mwakikunga, *RSC Adv.* **2017**, *7*, 21703.

[57] A. Verdaguer, J. J. Segura, J. Fraxedas, H. Bluhm, M. Salmeron, *J. Phys. Chem. C* **2008**, *112*, 16898.

[58] G. Tocci, A. Michaelides, *J. Phys. Chem. Lett.* **2014**, *5*, 474.

[59] S. Ø. Stub, E. Vøllestad, T. Norby, *J. Phys. Chem. C* **2017**, *121*, 12817.

CHAPTER 6

Beyond atmospheric adsorbates: Functionalization of ferroelectric $BaTiO_3$ surfaces

The purpose of this chapter is to investigate the effects of adsorbates other than the up to now studied water on the ferroelectric properties of $BaTiO_3$ thin films. In this regard, the process of chemical functionalization of $BaTiO_3$ thin films by aromatic para-aminobenzoic acid (pABA) molecules by microcontact technique will be discussed, as well as the characterization of such hybrid organic/ferroelectric heterostructures by different Atomic Force Microscopy-based modes. Effect of pABA molecular layer on ferroelectric properties was probed by identifying the polarization state, as well as by measuring hysteresis loops of pABA/$BaTiO_3$ heterostructures and capacitors by Piezoresponse force microscopy in imaging and switching spectroscopy mode.

6.1 Introduction

Due to the discontinuity of polarization at ferroelectric surfaces and consequential presence of detrimental depolarization field, ferroelectric materials come up with different ways to diminish it. External screening by adsorbates, including dipolar as well as charged ionic species, has been proven to be very effective in stabilizing ferroelectric phase, making physical and surface chemical properties of ferroelectric materials intrinsically inseparable.[1] This distinctive physico-chemical interconnection in ferroelectricity, which is bidirectional in the nature, is manifest in different works in which changes in the surface chemistry caused changes of physical properties such as imprint,[2] remanence,[3] or even increased tunneling electroresistance in FTJ devices.[4] By the same token, changes in ferroelectric polarization, which lead to modification of surface binding energies and barriers for reactions of reactant molecules,[5,6] enable ferroelectrics as tunable catalytic materials for green H_2 production and environmental remediation.[7–9]

Up to now, the most commonly studied ferroelectric-adsorbate interactions were the electrochemical couplings between ferroelectric polarization and atmospheric adsorbates such as H_2O (in molecular or dissociated form, as H_3O^+ and OH^- groups, as well as different peroxide-like species) and O_2.[10–13] Albeit adsorbates can have beneficial effects on ferroelectric properties, their spontaneous formation on ferroelectric surfaces not protected by electrodes is very difficult to control due to the electrochemical reactions at the solid-vapor interface with environment, possibly leading to surface reconstruction,[6] sample degradation,[14] dependence of sample's history[15] or polarization switching.[12,16–19] In this sense, uncontrolled environmental exposure can have potentially detrimental influence on ferroelectric devices used for instance for data storage, whereby the written information could be lost. On the other hand, interfacial chemistry plays important role in ferroelectric tunnel junctions (FTJs) applications, in the case when 2D materials are used as a top electrode: it has been demonstrated that one can tune electric boundary conditions by interface engineering of ferroelectric films in FTJ devices with a graphene top electrode, improving their performance and retention times.[4] Nevertheless, preparation of these structures on bare ferroelectric surfaces is a complex task, since it is often difficult to control the type and role of adsorbates trapped between the ferroelectric surface and the 2D electrode, which in turn can have unpredictable impact on the device performance.

The strategy we propose here in order to overcome these issues is the chemical modification of ferroelectric surfaces by controlled functionalization with organic molecules, thereby enabling stable and predictable surface chemistry, independent of external uncontrolled conditions and compatible with switching between ferroelectric states. Hybrid organic-inorganic materials are widely exploited in chemistry for myriad applications where the combination of properties leads to enhanced functionalities, in systems such as biocompatible core-shell nanoparticles[20] or metal-organic open frameworks,[21] to name a couple of relevant examples. Moreover, they have turned to be a breakthrough in the field of solar energy, where the emergence of hybrid organic perovskite solar cells has led to enhanced efficiencies.[22]

In this sense, the synthesis of hybrid organic-ferroelectric structures could pave the way towards chemically-controlled ferroelectric polarization, whereby the surface molecules could become an active capping layer which, besides having a protective role, could bring functional benefits such as improved polarization stability or increase of remanence.

While there is a growing body of literature on the interaction between ferroelectric surfaces and inorganic molecules (O_2, H_2O, NH_3 etc.),[4,11,16,17,23] less is known about the interaction between ferroelectrics and organic molecules.[24–28] Yet there is a catalogue of industrially-produced organic molecules with specific functionalities (i.e. acting as light,[29] magnetic field[30] or heat-sensitive elements[31]), which could be combined with ferroelectricity, opening the pathway to new multifunctional hybrid organic ferroelectric devices. Additionally, surface functionalization could enable new nanopatterning strategies based on selectively attaching organic molecules to pre-written ferroelectric domains or, conversely, use molecular attachment (via e.g. stamping or dip-pen nanolithography) to chemically write polarization or selectively tune ferroelectric properties. In this sense, selective reduction of metallic nanoparticles by photo generated charge was reported on up-polarized domains, whereby formed particles could be used as centers for the selective attachment of molecules functionalized with chemical groups that react preferentially with used metals.[32,33] However, possible influence of molecular entities through nanoparticles attachment on ferroelectric properties was not studied.

In this chapter, we investigate hybrid organic-inorganic heterostructures, based on the functionalization of BTO thin films with para-aminobenzoic acid (pABA) molecules and demonstrate the active role of these organic components on the stabilization of ferroelectric polarization. pABA molecules have been selected as candidates for this study due to their high

degree of delocalization of electrons throughout the benzene ring and its carboxylic and amino group substituents.[34] Free amino (–NH_2) group is an electron donor able to couple its lone electron pair with the high electron density of the benzene ring and further with the lone electron pairs of oxygen atoms in the carboxylic (COOH) group.[35] That means that pABA molecules can be considered as a fully delocalized electronic system,[35] whose structure is typically depicted by the resonance hybrid,[34,36] representing weighted averaged contribution of several resonance structures (distinct configurations of the electronic distribution within the molecule), as shown in **Figure 6.1**. The weighted contribution of each configuration in the resonant hybrid depends on its stability.

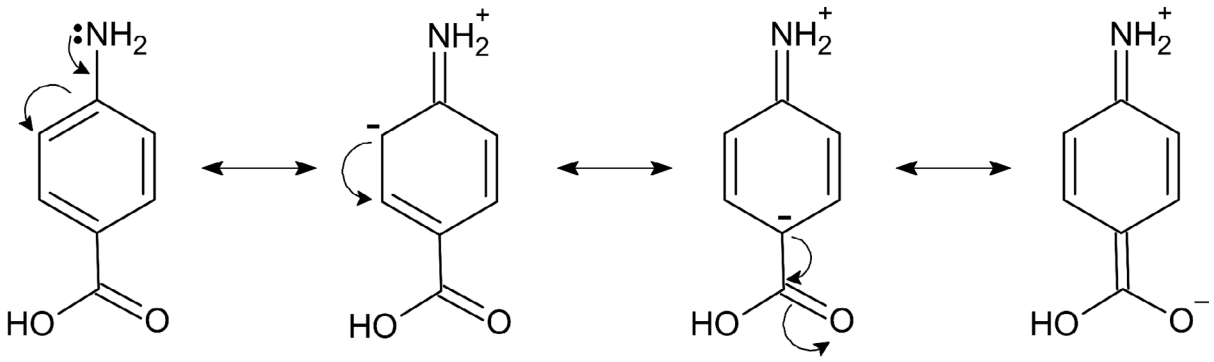

Figure 6.1 *Some resonance structures of pABA aromatic molecule contributing to the resonance hybrid. The free –NH_2 group is an electron donor able to couple its lone electron pair with the high electron density of benzene ring and further with lone electron pairs of oxygen atoms in the carbonyl (C=O) group and the -OH group of the carboxylic (COOH) substituent, giving rise to the resonance hybrid structure.*

Since small changes in electronegativities of substituting groups can cause different confinement of the delocalized electrons and modify their dipole moments, we expect that such aromatic molecules should be far more versatile in providing screening to ferroelectric surfaces which are natively charged, as compared to inorganic molecules or simple dipoles.

This chapter is organized as follows. First, I describe the BTO thin films functionalization by microcontact printing and its characterization by various chemically-sensitive AFM modes (e.g. KPFM, Bimodal AFM and AM-FM). Then, we focus on the effect of pABA organic layers on the ferroelectric properties. I demonstrate that the hybrid organic-ferroelectric structure leads to an enhancement of the coercive field of both polarization states, associated to an increase of ferroelectric polarization stability. Such behavior is shown to be linked to the tunability of the pABA resonance structure as a function of the underneath polarization: upward polarization attracts the delocalized electrons, acting as negative screening agents, towards the

substrate-anchoring carboxylic group, while downward polarization repels the delocalized electrons further from the surface towards the benzene ring.

Furthermore, we probe the screening efficiency of hybrid organic ferroelectric heterostructures in capacitor-like geometry, build up from pABA functionalized BTO thin films sandwiched between SRO bottom and multilayer graphene top electrode (Graphene/pABA/BTO/SRO/STO). Lastly, as it will be shown at the end of the chapter, pABA molecules play an additional "protective" role, by shielding ferroelectric polarization against potentially detrimental external influences such as surface oxidation, culprit of spontaneous polarization reversal in non-functionalized areas of the BTO thin film.

6.2 Functionalization of $BaTiO_3$ thin films with p-aminobenzoic acid molecules

High-quality epitaxial ferroelectric BTO/SRO bilayers were grown by PLD technique on as-received (001) oriented STO single crystalline substrates. The growth parameters, detailed preparation procedure and structural characterization of SRO/BTO bilayers have been explained previously in detail in Chapter 2. In this experiment, we used SRO/BTO bilayers with thicknesses of 30 nm and 14 nm, respectively.

BTO thin films were functionalized using 0.1 M solution of p-aminobenzoic acid (pABA, purified by sublimation, ≥ 99%, Sigma Aldrich) in gamma-butyrolactone (GBL, reagentplus ≥ 99%, Sigma Aldrich) solvent. Since pABA is hygroscopic, all reagents were stored and later used for solution preparation inside of a controlled humidity glove box.

Controlled nanopatterning of pABA molecules on BTO thin films was done by microcontact printing (μCP) using a polymeric stamp made of polydimethylsiloxane (PDMS) in order to create a pattern of molecular layers of pABA "ink" on the ferroelectric surface. In this experiment, 1 cm x 1 cm PDMS stamps with square-like features of 5 μm x 5 μm separated by 10 μm was used. First, PDMS stamp was inked with pABA solution in GBL by spreading 200 μl droplet of solution over it. This step is necessary in order to let pABA molecules adsorb onto the PDMS stamps. After 20 minutes, pABA solution was removed from PDMS surface and slightly dried using N_2 flow. The PDMS stamp was then placed in conformal contact with the BTO thin film during 15 minutes, after which it was carefully separated from the BTO

substrate. After functionalization, the BTO thin film was subjected to thermal annealing on a hot plate at 80 ºC during 30 min in order to evaporate the solvent.

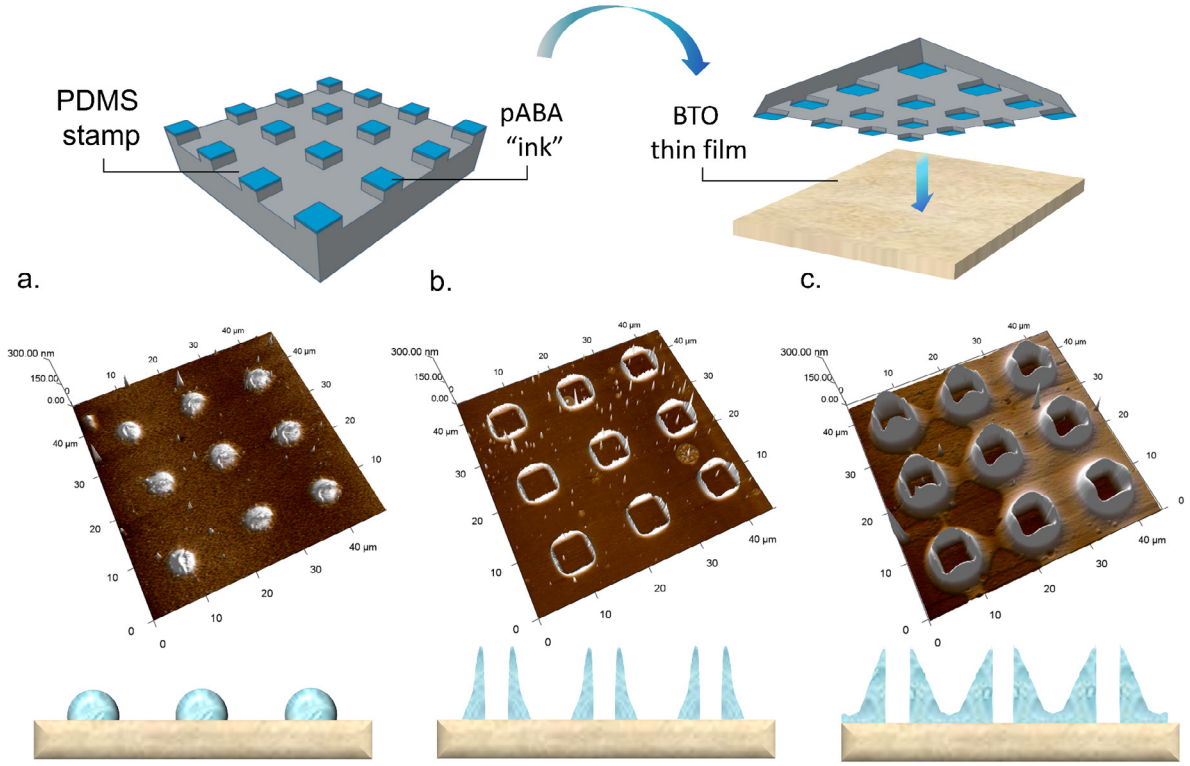

Figure 6.2 *Top: Schematic representation of microcontact printing (μCP) of pABA molecules on BTO thin films. The square features are 5x5 μm and are separated by 10 μm. Middle: 3D AFM topography images and the corresponding schematic representation of the cross-sections along the vertical axis of pABA molecular patterns on the BTO thin film surfaces (bottom). Three kinds of molecular patterns can be distinguished on the surface: (a) transfer of pABA molecules under the stamp squares; (b) transfer of pABA molecules only in the perimeter of the square-like features, while the rest of the surface remains clean; and (c) transfer of pABA at the square perimeter and also in the surrounding areas in-between the reliefs, either forming bridges connecting square-like features (light-brown areas, mainly on the left hand side) or completely covering the surface (right-hand side). The inner square areas of* ***Figure 1b*** *and 1c are pABA-free and represent bare BTO surface. AFM topography images have dimensions of 45 μm x 45 μm.*

Surface nanopatterning is a complex process that depends on many factors such as the ink and substrate chemical interaction, ambient humidity and temperature or the force applied to the stamp, etc., and more importantly it depends on the affinity of the molecules to be transferred towards the chosen substrate surface.[37] **Figure 6.2** shows a schematic representation of the μCP stamping process (top), together with the corresponding AFM 3D topography images (middle) of patterns observed to form on BTO surfaces after μCP. On the bottom are

schematically represented the cross-sections along the vertical axis of pABA molecular patterns on the BTO thin film surfaces.

Under optimal conditions, the transfer of pABA molecules happens under the stamp relief leading to a pattern of spherical islands of pABA as shown in **Figure 6.2 a**. The increase of the printing force or excess of ink can lead to the displacement of the molecules towards the side of the prominent features of the stamp as shown in **Figure 6.2 b**. In this case, the pABA molecules are found only in the perimeter of the square-like reliefs, leaving the inner and outer parts uncovered, i.e., with the BTO ferroelectric surface directly exposed as schematically shown at the bottom of the image. Finally, such conditions can also lead to the formation of patterns similar to those shown in **Figure 6.2 c**, where pABA molecules are present in high amounts at the perimeter of square-like features, but are also forming layers in the in-between areas. The observed inter-square molecular layers can partially cover the surface by forming "bridges" between neighboring squares (left hand side of **Figure 6.2 c**), or show a complete coverage as observed in the right-hand side of **Figure 6.2 c**. In both cases, the inner parts of the squares are molecule-free and represent bare BTO surface. Albeit the different patterns obtained, μCP printing is a useful technique for chemical patterning of BTO surfaces by pABA molecules providing us with surface features that are geometrically repeatable and easy to distinguish by simple topography scans.

In order to unambiguously prove the presence of pABA molecules on BTO surfaces we employed Kelvin Probe Force Microscopy (KPFM) and multifrequency AFM imaging (MF-AFM) in Bimodal and AM-FM mode. **Figure 6.3 a** shows AFM topography of pABA molecules on a micropatterned BTO sample. From the topography image, the presence of molecules in the perimeter of the square-like reliefs is evident, however it is not clear whether there are some molecular layers also inside or outside the square-like patterns.

Figure 6.3 b shows the corresponding contact potential difference (CPD) image obtained by KPFM. The observed CPD contrast between inner and outer regions of the square-like features points out to the different chemical composition of these two areas of the surface, corresponding to bare BTO surface and pABA-functionalized BTO surface. **Figures 6.3 c,d** show amplitude A_1 and phase φ_1 respectively of the fundamental resonance frequency f_1, used to measure the topography. **Figures 6.3 e,f** show amplitude A_2 and phase φ_2 of the second eigenmode imaged by Bimodal AFM, showing a darker contrast of the inner part of the squares as compared to the surrounding area (not including the topographic cross-talk with the squared

ring features). Furthermore, from AM-FM viscoelastic mapping, Young's modulus and indentation of the material are obtained and shown in **Figure 6.3 g** and **6.3 h**. It is clear that the area surrounding the square-like features exhibits lower values of the Young modulus as compared to their inner area (**Figure 6.3 g**) indicating the presence of soft molecules decreasing the stiffness of the surface as compared to bare BTO film. This is also in agreement with the higher indentation values observed in the softer pABA functionalized areas shown in **Figure 6.3 h**.

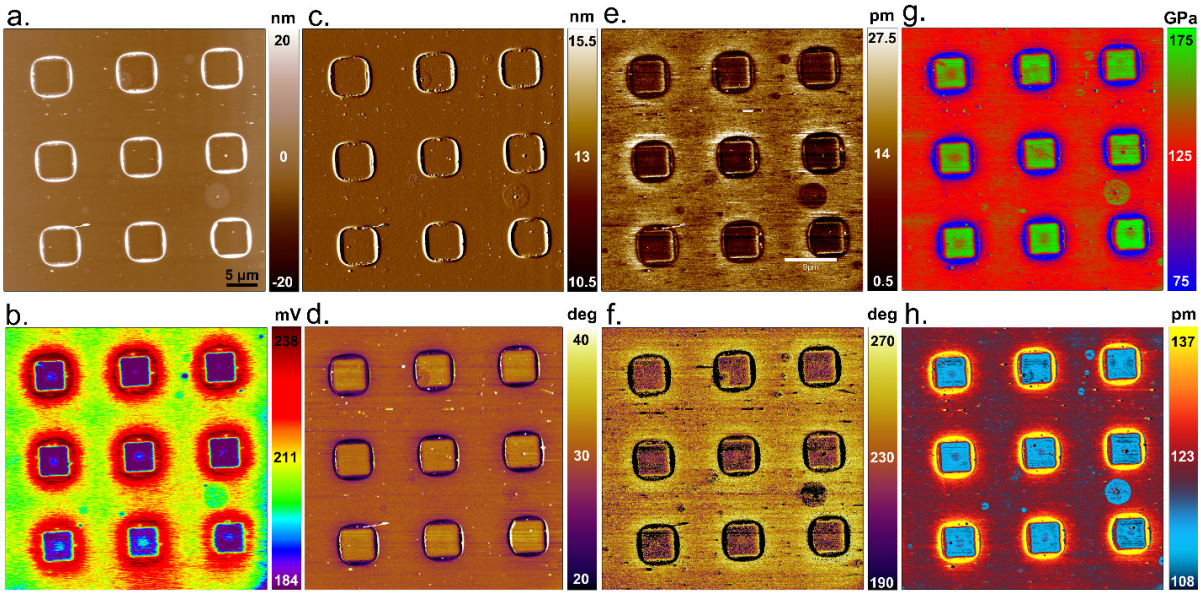

Figure 6.3 *AFM imaging of microcontact printed patterns of pABA molecules on a BTO thin film; (a) AFM tapping mode topography; (b) contact potential difference as measured by KPFM; (c) amplitude A_1 and (d) phase φ_1 of the fundamental resonant frequency f_1; (e) amplitude A_2 and (f) phase φ_2 of the second eigenmode at f_2, as imaged in Bimodal AFM; (g) Young's modulus and (h) Indentation obtained by AM-FM Viscoelastic Mapping. Value of fundamental resonance frequency was f_1 = 71.8 kHz and that of the second eigenmode was f_2 = 457.0 kHz, with a ratio f_2/f_1 = 6.4 Detailed explanation of images can be found in the main text.*

It is important to notice that all of these AFM modes are performed in intermittent (tapping), repulsive mode and are therefore very useful as non-invasive techniques for obtaining information about chemical and/or mechanical properties of functionalized samples with high lateral resolution without perturbing the surface: multifrequency AFM characterization proves the efficiency of the µCP patterning, providing direct evidence of BTO ferroelectric exposed surface inside the squares and the presence of pABA molecules everywhere around the square-like features.

Once the successful formation of pABA molecular layers by micropatterning is confirmed, it is important to determine the way in which pABA molecules bind to BTO surfaces. To this end, we used standard and micro-Fourie transform infrared spectroscopy (FT-IR), which enabled us to visualize and pinpoint exactly where to obtain an IR spectrum. **Figure 6.4** shows IR spectra in transmittance mode of pABA powder (**Figure 6.4 a**) and pABA-functionalized BTO surface (**Figure 6.4 b**). The spectra of the free pABA molecules demonstrates two strong peaks at 3459 and 3359 cm^{-1} originating from asymmetric and symmetric vibration of $–NH_2$ group. Peaks at 1621, 1571, 1520 and 1440 cm^{-1} are related to stretching C=C vibration of aromatic benzene ring, while peaks at 1308 and 1167 cm^{-1} belong to C-N stretching and C-H in plane vibrations of benzene ring, respectively. Two peaks at 1657 and 1277 cm^{-1} can be assigned to the stretching C=O and C-OH vibrations of the carboxylic –COOH group.[38,39] In the case of chemically functionalized BTO, peaks at 1657 and 1277 cm^{-1} disappear and two new peaks at 1625 and 1359 cm^{-1} appear. They correspond to the asymmetric and symmetric vibration of carboxylate anion (COO^-) respectively.[38] The observed frequency difference of 266 cm^{-1} between them suggests that carboxylic groups are deprotonated to COO^- and that pABA molecules are bound to the BTO surface by monodentate ester-like linkage.[40,41]

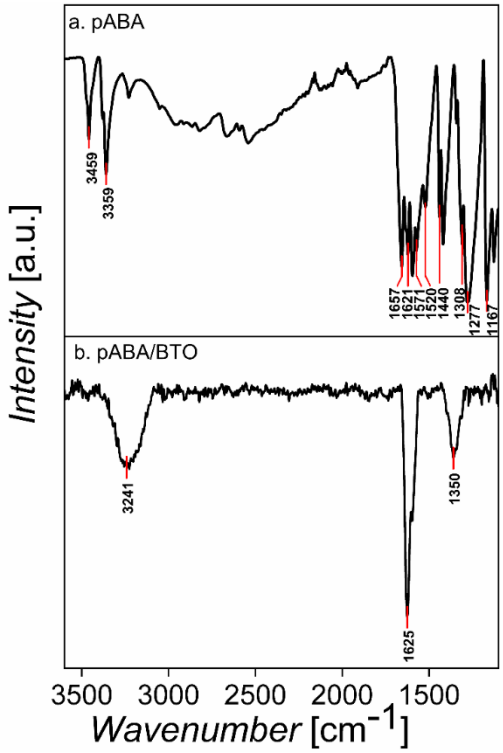

Figure 6.4 *Infrared (IR) spectra of (a) pure pABA powder and (b) pABA functionalized BTO thin film. In the case of chemically functionalized BTO, peaks at 1657 and 1277 cm^{-1} belonging to intact carboxylic group disappear and two new peaks at 1625 and 1359 cm^{-1} appear which correspond to asymmetric and symmetric vibration of carboxylate anion (COO^-).*

Due to the low concentration of molecules on the BTO surface, some relatively weak peaks cannot be detected. It ought to be mentioned that the surface of BTO was air-exposed prior to its functionalization and therefore substantially hydroxylated with –OH groups, as observed for BTO thin film surfaces in atmospheric conditions in Chapter 3. The obtained spectra suggest that pABA molecules bind to BTO surface via ester-like bonds which form between surface –OH groups and –OH from carboxylic groups, while carbonyl C=O groups remain intact. This is in agreement with studies of pABA functionalized TiO_2 surfaces[38,39] and therefore relevant to BTO thin films. Since pABA molecules are polar, the way in which they chemically attach to the BTO surface and therefore orientation of their dipole moments is of particular importance when coupled with ferroelectricity. Conversely, molecules' dipole moments could also be potentially altered by the polarization of the thin film. This bidirectional interplay will be investigated in the following section.

6.3 Coupling of pABA molecules and ferroelectric polarization in $BaTiO_3$ thin films

The properties of ferroelectric materials are connected to their surface chemistry as a consequence of the discontinuity of bound polarization charge at ferroelectric surfaces and resulting depolarization fields.[42] In order to delve into the impact that pABA surface-chemical modification has on the ferroelectric properties of BTO thin films, we used PFM in combination with ferroelectric switching spectroscopy measurements (SS-PFM). **Figure 6.5** shows topography, PFM phase images and hysteresis loops (of PFM amplitude and PFM phase) of as-grown BTO (**Figure 6.5 a,b,c**), non-functionalized BTO surface (**Figure 6.5 d,e,f**) and pABA-functionalized BTO thin film (**Figure 6.5 g,h,i**).

Figure 6.5 b shows the PFM phase image of electrically written ferroelectric domains. In this case ferroelectric lithography is done by applying a DC voltage of + 8 V and – 8 V to the tip while scanning in contact over an area of 3x3 and 1x1 μm^2, obtaining downward and upward polarized states, respectively. Phase contrast images show that the as-grown BTO thin film is out-of-plane up-polarized, as expected for BTO films grown under compressive strain on SRO buffered STO substrates.[43] SS-PFM hysteresis loops of as-grown BTO films reveal positive coercive voltage of V_c = 2.5 V and V_{bias} = + 0.75 V. The observed asymmetry of the loop, shifted to positive voltages, agrees with the preferential up-polarized state of as-grown BTO

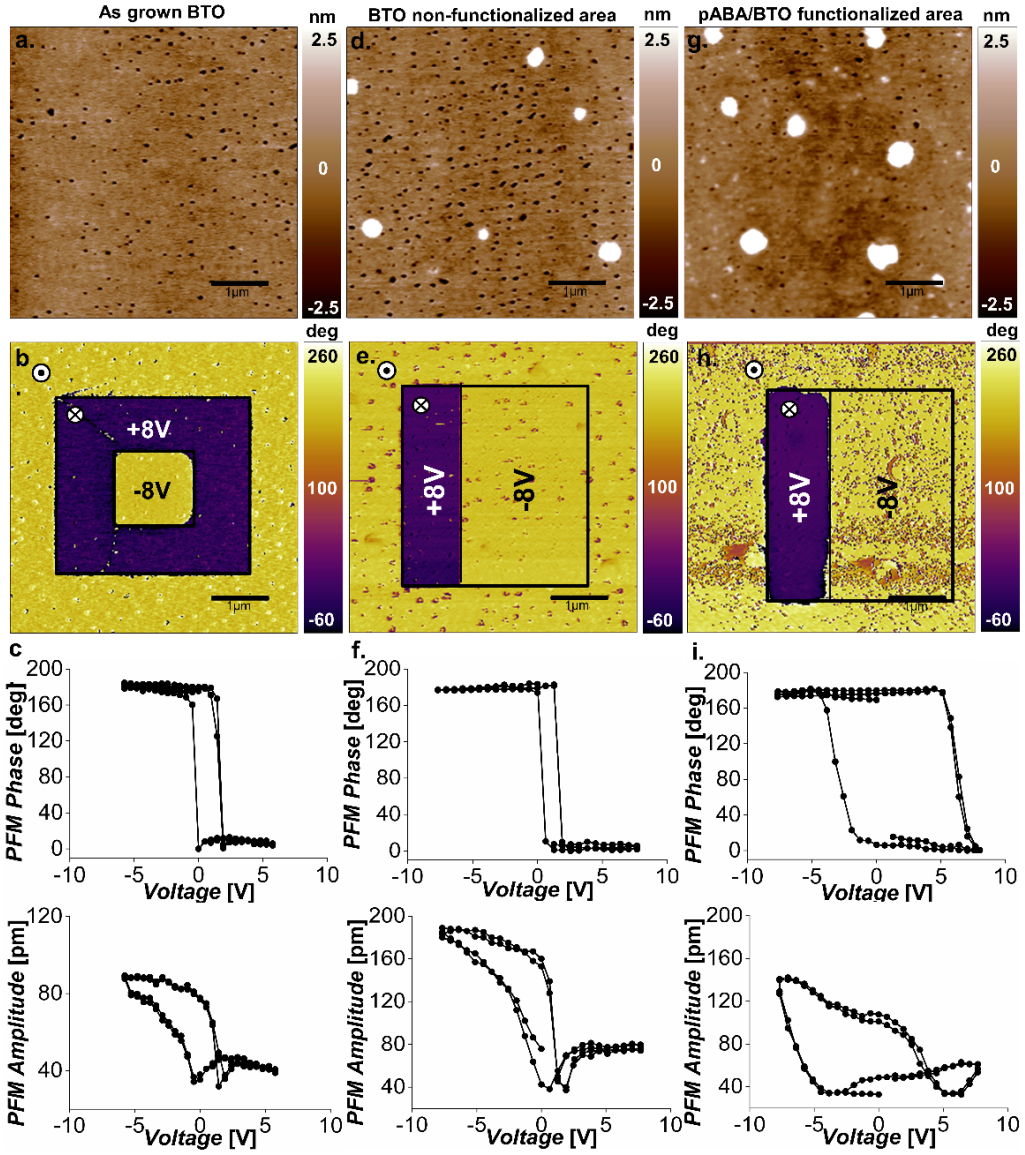

Figure 6.5 *Ferroelectric characterization of pristine and pABA-functionalized BTO thin films; AFM topography image of (a) pristine as-grown BTO film, (d) clean (non-functionalized) and (g) pABA-functionalized area of the same BTO thin film; PFM phase images of electrically written ferroelectric domains, by applying DC voltages of + 8 V and – 8 V to the AFM tip while scanning areas denoted by black lines in contact with (b) pristine as-grown BTO surface, (e) clean (non-functionalized) and (h) pABA-functionalized area of the same BTO thin film (pABA/BTO/SRO). From the phase contrast of PFM phase images, it can be seen that BTO film is up-polarized in all three cases; SS-PFM hysteresis loops and the corresponding amplitudes obtained on (c) pristine, (f) non-functionalized and (h) functionalized area of the same BTO thin film (pABA/BTO/SRO), where a drastic increase of the coercive field is observed as compared to pristine or non-functionalized BTO.*

thin film. Ferroelectric properties measured on the non-functionalized area of pABA-modified BTO thin film do not change significantly as compared to as-grown BTO as shown in **Figure 6.5 e,f**. After pABA-functionalization, BTO thin film keeps its as-grown up-polarized state

(**Figure 6.5 h**), but a drastic widening of PFM hysteresis loops of the hybrid organic-inorganic pABA/BTO/SRO heterostructure is observed, with a substantial enhancement of the coercivity up to V_c = 9.6 V and V_{bias} = + 1.6 V.

The overall increment of the coercive voltages, observed as a broadening of the hysteresis loops, can be interpreted as an enhancement of the stability of both, up and down polarization states due to the presence of pABA molecules on the BTO surface. In other words, the pABA molecules provide an efficient screening for both signs of the ferroelectric polarization. We propose that the change of the polarization state of the underneath ferroelectric film, and therefore the sign of the necessary screening charge, leads to a selective and reversible change of pABA resonance states' stability in its energetic landscape, with distinct delocalization of electrons.

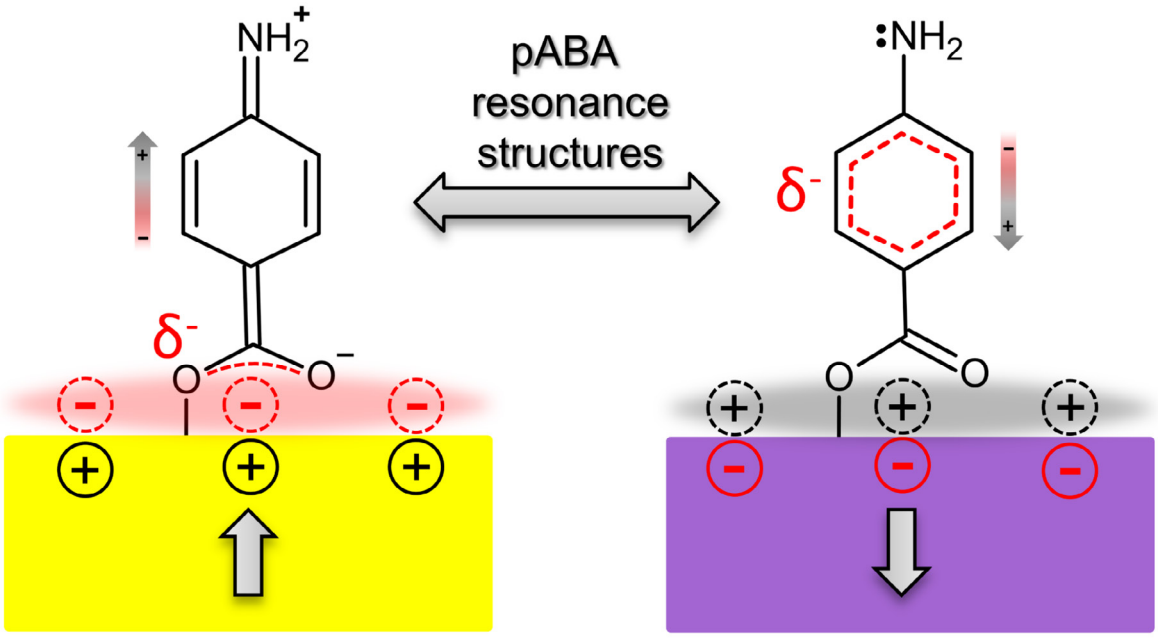

Figure 6.6 *Schematic representation of the BTO ferroelectric polarization screening mediated by two different pABA resonance structures, with distinct delocalization of electrons, induced by the polarization orientation of the underneath BTO film. In the case of up polarized state (left), pABA molecules delocalize electrons from the electrodonating amino group and benzene ring towards the carboxylic group and act as negative screening agents in the vicinity of the surface, making up-polarized state highly stable. Delocalized electrons are represented by red dashed lines. Reversibly, in the case of down polarized state, all negative charges in the vicinity of the surface are repelled and delocalized inside the benzene ring in order to maintain positive charge screening conditions, now making down-polarized state highly stable. Therefore, pABA molecules can be considered as self-regulating resonance structures for on-demand ferroelectric polarization screening and stabilization.*

In the case of up-polarized ferroelectric state which requires negative screening charge, delocalized electrons from electro-donating amino group and benzene ring are attracted towards the carboxylic group and act as additional negative screening agents in the vicinity of the surface (**Figure 6.6** left). Oppositely, down polarized BTO thin films will repel negative charges in the vicinity of the surface and delocalize the electrons inside of benzene ring in order to achieve more positive ferroelectric screening (**Figure 6.6** right). To this extent pABA molecules can act as highly tunable electroactive species, which thanks to their unique aromatic structure, can supply or take electrons to and from the vicinity of the ferroelectric surface on-demand, depending on the polarization direction of underneath ferroelectric film.

As a consequence of this behavior, a considerable improvement of ferroelectric phase stability is observed resulting in an increment of the coercive field (**Figure 6.5 i**). It has been previously reported that inorganic molecules physiosorbed on ferroelectric surfaces such as NH_3 are able to rotate upon polarization reversal and therefore expose their electropositive (hydrogen) or electronegative (nitrogen) atoms closer or further from ferroelectric surfaces.[4] However, in our case pABA molecules are chemisorbed which makes impossible to rotate them; instead it is its electronic density which moves along delocalized bonds in order to screen the surface polarization, leading to a more robust hybrid ferroelectric structure.

However, the enhancement of the coercive field upon the presence of a surface organic layer may also be the consequence of so called “passive layer” or “dead layer” effect. This term is normally used in the studies of ferroelectric capacitors, where it depicts the presence of a layer with low dielectric constant connected as a parasitic capacitor in series with the underneath ferroelectric. In some cases, this layer could be attributed to the existence of physico-chemically different overlayer with degraded properties (caused by film processing itself) or to the finite screening lengths of non-ideal metallic electrodes, while in other cases its existence was predicted even in the case of perfect interfaces.[44] Whatever might be its origin, the presence of such a layer and its thickness could affect the electric field sensed by the sample and modify the measured coercive voltage, which should depend on the thickness of such layer.[45]

Figure 6.7 b shows the dependence of the mean coercive voltage ($V_c = |V_{c-}| + |V_{c+}|)/2$) on the pABA molecular layer thickness as measured by SS-PFM for two BTO samples. For each sample, hysteresis loops were probed in several different positions corresponding to different thicknesses of the pABA molecular layer on the BTO thin film as measured from the AFM

topography height profiles. Topography height profiles measured for Sample 1 are shown in **Figure 6.7 a**, denoting three different thicknesses of about 15, 25 and 30 nm for pABA molecular layer. It can be seen that the mean coercive voltage of each sample is nearly constant in the range of measured thicknesses, which clearly shows that pABA molecules do not contribute to an increase of the coercive field as a simple dielectric "passive layer", but rather as an electroactive layer which is able to supply/take negative charges from the near surface region on demand in the screening process dictated by the polarization of the underneath film. De facto, the pABA layer acts as a top electrode, which is why the properties of the effective capacitor are independent of the electrode thickness.

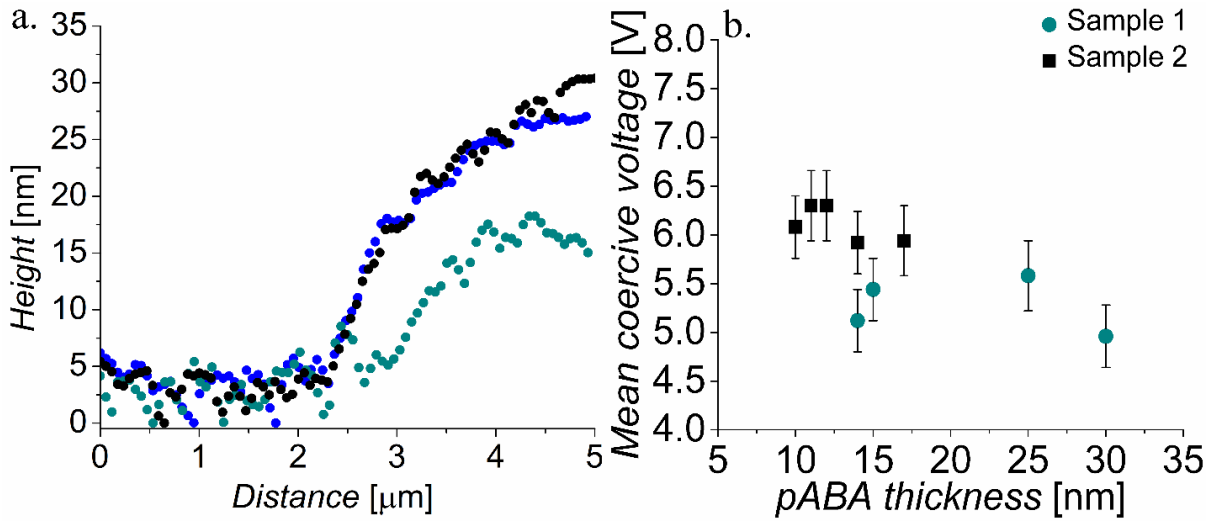

Figure 6.7 *(a) Topography height profiles across areas with different pABA molecular layer thickness measured for the sample 2; (b) Mean coercive voltage* $V=(|V_{c-}|+|V_{c+}|)/2$ *as a function of the thickness of pABA molecular layer for two BTO samples.*

6.4 Tunable electroactive $BaTiO_3$/pABA/2D interfaces

The combination of two-dimensional (2D) materials with ferroelectric films may result in novel properties of these hybrid materials arising from interface coupling between their intrinsic properties.[46–48] However, in ferroelectric oxides, and considering graphene as an archetypal 2D electrode material, it is hard to control the interface composition and the presence of intercalated molecules due to the transfer process of the graphene itself and also due the ubiquitous presence of surface adsorbates on ferroelectric surfaces,[11] which moreover strongly depends on the polarization state.[12,15,49] One way to overcome this issue is the

deliberate chemical functionalization of the ferroelectric surface, enabling a controlled tuning of the interface adsorbates: since adsorbates are inevitable, let us at least chose them ourselves so that they work in our favor. A useful adsorbate layer has to meet several requirements: i) it has to provide electrical screening to the bound charges and depolarization fields, so that ferroelectric polarization is stable and ii) it has to be able to adapt to the change in screening needs upon polarization reversal, so that the polarization can be switched. As we have just argued in the previous sections, pABA meets both criteria.

In our study, we transferred multilayer graphene patches to pABA-functionalized BTO thin films, in order to build hybrid organic-inorganic capacitor-like structures using graphene as the 2D top electrode (**Figure 6.8 a**). Graphene sheets with thickness between 10-20 nm were obtained by mechanical exfoliation of highly-oriented pyrolytic graphite (HOPG, SPI Supplies) using adhesive tape.[50] During this process, normal force is exerted on the HOPG surface in order to overcome the van der Waals attraction forces and to micromechanically cleave graphite sheets. Achieving very thin layers required several exfoliation steps. After exfoliation, the obtained multilayer graphene sheets were deposited onto pABA-functionalized BTO and used as top electrodes for PFM characterization. Beside other ways for graphene preparation and transfer,[51] mechanical exfoliation[50] was chosen in this work, since it doesn't involve contact of the functionalized substrate with any kind of solvents during the graphene transfer and avoids additional chemical modifications that might arise.

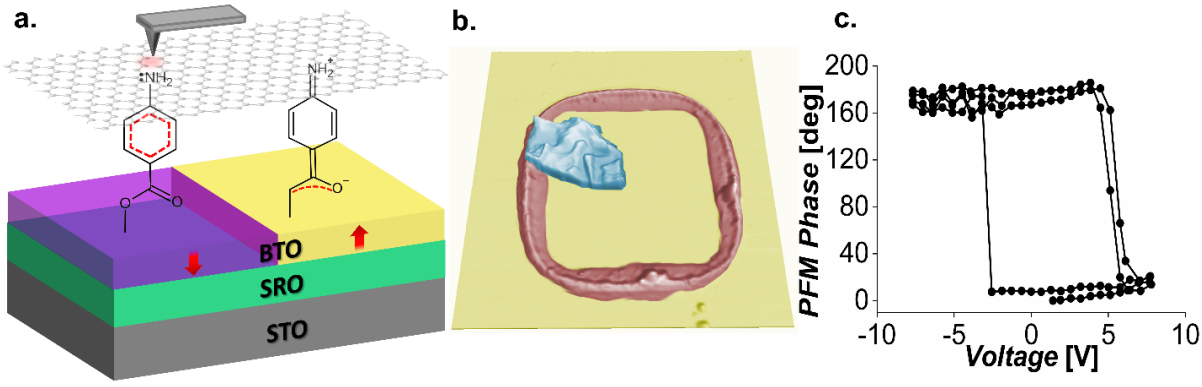

Figure 6.8 *Capacitor structures multilayer graphene/pABA/BTO/SRO; (a) Schematic representation of the different configurations the electroactive molecules are going through during hysteresis loop measurements over capacitor; (b) AFM 3D topography of pABA molecules (red) deposited on BTO thin films (yellow) in contact with multilayer graphene sheet (blue) and (c) SS-PFM hysteresis loops measured through graphene top electrode, closely resembling those measured directly on pABA molecules.*

3D topography image of the μCP deposited pABA molecules captured underneath graphene patch is presented in **Figure 6.8 b**. In order to probe hysteresis cycle of pABA molecules underneath the graphene patch, an AFM tip was placed in contact with it, as depicted in **Figure 6.8 a**, while voltage was cycled between -7.5 V and 7.5 V. It is important to mention that in this configuration, while the electric excitation signal in PFM spreads over the whole graphene electrode, the reading of the electromechanical response is strictly local and only senses the signal arising below the tip, meaning that the obtained hysteresis cycle corresponds uniquely to that of the graphene/pABA/BTO/SRO stack. The obtained hysteresis loop (**Figure 6.8 c**) has similar characteristics to those measured directly on top of the pABA molecules as shown in **Figure 6.5 i**. Therefore, an increment of the coercive field remains when the PFM hysteresis cycles are measured using the multilayer graphene as top electrode, suggesting that pABA molecules are efficient buffer layers between the ferroelectric material and a 2D electrode such as graphene.

6.5 pABA molecules as capping layers of $BaTiO_3$ thin films

As discussed in Chapter 3, the exposure of ferroelectric surfaces to ambient conditions can lead to surface reconstruction, sample degradation, aging effects or ferroelectric switching,[15] based on chemically-induced polarization reversal arising from environmental surrounding conditions, such as changes of oxygen partial pressure or relative humidity.[12,16–18] In this regard, besides acting as electroactive screening agents, the presence of organic molecular species on ferroelectric surfaces can also take the role of active capping layers to protect the ferroelectrics from detrimental interaction with the ambient.

Figure 6.9 shows the topography (**Figure 6.9 a,b**) and contact potential difference (CPD) images obtained by KPFM measurements (**Figure 6.9 c,d**) of two as-grown up-polarized samples with distinct pABA molecular distribution, schematically represented in **Figure 6.9 e,f**. The sample depicted in **Figure 6.9 a,c,e** (*Sample C*) has the same pABA molecular distribution shown in **Figure 6.3**, which corresponds to the presence of pABA molecules everywhere around square-like reliefs, while their inner surfaces represent bare BTO surface. On the other hand, in the sample shown in **Figure 6.9 b,d,f** (*Sample D*), some of the areas in between the squares are not fully functionalized, and pABA layer forms “bridges” between neighboring squares (left hand side of **Figure 6.9 b,f**).

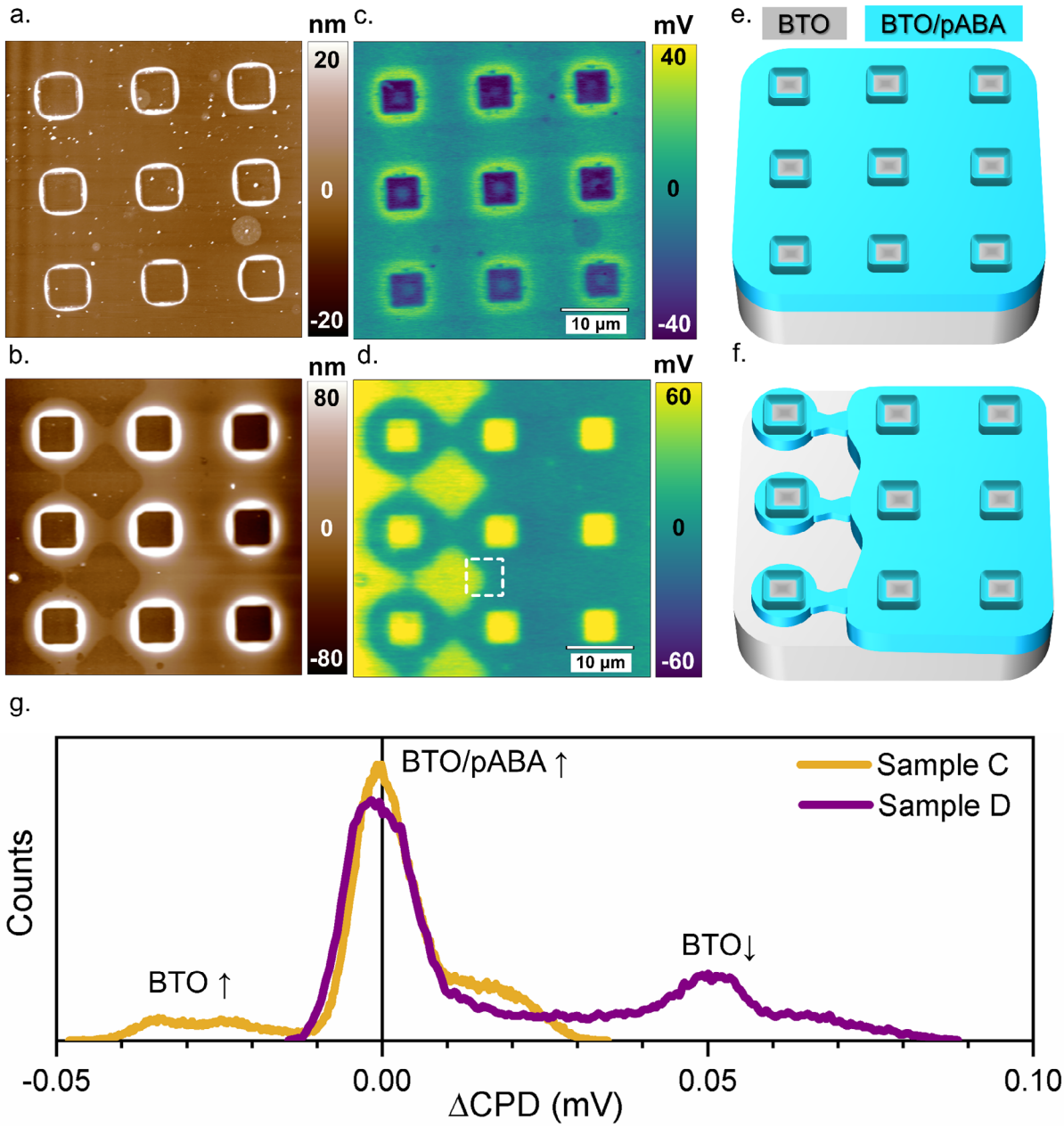

Figure 6.9 *KPFM characterization of microcontact printed patterns of pABA molecules on BTO thin films; (a), (b) AFM topography and (c), (d) corresponding contact potential difference (CPD) images obtained by KPFM for samples C and D with distinct pABA molecular distribution schematically represented in (e) and (f), respectively. Blue areas represent pABA functionalized BTO, while gray areas denote bare, molecules-free BTO; (g) Histogram analysis of CPD images for samples C and D, showing opposite trend of CPD evolution in the areas non-covered with pABA molecules as compared to functionalized BTO areas (see detailed explanation of the CPD contrasts in the text).*

In both cases, the inner parts of the squares are molecule-free and represent bare BTO surface. In the histogram analysis of KPFM data (**Figure 6.9 g**), the three main areas of CPD identified in **Figure 6.9 c,d** are quantified, corresponding to areas functionalized with pABA molecules

in samples *C* and *D (green)* and non-functionalized areas of sample *C*, at $\Delta CPD \sim$ - 35 mV (blue) and sample *D* at $\Delta CPD \sim$ + 50 mV (yellow), respectively.

In order to delve into relation between ferroelectric properties and electronic surface states of pABA-functionalized BTO we performed PFM characterization of both samples. Ferroelectric characterization of sample *C* has been explained earlier in the text (Section 6.3). In this case, bare and pABA-functionalized BTO are both up-polarized, and no changes in polarization state are observed after chemical modification **(Figure 6.5 h**).

Oppositely to sample *C*, **Figure 6.10** a,b shows KPFM and the corresponding PFM phase image of sample *D*, superimposed over topography 3D image of the area indicated by dashed rectangle on **Figure 6.9 d**. In this case, the PFM phase image (**Figure 6.10 a**) clearly shows 180˚ difference between bare and pABA-functionalized BTO indicating the opposite polarization direction in two mentioned regions and therefore spontaneous polarization switching in one of the studied areas.

To further confirm this point, we checked the polarization direction in bare and pABA-functionalized BTO areas of sample *D* by electrically writing consecutive stripes using + 8 V and – 8V voltages applied to the AFM tip. PFM phase images shown in **Figure 6.10 c,d** demonstrate that in sample *D*, pABA functionalized BTO surface keeps it's up-polarized state, while neighboring bare BTO switches polarization from as grown up- to down-polarized state. Further ferroelectric switching measurements in different parts of the sample confirmed that this polarization switching happened throughout the sample whenever BTO was not covered by a pABA molecular layer. Finally, the corresponding hysteresis loops of PFM amplitude and PFM phase measured by SS-PFM on the two different areas are presented in **Figure 6.10 e,f**, showing similar values of coercivity for non-functionalized (and down-switched) BTO and the persistence of coercive field increase of pABA/BTO hybrid heterostructures. It is also worth mentioning that although during PFM measurements we scan the surface in contact mode, there are no topographical changes of the pABA functionalized BTO even when high voltages are applied during ferroelectric poling, which ensures the presence of pABA molecules on the surface during PFM contact measurements.

Following from the work developed in Chapter 3, we believe that polarization switching in bare BTO happened as a consequence of an overall surface oxidation process spontaneously

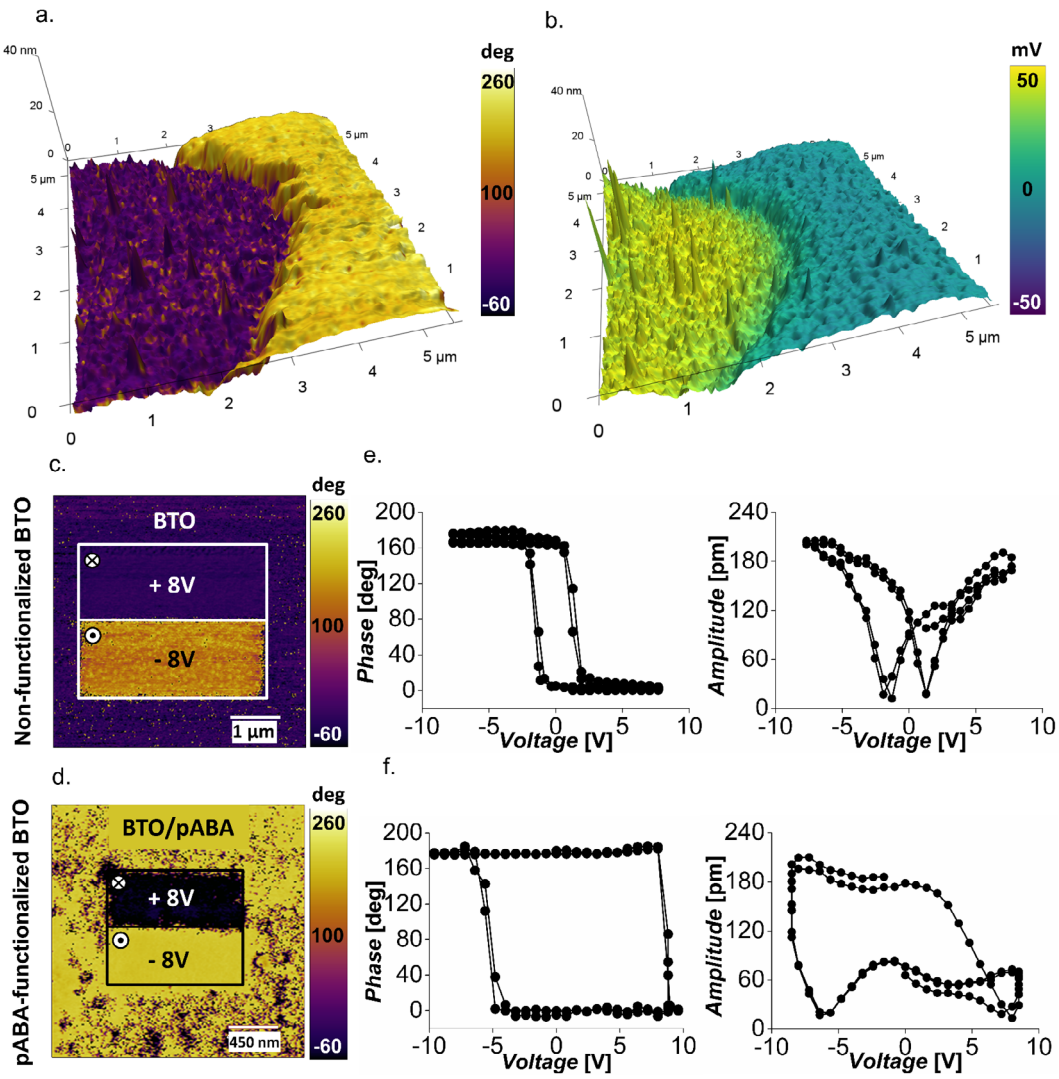

Figure 6.10 *PFM and KPFM characterization of sample D; (a) PFM phase and (b) CPD superimposed over 3D topography image, that correspond to the area denoted by dashed square in* ***Figure 6.9 d*** *and which comprises boundary region between pristine and pABA functionalized BTO. PFM phase is showing 180º difference between areas of pristine and pABA functionalized BTO indicating polarization switching; PFM Phase images obtained after electrical writing of the opposite polarity stripe-like domains (denoted by rectangles) by biased AFM tip on pristine (c) and pABA functionalized BTO (d) surfaces of sample D. Resulting PFM phase images are showing that pABA functionalized BTO surface keeps it's up-polarized state, while neighboring bare BTO switches polarization from as grown up- to down-polarized state; SS-PFM hysteresis loops of PFM amplitude and phase measured on (e) pristine and (f) pABA-functionalized BTO demonstrating increased coercivity in the presence of pABA molecules.*

triggered by uncontrolled environmental conditions, which caused destabilization of the up-polarized state, as schematically represented in **Figure 6.11**. Ferroelectric surfaces are electrochemically active and therefore every process that includes formation of charged species (ions) or highly reactive oxido-reducing species such as free radicals could trigger surface oxidation. The latter is always followed by negative charge loss, which in the case of up-

polarized BTO probably weakens screening and therefore could have direct impact on the up-polarized state stability. In our case, oxidation of water-mediated adsorbates on non-functionalized areas of the sample could also cause chemically-assisted polarization switching to preferred down-polarized state. Other possible causes include appearance of oxidizing hydroxyl OH· radicals[52] during heating/cooling related with functionalization process, change of local pH at the surface during solution deposition[19] or even radiation-mediated surface reactions.[12]

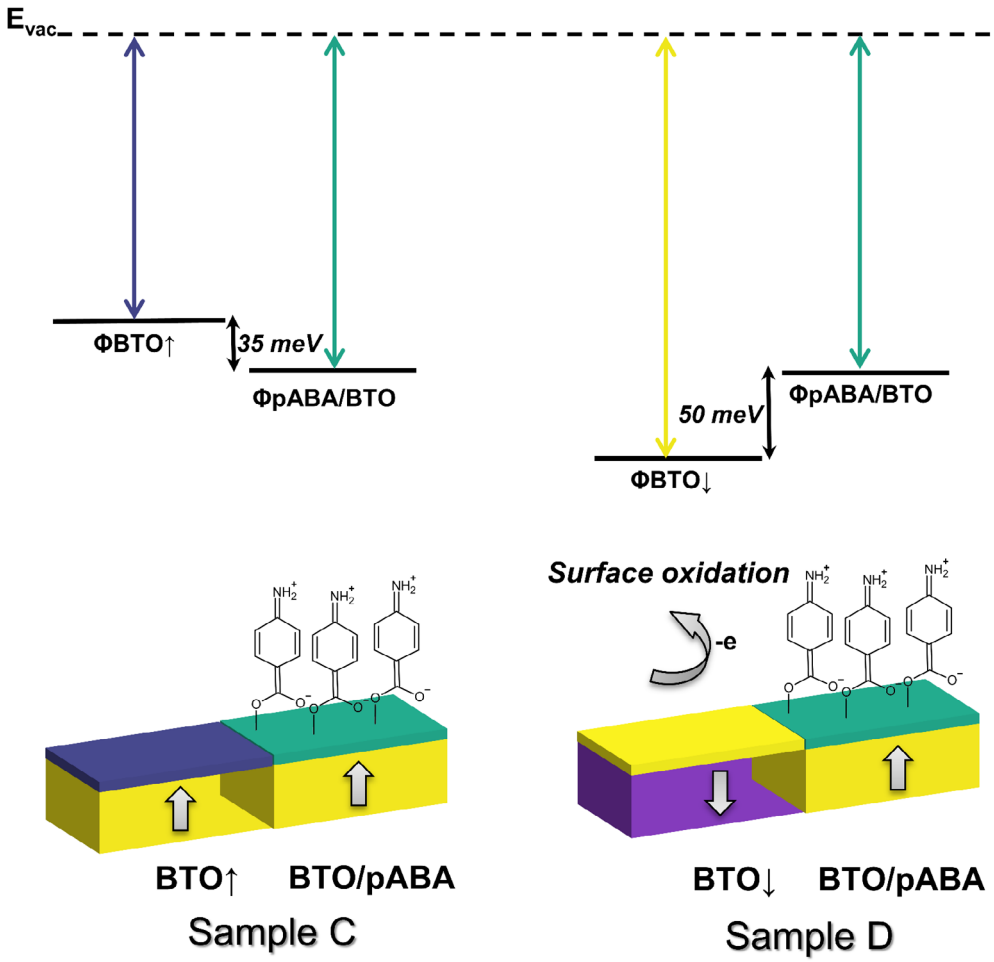

Figure 6.11 *Scheme of work functions of pristine and pABA functionalized surfaces for samples C and D, explaining the oxidation-protective role of the pABA capping layer; pABA molecules present in the functionalized areas prevented the spontaneous ferroelectric polarization switching observed for the exposed areas of the thin film.*

On the other hand, in Chapter 3 we have shown how exposure of sample to radiation or heating in vacuum could also lead to complete switch of ferroelectric polarization from up to down state. Here, we are not getting into the exact cause of oxidation process, but it is important to

stress out that due to the surface sensitivity of polar ferroelectric materials which mediate physics of their interior, these materials are highly susceptible to distinct modifications of their ferroelectric properties due to changes in ambient conditions such as temperature,[12] pressure[16] or even relative humidity.[12,17] In contrast, the chemically-modified BTO area was able to preserve its up-polarized state due to the presence of pABA protective molecular layer, which provides improved stability to functionalized areas.

6.6 Conclusions

In this chapter we have demonstrated the synthesis of hybrid organic-inorganic ferroelectric heterostructures and capacitors, composed of ferroelectric BTO thin films chemically coupled to electroactive pABA molecules. Aromatic pABA molecules are shown to be good candidates for the chemical functionalization of ferroelectric surfaces, able to replace naturally existing atmospheric adsorbates and create a controlled and electrically tunable screening layer.

We believe that the unique structural properties of aromatic pABA molecules, which allow the delocalization of electrons of benzene ring and its amino and carboxylic substituents over the whole system, lead to resonance structures (i.e. distinct configurations of the electronic charge density within the molecule) with different dipolar balance and consequently versatile response to polarization changes in the ferroelectric. Thanks to the chemical attachment of pABA molecules to the BTO surface, the ferroelectric polarization of the thin film becomes coupled to the stability of pABA resonance states, which in turn respond to the screening necessities of the underneath polarization by conforming their electronic density. In this regards, pABA molecules can be considered as self-regulating resonance structures for on-demand ferroelectric polarization screening and stabilization, as demonstrated by the increase of coercive voltage in the presence of pABA molecules in SS-PFM measurements.

In addition, it has been demonstrated that pABA molecules can be used as capping or protective layers of ferroelectric polarization against uncontrolled external parameters which can induce surface oxidation. It was shown that while unprotected BTO surfaces experience polarization reversal upon oxidation, pABA-functionalized areas remain with unchanged polarization, as demonstrated by PFM and ferroelectric lithography experiments. Therefore, the use of pABA molecules could provide two potential benefits to ferroelectric thin films: 1) improvement of ferroelectric phase stability in terms of coercive field increment and 2) they could be employed

as polarization-capping layer, able to “shield” polarization from uncontrollable environmental factors.

Finally, fabrication of capacitor-like graphene/pABA/BTO/SRO hybrid heterostructures revealed that chemical functionalization of ferroelectric interfaces using pABA molecules could be a useful pathway for stabilization of the polarization in thin film capacitors. This may be of particular interest in the case of ultra-thin films, whereby the polarization stability of ultra-thin films could be enhanced. In order to test this possibility, additional experiments on ultra-thin films will be needed. On the other note, substitution of benzene ring with the same groups but in different positions, e.g. ortho (oABA) or meta (mABA), could lead to different binding conformation of these molecules on BTO surfaces with distinctive coupling to the ferroelectric polarization, possibly causing different delocalization of electrons from those in para (p) position (if at all). These might be interesting topics of research for the future works.

Altogether, these results could have a strong impact in the field of interface engineering of nanodevices, whereby interfaces have a significant influence on the overall device performance, branching for example in ferroelectric tunnel junctions.

References

[1] S. V. Kalinin, Y. Kim, D. D. Fong, A. N. Morozovska, *Reports Prog. Phys.* **2018**, *81*, 036502.

[2] H. Lee, T. H. Kim, J. J. Patzner, H. Lu, J. W. Lee, H. Zhou, W. Chang, M. K. Mahanthappa, E. Y. Tsymbal, A. Gruverman, C. B. Eom, *Nano Lett.* **2016**, *16*, 2400.

[3] F. Liu, I. Fina, G. Sauthier, F. Sánchez, A. M. Rappe, J. Fontcuberta, *ACS Appl. Mater. Interfaces* **2018**, *10*, 23968.

[4] H. Lu, A. Lipatov, S. Ryu, D. J. Kim, H. Lee, M. Y. Zhuravlev, C. B. Eom, E. Y. Tsymbal, A. Sinitskii, A. Gruverman, *Nat. Commun.* **2014**, *5*, 1.

[5] A. Kakekhani, S. Ismail-Beigi, E. I. Altman, *Surf. Sci.* **2016**, *650*, 302.

[6] A. Kakekhani, S. Ismail-Beigi, *ACS Catal.* **2015**, *5*, 4537.

[7] A. Kakekhani, S. Ismail-Beigi, *J. Mater. Chem. A* **2016**, *4*, 5235.

[8] Y. Zhang, M. Xie, V. Adamaki, H. Khanbareh, C. R. Bowen, *Chem. Soc. Rev.* **2017**, *46*, 7757.

[9] C. Wang, N. Tian, T. Ma, Y. Zhang, H. Huang, *Nano Energy* **2020**, *78*, 105371.

[10] J. J. Segura, N. Domingo, J. Fraxedas, A. Verdaguer, *J. Appl. Phys.* **2013**, *113*, 0.

[11] N. Domingo, E. Pach, K. Cordero-Edwards, V. Pérez-Dieste, C. Escudero, A. Verdaguer, *Phys. Chem. Chem. Phys.* **2019**, *21*, 4920.

[12] I. Spasojevic, G. Sauthier, J. M. Caicedo, A. Verdaguer, N. Domingo, *Appl. Surf. Sci.* **2021**, *565*, 150288.

[13] J. L. Wang, F. Gaillard, A. Pancotti, B. Gautier, G. Niu, B. Vilquin, V. Pillard, G. L. M. P. Rodrigues, N. Barrett, *J. Phys. Chem. C* **2012**, *116*, 21802.

[14] R. P. Dahl-Hansen, J. M. Polfus, E. Vøllestad, B. Akkopru-Akgun, L. Denis, K. Coleman, F. Tyholdt, S. Trolier-Mckinstry, T. Tybell, *J. Appl. Phys.* **2020**, *127*, 0.

[15] N. Domingo, I. Gaponenko, K. Cordero-Edwards, N. Stucki, V. Pérez-Dieste, C. Escudero, E. Pach, A. Verdaguer, P. Paruch, *Nanoscale* **2019**, *11*, 17920.

[16] R. V. Wang, D. D. Fong, F. Jiang, M. J. Highland, P. H. Fuoss, C. Thompson, A. M. Kolpak, J. A. Eastman, S. K. Streiffer, A. M. Rappe, G. B. Stephenson, *Phys. Rev. Lett.*

2009, *102*, 2.

[17] J. Shin, V. B. Nascimento, G. Geneste, J. Rundgren, E. W. Plummer, B. Dkhil, S. V. Kalinin, A. P. Baddorf, *Nano Lett.* **2009**, *9*, 3720.

[18] M. J. Highland, T. T. Fister, M. I. Richard, D. D. Fong, P. H. Fuoss, C. Thompson, J. A. Eastman, S. K. Streiffer, G. B. Stephenson, *Phys. Rev. Lett.* **2010**, *105*, 1.

[19] Y. Tian, L. Wei, Q. Zhang, H. Huang, Y. Zhang, H. Zhou, F. Ma, L. Gu, S. Meng, L.-Q. Chen, C.-W. Nan, J. Zhang, *Nat. Commun.* **2018**, *9*, 3809.

[20] K. Chatterjee, S. Sarkar, K. Jagajjanani Rao, S. Paria, *Adv. Colloid Interface Sci.* **2014**, *209*, 8.

[21] A. E. Baumann, D. A. Burns, B. Liu, V. S. Thoi, *Commun. Chem.* **2019**, *2*, 1.

[22] C. Pereyra, H. Xie, M. Lira-Cantu, *J. Energy Chem.* **2021**, *60*, 599.

[23] I. Efe, N. A. Spaldin, C. Gattinoni, *J. Chem. Phys.* **2021**, *154*, 024702.

[24] Y. Yun, E. I. Altman, *J. Am. Chem. Soc.* **2007**, *129*, 15684.

[25] D. Li, M. H. Zhao, J. Garra, A. M. Kolpak, A. M. Rappe, D. A. Bonnell, J. M. Vohs, *Nat. Mater.* **2008**, *7*, 473.

[26] M. H. Zhao, D. A. Bonnell, J. M. Vohs, *Surf. Sci.* **2008**, *602*, 2849.

[27] Z. Zhang, R. González, G. Díaz, L. G. Rosa, I. Ketsman, X. Zhang, P. Sharma, A. Gruverman, P. A. Dowben, *J. Phys. Chem. C* **2011**, *115*, 13041.

[28] Z. Zhang, P. Sharma, C. N. Borca, P. A. Dowben, A. Gruverman, *Appl. Phys. Lett.* **2010**, *97*, 243702.

[29] Y. Zhao, S. Ippolito, P. Samorì, *Adv. Opt. Mater.* **2019**, *7*, 1900286.

[30] E. Coronado, *Nat. Rev. Mater.* **2020**, *5*, 87.

[31] G. Lovat, D. Forrer, M. Abadia, M. Dominguez, M. Casarin, C. Rogero, A. Vittadini, L. Floreano, *J. Phys. Chem. C* **2017**, *121*, 13738.

[32] S. V. Kalinin, D. A. Bonnell, T. Alvarez, X. Lei, Z. Hu, R. Shao, J. H. Ferris, *Adv. Mater.* **2004**, *16*, 795.

[33] S. V. Kalinin, D. A. Bonnell, T. Alvarez, X. Lei, Z. Hu, J. H. Ferris, Q. Zhang, S. Dunn, *Nano Lett.* **2002**, *2*, 589.

[34] P. Vollhardt, N. E. Shore, *Organic Chemistry: Structure and Function*, W.H. Freeman

& Co. Ltd, **2014**.

[35] A. P. Cismesia, G. R. Nicholls, N. C. Polfer, *J. Mol. Spectrosc.* **2017**, *332*, 79.

[36] L. Pauling, *J. Am. Chem. Soc.* **1931**, *53*, 3225.

[37] A. Perl, D. N. Reinhoudt, J. Huskens, *Adv. Mater.* **2009**, *21*, 2257.

[38] S. Yang, Y. Ishikawa, H. Itoh, Q. Feng, *J. Colloid Interface Sci.* **2011**, *356*, 734.

[39] B. Li, Y. Chen, Z. Liang, D. Gao, W. Huang, *RSC Adv.* **2015**, *5*, 94290.

[40] A. Tanskanen, M. Karppinen, *Sci. Rep.* **2018**, *8*, 1.

[41] Y. X. Weng, L. Li, Y. Liu, L. Wang, G. Z. Yang, *J. Phys. Chem. B* **2003**, *107*, 4356.

[42] A. N. Morozovska, E. A. Eliseev, N. V. Morozovsky, S. V. Kalinin, *Phys. Rev. B* **2017**, *95*, 1.

[43] P. Zubko, H. Lu, C. W. Bark, X. Martí, J. Santiso, C. B. Eom, G. Catalan, A. Gruverman, *J. Phys. Condens. Matter* **2017**, *29*, 284001.

[44] M. Stengel, N. A. Spaldin, *Nature* **2006**, *443*, 679.

[45] A. K. Tagantsev, G. Gerra, *J. Appl. Phys.* **2006**, *100*, 51607.

[46] T. Li, A. Lipatov, H. Lu, H. Lee, J.-W. Lee, E. Torun, L. Wirtz, C.-B. Eom, J. Íñiguez, A. Sinitskii, A. Gruverman, *Nat. Commun.* **2018**, *9*, 3344.

[47] T. Li, P. Sharma, A. Lipatov, H. Lee, J. W. Lee, M. Y. Zhuravlev, T. R. Paudel, Y. A. Genenko, C. B. Eom, E. Y. Tsymbal, A. Sinitskii, A. Gruverman, *Nano Lett.* **2017**, *17*, 922.

[48] Y. Li, X. Y. Sun, C. Y. Xu, J. Cao, Z. Y. Sun, L. Zhen, *Nanoscale* **2018**, *10*, 23080.

[49] K. Cordero-Edwards, L. Rodríguez, A. Calò, M. J. Esplandiu, V. Pérez-Dieste, C. Escudero, N. Domingo, A. Verdaguer, *J. Phys. Chem. C* **2016**, *120*, 24048.

[50] K. S. Novoselov, A. K. Geim, S. V. Morozov, D. Jiang, Y. Zhang, S. V. Dubonos, I. V. Grigorieva, A. A. Firsov, *Science* **2004**, *306*, 666.

[51] S. Ullah, X. Yang, H. Q. Ta, M. Hasan, A. Bachmatiuk, K. Tokarska, B. Trzebicka, L. Fu, M. H. Rummeli, *Nano Res.* **2021**, *14*, 3756.

[52] C. Wang, N. Tian, T. Ma, Y. Zhang, H. Huang, *Nano Energy* **2020**, *78*, 105371.

CHAPTER 7

Conclusions

The purpose of this thesis was to explore the interplay between ferroelectric properties and surface chemistry in $BaTiO_3$. My first goal was optimization of conditions for $BaTiO_3$ epitaxial thin films growth by pulsed laser deposition, to achieve well-defined reproducible ferroelectric properties. This enabled the use of thin films with similar surface composition and ferroelectric properties throughout different experiments in this thesis.

Surface chemical composition of $BaTiO_3$ samples and its correlation with ferroelectric properties and domain orientation was studied in different conditions and time frames by XPS, PFM and XRD, whereby the following conclusions are made:

- Surface chemical composition of monodomain $BaTiO_3$ thin film, barely exposed to ambient after the growth, evidences that its surface already contains adsorbate species such as molecular H_2O and surface OH groups, stemming from water dissociation reactions happening readily upon surface exposure, as well as products of surface oxidation in the form of Ti-peroxo complex compounds.

- Measurements of the hitherto scarcely-studied Ba 3d spectral region show the presence of an additional specie, namely barium peroxide (BaO_2), detected unequivocally for the first time after annealing in O_2 atmosphere, which is ubiquitous in all $BaTiO_3$ surfaces studied in this thesis.

- I have found that annealing or exposing the samples to high flux X-rays in vacuum, triggers uniform polarization switching in $BaTiO_3$ thin films and changes their ferroelectric properties, such as coercive voltage and imprint of hysteresis loops.

- This surface charge-assisted polarization reversal became very valuable, since I could study the difference in adsorbates' concentration on $BaTiO_3$ surfaces as a function of polarization. I observed that down-polarized $BaTiO_3$ surfaces exhibit a higher concentration of oxidized surface species, revealing their enhanced oxidizing character. Furthermore, down-polarized surfaces of $BaTiO_3$ are also more hydrophilic.

- Diffraction and PFM measurements show that (100) $BaTiO_3$ single crystal exhibits different domain orientation in the bulk and near the surface (so called "skin"). Near-surface domain orientation further changes after the phase transition: mainly in-plane polarized single crystal ($a/c \approx 5$) becomes predominantly out-of-plane ($a/c \approx 0.2$) and down polarized after the first phase transition in low relative humidity conditions. Prevalence of out-of-plane down-polarized *c* domains after the phase transition can be related to the finding that down polarized surfaces are more hydrophilic, which may help to nucleate down polarization state.

- Dynamic in-situ AP-XPS experiments, performed during paraelectric-to-ferroelectric phase transition in water vapor atmosphere, uncovered abrupt changes in coverages of all adsorbed oxygen-containing species around the Curie temperature of $BaTiO_3$ single crystals. The most striking observation is that the concentration of adsorbed molecular water decreases sharply upon the emergence of ferroelectric polarization, while at the same time the concentration of surface OH groups and peroxide species rises. This is a direct experimental evidence of *ferrocatalytically*-assisted water dissociation, triggered by the emergence of downwards-oriented polarization and induced stray electric fields.

- The onset of ferroelectricity as the driving force for surface redox reactions has been corroborated by following the surface charge dynamics during the paraelectric-to-ferroelectric transition. The time period of the experimentally observed enhanced ferrocatalytic activity is of the same order as the time during which down-polarized surface

remains charge-imbalanced after the phase transition to ferroelectric state bellow T_c, evidenced by the divergence of photoelectrons' kinetic energy.

Since the interaction between ferroelectric polarization and the surface chemistry is bidirectional, I focused my next efforts on studying the effect of relative humidity and water on ferroelectric polarization dynamics by PFM. The following conclusions can be drawn:

- Writing of ferroelectric stripe-like domains in $BaTiO_3$ thin films, performed in wide range of RH between 2.5 % and 60 %, demonstrates that the critical speed for domain writing increases non-monotonically with humidity: while for RH above 20 % domains can be written at speeds of 600 μm/s or faster, in dry atmospheres with RH below 5 % the critical writing speed slows down to below 60 μm/s.

- The logarithm of domains' size shows linear dependence on the writing speed logarithm, with increasing negative slopes as RH decreases, pointing out to the highest sensitivity of the domain size to the writing speed in dry conditions, caused by the overall unfavourable screening.

- Domain walls dynamics perpendicular to the tip scanning speed demonstrates creep-like motion of domain walls, with a dynamic coefficient μ dependent on RH conditions. This suggests that domain wall motion is influenced by two different mechanisms below and above critical value of RH ~ 10 %: while below 10 %, due to the presumably poor screening conditions, creep-like domain wall motion is mostly governed by internal pinning potentials, for RH > 10 % external screening by surface charges becomes more efficient and switching dynamics is dominated by the mobility of charges able to reach the screening front.

- Characteristic dependence of the domain size as a function of RH at constant writing speed closely resembles the measured dependence of the adsorbed water layer thickness as a function of RH (called *adsorption isotherm*), therefore highlighting the important influence of *adsorbed water thickness* on the observed domain sizes.

- The characteristic shape of water adsorption isotherms, generally measured on oxide surfaces, and also observed in our case, may result from the distinct structures that water molecules form on the surface upon adsorption, namely ice-like, liquid-like, or their co-

existence. This is of particular importance for ferroelectric surfaces, since existence of different *water structures* as a function of RH could impose distinct dipolar and ionic screening capabilities of such layers, altogether influencing the stability, size, critical writing speed and even domain wall creep dynamics of ferroelectric domains.

- Calculations of the lateral extent of water meniscus show that it has negligible effect on the domain size, given that its calculated thermodynamic radius in static limit, unfeasible in our dynamic conditions, stays bellow the size of our smallest domains of ≈ 40 nm.

I have also demonstrated that deliberate functionalization of BaTiO3 thin films with aromatic para-aminobenzoic acid molecules, characterized by a tunable delocalized electronic configuration, can provide several potential benefits to ferroelectric thin films, namely:

- With respect to surface functionalization, it has been found that ABA molecules chemically attach to hydroxylized ferroelectric surfaces via the formation of ester bonds.

- Coupling of aromatic pABA molecules with ferroelectricity provides efficient and versatile electric screening via changes in molecules' electronic configuration, imposed by the polarization direction of the ferroelectric underneath. Such organic/ferroelectric hybrid heterostructure shows enhanced polarization stability of both polar states, observed as an increase of coercive voltage.

- pABA molecules act as "protective" polarization-capping layer, shielding ferroelectric polarization from detrimental and often uncontrollable environmental factors.

- Enhanced stability of hybrid pABA/ferroelectric structures is extended when these are incorporated into the capacitors with multilayer graphene top electrodes, allowing the control of the BTO/graphene interface composition.

Future work

Beyond answering all the scientific questions exposed above, the research developed in this thesis has also opened some new avenues that may deserve the attention for the future research work:

- Considering that the same growth conditions were successfully employed for the preparation of epitaxial $BaTiO_3$ thin film on different scandate substrates with preferential up-polarized state, it would be of interest to explore the possible influence of substrate and strain on the ferroelectric surface chemical composition and redox activity.

- Pyrocatalytic reactions around the Curie point could be further investigated on several ways: i) by following evolution of Ti 2p, Ba 3d and C 1s spectral regions as a function of temperature, in order to gain complementary information about the surface redox activity, ii) by performing the experiment at higher cooling rates, which should further enhance the concentration of catalytic products and iii) it would be useful to incorporate high-sensitivity gas detectors within XPS set-up, that would allow to measure in-situ low concentrations of potentially surface desorbed gases during heat/cool cycles, such as H_2, which is not possible to detect in AP-XPS experiments.

- In the frame of ferroelectric lithography experiments in different RH conditions, one could perform similar experiment on as-grown down-polarized surfaces. Due to the different hydrophilicity of up- and down- polarized surfaces, we should expect that the critical writing speed, domain switching dynamics and domain size as a function of RH should be different in these two cases. Additionally, it would be of interest to study how the mechanical writing of stripe-like ferroelectric domains (i.e. by inducing stress by non-biased AFM tip) in the same RH range affects the critical writing speed.

- Finally, another interesting opportunity for the future work would be to explore how the substitution of benzene ring by the same groups but in different positions, e.g. in ortho (oABA) or meta (mABA), would affect screening on ferroelectric surfaces. The latter could be affected by different binding conformations of the molecules on the $BaTiO_3$ surface and also different resonant structures from those in para (p) position, which would have direct influence on ferroelectric polarization screening. On the other hand, in the case

of ultra-thin films typically used in FTJ applications for which stable polarization state is essential yet hard to achieve, owing to the reduced thickness of the capacitors, the functionalization with pABA molecules might be a useful strategy to increase ferroelectric phase stability and tunneling electroresistance.